



**Bulletin 54
(Part 3 of 3 Parts)**

AD-A148 133

THE SHOCK AND VIBRATION BULLETIN

**Part 3
Structural Dynamics,
Machinery Dynamics and
Vibration Problems**

JUNE 1984

**A Publication of
THE SHOCK AND VIBRATION
INFORMATION CENTER
Naval Research Laboratory, Washington, D.C.**



**DTIC
ELECTE**
AUG 15 1984
S
A

**Office of
The Under Secretary of Defense
for Research and Engineering**

Approved for public release; distribution unlimited.

84 08 09 048

DTIC FILE COPY

SYMPOSIUM MANAGEMENT

THE SHOCK AND VIBRATION INFORMATION CENTER

J. Gordan Showalter, Acting Director

Rudolph H. Volin

Jessica Hileman

Elizabeth A. McLaughlin

Mary K. Gobbett

Bulletin Production

**Publications Branch, Technical Information Division,
Naval Research Laboratory**

**Bulletin 54
(Part 3 of 3 Parts)**

THE SHOCK AND VIBRATION BULLETIN

JUNE 1984

**A Publication of
THE SHOCK AND VIBRATION
INFORMATION CENTER
Naval Research Laboratory, Washington, D.C.**

The 54th Symposium on Shock and Vibration was held in Pasadena, California, October 18-20, 1983. The Jet Propulsion Laboratory in Pasadena was the host.

**Office of
The Under Secretary of Defense
for Research and Engineering**



CONTENTS

PAPERS APPEARING IN PART 3

Structural Dynamics

A-1

STRUCTURAL MODIFICATIONS BY VISCOELASTIC ELEMENTS; 1
P. J. Riehle, Anatrol Corporation, Cincinnati, OH

STOCHASTIC DYNAMIC ANALYSIS OF A STRUCTURE WITH FRICTIONAL JOINTS 11
Q. L. Tian and Y. B. Liu, Institute of Mechanics, Chinese Academy of Sciences and D. K. Liu,
Space Science & Technology Centre, Chinese Academy of Sciences, Beijing, China

MODAL ANALYSIS OF STRUCTURAL SYSTEMS INVOLVING NONLINEAR COUPLING 19
R. A. Ibrahim, T. D. Woodall, and H. Heo, Department of Mechanical Engineering, Texas Tech
University, Lubbock, TX

DISCRETE MODIFICATIONS TO CONTINUOUS DYNAMIC STRUCTURAL SYSTEMS 29
Y. Okada, Ibaraki University, Hitachi, Japan, B. P. Wang, University of Texas at Arlington,
Arlington, TX, and W. D. Pilkey, University of Virginia, Charlottesville, VA

REANALYSIS OF CONTINUOUS DYNAMIC SYSTEMS WITH CONTINUOUS MODIFICATIONS 35
B. P. Wang, University of Texas at Arlington, Arlington, TX, Y. Okada, Ibaraki University, Hitachi, Japan,
and W. D. Pilkey, University of Virginia, Charlottesville, VA

A POLE-FREE REDUCED-ORDER CHARACTERISTIC DETERMINANT METHOD FOR LINEAR VIBRATION
ANALYSIS BASED ON SUB-STRUCTURING 43
B. Dawson, Polytechnic of Central London, London, England, and M. Davies, University of Surrey,
Guildford, Surrey, England

DETERMINATION OF SHEAR COEFFICIENT OF A GENERAL BEAM CROSS SECTION BY FINITE
ELEMENT METHOD 51
C. M. Friedrich and S. C. Lin, Westinghouse Electric Corporation, Bettis Atomic Power Laboratory,
West Mifflin, PA

Machinery Dynamics

GEAR CASE VIBRATION ISOLATION IN A GEARED TURBINE GENERATOR 59
R. P. Andrews, Westinghouse Electric Corporation, Marine Division, Sunnyvale, CA

EFFECT OF COUPLED TORSIONAL-FLEXURAL VIBRATION OF A GEARED SHAFT SYSTEM ON THE
DYNAMIC TOOTH LOAD 67
S. V. Neriya, R. B. Bhat, and T. S. Sankar, Concordia University, Montreal, Quebec, Canada

PRECISION MEASUREMENT OF TORSIONAL OSCILLATIONS INDUCED
BY GEAR ERRORS 77
S. L. Shmutter, Ford Motor Company, Manufacturing Processes Laboratory, Dearborn, MI

THE ANALYSIS BY THE LUMPED PARAMETER METHOD OF BLADE PLATFORM FRICTION
DAMPERS USED IN THE HIGH PRESSURE FUEL TURBOPUMP OF THE
SPACE SHUTTLE MAIN ENGINE 89
R. J. Dominic, University of Dayton Research Institute, Dayton, OH

Vibration Problems

TRANSIENT VIBRATION TEST CRITERIA FOR SPACECRAFT HARDWARE 99
D. L. Kern and C. D. Hayes, Jet Propulsion Laboratory, California Institute of Technology, Pasadena, CA

VIBRATIONAL LOADING MECHANISM OF UNITIZED CORRUGATED CONTAINERS WITH
CUSHIONS AND NON-LOAD-BEARING CONTENTS 111
T. J. Urbanik, Forest Products Laboratory, USDA Forest Service, Madison, WI

LEAKAGE-FLOW INDUCED VIBRATIONS OF A CHIMNEY STRUCTURE SUSPENDED IN A LIQUID FLOW	123
H. Chung, Components Technology Division, Argonne National Laboratory, Argonne, IL	
THE EXPERIMENTAL PERFORMANCE OF AN OFF-ROAD VEHICLE UTILIZING A SEMI-ACTIVE SUSPENSION	135
E. J. Krasnicki, Lord Corporation, Erie, PA	
EFFECT OF AIR CAVITY ON THE VIBRATION ANALYSIS OF LOADED DRUMS	143
S. De, National Research Institute, W. Bengal, India	

PAPERS APPEARING IN PART 1

Welcome

WELCOME

Robert J. Parks, Associate Director, Space Science and Exploration, Jet Propulsion Laboratory, Pasadena, CA

Keynote Address

KEYNOTE ADDRESS

Robert S. Ryan, George C. Marshall Space Flight Center, Huntsville, AL

Invited Papers

DNA ICBM TECHNICAL R&D PROGRAM

Colonel Maxim I. Kovel, Director, Shock Physics Directorate, Defense Nuclear Agency, Washington, DC

SOME DYNAMICAL ASPECTS OF ARMY MISSILE SYSTEMS

Dr. James J. Richardson, Chief, Structures and Mechanics, U.S. Army Missile Command, Redstone Arsenal, AL

AIR FORCE SPACE TECHNOLOGY CENTER SPACE TECHNOLOGY – EMPHASIS 84

Colonel Frank J. Redd, Vice Commander, Air Force Space Technology Center, Kirtland AFB, NM

REFLECTIONS ON TRENDS IN DYNAMICS – THE NAVY'S PERSPECTIVE

Henry C. Pusey, Consultant, NKF Engineering Associates, Inc., Vienna, VA

ELIAS KLEIN MEMORIAL LECTURE – MODAL TESTING – A CRITICAL REVIEW

Strether Smith, Lockheed Palo Alto Research Laboratory, Palo Alto, CA

SOLUTIONS TO STRUCTURAL DYNAMICS PROBLEMS

Dr. George Morosow, Martin Marietta Corporation, Denver, CO

WHERE IS THE REAL LITERATURE ON AIRBLAST AND GROUND SHOCK?

Dr. Wilfred E. Baker, Southwest Research Institute, San Antonio, TX

MIL-STD-810D

TAILORING INITIATIVES FOR MIL-STD-810D ENVIRONMENTAL TEST METHODS AND ENGINEERING GUIDELINES

David L. Earls, Air Force Wright Aeronautical Laboratories, Wright-Patterson AFB, OH

ACCELERATION RESPONSES OF TYPICAL LRU'S SUBJECTED TO BENCH HANDLING AND INSTALLATION SHOCK

H. Caruso and E. Szymkowiak, Westinghouse Electric Corporation, Baltimore, MD

IMPACT OF 810D ON DYNAMIC TEST LABORATORIES

Dr. Allen J. Curtis, Hughes Aircraft Company, El Segundo, CA

THE CHANGING VIBRATION SIMULATION FOR MILITARY GROUND VEHICLES

Jack Robinson, Materials Testing Directorate, Aberdeen Proving Ground, MD

PANEL DISCUSSION – MIL-STD-810D

PAPERS APPEARING IN PART 2

Ship Shock

TWO-DIMENSION SHOCK RESPONSE OF A MASS ON ENERGY-ABSORBING SHOCK MOUNTS

R. E. Fortuna and V. H. Neubert, The Pennsylvania State University, University Park, PA

OPTIMUM DESIGN FOR NONLINEAR SHOCK MOUNTS FOR TRANSIENT INPUTS

K. Kasraie, Firestone Tire & Rubber Company, Central Research Laboratories, Akron, OH and V. H. Neubert, The Pennsylvania State University, University Park, PA

THE DEVELOPMENT OF A METHOD FOR THE SHOCK-RESISTANT SECURING OF LARGE BATTERIES IN SUBMARINES

A. Jansen, Royal Netherlands Navy, The Hague

SHIPBOARD SHOCK RESPONSE OF THE MODEL STRUCTURE DSM; EXPERIMENTAL RESULTS VERSUS RESPONSES PREDICTED BY EIGHT PARTICIPANTS

R. Regoord, TNO-IWECO, Delft, the Netherlands

DIRECT ENERGY MINIMIZATION APPROACH TO WHIPPING ANALYSIS OF PRESSURE HULLS

K. A. Bannister, Naval Surface Weapons Center, White Oak, Silver Spring, MD

Shock

WATER IMPACT LABORATORY AND FLIGHT TEST RESULTS FOR THE SPACE SHUTTLE SOLID ROCKET BOOSTER AFT SKIRT

D. A. Kross, NASA/Marshall Space Flight Center, Marshall Space Flight Center, AL, N. C. Murphy, United Space Boosters, Inc., Huntsville, AL, and E. A. Rawls, Chrysler Corporation, New Orleans, LA

AN OBJECTIVE ERROR MEASURE FOR THE COMPARISON OF CALCULATED AND MEASURED TRANSIENT RESPONSE HISTORIES

T. L. Geers, Lockheed Palo Alto Research Laboratory, Palo Alto, CA

ALTERNATIVE SHOCK CHARACTERIZATIONS FOR CONSISTENT SHOCK TEST SPECIFICATION

T. J. Beca, Sandia National Laboratories, Albuquerque, NM

SHOCK RESPONSE ANALYSIS BY PERSONAL COMPUTER USING THE EXTENDED IFT ALGORITHM

C. T. Morrow, Consultant, Encinitas, CA

LEAST FAVORABLE RESPONSE OF INELASTIC STRUCTURES

F. C. Chang, T. L. Paez, and F. Ju, The University of New Mexico, Albuquerque, NM

LOW VELOCITY, EXPLOSIVELY DRIVEN FLYER PLATE DESIGN FOR IMPACT FUZE DEVELOPMENT TESTING

R. A. Benham, Sandia National Laboratories, Albuquerque, NM

EXPERIMENTAL INVESTIGATION OF VIBROIMPACT OF TWO OSCILLATORS

C. N. Bapat and S. Sankar, Concordia University, Montreal, Quebec, Canada

MODELS FOR SHOCK DAMAGE TO MARINE STRUCTURAL MATERIALS

D. W. Nicholson, Naval Surface Weapons Center, White Oak, Silver Spring, MD

A STUDY OF THE EFFECT OF MASS LOADING ON THE SHOCK ENVIRONMENT

Q. Z. Wang, Beijing Institute of Strength and Environment Engineering, Beijing, China and H. B. Lin, Chinese Academy of Space Technology, Beijing, China

Blast and Ground Shock

ASSESSMENT OF SEISMIC SURVIVABILITY

R. E. McClellan, The Aerospace Corporation, El Segundo, CA

GROUND SHOCK EFFECT ON SOIL FIELD INCLUSIONS

R. E. McClellan, The Aerospace Corporation, El Segundo, CA

PENETRATION OF SHORT DURATION AIRBLAST INTO PROTECTIVE STRUCTURES

J. R. Britt and J. L. Drake, Applied Research Associates, Southern Division, Vicksburg, MS

A COMPUTATIONAL PROCEDURE FOR PEAK INSTRUCTURE MOTIONS AND SHOCK SPECTRA FOR CONVENTIONAL WEAPONS

S. A. Kiger, J. P. Balsara, and J. T. Baylot, USAE Waterways Experiment Station, Vicksburg, MS

PRELIMINARY DESIGN CRITERIA AND CERTIFICATION TEST SPECIFICATIONS FOR BLAST RESISTANT WINDOWS

G. E. Meyers, W. A. Keenan, and N. F. Shoemaker, Naval Civil Engineering Laboratory, Port Hueneme, CA

SESSION CHAIRMEN AND COCHAIRMEN

<u>Date</u>	<u>Session Title</u>	<u>Chairmen</u>	<u>Cochairmen</u>
Tuesday, 18 Oct. A.M.	Opening Session	Dr. Ben Wada, The Jet Propulsion Laboratory, Pasadena, CA	Dr. J. Gordan Showalter, The Shock & Vibration Information Center, Naval Research Laboratory, Washington, DC
Tuesday, 18 Oct. P.M.	Elias Klein Memorial Lecture Plenary A	Dr. J. Gordan Showalter, Shock and Vibration Information Center, Naval Research Laboratory Washington, DC	
Tuesday, 18 Oct. P.M.	Ship Shock	Mr. Gene Remmers, David Taylor Naval Ship Research and Development Center, Bethesda, MD	Dr. Michael Paksyta, NKF Engineering Associates, Vienna, VA
Tuesday, 18 Oct. P.M.	Space Vibration	Mr. Jerome Pearson, Air Force Wright Aeronautical Laboratories, Wright-Patterson AFB, OH	Mr. John Garba, Jet Propulsion Laboratory, Pasadena, CA
Wednesday, 19 Oct. A.M.	Plenary B	Mr. William J. Walker, Boeing Aerospace Company, Seattle, WA	Dr. George Morosow, Martin Marietta Corporation, Denver, CO
Wednesday, 19 Oct. A.M.	Structural Dynamics	Mr. Edward Fleming, The Aerospace Corporation, Los Angeles, CA	Dr. John Gubeer, McDonnell Douglas Astronautics Company, St. Louis, MO
Wednesday, 19 Oct. A.M.	MIL-STD-810D Session I, Rationale	Mr. John Wafford, Aeronautical Systems Division, Wright Patterson AFB, OH	Mr. Robert Hancock, Vought Corporation, Dallas, TX
Wednesday, 19 Oct. P.M.	Shock	Mr. Ami Frydman, Harry Diamond Laboratories, Adelphi, MD	Mr. Martin Walchak, Harry Diamond Laboratories, Adelphi, MD
Wednesday, 19 Oct. P.M.	MIL-STD-810D Session II, Implementation and Use	Mr. Rudolph H. Volin, Shock and Vibration Information Center, Washington, DC	Mr. W. W. Parmenter, Naval Weapons Center, China Lake, CA
Thursday, 20 Oct. A.M.	Blast/Ground Shock	Mr. William Flathau, U.S. Army Engineer Waterways Experiment Station, Vicksburg, MS	Mr. George Coulter, U.S. Army Ballistic Research Laboratory, Aberdeen Proving Ground, MD
Thursday, 20 Oct. A.M.	Machinery Dynamics	Dr. David Fleming, NASA Lewis Research Center, Cleveland, OH	Dr. Hanson Huang, Naval Surface Weapons Center, Silver Spring, MD
Thursday, 20 Oct. P.M.	Vibration Problems	Dr. Robert S. Reed, Jr., Naval Surface Weapons Center, Silver Spring, MD	Dr. Larry Pinson, NASA Langley Research Center, Hampton, VA
Thursday, 20 Oct. P.M.	Short Discussion Topics	Mr. Howard Camp, Jr., U.S. Army Electron Research and Development Command, Ft. Monmouth, NJ	Mr. E. Kenneth Stewart, U.S. Army Armament Research and Development Command, Picatinny Arsenal Dover, NJ

STRUCTURAL DYNAMICS

STRUCTURAL MODIFICATIONS BY VISCOELASTIC ELEMENTS

Paul J. Riehle
Anatrol Corporation
Cincinnati, Ohio

This paper describes a modeling technique which predicts the reduction in vibration transmitted from one structure to another through a viscoelastic isolation system. Analytical or experimental representations of structure compliances and viscoelastic element stiffness and damping values are used in the analysis. Predicted results of an isolation system are presented and compared to experimentally obtained results.

INTRODUCTION

The use of modal analysis as an effective tool for the definition and solution of structural noise and vibration problems has been increasing in recent years. One of the more interesting developments in this area deals with modeling individual components to predict the overall system behavior. Although this approach has been limited to low frequency ranges, it has enabled designers working on structural dynamics to recommend changes to each individual component and predict their effect on the overall system. The particular value of the modeling approach is that the dynamics of a complete system can be predicted if the dynamic properties of the individual components and their connecting elements are known. However, until recently those developments have been concentrated on the joining of structures by links of constant stiffness [1]. Such developments could be more useful to designers if such links could be of the viscoelastic type and the analysis extended to high frequency.

Introducing viscoelastic links between structures affects not only the damping; but, also the isolation characteristics. In this paper, a general impedance model is developed for joining two structures at a number of locations by viscoelastic elements. The model can be used to predict structural compliances of linked structures, vibration transmissibility and isolation effectiveness resulting from the dynamic characteristics of the viscoelastic links. The frequency range of analysis can be extended using the general impedance linking model because, unlike

present modal analysis linking techniques, it is not limited by the need to extract modal parameters. The general impedance linking model computations are performed on a frequency basis using physical coordinates rather than a modal parameter basis.

The predicted results will be based on knowing the directional and cross frequency response functions at each of the structural attachment points and the dynamic properties of the viscoelastic elements. The properties of the viscoelastic elements can be incorporated into the analysis in either of two different ways. The first is to use fixed stiffness and damping values for the element, which could be either assumed or measured experimentally. The second is to use the measured properties of the viscoelastic material along with the shape of the viscoelastic element to compute its stiffness and damping values [2] [3]. The properties of the viscoelastic material can be used in the program in the form of analytical functions of temperature, frequency, and static preload.

As an example two single-degree-of-freedom systems were linked together with a viscoelastic element at different temperatures and also with different thicknesses. Although the analysis is applicable to a wide range of damping and isolation situations, it will be verified experimentally in this paper for the case of an isolation problem where a compressor is mounted via four viscoelastic isolators to a flexible plate. The agreement between the measured and computed transmissibility is shown to be good over a wide frequency range.

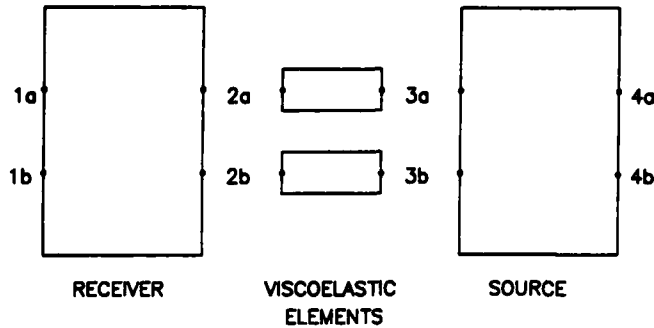


Figure 1: Block Diagram of System Model

ANALYSIS

The linking analysis assumes two bodies, a receiver and a source, to be joined together by two viscoelastic elements as shown in Figure 1. To predict the dynamic characteristics of the linked bodies it is necessary to know the compliance at the attachment points of the receiver and source structures and the stiffness and damping properties of the viscoelastic elements.

Extending the work performed by Klosterman [4] and VanLoon [5], the general impedance method [6] is used to derive the equations of motion of the system. By assuming only one direction of motion and adopting the sign conventions shown in Figure 2, it can be shown that:

$$H_{1a1a}F_{1a} + H_{1a1b}F_{1b} + H_{1a2a}F_{2a} + H_{1a2b}F_{2b} = X_{1a} \quad (1)$$

$$H_{1b1a}F_{1a} + H_{1b1b}F_{1b} + H_{1b2a}F_{2a} + H_{1b2b}F_{2b} = X_{1b} \quad (2)$$

$$H_{2a1a}F_{1a} + H_{2a1b}F_{1b} + H_{2a2a}F_{2a} + H_{2a2b}F_{2b} = X_{2a} \quad (3)$$

$$H_{2b1a}F_{1a} + H_{2b1b}F_{1b} + H_{2b2a}F_{2a} + H_{2b2b}F_{2b} = X_{2b} \quad (4)$$

where:

X_i = displacement at point i ,
 F_j = force at point j , and

$$H_{ij} = \frac{X_i}{F_j} = \begin{cases} \text{directional compliance} \\ \text{between point } i \text{ and } j \text{ when} \\ i=j, \text{ or} \\ \text{cross compliance between} \\ \text{point } i \text{ and } j \text{ when } i \neq j. \end{cases}$$

Rewriting in matrix form:

$$\begin{bmatrix} H_{1a1a} & H_{1a1b} \\ H_{1b1a} & H_{1b1b} \end{bmatrix} \begin{Bmatrix} F_{1a} \\ F_{1b} \end{Bmatrix} + \begin{bmatrix} H_{1a2a} & H_{1a2b} \\ H_{1b2a} & H_{1b2b} \end{bmatrix} \begin{Bmatrix} F_{2a} \\ F_{2b} \end{Bmatrix} = \begin{Bmatrix} X_{1a} \\ X_{1b} \end{Bmatrix} \quad (5)$$

$$\begin{bmatrix} H_{2a1a} & H_{2a1b} \\ H_{2b1a} & H_{2b1b} \end{bmatrix} \begin{Bmatrix} F_{1a} \\ F_{1b} \end{Bmatrix} - \begin{bmatrix} H_{2a2a} & H_{2a2b} \\ H_{2b2a} & H_{2b2b} \end{bmatrix} \begin{Bmatrix} F_{2a} \\ F_{2b} \end{Bmatrix} = \begin{Bmatrix} X_{2a} \\ X_{2b} \end{Bmatrix} \quad (6)$$

simplifying:

$$[H_{11R}] \{F_1\} + [H_{12R}] \{F_2\} = \{X_1\} \quad (7)$$

$$[H_{21R}] \{F_1\} + [H_{22R}] \{F_2\} = \{X_2\} \quad (8)$$

where the subscript R indicates compliance measurements on the receiving structure.

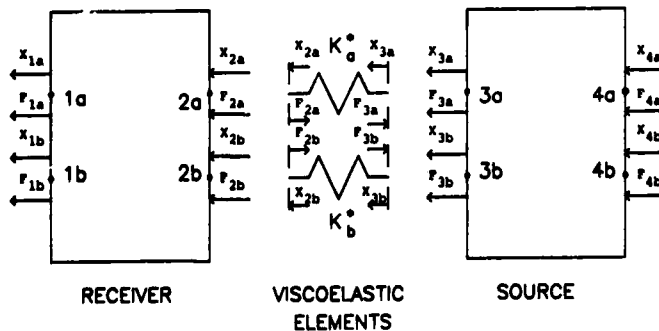


Figure 2: General Impedance Symbol and Sign Convention

Similarly the equations of motion for the source become:

$$\begin{matrix} H_{3a3a} & H_{3a3b} & F_{3a} + & H_{3a4a} & H_{3a4b} & F_{4a} = & X_{3a} \\ H_{3b3a} & H_{3b3b} & F_{3b} + & H_{3b4a} & H_{3b4b} & F_{4b} = & X_{3b} \\ H_{4a3a} & H_{4a3b} & F_{3a} + & H_{4a4a} & H_{4a4b} & F_{4a} = & X_{4a} \\ H_{4b3a} & H_{4b3b} & F_{3b} + & H_{4b4a} & H_{4b4b} & F_{4b} = & X_{4b} \end{matrix}$$

simplifying:

$$[H_{33S}] \{F_3\} + [H_{34S}] \{F_4\} = \{X_3\} \quad (11)$$

$$[H_{43S}] \{F_3\} + [H_{44S}] \{F_4\} = \{X_4\} \quad (12)$$

where the subscript S indicates compliance measurements on the source structure. The components of equations (7), (8), (11), and (12) may be expanded to include many attachment points with up to three directions of motion for each point.

If the viscoelastic elements are assumed to be massless links and either extended or compressed in only one direction, their equations of motion are:

$$K_a^* (X_{3a} - X_{2a}) = F_{2a} \quad (13)$$

$$K_b^* (X_{3b} - X_{2b}) = F_{2b} \quad (14)$$

$$K_a^* (X_{2a} - X_{3a}) = F_{3a} \quad (15)$$

$$K_b^* (X_{2b} - X_{3b}) = F_{3b} \quad (16)$$

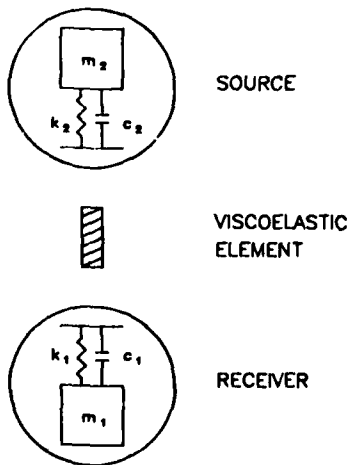


Figure 3: Linked Single Degree-of-Freedom Systems Model

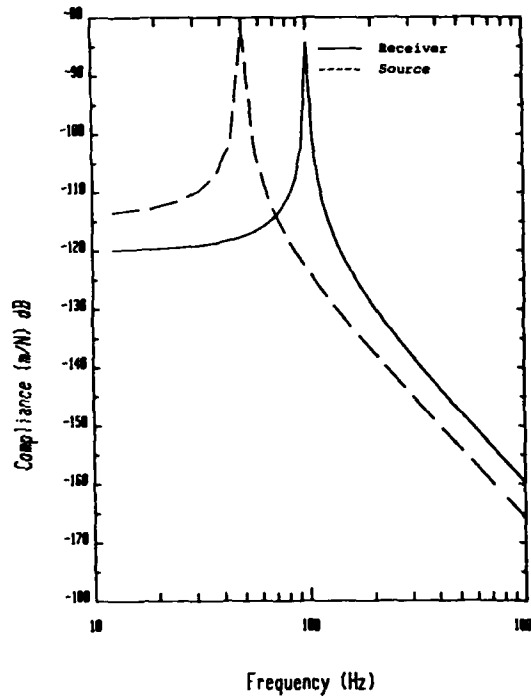


Figure 4: Compliance of Single Degree-of-Freedom Systems

where $K^* = k(1+jn)$ = complex stiffness

and k and n are the stiffness and loss factor of the viscoelastic element, respectively.

Rewriting in matrix form:

$$\begin{matrix} K_a^* & 0 & X_{3a} & -K_a^* & 0 & X_{2a} & = & F_{2a} \\ 0 & K_b^* & X_{3b} & 0 & K_b^* & X_{2b} & = & F_{2b} \end{matrix} \quad (17)$$

$$\begin{matrix} K_a^* & 0 & X_{2a} & -K_a^* & 0 & X_{3a} & = & F_{3a} \\ 0 & K_b^* & X_{2b} & 0 & K_b^* & X_{3b} & = & F_{3b} \end{matrix} \quad (18)$$

simplifying:

$$[K^*] \{X_3\} - [K^*] \{X_2\} = \{F_2\} \quad (19)$$

$$[K^*] \{X_2\} - [K^*] \{X_3\} = \{F_3\} \quad (20)$$

The components of equations (19) and (20) may likewise be expanded to include many viscoelastic elements with up to three directions of motion for each element.

The dynamic compliances, H, and the complex stiffnesses, K, of the system can be obtained from experimental data, analytical expressions, or a combination of the two. If

experimental compliance data is to be used and the modal density is low, the amount of data which needs to be measured can be reduced by using a curve fitting technique such as the complex exponential algorithm [7] to complete the compliance matrix. If the modal density is high over a desired frequency band, the frequency band can be subdivided into bands which have lower modal density or all the data needed for the compliance matrix can be measured directly. Likewise, experimental or analytical expressions can be used to describe the complex stiffness of the viscoelastic elements.

Provided that compliances and complex stiffnesses can be measured or predicted, the system equations can be solved simultaneously. Combining equations (7), (8), (11), (12), (19), and (20) into matrix form gives:

$$\begin{bmatrix} 1 & 0 & 0 & 0 & K^* & -K^* \\ 0 & 1 & 0 & 0 & -K^* & K^* \\ -H_{12R} & 0 & 1 & 0 & 0 & 0 \\ 0 & -H_{43S} & 0 & 1 & 0 & 0 \\ -H_{22R} & 0 & 0 & 0 & 1 & 0 \\ 0 & -H_{33S} & 0 & 0 & 0 & 1 \end{bmatrix} \begin{Bmatrix} F_2 \\ F_3 \\ X_1 \\ X_4 \\ X_2 \\ X_3 \end{Bmatrix} = \begin{Bmatrix} 0 \\ 0 \\ H_{11R}F_1 \\ H_{44S}F_4 \\ H_{21R}F_1 \\ H_{34S}F_4 \end{Bmatrix} \quad (21)$$

After several row and column operations, equation (21) becomes:

$$\begin{bmatrix} 1 & 0 & 0 & 0 & K^* & -K^* \\ 0 & 1 & 0 & 0 & -K^* & K^* \\ -H_{12R} & 0 & 1 & 0 & 0 & 0 \\ 0 & -H_{43S} & 0 & 1 & 0 & 0 \\ 0 & 0 & 0 & 0 & 1+H_{22R}K^* & -H_{22R}K^* \\ 0 & 0 & 0 & 0 & -H_{33S}K^* & 1+H_{33S}K^* \end{bmatrix} \begin{Bmatrix} F_2 \\ F_3 \\ X_1 \\ X_4 \\ X_2 \\ X_3 \end{Bmatrix} = \begin{Bmatrix} 0 \\ 0 \\ G_{11R}F_1 \\ G_{44S}F_4 \\ H_{21R}F_1 \\ H_{34S}F_4 \end{Bmatrix}$$

Equation (22) can then be partitioned and the following matrix equation extracted:

$$\begin{bmatrix} 1+H_{22R}K^* & -H_{22R}K^* \\ -H_{33S}K^* & 1+H_{33S}K^* \end{bmatrix} \begin{Bmatrix} X_2 \\ X_3 \end{Bmatrix} = \begin{Bmatrix} H_{21R}F_1 \\ H_{34S}F_4 \end{Bmatrix} \quad (23)$$

At this time two assumptions can be made. First, all the elements in the vector $\{F_i\}$ are zero, thus the product, $-G_{21R}F_1$, is zero. This is true if the points 1a and 1b in Figure 2 do not have an external force applied to them. Second, if the force output of the source can be characterized, it must be input through the points, 4a and 4b, shown in Figure 2. If only the relative magnitude

of the displacement vectors $\{X_2\}$ and $\{X_3\}$ are desired, the magnitude of F_4 is arbitrary. Now matrix equation (23) becomes:

$$\begin{bmatrix} 1+H_{22R}K^* & -H_{22R}K^* \\ -H_{33S}K^* & 1+H_{33S}K^* \end{bmatrix} \begin{Bmatrix} X_2 \\ X_3 \end{Bmatrix} = \begin{Bmatrix} 0 \\ H_{34S}F_4 \end{Bmatrix} \quad (24)$$

where F_4 may be a known quantity or an arbitrary constant. From this set of equations $\{X_2\}$ and $\{X_3\}$ can be determined. The remaining unknowns from matrix equation (22) can be found with the following equations:

$$\{F_2\} = [K^*] \{X_3\} - [K^*] \{X_2\} \quad (25)$$

$$\{F_3\} = [K^*] \{X_2\} - [K^*] \{X_3\} \quad (26)$$

$$\{X_1\} = [H_{11R}] \{F_1\} + [H_{12R}] \{F_2\} \quad (27)$$

noting again that $\{F_1\}=0$, equation (27) becomes:

$$\{X_1\} = [H_{12R}] \{F_2\} \quad (28)$$

Also:

$$\{X_4\} = [H_{44S}] \{F_4\} + [H_{43S}] \{F_3\} \quad (29)$$

If $\{F_4\}$ is a known quantity, these equations will yield correct force and displacement values; otherwise, the values will be relative to the arbitrary value of force $\{F_4\}$. Equations (24) through (26), (28) and (29) can be solved for any number of discrete frequency values to generate the displacements, $\{X_1\}$, $\{X_2\}$, $\{X_3\}$, and $\{X_4\}$, and the forces, $\{F_2\}$ and $\{F_3\}$, over a specified frequency band. Since the analysis can be performed on compliance data directly, the need for extracting modal parameters as required by other structural modification techniques [1] is eliminated. This type of analysis is very advantageous when the structures to be modified or coupled possess high modal density over the frequency band of interest.

Of particular interest when structures are coupled by viscoelastic elements is the isolation performance of the viscoelastic element. One measure of isolation performance is displacement transmissibility, defined as the ratio of the displacement of the receiver to the displacement of the source. A transmissibility measurement across a viscoelastic element in Figure 2 can be found by dividing the appropriate displacements calculated in equations (24), (28) and (29).

In general, as pointed out by Ungar and Dietrich [8] and halvorsen and Smiley [9], transmissibility provides an accurate description of isolator performance only with certain types of idealized sources. A better indicator of isolator performance is isolation

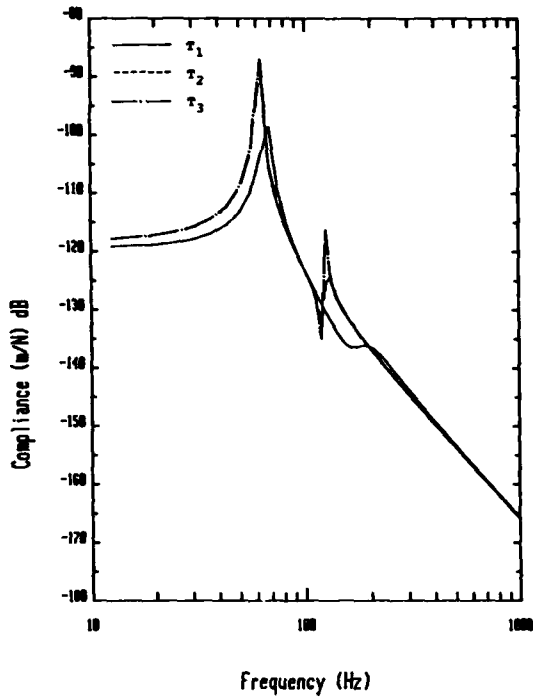


Figure 5: Predicted Source Compliance of Coupled Systems for Various Link Temperatures

effectiveness, which takes into account the output characteristics of the source. Isolation effectiveness is defined as the ratio of the receiver displacement, with the receiver and source structures connected with a rigid link, to the receiver displacement with the receiver isolated from the source. Assuming the dynamic response of the source is independent of the load, the above analysis will predict isolator effectiveness. After calculating the displacement of the receiver for the isolated case, the calculations are repeated for the rigidly attached case by replacing the stiffness of the viscoelastic elements with a stiffness of at least two orders of magnitude greater than the source and receiver.

The above derivation is based on the system configuration shown in Figure 2 with only one direction of motion. By a similar process the analysis can be expanded to include many more points and viscoelastic elements with up to three directions of motion.

MODELING RESULTS AND EXPERIMENTAL VERIFICATION

Single Degree-Of-Freedom Model

To demonstrate the impedance linking model, a computer program was developed which

incorporated Equations (24) through (26), (28) and (29). As a first test the source and receiver systems shown in Figure 3 were modeled using the analytically generated compliance data shown in Figure 4. A viscoelastic material with known dynamic properties was used to link the two single degree-of-freedom systems together in the computer model. The computer model was run using three link temperatures and three link thicknesses to predict the dynamic characteristics of the coupled systems. Figure 5 shows the source compliance predicted for three temperatures and Figure 6 shows the source compliance predicted for a viscoelastic link with different thicknesses. The link stiffness and damping varied over the frequency span as a function of the material properties.

The vibration transmissibility across the viscoelastic link was also predicted with the impedance linking model for the temperature and thickness cases. Figures 7 and 8 show the vibration transmissibility for the three temperature and thickness cases, respectively. The transmissibility is a measure of the amount of vibration transmitted from the source to the receiver through the viscoelastic element. Transmissibility is frequently used as a measure of the

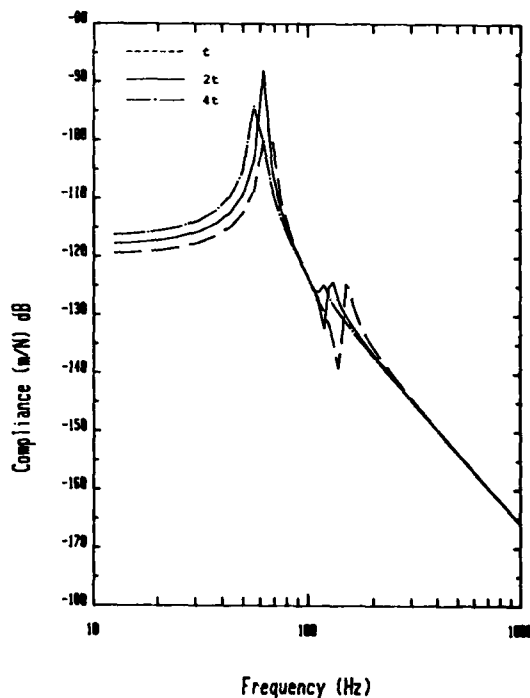


Figure 6: Predicted Source Compliance of Coupled Systems for Various Link Thicknesses

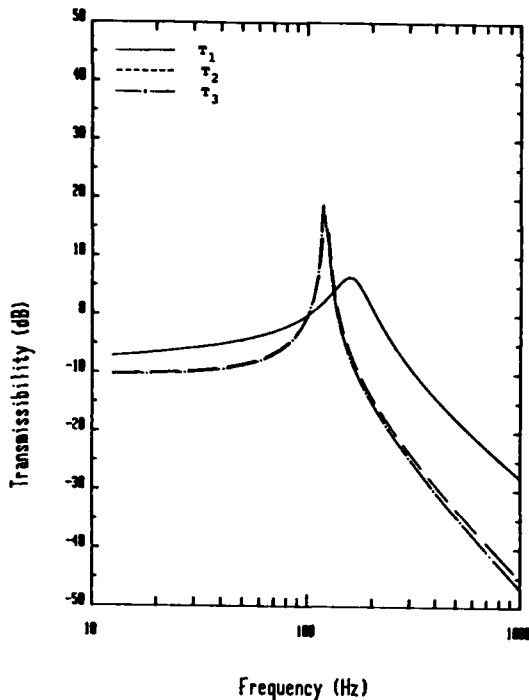


Figure 7: Predicted Transmissibility of Coupled Systems for Various Link Temperatures

performance of an isolator; however, transmissibility does not include the characteristics of the source. The predicted isolation effectiveness for the three temperature and thickness cases is shown in Figures 9 and 10, respectively. Source dynamic characteristics can be seen in isolation effectiveness as additional drops in the isolation effectiveness. Resonances in the source are not seen in transmissibility but are seen in isolation effectiveness.

Compressor and Plate Model

To verify the predictions of the linking model, the problem of isolating a refrigeration compressor from a flexible plate at four attachment points was considered. Driving point and cross compliance measurements were made at the attachment points of the compressor and plate. Typical directional compliances on the compressor and plate are shown in Figures 11 and 12 for one of the attachment locations. Four hypothetical viscoelastic elements were used to isolate the compressor from the plate. The predicted transmissibility across one attachment point at three temperatures is shown in Figure 13. Predicted isolation effectiveness is

displayed in Figure 14 for the compressor and plate combination.

To verify the transmissibility predictions, the compressor was actually linked to the plate with four isolators. Because the material properties of the viscoelastic links were not known as a function of frequency and temperature, the static stiffness and damping were measured and used in the model rather than actual material properties and geometry. The computed and measured transmissibility across one isolator in the isolation system is shown in Figure 15. The agreement between computed and measured transmissibility is very good considering the links were modeled using the constant static stiffness and damping values.

SUMMARY AND CONCLUSIONS

An approach for predicting the dynamic characteristics of structures when joined by viscoelastic elements has been presented. This approach requires two sets of information--the compliance of the receiver and source structures and the stiffness and damping values of the viscoelastic elements. The general impedance method was used to set up a model for coupling the source to the receiver with viscoelastic elements. From the

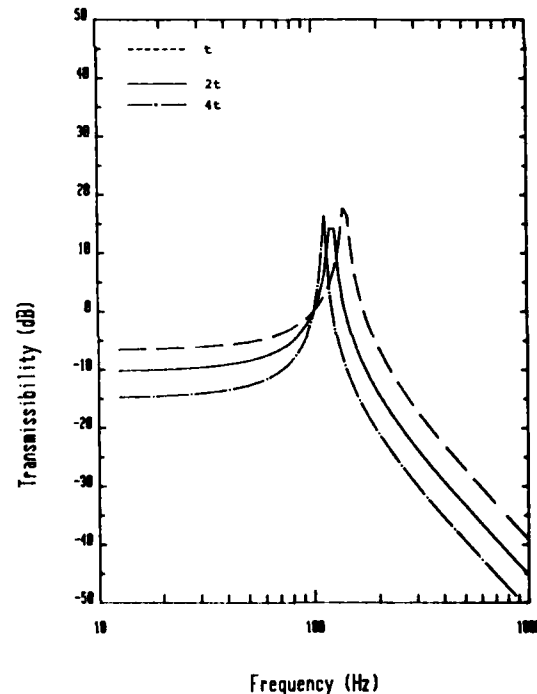


Figure 8: Predicted Transmissibility of Coupled Systems for Various Link Thicknesses

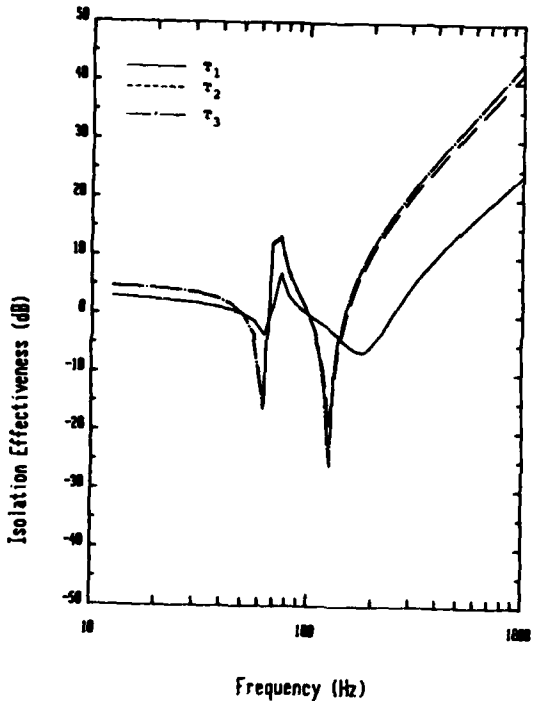


Figure 9: Predicted Isolation Effectiveness of Coupled Systems for Various Link Temperatures

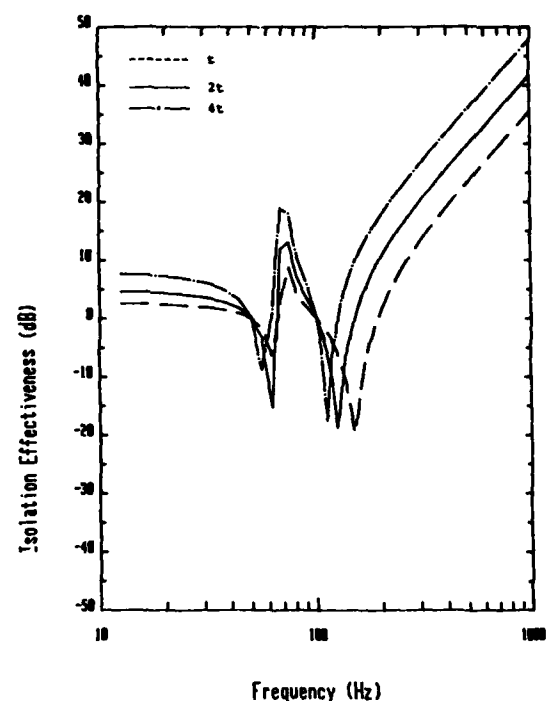


Figure 10: Predicted Isolation Effectiveness of Coupled Systems for Various Link Thicknesses

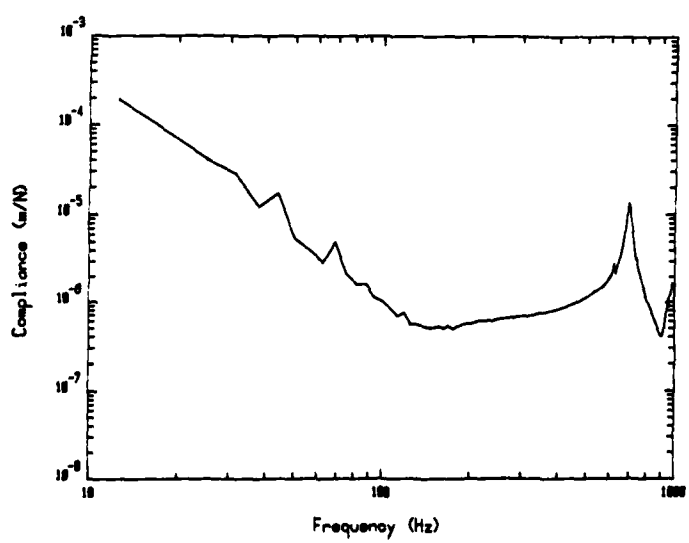


Figure 11: Compliance Measured at One Compressor Attachment Point

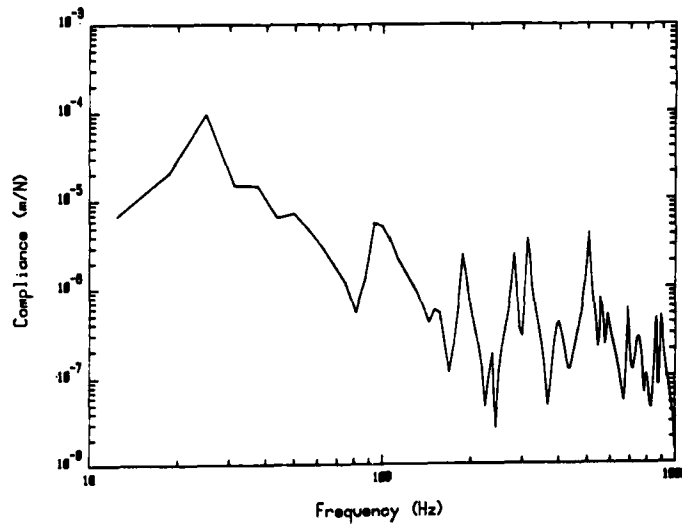


Figure 12: Compliance Measured at One Plate Attachment Point

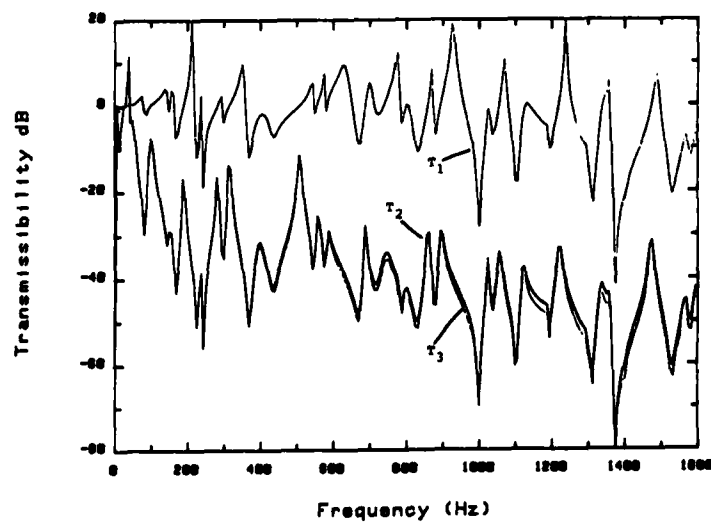


Figure 13: Predicted Transmissibility of the Compressor-Plate System for Various Link Temperatures

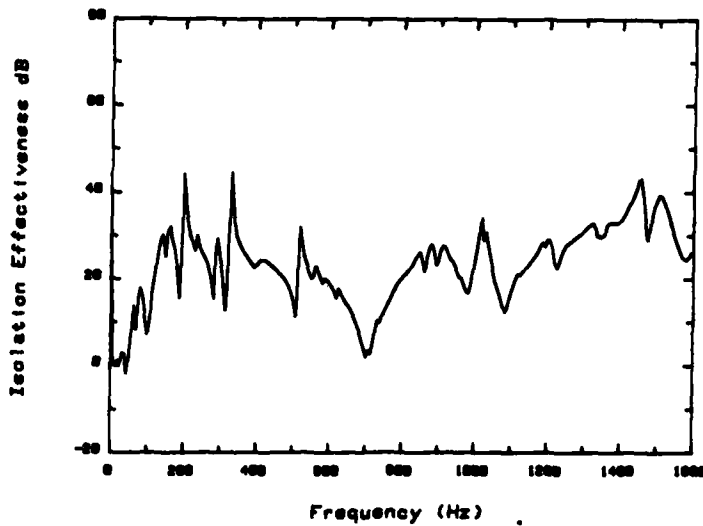


Figure 14: Predicted Isolation Effectiveness

odel, structural compliance, displacement transmissibility and isolation effectiveness are predicted. The effectiveness of the approach was demonstrated in a practical application involving isolation of a compressor from a base plate.

Developments are now underway to add rotational characteristics of the source and receiver structures and the isolation elements to the model. The inclusion of rotational effects, which have been largely ignored in previous modeling work, should improve the accuracy of the modeling results.

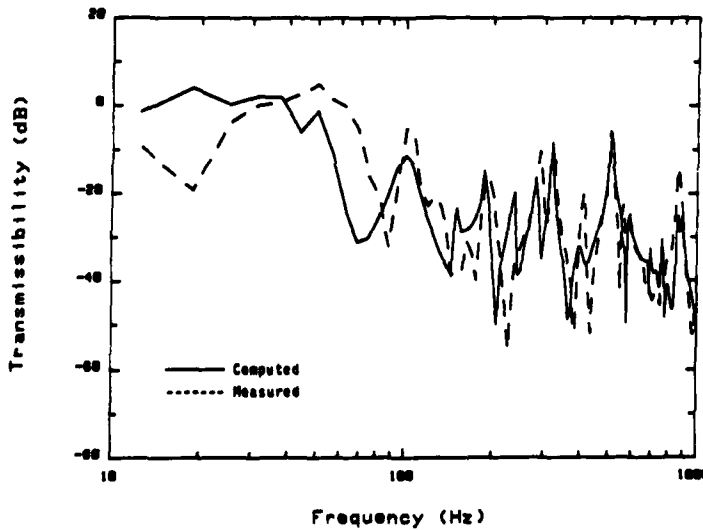


Figure 15: Transmissibility of the Compressor Plate System

REFERENCES

1. Formenti and Welaratna, "Structural Dynamics Modification - An Extension to Modal Analysis", SAE 811043, October, 1981.
2. D.I.G. Jones, "Temperature-Frequency Dependence of Dynamic Properties of Damping Materials", Journal of Sound and Vibration, Vol. 33, No. 4, 1974.
3. L.C. Rogers, "On Modeling Viscoelastic Behavior", Shock and Vibration Bulletin 51, Part 1, pp 55-69, 1981.
4. Klosterman, Albert L., "On the Experimental Determination and Use of Modal Representations of Dynamic Characteristics", PhD Thesis University of Cincinnati, 1971.
5. VanLoon, Patrick, "Modal Parameters of Mechanical Structures", PhD Thesis Katholieke Universiteit te Leuven, 1974.
6. Tse, Morse and Hinkle, Mechanical Vibrations, Allyn and Bacon, Inc., 2nd Ed., 1978, pp 45-51, 169-175.
7. Brown, Allemang, Zimmerman and Mergeay, "Parameter Estimation Techniques for Modal Analysis", SAE 790221, February, 1979.
8. Ungar and Dietrich, "High-Frequency Vibration Isolation", Journal of Sound and Vibration, Vol. 4, No. 2, 1966.
9. Halvorsen and Smiley, "Isolation of Engine Components", Presented at Noise-Con 79 at Purdue University in West Lafayette, Indiana, 1979.

STOCHASTIC DYNAMIC ANALYSIS
OF A STRUCTURE WITH FRICTIONAL JOINTS

Qian-Li Tian, Yu-Bio Liu

Institute of Mechanics,
Chinese Academy of Sciences

Da-Kang Liu

Space Science & Technology Centre,
Chinese Academy of Sciences

Since about 90% of the damping in a structure is originated from the joints, an efficient method to reduce vibration level of the structure is to increase the damping in these joints. Damping in the joints can be increased to a required level either by using inserts such as polymer or metal foils, or by some special surface treatment. The coulomb friction due to relative motion at the interfaces is insensitive to environmental temperature. So, it can provide a cheap and efficient source of damping, if it is well controlled.

In this paper, a stochastic-dynamic-analysis is presented for a structure with frictional joints. It is assumed that the structure is excited by a stationary stochastic process with Gaussian distribution and the statistical linearization is made to transform the frictional forces to equivalent viscous damping forces. A localized damping modification method is used to calculate its response spectrum and corresponding statistical characteristics.

INTRODUCTION

It has been known that by increasing the damping of a structure one can significantly improve its ability to withstand vibration excitation. Unfortunately, modern engineering structures, especially the space structures, often use low density/high strength materials and integrated construction to meet the needs of low weight, hence its damping

capacity is very limited. So, viscoelastic damping technology was developed rapidly. But the behavior of the viscoelastic materials are too sensitive to the environmental temperature, and it will be vaporized in the high vacuum condition, therefore its usage is limited. It has been discovered that the slip in blade roots can provide damping

for turbine and compressor blades. Since using Coulomb friction, which always exists in the structure joints, is an economic method, it attracts many researchers. As is well known, modern structures are always subjected to various kinds of loading, such as earthquake, wind, wave etc. In its service life, the moderate loading condition occurs most frequently and the extreme condition is of rare occurrence, so, if the structure was designed to bear extreme loading, it would be too heavy and costly. If it can be designed to bear the moderate loading and let some frictional joints remain locked as rigid joints under this condition, but have interfacial slip during an extreme condition, the frictional damping will dissipate the vibration energy, and reduce the vibration level in the extreme condition. When the joints are carefully designed and fabricated, maximum energy can thus be dissipated through this slipping, and the designed structure will be light and cheap. A key point to applying such a vibration reducing technology is its ability to analyze the dynamic response of such a structure. Owing to the nonlinearity of the frictional force, the dynamic analysis of such a structure is rather difficult, especially under the stochastic excitation. In this paper, an approximate linearized method is presented for analyzing such structures.

LOCAL MODIFICATION DYNAMIC ANALYSIS

A complex structure always has many degrees of freedom, but the discrete damping inserts usually have much less degrees of freedom than those of the structure. For an optimum design, the damping parameters and locations of these inserts must be calculated for several times. If in each time, the calculation

was executed on the whole system, the computation time would be very long. The local modification methods given by references (1) (2) can greatly reduce the computation time. But ref. (1) (2) deal with linear damping modifications, while frictional damping is nonlinear, so it is necessary to transform the friction forces to equivalent viscous damping forces. From ref. (1) (2), the equation of motion of a general structure with discrete frictional inserts has the form

$$\underline{M}\ddot{\underline{X}} + \underline{C}\dot{\underline{X}} + \underline{K}\underline{X} + \underline{F} = \underline{P} \quad (1)$$

in which, subscripts '-' denotes matrix, subscripts '.' denotes vector, \underline{P} is the external load vector, \underline{F} is a frictional force vector, which is acted at some joints on the structure as shown in fig. 1.

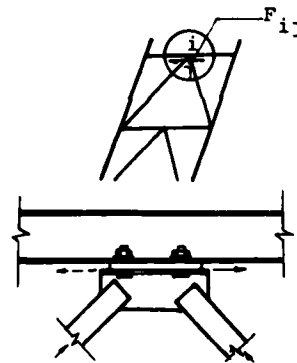


Fig.1. Frictional Joint

Among the forces one is

$F_{ij} = F_{0ij} \operatorname{sgn}(\dot{x}_i - \dot{x}_j)$, where $\dot{x}_i - \dot{x}_j = \dot{x}$ is the relative velocity between the two ends of joints. Assuming that the structure is excited by a stationary stochastic process with the Gaussian distribution, the statistical linearization method can be used to transform the friction forces to equivalent viscous forces. (4) Let

$$F_{0ij} \operatorname{sgn}(\dot{x}_i - \dot{x}_j) = C_{ij}(\dot{x}_i - \dot{x}_j) \quad (2)$$

multiply both sides of eq.(2) by \dot{x} exp

Experiments have shown that a base isolator which employs a combination of the coulomb and viscous damping is a very simple and effective aseismic device. The maximum ground acceleration that can be transmitted to the superstructure will be controlled by this device. A structure with frictional base isolator is a special example of the structure with frictional joints. Consider the lumped mass-spring model of a cantilever structure (fig.2) on an isolator which employs a combination of the coulomb and viscous damping.

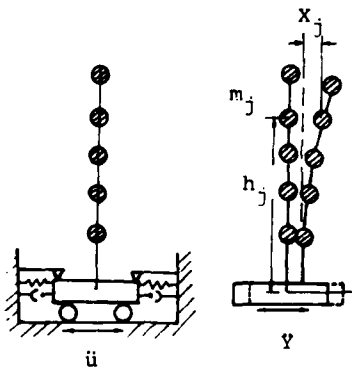


Fig.2. Base Isolated Structure

The equation of motion of this system can be written as

$$M\ddot{x} + C\dot{x} + Kx = -Ml\ddot{y} \quad (14)$$

$$\text{and } Q + m_o\ddot{y} + C\dot{y} + ky = c\dot{u} + ku + F \quad (15)$$

Eg.(14) is the equation of motion of the clamped upper-structure excited by a base acceleration movement \ddot{y} , where l is a unit vector in which every element is 1. Eg.(15) is the equation of motion of the base isolator, where m_o is its mass, k , c are its stiffness and viscous damp-

ing, Q is the shearing force at the root section of the clamped upperstructure, while which has a base motion \ddot{y} , u is the displacement of the ground motion, F is coulomb force, $F = F_o \text{sgn}(\dot{z})$, $\dot{z} = \dot{y} - \dot{u}$ and $\text{sgn}(\dot{z}) = \frac{\dot{z}}{|\dot{z}|}$

Owing to the nonlinearity of the coulomb force, the dynamic response of the system cannot be calculated directly by a general program such as SAPV, even when it is subjected to a base excitation as simple as a harmonic movement, i.e.,

$$\ddot{u} = \ddot{u}_o \exp[i(\omega t + \phi)]$$

where $i = \sqrt{-1}$

$F, Y, X,$ and Q can be expressed by

$$F = F_o \text{sgn}(\dot{z}) = \frac{4F_o}{n} \sum_{j=1,3,5,\dots}^{\infty} \frac{\sin j\omega t}{j} \quad (16)$$

$$Y = \sum_{j=1,3,5,\dots}^{\infty} Y_j \quad (17)$$

$$X = \sum_{j=1,3,5,\dots}^{\infty} X_j \quad (18)$$

$$Q = \sum_{j=1,3,5,\dots}^{\infty} Q_j \quad (19)$$

Then an infinite linear equations system can be obtained

$$m_o\ddot{y}_j + C\dot{y}_j + ky_j + Q_j = \frac{4F_o}{j\pi} \sin j\omega t + K_{1j}(ku + c\dot{u}) \quad (20)$$

$j=1,3,5,\dots,\infty$

$$\text{where } K_{1j} = 1 \quad \text{when } j = 1$$

$$K_{1j} = 0 \quad \text{when } j \neq 1$$

$$\text{Let } Q_j = \bar{Q}_j \ddot{y}_j$$

then eg. (20) becomes

$$(m_o + \bar{Q}_j)\ddot{y}_j + C\dot{y}_j + ky_j = \frac{4F_o}{j\pi} \sin j\omega t + k_{1j}(ku + c\dot{u}) \quad (21)$$

$j=1,3,5,\dots,\infty$

where \bar{Q}_j is the shearing force at the root section of the clamped structure, which can be calculated by SAPV, while the structure is subjected to an unit horizontal base motion $\cos(j\omega t + \phi)$. As each equation in eqs.(21) is an equation of motion of one degree of freedom with a frequency dependently mass, eqs.(21) can be solved easily.

$$\text{Let } \alpha = \frac{C}{\sqrt{m_0 k}} = \frac{C}{C_c}, \quad \beta_j = \omega_j / \omega_a,$$

$$\omega_j = j\omega, \quad \omega_a = \sqrt{\frac{k}{m_0}}, \quad 2\alpha\beta_j = S_j$$

$$1 - \beta_j^2 (1 + \frac{\bar{Q}_j}{m_0}) = C_j, \quad C_j^2 + S_j^2 = R_j^2$$

then we have

$$y(t) = u_0 \left[\frac{\sqrt{1+S^2}}{R} \cos(\omega t + \phi - \gamma_1) + \sum_{j=1,3,5,\dots}^{\infty} \frac{4F_0}{\pi k n R_n u_0} \sin(j\omega t - \theta_j) \right] \quad (22)$$

$$z(t) = u_0 \left[\frac{1-C_1}{R_1} \cos(\omega t + \phi - \theta_1) + \sum_{j=1,3,5,\dots}^{\infty} \frac{4F_0}{\pi k u_0} \frac{1}{n R_n} \sin(j\omega t - \theta_j) \right] \quad (23)$$

and from $\dot{z}(0) = 0$, One obtains

$$\phi = \theta_1 + \arcsin \left(\frac{R_1}{1-C_1} \frac{4F_0}{\pi k u_0} \sum_{j=1,3,5,\dots}^{\infty} \frac{C_j}{R_j^2} \right) \quad (24)$$

where

$$\gamma_j = \tan^{-1} \frac{S_j (1-C_j)}{R_j^2}$$

and

$$\theta_j = \tan^{-1} \frac{S_j}{C_j}$$

Each term of the series solution can be obtained from SAPV and its convergence is very rapid, so a few terms are enough to get an accurate enough result. When the structure is excited by a base movement with a stationary stochastic process, above solution is no longer valid. By using stochastic linearization method the nonlinear coulomb force can be transformed to an equivalent linear viscous damping force as in eq.(3).

Let $C = C_0 + C_{eq}$.

where C_0 is the viscous damping of the isolator, C_{eq} is the equivalent viscous damping given by eq.(3), then eq.(15) becomes

$$Q + m_0 \ddot{y} + ky + c\dot{y} = ku + c\dot{u} \quad (25)$$

Assuming the acceleration of ground motion u can be represented by a discrete spectrum, i.e.

$$\ddot{u} = \sum_{j=1}^n \sqrt{2S_{\ddot{u}}(\omega_j)} \omega \cos(\omega_j t + \psi_j) \quad (26)$$

where $S_{\ddot{u}}(\omega_j)$ is the spectrum of ground motion, and ψ_j is a random phase angle uniformly distributed between 0 to 2π . Integrating eq.(26) and substituting it with eqs.(17),(19) into eq.(25), the absolute and relative velocity can be obtained

$$\dot{y}(t) = \sum_{j=1}^n \frac{\dot{u}_j \sqrt{1+S_j^2}}{R_j} \cos(\omega_j t + \psi_j - \gamma_j) \quad (27)$$

$$\dot{z}(t) = \sum_{j=1}^n \dot{u}_j \frac{1-C_j}{R_j} \cos(\omega_j t + \psi_j - \theta_j) \quad (28)$$

where $\dot{u}_j = \frac{\sqrt{2S_{\ddot{u}}(\omega_j)} \omega}{\omega_j}$

From Parseval equation, the variance of \dot{z} can be obtained

$$\sigma_{\dot{z}\dot{z}}^2 = \sum_{j=1}^n \dot{u}_j^2 \left(\frac{1-C_j}{R_j} \right)^2 \quad (29)$$

Take notice of

$$\alpha = \frac{C}{C_c} = \frac{C_0 + C_{eq}}{C_c} = \xi + \sqrt{\frac{2}{\pi}} \frac{F_0}{C_c \sigma_{\dot{z}\dot{z}}^2}$$

α and $\sigma_{\dot{z}\dot{z}}^2$ can be determined by iterations or by a graphical method. Then the variance of the shear force at the root section can be calculated as

$$\sigma_{Q_0}^2 = \sum_{j=1}^n S_{\ddot{u}}(\omega_j) \omega \bar{Q}_j^2 \frac{1+S_j^2}{R_j^2} \quad (30)$$

The mean value of the maximum response can be approximated by using the following relation (4)

$$E(Q_m) = \sigma_{QQ} \sqrt{2 \ln n T + \frac{5772}{2 \ln n T}}$$

where

$$v = \frac{1}{2\pi} \frac{\sum_{j=1}^n \omega_j^2 S_{QQ}(\omega_j)}{\sum_{j=1}^n S_{QQ}(\omega_j)}$$

and T is the duration of the process.

EXAMPLE.

A cantilever structure was damaged during a strong earthquake. The frictional base isolator was designed in hope to improve its ability to withstand seismic excitation. Parametric studies were carried out to show the influences of different damping ratios and natural frequencies of the isolator on the variance of the shearing force at the root section. The model of the structure for calculation is a lumped mass-spring system as shown in fig.2. The fundamental frequency of the original system is $f_0 = 4.56\text{Hz}$, Adopting the spectrum of ground motion suggested by Kanai and Tajimi

$$S_{\ddot{u}g}(\omega) = \frac{1 + 4\beta_g^2 (\omega/\omega_g)^2}{[1 - (\omega/\omega_g)^2]^2 + 4\beta_g^2 (\omega/\omega_g)^2} S_0$$

where $\beta_g = 0.642$ $\omega_g = 15.5 \text{ rad./sec}$

$$S_0 = 4.8 \text{ cm}^2/\text{Sec}^2$$

the calculated results are shown in Table 1. (See next page)

In table 1. the first row gives the synthesis damping ratio α of the isolator, and the first column is f_a , the natural frequency of that system, assuming the upperstructure as a rigid cantilever. From table 1, it is obvious that σ_{QQ}^2 will increase when the f_a increases, and reaches the maximum at $f_a = 12.04\text{Hz}$, at which frequency the actual fundamental frequency of the base isolated system is decreased to 2.5Hz due to the addition of the inertia force, and just falls into the high energy frequency band of the earthquake spectrum. when $f_a = \infty$, the isolator is locked and the upperstructure is a clamped cantilever, the variance of shear force is $7.07 \times 10^6 (\text{kg/cm}^2)$. Table 1 shows that the values located above the dotted line are all less than 7.07. It means that the isolator attenuates the response, and this attenuation will be enhanced when α increases. On the contrary, the values located below the dotted line are all greater than 7.07, it means that the isolator will multiply the response, in these cases. So, while designing a base isolator, its damping and natural frequency must be carefully controlled. Coulumb friction is limited by normal pressure and frictional coefficient, which is difficult to be adjusted, so combining it with viscoelastic damping is a better design.

CONCLUDING STATEMENT

A statistical linearized method for the analysis of the dynamic response of a structure with some frictional joints was presented. We are sure that by adjusting the locations, dampings, and stiffnesses of these joints, the structural response could be minimized over a wide frequency range.

Table 1.

$10^{-6} \sigma_{00}^2$ varies with f_a and α (kg/cm^2)²

$f_a \backslash \alpha$	0.1	0.2	0.3	0.4	0.5
1.5	1.98	1.19	0.85	0.704	0.639
2.5	5.91	3.16	2.20	1.80	1.55
4.56	13.3	7.19	5.06	4.10	3.54
12.04	178.0	107.4	70.1	49.9	37.5
∞	7.07				

REFERENCES

1. Q.L.Tian, et.al., "Dynamic Analysis of A Large structure with Artificial Damping" Shock and Vibration Bull. No.52, pt.4. pp.147-153 1982
2. Q.L.Tian, "The Dynamic Analysis of A Structure Having Discrete Dampers" Acta Mechanica Solida Sinica (Chinese) 1983 No.2 pp.186-196
3. Q.L.Tian, S.C.Li, "To Calculating the Frictional Isolation Problem by SAP5" Journal of Vibration and Shock (Chinese) 1982. No.4. pp.28-33
4. M.Apetaur, "Linearization of Friction in Stochastically Excited Dynamic Systems" Proc. of VIII th Int. Conf. on Non-Linear Osc. 1978 pp.105
5. B.Westermo, F.Udwadia, "Periodic Response of a sliding Oscillator System to Harmonic Excitation" Int. Jour. of Earthq. Engng. and Struct. Dyn. 11(1) 1983.
6. C.F.Beards, "Damping in Structural Joints" The Shock and Vibration Digest 11(9) 1979.

MODAL ANALYSIS OF STRUCTURAL SYSTEMS
INVOLVING NONLINEAR COUPLING

R. A. Ibrahim, T. D. Woodall, and H. Heo
Department of Mechanical Engineering
Texas Tech University
Lubbock, Texas 79414

A nonlinear analysis of the interaction of the normal modes of a three degree-of-freedom structure is presented. The asymptotic approximation method, due to Struble, is employed to solve for the structure response under harmonic excitation. Several possible autoparametric resonance conditions are predicted, and the investigation is confined to the time domain response in the neighborhood of the internal resonance conditions $\omega_i = |\omega_j \pm \omega_k|$, where ω_i , ω_j and ω_k are three normal mode frequencies. For these internal resonance conditions the structure achieves a quasi-steady state response. The transient response reveals peak amplitudes of almost 2.3 times the quasi-state amplitude for the nonexcited modes. An exchange of energy between the excited mode and the nonexcited modes is noticed.

INTRODUCTION

Within the scope of the classical theory of small oscillations of multi-degree-of-freedom systems, it is possible to perform a linear transformation into the principal coordinates which results in an uncoupled set of equations of motion. The corresponding solutions are harmonic and quite adequate to describe the response of the system as long as the corresponding motions are not far from the stable static equilibrium configuration. However, for some systems it is not always possible to get a response to remain near that stable configuration and unexpected types of responses (such as multiple solutions, amplitude jump and autoparametric interaction) can take place. The response of dynamic systems in such situations can be predicted by considering the nonlinear terms which couple the normal modes involved in the response.

Breitbach [1] classified aeroelastic structural nonlinearities into distributed nonlinearities which are continuously activated through the whole structure by elasto-dynamic deformations, and concentrated ones which act locally lumped especially in control mechanisms or in the connecting parts between wing and external stores. Barr [2] discussed three types of nonlinearities. These are elastic, inertia and damping nonlinearities. Elastic nonlinearities stem from nonlinear strain

displacement relations which are inevitable. Inertial nonlinearities are derived, in a Lagrangian formulation, from the kinetic energy. The equations of motion of a discrete mass dynamic system, with holonomic (scleronomous) constraints, in terms of the generalized coordinate q_i are [3]

$$\sum_{j=1}^n m_{ij} \ddot{q}_j + \sum_{j=1}^n \sum_{k=1}^n [j k, i] \dot{q}_j \dot{q}_k + \frac{\partial v}{\partial q_i} = Q_j \quad (1)$$

where $[j k, i]$ is the Christoffel symbol of the first kind and is given by the expression

$$[j k, i] = \frac{1}{2} \left(\frac{\partial m_{ij}}{\partial q_k} + \frac{\partial m_{ik}}{\partial q_j} - \frac{\partial m_{jk}}{\partial q_i} \right) \quad (2)$$

The metric tensor m_{ij} and the Christoffel symbol are generally functions of the q_k and for motion about equilibrium configuration they can be expanded in a Taylor series about that state. Thus from inertial sources quadratic, cubic, and higher power nonlinearities can arise. V is the potential energy.

If the coordinate linear coupling is removed through linear normal coordinates, the resulting new modes will possess nonlinear coupling. The smallness of nonlinearities and

any parametric terms does not prevent them from having an overwhelming effect on the response in the course of time. These added terms can be regarded as a means of energy exchange between the normal modes. The nonlinear normal mode coupling may give rise to what are effectively parametric instability phenomena within the system. The parametric action is not due to the external loading but to the motion of the system itself and, hence is described as autoparametric [4]. The feature of autoparametric coupling is that responses of one part of the system give rise to loading of another part through time dependent coefficients in the corresponding equation of motion. Such modal interaction arises in many aeroelastic configurations such as wing with a store or a Tee-tail plane in bending.

With autoparametric coupling the structure may experience instability of internal resonance. Internal resonance can exist between two or more modes depending on the degree of nonlinearity admitted into the equations of motion. Thus, with quadratic nonlinearities, two modes i and j having linear natural frequencies ω_i and ω_j are in internal resonance if $\omega_i = 2\omega_j$, or three modes i, j, k can be in internal resonance if $\omega_i = |\omega_j \pm \omega_k|$. With a cubic nonlinearity two modes i, j are in internal resonance of the types $\omega_i = \frac{2}{3}\omega_j$ or $\omega_i = \frac{1}{3}\omega_j$. If an external harmonic excitation frequency near one of the frequencies involved in the internal resonance relation is applied to the system, all related modes enter into the response in varying degrees and sometimes the response of the mode that would be expected to be excited most is suppressed by the existence of others [5].

The objective of the present paper is to examine the behavior of a nonlinear three degree-of-freedom aeroelastic model under external forced excitation. The asymptotic expansion method developed by Struble [6] is

employed and predicts several internal resonance conditions. This study is limited to the response of the structure in the neighborhood of the sum and difference internal resonance conditions. The responses are obtained by numerical integration and the amplitude-time history responses are obtained. Complete interaction of the involved modes takes place for the sum and difference cases with energy flow between the modes with a suppression for the externally excited modes.

BASIC MODEL AND EQUATIONS OF MOTION

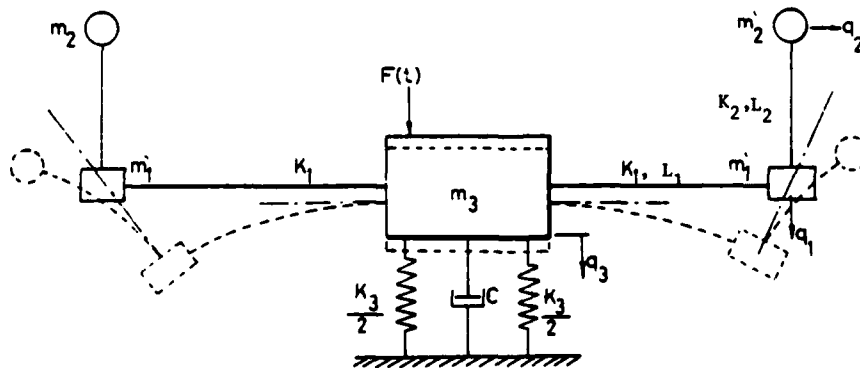
Figure (1) shows the basic structure model. It consists of the main system mass m_3 which carries two coupled beams with tip masses m_1 and m_2 . The stiffness of the two beams and the main system are k_1 , k_2 and k_3 respectively. Under harmonic excitation $F_0 \cos \Omega t$ acting on the main mass, the motion of the three main elements will be described by the generalized coordinates q_1 , q_2 and q_3 . In order to determine the kinetic and potential energies of the structure, the deflection of each beam will be assumed to follow the static deflection curve (see figure (2)).

$$Y = \frac{q_1}{2k_1} (3k_1 s^2 - s^3)$$

The local axial drop Δ_1 is

$$\begin{aligned} \Delta_1 &= ds - (ds^2 - dy^2)^{1/2} \\ &\approx \frac{1}{2} \left(\frac{\partial y}{\partial s} \right)^2 ds \end{aligned}$$

The axial drop at the tip Δ_t is:



Fig(1) Schematic diagram of the system and its coordinates

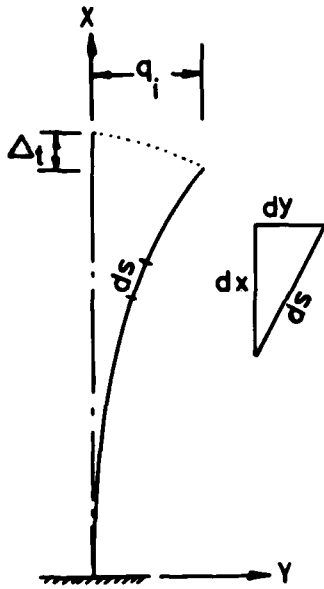


Fig. (2) Axial drop Δ_t of the cantilever free end due to lateral deflection q_1 .

$$\Delta_t = \frac{1}{2} \int_0^L \left(\frac{\partial y}{\partial s} \right)^2 ds$$

Substituting for y gives:

$$\Delta_t = \frac{3}{5k_1} q_1^2$$

$$T = \frac{1}{2} [m_1 + m_2 (1 + \frac{9k_2}{4k_1^2})] \dot{q}_1^2$$

$$+ \frac{1}{2} m_2 \dot{q}_2^2 + \frac{1}{2} (m_1 + m_2 + m_3) \dot{q}_3^2$$

$$+ \frac{3}{2} m_2 \frac{k_2}{k_1} \dot{q}_1 \dot{q}_2 + (m_1 + m_2) \dot{q}_1 \dot{q}_3$$

$$+ \frac{9}{20} m_2 \frac{k_2}{k_1} (q_1 \dot{q}_2^2 + 5q_1 \dot{q}_1 \dot{q}_3)$$

$$+ \frac{3}{2} \frac{m_2}{k_1} (\frac{1}{5} q_1 \dot{q}_1 \dot{q}_2 + q_1 \dot{q}_2 \dot{q}_3 + \dot{q}_1 q_2 \dot{q}_3$$

$$+ \dot{q}_1^2 q_2) + \frac{12}{10} \frac{m_2}{k_2} (q_2 \dot{q}_2 \dot{q}_3 + \dot{q}_1 q_2 \dot{q}_2)$$

$$+ \frac{9}{2k_1} [\frac{4}{25} (m_1 + m_2) + \frac{9}{16} m_2 \frac{k_2}{k_1}] q_1^2 \dot{q}_1^2$$

$$+ \frac{9}{5} \frac{m_2}{k_1 k_2} (q_1 q_2 \dot{q}_2^2 + \dot{q}_1 q_2^2 \dot{q}_2)$$

$$v = \frac{1}{2} [k_1 q_1^2 + k_2 q_2^2 + k_3 q_3^2]$$

where the gravitational potential energy has been ignored and terms up to fourth order have been retained. Applying the Lagrange's equation leads to the following equations of motion:

$$\begin{bmatrix} m_{11} & m_{12} & m_{13} \\ m_{21} & m_{22} & 0 \\ m_{31} & 0 & m_{33} \end{bmatrix} \begin{Bmatrix} \ddot{q}_1 \\ \ddot{q}_2 \\ \ddot{q}_3 \end{Bmatrix} +$$

$$\begin{bmatrix} k_{11} & 0 & 0 \\ 0 & k_{22} & 0 \\ 0 & 0 & k_{33} \end{bmatrix} \begin{Bmatrix} q_1 \\ q_2 \\ q_3 \end{Bmatrix} =$$

$$\begin{Bmatrix} 0 \\ 0 \\ F_0 \cos \Omega t \end{Bmatrix} - \begin{Bmatrix} \Psi_1 \\ \Psi_2 \\ \Psi_3 \end{Bmatrix} \quad (1)$$

$$\text{or } [m]\{\ddot{q}\} + [k]\{q\} = \{\Psi(q, \dot{q}, \ddot{q}, t)\} \quad (2)$$

The nonlinear functions Ψ_i are:

$$\begin{aligned} \Psi_1 = & k_{11}(q_1 \ddot{q}_3 + 0.4q_1 \ddot{q}_1 + 0.2\dot{q}_1^2) \\ & + 0.2k_{12}(q_1 \ddot{q}_2 + 10\ddot{q}_1 q_2 + 10\dot{q}_1 \dot{q}_2 \\ & + 5q_3 \ddot{q}_3) + k_{22}(q_2 \ddot{q}_2 + \dot{q}_2^2) \end{aligned}$$

$$\begin{aligned} \Psi_2 = & k_{12}(q_1 \ddot{q}_3 + 0.2q_1 \ddot{q}_1 - 0.8\dot{q}_1^2) \\ & + k_{22}(\ddot{q}_1 q_2 + q_2 \ddot{q}_3) \end{aligned} \quad (3)$$

$$\begin{aligned} \ddot{v}_3 = & k_{11}(q_1 \ddot{q}_1 + \dot{q}_1^2) + k_{12}(\ddot{q}_1 q_2 \\ & + q_1 \ddot{q}_2 + 2\dot{q}_1 \dot{q}_2) + k_{22}(q_2 \ddot{q}_2 + \dot{q}_2^2) \end{aligned}$$

where the coefficients m_{ij} , k_{ij} , and l_{ij} are:

$$\begin{aligned} m_{11} &= m_1 + m_2 [1 + 2.25(l_2/l_1)^2], \\ m_{12} &= m_{21} = 1.5 m_2 (l_2/l_1) \\ m_{22} &= m_2 \\ m_{13} &= m_{31} = m_1 + m_2 \\ m_{33} &= m_1 + m_2 + m_3 \\ K_{11} &= K_1 = \frac{48 EI_1}{12 l_1^3} \quad i = 1, 2 \\ K_{33} &= K_3 \\ l_{11} &= 2.25 m_2 l_2^2 / l_1^2 \\ l_{12} &= 1.5 m_2 / l_1 \\ l_{22} &= 1.2 m_2 / l_2 \end{aligned} \quad (4)$$

l_1 and l_2 are the lengths of the two beams.

It is seen that the set of equations of motion include autoparametric coupling such as $l_{11}q_1\ddot{q}_1$, $l_{12}q_1\ddot{q}_2$, ... etc. The left-hand side of (1) encompasses linear symmetric inertia and stiffness matrices. The homogeneous part of (1) yields the linear eigenvalues and eigenvectors of the structure.

Transformation into Principal Coordinates

Any possible solution of equations (1) gives the total motion as a sum of responses in its characteristic modes of vibration. In order to derive the solution in terms of these modes a transformation from generalized coordinates into principal ones should be carried out. In an undamped linear vibrating system the principal coordinates of the system are the natural coordinates and each principal mode responds to an applied force as a single degree of freedom.

It is common practice to carry out the transformation, first, for the undamped linear homogeneous equations and then introduce

damping terms after the equations have been transformed into principal coordinates. Simplifications can be achieved by assuming viscous damping and the modal damping matrix is taken to be diagonal thus implying that the modes are not coupled by damping forces in the structure. It is clear that the main objective of excluding damping coupling is to predict only the influence of nonlinear coupling upon the structural dynamic behavior.

The following transformation will be applied:

$$\{q\} = [R]\{Y\} \quad (5)$$

to the system of equations of motion (1). R is the matrix of eigenvectors, or modal matrix, which must be nonsingular. This modal matrix is derived from the linear homogeneous equations (1); i.e., the left-hand side. It has the form:

$$[R] = \begin{bmatrix} 1 & 1 & 1 \\ n_1 & n_2 & n_3 \\ \rho_1 & \rho_2 & \rho_3 \end{bmatrix} \quad (6)$$

where each column represents the eigenvector of the corresponding normal mode. $\{Y\}$ is the vector of the principal coordinates. Having introduced transformation (5), the equations of motion (1) will take the form:

$$\begin{aligned} \{\ddot{Y}\} + [2\zeta\omega]\{\dot{Y}\} + [\omega^2]\{Y\} \\ = \{\bar{V}(\bar{Y}, \dot{\bar{Y}}, \ddot{\bar{Y}}, t)\} \end{aligned} \quad (7)$$

Response of the System

Equations (7) can be written in the standard form of Bogoliuboff and Mitropolski [7]:

$$\begin{aligned} \ddot{Y}_i + S_1^2 v^2 Y_i = \epsilon \{ \epsilon^{-1} (S_1^2 v^2 - r_1^2) Y_i \\ - 2r_1 \zeta_i \dot{Y}_i + F_i(Y_j, \dot{Y}_j, \ddot{Y}_j) \\ + f_i \cos nvt \} \quad i, j = 1, 2, 3 \end{aligned} \quad (8)$$

where $Y_i = \bar{Y}_i / Y_0$, $\tau = \omega_3 t$,

$$Y_0 = F_0 / K_3 \quad \epsilon = Y_0 / l_1$$

$$r_1 = \omega_1 / \omega_3 \quad n v = n / \omega_3$$

where n is an integer such that $v \approx 1 \pm 0(\epsilon)$. S_1 are rational numbers such that $|S_1^2 v^2 - r_1^2| \ll \epsilon$.

The solution of equations (8) can be obtained by employing the approximate asymptotic method outlined by Struble [6]. The solution is taken in the form:

$$Y_1 = A(\tau)\cos[r_1\tau+\phi_1(\tau)] + \epsilon a_1 + \epsilon^2 a_2 + \dots$$

$$Y_2 = B(\tau)\cos[r_2\tau+\phi_2(\tau)] + \epsilon b_1 + \epsilon^2 b_2 + \dots \quad (9)$$

$$Y_3 = D(\tau)\cos[\tau+\phi_3(\tau)] + \epsilon d_1 + \epsilon^2 d_2 + \dots$$

where $A, B, D, \phi_1, \phi_2,$ and ϕ_3 are slowly varying functions of the time parameter τ , and exhibit only long period perturbations. The additive perturbations $a_1, b_1,$ and d_1 depict higher harmonics of motion. Substituting the expansions (9) in (8) and equating the coefficients of equal powers in ϵ leads to a further set of equations. Those terms of order zero in ϵ are called variational equations while the equations arising from coefficients of $\epsilon, \epsilon^2, \dots$ etc. are referred to as perturbational equations. At each step of the iteration process the variational equations are associated with the fundamental harmonic terms

$\left\{ \begin{matrix} \cos \\ \sin \end{matrix} (r_1\tau+\phi_1) \right\}, \left\{ \begin{matrix} \cos \\ \sin \end{matrix} (r_2\tau+\phi_2) \right\},$ and $\left\{ \begin{matrix} \cos \\ \sin \end{matrix} (\tau+\phi_3) \right\}$ and the perturbation equations with the remaining nonresonant terms. If a term appears which is "nearly" resonant it is transferred to the variational equations. In the present investigation the approximation is performed up to first order. In this procedure terms involving second derivatives of the amplitudes and phases, and the product of their first derivatives will be neglected since the amplitude and phases are slowly varying functions of time. At the same time first order derivative terms on the right-hand side will also be ignored since they are of order ϵ .

Variational Equations

$$-2Ar_1\dot{\phi}_1 = A(S_1^2v^2 - r_1^2) \quad (10)$$

$$-2\dot{A}r_1 = 0$$

$$-2Br_2\dot{\phi}_2 = B(S_2^2v^2 - r_2^2) \quad (11)$$

$$-2\dot{B}r_2 = 0$$

$$-2D\dot{\phi} = D(S_3^2v^2 - 1) \quad (12)$$

$$-2\dot{D} = 0$$

First-Order Perturbational Equations

$$\begin{Bmatrix} \ddot{a}_1 \\ \ddot{b}_1 \\ \ddot{d}_1 \end{Bmatrix} + \begin{bmatrix} r_1^2 & 0 & 0 \\ 0 & r_2^2 & 0 \\ 0 & 0 & r_3^2 \end{bmatrix} \begin{Bmatrix} a_1 \\ b_1 \\ d_1 \end{Bmatrix} =$$

$$\begin{Bmatrix} f_1 \\ f_2 \\ f_3 \end{Bmatrix} \cos m\tau + \begin{bmatrix} L_1 & L_2 & L_3 \\ M_1 & M_2 & M_3 \\ N_1 & N_2 & N_3 \end{bmatrix} \begin{Bmatrix} A^2 \\ B^2 \\ D^2 \end{Bmatrix}$$

$$+ \begin{bmatrix} L_4 & L_5 & L_6 \\ M_4 & M_5 & M_6 \\ N_4 & N_5 & N_6 \end{bmatrix} \begin{Bmatrix} A^2 \cos(2r_1\tau+2\phi_1) \\ B^2 \cos(2r_2\tau+2\phi_2) \\ D^2 \cos(2r_3\tau+2\phi_3) \end{Bmatrix}$$

(13)

$$+ \begin{bmatrix} 2\zeta_1 r_1 & 0 & 0 \\ 0 & 2\zeta_2 r_2 & 0 \\ 0 & 0 & 2\zeta_3 \end{bmatrix} \begin{Bmatrix} A \sin(r_1\tau+\phi_1) \\ B \sin(r_2\tau+\phi_2) \\ D \sin(\tau+\phi_3) \end{Bmatrix}$$

$$+ \begin{bmatrix} L_7 & L_9 & L_{11} \\ M_7 & M_9 & M_{11} \\ N_7 & N_9 & N_{11} \end{bmatrix} \begin{Bmatrix} AB \cos((r_1-r_2)\tau+\phi_1-\phi_2) \\ AD \cos((r_1-1)\tau+\phi_1-\phi_3) \\ BD \cos((r_2-1)\tau+\phi_2-\phi_3) \end{Bmatrix}$$

$$+ \begin{bmatrix} L_8 & L_{10} & L_{12} \\ M_8 & M_{10} & M_{12} \\ N_8 & N_{10} & N_{12} \end{bmatrix} \begin{Bmatrix} AB \cos((r_1+r_2)\tau+\phi_1+\phi_2) \\ AD \cos((r_1+1)\tau+\phi_1+\phi_3) \\ BD \cos((r_2+1)\tau+\phi_2+\phi_3) \end{Bmatrix}$$

The second expression on the right-hand side represents a nonoscillatory component. However, these terms will be omitted since they are not resonant.

External and Internal Resonance Conditions

The first order perturbational equations contain secular terms which define external and internal resonance conditions. It is found that the following conditions are possible to exist when the first mode is externally excited:

$$(1) \quad m\nu = r_1 \quad (2) \quad m\nu = r_1$$

$$r_1 = r_2 + 1 \quad r_1 = |r_2 - 1|$$

$$(3) \quad mv = r_1 \quad (4) \quad mv = r_1 \quad (14)$$

$$r_2 = 2r_1 \quad 1 = 2r_1$$

$$(5) \quad mv = r_1 \quad (6) \quad mv = r_1$$

$$r_1 = 2r_2 \quad r_1 = 2$$

If the second mode is excited, the following conditions are obtained:

$$(1) \quad mv = r_2 \quad (2) \quad mv = r_2$$

$$r_2 = r_1 + 1 \quad r_2 = |r_1 - 1|$$

$$(3) \quad mv = r_2 \quad (4) \quad mv = r_2 \quad (15)$$

$$r_1 = 2r_2 \quad 1 = 2r_2$$

$$(5) \quad mv = r_2 \quad (6) \quad mv = r_2$$

$$r_2 = 2r_1 \quad r_2 = 2$$

A third group is obtained if the third mode is excited:

$$(1) \quad mv = 1 \quad (2) \quad mv = 1$$

$$1 = r_1 + r_2 \quad 1 = |r_1 - r_2|$$

$$(3) \quad mv = 1 \quad (4) \quad mv = 1 \quad (16)$$

$$r_1 = 2 \quad r_2 = 2$$

$$(5) \quad mv = 1 \quad (6) \quad mv = 1$$

$$2r_1 = 1 \quad 2r_2 = 1$$

The investigation will be confined to examine the behavior of the structure in the neighborhood of the sum and difference internal resonance conditions in relations (15) and (16).

First-Order Variational Equations

i. $mv = r_2$ and $r_2 = r_1 + 1$

Transferring the resonance terms corresponding to this condition to the fundamental variational equations gives:

$$-\bar{A}\phi_1' = -\gamma\bar{A} + \frac{L_{11}\bar{B}\bar{D}}{r_1^2|L_{11}|} \cos \theta$$

$$-\bar{A}' = \eta_1\bar{A} + \frac{L_{11}\bar{B}\bar{D}}{r_1^2|L_{11}|} \sin \theta$$

$$-\bar{B}\phi_2' = -S_2\gamma\bar{B} + \frac{M_{10}\bar{A}\bar{D}}{r_1r_2|L_{11}|} \cos \theta + r_1 \cos \phi_3$$

$$-\bar{B}' = \eta_2\bar{B} - \frac{M_{10}\bar{A}\bar{D}}{r_1r_2|L_{11}|} \sin \theta + r_1 \sin \phi_3$$

$$-\bar{D}'\phi_3 = -S_3\gamma\bar{D} + \frac{N_7\bar{A}\bar{B}}{r_1|L_{11}|} \cos \theta \quad (17)$$

$$-\bar{D}' = \eta_3\bar{D} + \frac{N_7\bar{A}\bar{B}}{r_1|L_{11}|} \sin \theta$$

where $\theta = \phi_1 - \phi_2 + \phi_3$, prime denotes differentiation with respect to new time parameter T such that:

$$\tau = \frac{2T}{\epsilon} \frac{1}{f_2|L_{11}|}, \quad r_1 = \frac{2c_1}{f_2|L_{11}|} \quad (18)$$

$$\begin{Bmatrix} A \\ B \\ D \end{Bmatrix} = \frac{\delta_2}{r_1|L_{11}|} \begin{Bmatrix} \bar{A} \\ \bar{B} \\ \bar{D} \end{Bmatrix}$$

$$\gamma = \frac{r_1^2 - S_1v^2}{r_1\epsilon} \frac{1}{f_2|L_{11}|}, \quad S_1 = \frac{r_1}{r_2}$$

For the other three cases the corresponding variational equations are obtained and all the four sets are solved numerically by using the IBM Continuous System Modeling Program (CSMP--see IBM User's Manual GH20-0367 or Speckhart [8]).

DISCUSSION OF THE RESULTS

The steady-state solution of the four sets of variational equations can generally be obtained by setting the left-hand sides to zero. However, the resulting six nonlinear algebraic equations are found incompatible because they contain only five unknowns. These are $\bar{A}, \bar{B}, \bar{D}, \theta$, and ϕ_3 as can be seen from equations (17) for example. This means either that one or more of the variables do not achieve steady state or that one of the equations is related to another through their coefficients (which implies that the virtual number of these equations is five). These equations are consistent if the damping of the first and third modes is neglected. This situation leads to four algebraic equations in four unknowns. Another case for which the equations become compatible is that the damping ratio $\eta_1/\eta_3 = r_1/r_2$. These different cases have been treated for a structure containing a liquid by Ibrahim and Barr [9].

It is the main purpose of this study to determine the transient and the unsteady-state responses of the system in the time domain for

the general case $\frac{\eta_1}{\eta_j} \neq \frac{r_1}{r_j}$. The importance of the transient response is to reveal the peak deflection of the structure component which will serve as a measure of the peak stress. The unsteady state response will give insight to the interaction of the involved modes in the neighborhood of internal and external resonance conditions. Several runs are obtained from the numerical simulation and a number of responses are presented in figures (3) through (5).

Figure (3) shows the time history response for the case $r_2 = 1 + r_1$, and damping parameters $\eta_1 = \eta_3 = 0.1$, and $\eta_2 = 0.2$. It is seen that the second mode (which is being externally excited $n\nu = r_2$) is suppressed. The system exhibits a quasi-steady state response of very small fluctuations in the amplitudes. In this case the amplitudes of the system never reach constant values. The transient response shows that the peak deflections of the first and third modes are almost 2.3 times the mean value of the quasi-state response. Another remarkable feature is that both first and third

modes are exchanging energy with the second mode. The same features are evident for the case of the internal resonance $n\nu = r_3 = 1$, $r_3 = r_1 + r_2$ which is given in figures (4,5). The structure response for difference internal resonance $r_2 = r_3 - r_1$ has the same features of the sum cases.

For the damping-frequency condition $\frac{\eta_1}{\eta_3} = \frac{r_1}{r_3}$,

and internal resonance condition $r_2 = r_1 + r_3$, the structure achieves a steady state response as shown in figure (6). The transient response has a peak value of almost 2.3 times the steady state response for the first and third modes. An exchange of energy between the first and third modes and the second modes is observed with a suppression to the second mode.

CONCLUSIONS

The response of a nonlinear three degree-of-freedom structure is obtained in the neighborhood of the internal resonance relations $\omega_j = |\omega_k \pm \omega_l|$. The numerical integration of the variational equations exhibits complete interaction between the three modes. An energy flow between the externally excited mode and other modes is observed with suppression to the motion of the excited mode.

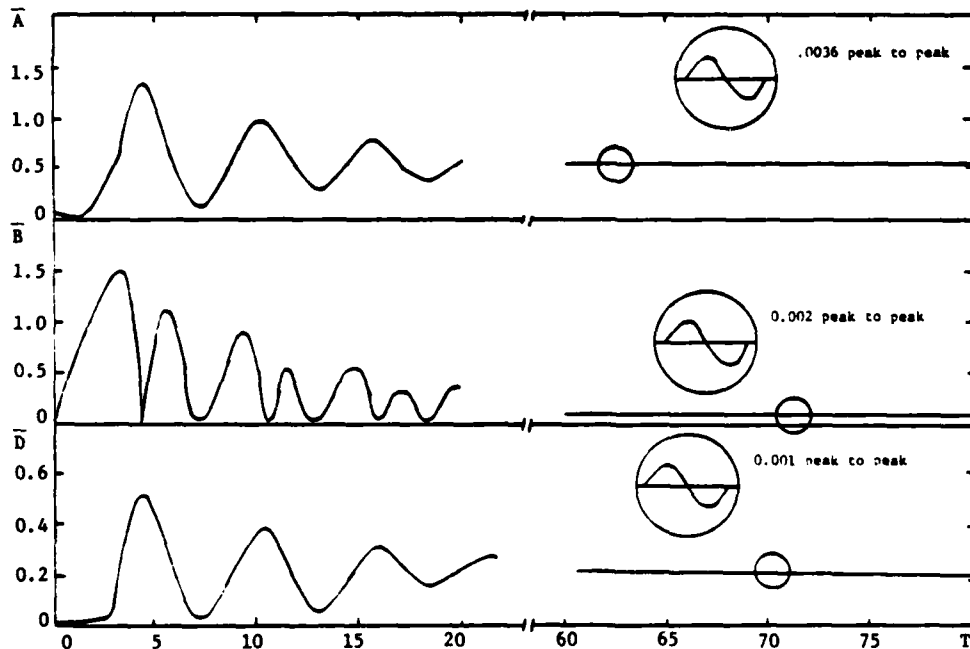


Fig. (3) CSMP time history response of three mode interaction with autoparametric resonance $n\nu = r_2$, $r_2 = r_1 + r_3$, ($\eta_1 = \eta_3 = 0.1$, $\eta_2 = 0.2$)

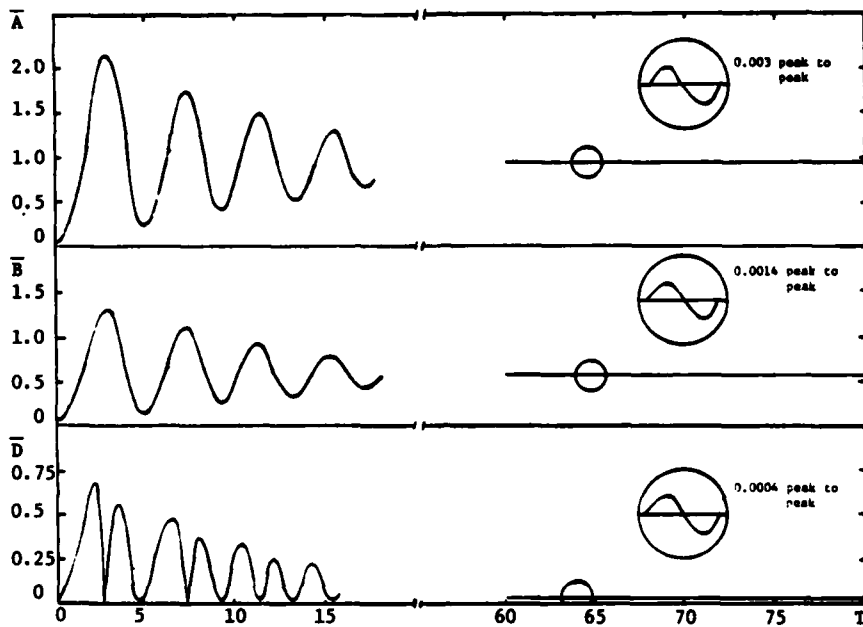


Fig. (4) CSMP time history response of three mode interaction with autoparametric resonance $\nu = r_3$, $r_3 = r_1 + r_2$ ($\eta_1 = \eta_2 = 0.05$, $\eta_3 = 0.2$)

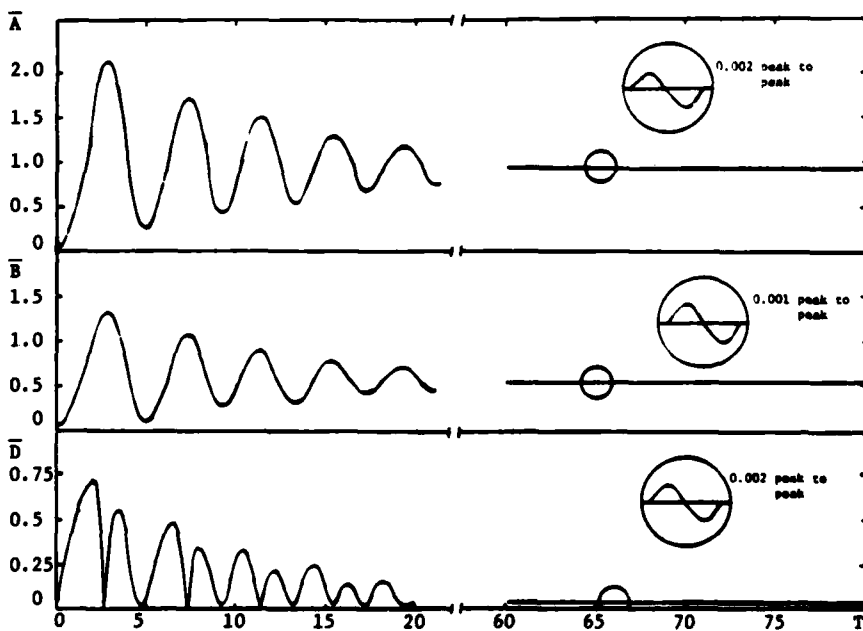


Fig. (5) CSMP time history response of three mode interaction with autoparametric resonance $\nu = r_3$, $r_3 = r_1 + r_2$ ($\eta_1 = \eta_2 = 0.1$, $\eta_3 = 0.2$)

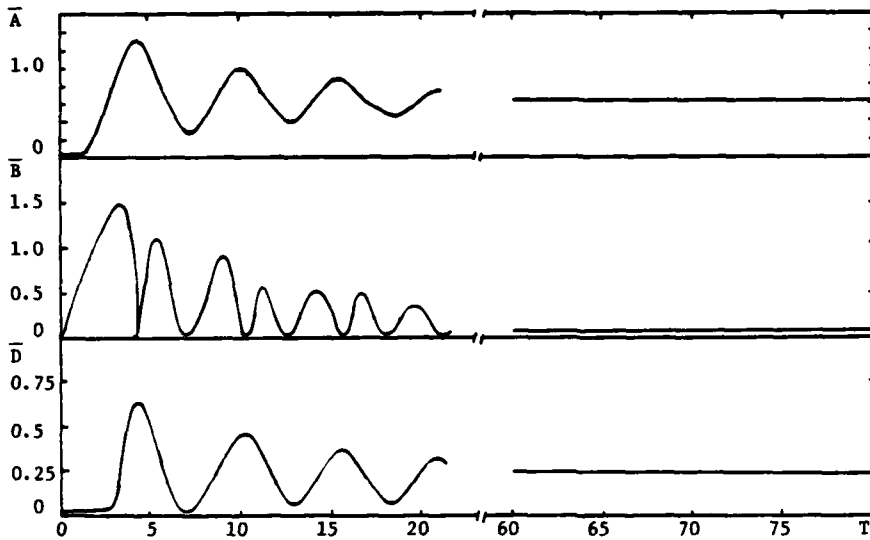


Fig. (6) CSMP time history response of three mode interaction with autoparametric

$$\text{resonance } n\nu = r_2, r_2 = r_1 + r_3, \text{ for } \frac{\eta_1}{\eta_3} = \frac{r_1}{r_3}. \quad (\eta_1 = 0.068, \eta_3 = 0.1, \eta_2 = 0.2)$$

REFERENCES

1. E. Breitbach, "Effect of Structural Non-linearities on Aircraft Vibration and Flutter," AGARD Report No. 665, September 1977.
2. A. D. S. Barr, "Some Developments in Parametric Stability and Nonlinear Vibration," *Proceedings of International Conference of Recent Advances in Structural Dynamics*, ISVR, Southampton, England, pp. 545-568, 1968.
3. D. T. Greenwood, *Classical Dynamics*, Prentice-Hall, Inc., Englewood, N. J., 1977.
4. N. Minorsky, *Nonlinear Oscillations*, Van Nostrand Co., New York, 1962.
5. R. A. Ibrahim and A. D. S. Barr, "Parametric Vibration, Part II: Mechanics of Nonlinear Problems," *The Shock and Vibration Digest* 10(2), 9-24, 1978.
6. R. A. Struble, *Nonlinear Differential Equations*, McGraw-Hill, New York, 1962.
7. N. M. Bogoliuboff and Yu. A. Mitropoliskii, *Asymptotic Methods in the Theory of Nonlinear Oscillations*, Gordon and Breach Science Publishers, New York, 1962.
8. F. H. Speckhart, *A Guide to Using CSMP - The Continuous System Modeling Program*, Prentice-Hall, Englewood Cliffs, N. J., 1976.
9. R. A. Ibrahim and A. D. S. Barr, "Auto-parametric Resonance in a Structure Containing a Liquid, Part II: Three Mode Interaction," *J. Sound Vib.* 42(2), pp. 181-200, (1975).

DISCRETE MODIFICATIONS TO CONTINUOUS DYNAMIC STRUCTURAL SYSTEMS

Yohji Okada
Associate Professor
Ibaraki University
Hitachi, JAPAN

Bo Ping Wang
Associate Professor
Dept. of Mechanical Engineering
University of Texas at Arlington
Arlington, Texas 76019

Walter D. Pilkey
Professor
University of Virginia
Dept. of Mechanical & Aerospace Engineering
Charlottesville, Virginia 22901

The problem of introducing discrete elements such as springs or masses to continuous dynamic systems is considered. A method is developed for the efficient analysis of such modified systems. After a transfer matrix analysis of the original system, appropriate transfer matrices are condensed and stored. Then the effect of the discrete modifications is introduced. The proposed technique is applied to a helicopter model.

INTRODUCTION

Discrete elements such as intermediate supports and vibration absorbers are often introduced to engineering structures to improve their dynamic characteristics. For discrete models of multi-degree of freedom systems, this problem has received considerable attention. See, for example, the survey of Reference 1. The purpose here is to present a solution procedure for continuous systems. In particular, discrete modifications to a continuous mass helicopter model are treated.

In reanalysis it is the goal to formulate a procedure whereby the complexity of the analysis of the modified system depends on the number of modifications or appendages and not on the degrees of freedom of the original system. This permits efficient parametric studies of the effect of modifying the structure to be performed. It follows that structural systems can be synthesized, i.e., designed, to achieve prescribed or optimized responses.

The continuous system will be analyzed here using transfer matrices [2]. Modifications are to be incorporated in the analysis as "pseudo-loads".

PROBLEM FORMULATION

The proposed method will be illustrated using a continuous beam with two point modifications (Fig. 1). Suppose the field (transfer) matrices for regions A, B, and C of the unmodified beam of Fig. 1, are \underline{U}^A , \underline{U}^B , and \underline{U}^C . Let the state vector be defined as

$$\underline{s} = [w \quad \theta \quad M \quad V]^T \quad (1)$$

where the deflection, slope, moment, and shear force along the beam are given by w , θ , M , and V , respectively. The state vectors at stations 0, 1, 2, 3 are designated by \underline{s}_0 , \underline{s}_1 , \underline{s}_2 , \underline{s}_3 . From standard transfer matrix theory, the state variables at station i and $i+1$ are related by

$$\underline{s}_{i+1} = \underline{U}^F \underline{s}_i + \underline{F}^F \quad (2)$$

where a superscript bar indicates an applied loading and superscript F represents region F.

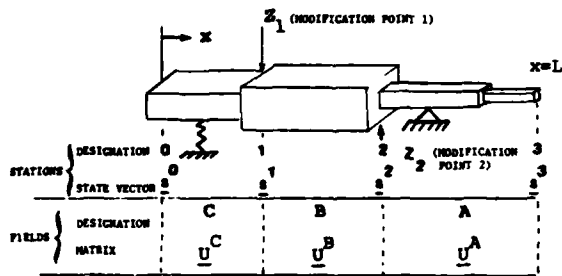


Fig. 1 A Beam with Two Concentrated Modifications

Point modifications are to be represented by the displacement dependent pseudo-loads \underline{f}^i and \underline{f}^i , which are reaction forces (and moments) on the modified structure. These pseudo-loads are functions of the response variables at the attachment points as well as the impedance of the attachments. At station i, the effect of a modification is incorporated using the pseudo-load \underline{f}^i in the form

$$\underline{s}^{i+1} = \underline{s}^{i-} - \underline{f}^i, \quad \underline{f}^i = \underline{Z}^i \underline{s}^i \quad (3)$$

where \underline{Z}^i is impedance of the modification.

The progressive matrix multiplication of the transfer matrix method provides the state vector \underline{s} at the right-hand end.

$$\underline{s}^3 = \underline{U}^{ABC} \underline{s}^0 + (\underline{F}^A + \underline{U}^A \underline{F}^B + \underline{U}^{AB-C} \underline{F}^C) + (\underline{U}^A \underline{f}^2 + \underline{U}^{AB} \underline{f}^1) \quad (4)$$

where the second term on the right hand side represents the influence of the applied load and the third term is the contribution of the pseudo load terms.

$$\underline{U}^{ABC} = \underline{U}^A \underline{U}^B \underline{U}^C, \quad \underline{U}^{AB} = \underline{U}^A \underline{U}^B$$

Suppose that on the left boundary the two elements s_i^0 and s_j^0 are the unspecified state variables, while s_k^3 and s_l^3 are zeros on the right end. That is,

$$\underline{s}^0 = \begin{bmatrix} \vdots \\ S_i^0 \neq 0 \\ \vdots \\ S_j^0 \neq 0 \\ \vdots \end{bmatrix}, \quad \underline{s}^3 = \begin{bmatrix} \vdots \\ S_k^3 = 0 \\ \vdots \\ S_l^3 = 0 \\ \vdots \end{bmatrix} \quad (5)$$

The zero state variables s_k^3 and s_l^3 are found from Eq. (3) to be

$$\begin{aligned} s_k^3 &= U_{ki}^{ABC} s_i^0 + U_{kj}^{ABC} s_j^0 + U_{k3}^{AB} M_1 + U_{k4}^{AB} f_1 \\ &+ U_{k3}^A M_2 + U_{k4}^A f_2 + U_{k5}^{ABC} = 0 \end{aligned} \quad (6)$$

$$\begin{aligned} s_l^3 &= U_{li}^{ABC} s_i^0 + U_{lj}^{ABC} s_j^0 + U_{l3}^{AB} M_1 + U_{l4}^{AB} f_1 \\ &+ U_{l3}^A M_2 + U_{l4}^A f_2 + U_{l5}^{ABC} = 0 \end{aligned}$$

where the pseudo-loads contain forces f_k and moments M_k , i.e.,

$$\underline{f}^1 = \begin{bmatrix} f_1 \\ M_1 \end{bmatrix}, \quad \underline{f}^2 = \begin{bmatrix} f_2 \\ M_2 \end{bmatrix} \quad (7)$$

and U_{15}^{ABC} is the i th term of $\underline{F}^A + \underline{U}^A \underline{F}^B + \underline{U}^{AB-C}$. Other terms in Eq. (6) have similar definitions.

Solve Eq. (6) for the initial unknown state variables.

$$\begin{bmatrix} S_i^0 \\ S_j^0 \end{bmatrix} = - \begin{bmatrix} U_{ki} & U_{kj} \\ U_{li} & U_{lj} \end{bmatrix}^{-1} \left[\begin{bmatrix} U_{k5} \\ U_{l5} \end{bmatrix} + \begin{bmatrix} U_{k3}^{AB} & U_{k4}^{AB} & U_{k5}^{AB} & U_{k3}^A \\ U_{l3}^{AB} & U_{l4}^{AB} & U_{l5}^{AB} & U_{l3}^A \end{bmatrix} \begin{bmatrix} f_1 \\ M_1 \\ f_2 \\ M_2 \end{bmatrix} \right] \quad (8)$$

where $\underline{U} = \underline{U}^{ABC}$ is the global transfer matrix for the system. The transfer matrices can be used to compute the deflection and slope at the attachments. Thus,

$$\begin{aligned} \begin{bmatrix} w \\ \theta \end{bmatrix}^1 &= \begin{bmatrix} U_{1i}^C & U_{1j}^C \\ U_{2i}^C & U_{2j}^C \end{bmatrix} \begin{bmatrix} S_i^0 \\ S_j^0 \end{bmatrix} + \begin{bmatrix} U_{15}^C \\ U_{25}^C \end{bmatrix} \\ \begin{bmatrix} w \\ \theta \end{bmatrix}^2 &= \begin{bmatrix} U_{1i}^{BC} & U_{1j}^{BC} \\ U_{2i}^{BC} & U_{2j}^{BC} \end{bmatrix} \begin{bmatrix} S_i^0 \\ S_j^0 \end{bmatrix} + \begin{bmatrix} U_{15}^{BC} \\ U_{25}^{BC} \end{bmatrix} + \begin{bmatrix} U_{13}^B & U_{14}^B \\ U_{23}^B & U_{24}^B \end{bmatrix} \begin{bmatrix} f_1 \\ M_1 \end{bmatrix} \end{aligned} \quad (9)$$

Use the initial parameters of Eq. (8) to find

$$\begin{bmatrix} w \\ w_1 \\ \theta \\ \theta_1 \end{bmatrix} = \begin{bmatrix} \vdots \\ Q \\ \vdots \end{bmatrix} \begin{bmatrix} f_1 \\ f_2 \\ M_1 \\ M_2 \end{bmatrix} + \begin{bmatrix} \vdots \\ L \\ \vdots \end{bmatrix} \quad (10)$$

where [Q] is the mobility matrix

$$[Q] = - \begin{bmatrix} U_{1i}^c & U_{1j}^c \\ U_{1i}^{bc} & U_{1j}^{bc} \\ U_{2i}^c & U_{2j}^c \\ U_{2i}^{bc} & U_{2j}^{bc} \end{bmatrix} \begin{bmatrix} U_{ki} & U_{kj} \\ U_{li} & U_{lj} \end{bmatrix}^{-1} \begin{bmatrix} U_{k1}^{ab} & U_{k2}^{ab} & U_{k3}^{ab} \\ U_{l1}^{ab} & U_{l2}^{ab} & U_{l3}^{ab} \end{bmatrix} \begin{bmatrix} U_{k3} \\ U_{l3} \end{bmatrix} + \begin{bmatrix} 0 & 0 & 0 & 0 \\ U_{11}^b & 0 & U_{12}^b & 0 \\ 0 & 0 & 0 & 0 \\ U_{21}^b & 0 & U_{22}^b & 0 \end{bmatrix} \quad (11)$$

and [L] is the response due to applied loading at the modification points

$$[L] = \begin{bmatrix} U_{1B}^c \\ U_{1S}^{bc} \\ U_{2B}^c \\ U_{2S}^{bc} \end{bmatrix} - \begin{bmatrix} U_{1i}^c & U_{1j}^c \\ U_{1i}^{bc} & U_{1j}^{bc} \\ U_{2i}^c & U_{2j}^c \\ U_{2i}^{bc} & U_{2j}^{bc} \end{bmatrix} \begin{bmatrix} U_{ki} & U_{kj} \\ U_{li} & U_{lj} \end{bmatrix}^{-1} \begin{bmatrix} U_{kS} \\ U_{lS} \end{bmatrix} \quad (12)$$

The forces and displacements at the attachments are related by the impedance matrix

$$\begin{bmatrix} f_1 \\ f_2 \\ M_1 \\ M_2 \end{bmatrix} = \begin{bmatrix} Z_1 & 0 & 0 & 0 \\ 0 & Z_2 & 0 & 0 \\ 0 & 0 & G_1 & 0 \\ 0 & 0 & 0 & G_2 \end{bmatrix} \begin{bmatrix} w_1 \\ w_2 \\ \theta_1 \\ \theta_2 \end{bmatrix} = [Z] \begin{bmatrix} w_1 \\ w_2 \\ \theta_1 \\ \theta_2 \end{bmatrix} \quad (13)$$

Finally, the displacements in Eq. (10) can be eliminated using Eq. (10) in (13)

$$\begin{bmatrix} f_1 \\ f_2 \\ M_1 \\ M_2 \end{bmatrix} = ([I] - [Z][Q])^{-1} [Z][L] \quad (14)$$

where [I] is the unit diagonal matrix. This expression can be used to calculate the pseudo loads. Then, displacements and forces can be calculated at any point using the usual transfer matrix method.

This formulation permits a variety of dynamic problems to be solved efficiently. For most reanalysis problems, the matrix [Q] must be stored. In the case where the natural frequencies of the modified system are to be calculated, [Q] would have to be stored in a sufficient number of discrete frequencies to conduct the frequency search.

A more reasonable use of this formulation would be to perform a synthesis problem such as one whereby the resonant frequency of the

modified system is prescribed and the characteristics of the modifications necessary to achieve the desired frequency are to be computed. In this case, the [Q] matrix is calculated for the specified resonant frequency and then compute the [Z] matrix that leads to the satisfaction of the frequency equation

$$\det([I] - [Z][Q]) = 0 \quad (15)$$

For a steady-state reanalysis problem, Eqs. (13) and (14) can be employed to determine the pseudo-loads and the displacements at the location of the modification. If the displacements throughout the entire modified structure are needed, then 2x2 and 4x2 matrices on the right hand side of Eq. (8) should be stored so that Eq. (8) can be used to compute

the initial state variables s_1^0 and s_2^0 . Also, several point transfer matrices should be stored in order to calculate the corresponding point responses. This would require relatively large storage memories, but for modifications, the response calculations would be very efficient.

NUMERICAL EXAMPLE

This formulation will be illustrated using the two beam helicopter model of Fig. 2. The concept and limitations (e.g., symmetry) for a two beam model are discussed extensively in Reference 3. For our purposes here the fuselage is idealized as a continuous beam divided into three segments. The two blades are also treated as beams. The effect of the blades on the response of the fuselage is obtained by computing the impedance of the blades and assuming the blades and fuselage are connected by a single extension spring. Since the formulation above accepts two modifications represented by their impedances, it is convenient to let the blade be incorporated as one of the two modifications, even though nothing is to be modified on the blades. The other attachment is chosen to be a simple absorber, which will indeed be modified. Proper variation of the absorber parameters will permit the effect of the absorber on the dynamic response of the helicopter to be studied. The external loading, which is the aerodynamic vibration of the blades, is applied to the beam at the interface of the blade to the fuselage.

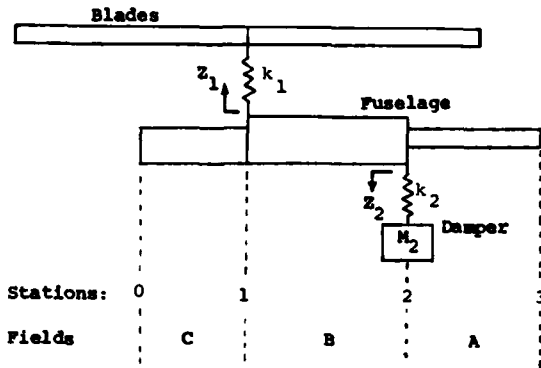


Fig. 2 Helicopter Model

The impedance Z_1 corresponding to the force transmitted from the blade to the fuselage is found using a beam analysis of the blades. The state vector at the outer edge of a blade would be

$$s = [w \quad \theta \quad M=0 \quad V=0]^T \quad (15)$$

and that for the blade center at the interface is

$$\underline{s}^{Bl} = [w \quad \theta=0 \quad M \quad V]^T \quad (16)$$

where the blade is designated by superscript Bl . Suppose that these two state vectors are expressed in terms of each other using a transfer matrix. Then the deflection and force at the interface are related by

$$\frac{V^{Bl}}{w^{Bl}} = \frac{U_{21}^{Bl} U_{44}^{Bl} - U_{31}^{Bl} U_{43}^{Bl}}{U_{11}^{Bl} U_{33}^{Bl} - U_{21}^{Bl} U_{31}^{Bl}} n_b \quad (17)$$

where n_b , the number of blades, has been included to account for multiple blades. If the stiffness k_1 of the interface spring is included, the impedance Z_1 for the blades becomes

$$Z_1 = \frac{K_1 (U_{21}^{Bl} U_{44}^{Bl} - U_{31}^{Bl} U_{43}^{Bl}) n_b}{(U_{11}^{Bl} U_{33}^{Bl} - U_{21}^{Bl} U_{31}^{Bl}) K_1 + (U_{21}^{Bl} U_{44}^{Bl} - U_{31}^{Bl} U_{43}^{Bl}) n_b} \quad (18)$$

The impedance of the absorber is readily found to be

$$Z_2 = \frac{m_2 K_2 \omega^2}{m_2 \omega^2 - K_2} \quad (19)$$

The impedance of Eqs. (18) and (19) can now be incorporated in Eq. (14) to perform an efficient study of the effect of modifying the parameters of the absorber. The blades will not be modified so that Z_1 will not vary.

The sensitivity of the response to a varying absorber (Z_2) is to be determined.

Table 1
Physical Properties of the Helicopter Model

	Fuselage			Blades	
	C	B	A	$n_b = 2$	
EI	6.25 T	10.8 T	1.8 T	24 G	$N \cdot m^2$
ρ (density)	440	440	40	11.84	Kg/m
l (length)	1.2	1.2	1.6	2.5	m

$$k_1 = 40 \text{ GN/m}$$

The physical parameters for the helicopter model are provided in Table 1. The reanalysis scheme proposed above will be employed to study the effect of the stiffness k_2 on the fuselage vibration of the aerodynamic disturbance of the blade. The disturbing force from the blade is approximated as a constant amplitude sinusoidal force transmitted through the interface. Let the mass M_2 of the vibration absorber be 200 kg and let the stiffness k_2 vary as

Case 1: 7.2 MN/m ($\omega_{\text{absorber}} = 30.2 \text{ Hz}$)

Case 2: 17.7 MN/m ($\omega_{\text{absorber}} = 47.3 \text{ Hz}$)

Case 3: 28.2 MN/m ($\omega_{\text{absorber}} = 50.7 \text{ Hz}$)

Case 4: 38.6 MN/m ($\omega_{\text{absorber}} = 70 \text{ Hz}$)

where ω_{absorber} is the natural frequency of the absorber.

Figure 3 shows the vibration magnitude at the blade-fuselage interface versus the applied loading frequency for the four values of k_2 , the absorber stiffness. Two resonant frequencies are displayed. Regardless of the change in k_2 , one resonant frequency remains close to 42 Hz, while the other moves from 35 to 67 Hz as k_2 increases. This relationship is also shown in Figure 4. If the operating frequency range of the system is specified, these sorts of results are useful in using modifications to control undesirable vibrations.

For this simple helicopter example with a single modification, the computation of the frequency response is twice as efficient if the reanalysis formulation is employed relative to resolving the original problems. Reanalysis

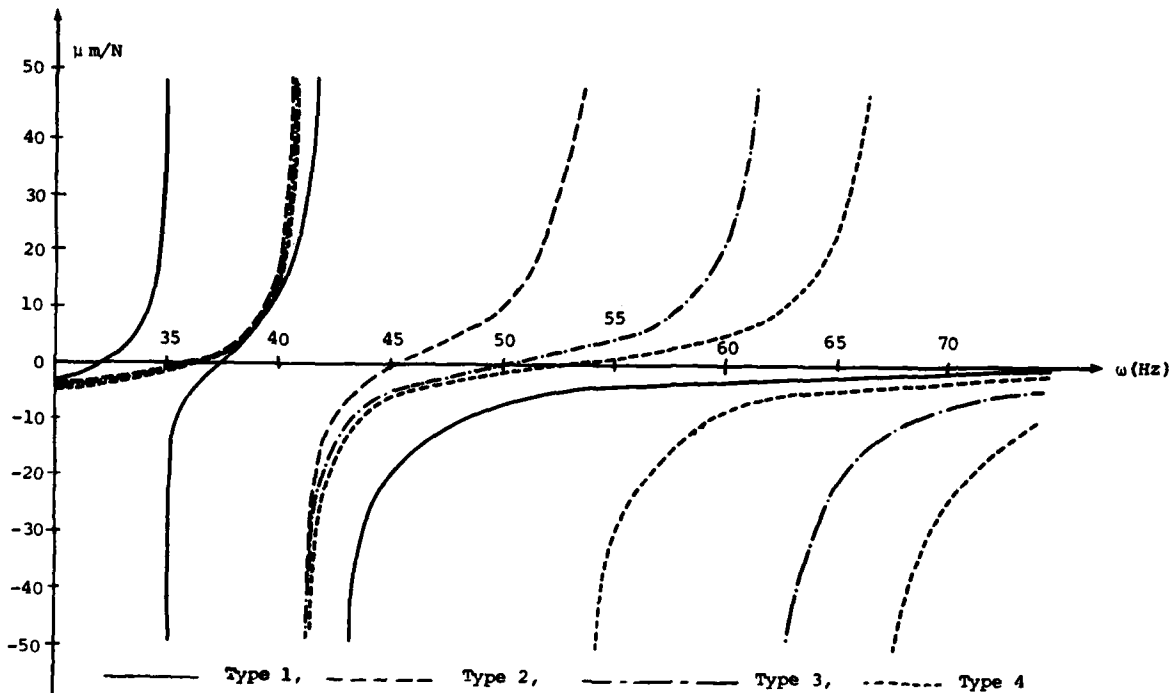


Fig. 3 Frequency Response

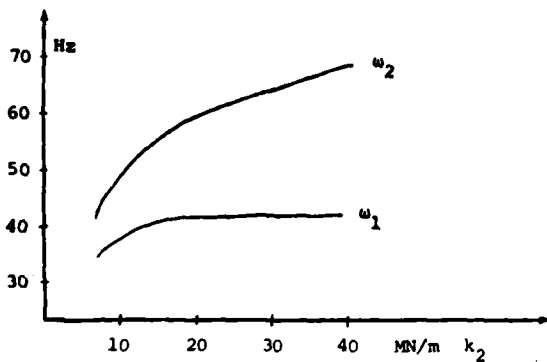


Fig. 4 Resonant Frequencies vs. stiffness k_2

should be substantially more efficient if the original system is more complex or if more modifications are considered.

CONCLUSIONS

An efficient reanalysis procedure has been formulated for studying the dynamic effects of point modifications to a continuous system. In particular, the formulation applies to systems with a line-like geometry which are readily analyzed with the transfer matrix method. The numerical example illustrates the effectiveness

of the approach in the preliminary designs study of a simple helicopter model. This formulation is appropriate for application to many engineering systems that are properly modeled as line type structures.

ACKNOWLEDGMENTS

This work was supported by the Army Research Office, Research Triangle Park, N.C. W. Pilkey's effort was supported by the NAVSEA Research Chair at the Naval Postgraduate School, Monterey.

REFERENCES

1. B.P. Wang, A.B. Palazzolo, and W.D. Pilkey, "Reanalysis, Modal Synthesis and Dynamic Design," Chapter 8, State of the Art Review of Finite Element Methods, edited by A. Noor and W. Pilkey, ASME, 1983.
2. W.D. Pilkey and P.Y. Chang, Modern Formulas for Statics and Dynamics: A Stress-Strain Approach, McGraw Hill, New York, 1978.
3. M.J. Rutkowski, "The Vibration Characteristics of a Coupled Helicopter Roto-Fuselage by a Finite Element Analysis," AVRADCOM Technical Report 82-A-15, January, 1983.

DISCUSSION

Voice: Have you applied this approach to transient problems?

Mr. Pilkey: No, we haven't, but there are some formulations, mostly in the Japanese literature, where they do. But there is no great advantage to applying it directly to transient problems because it is clear that you can do it. I don't think the formulation would vary at all, other than superimposing a transient formulation on top of this.

Voice: What do you consider to be a small computer?.

Mr. Pilkey: We use a TERAk. We also use an IBM, but we cheat often, and we also use a PRIME and a VAX. There are structural modification systems for sale. Some of them that are advertised here at the conference can be run on various machines like a Hewlett-Packard.

Voice: How many degrees of freedom are you talking about?

Mr. Pilkey: It is unlimited in the number of degrees of freedom. It has nothing to do with the number of degrees of freedom of the original system. It is a function only of the number of degrees of freedom of the changes that you make in the system.

Voice: We are talking about the modal results which might have come from a NASTRAN analysis or any other analysis of the original system.

Mr. Pilkey: I spent yesterday morning at MSC right down the road. At various times, they have put reanalysis in NASTRAN, and they have decided it is more of a pain than it is worth. They found many people eventually wanted to go back to the original system. So they have taken reanalysis out. There is one aspect of reanalysis that remains within NASTRAN. That is the modal synthesis that is a very similar formulation to this, and that is in NASTRAN and many other codes.

Voice: Could you qualify your statement about being exact?

Mr. Pilkey: It is exact. No qualification is needed.

Voice: Even if you look at an approximate system and come up with a set of eigenvalues?

Mr. Pilkey: Yes, then I have a qualifier. If you have an approximate representation of the original system, it remains approximate no matter what you do to it. However, the formulation is exact. But, of course, if you fed in an approximate original system, you made it approximate, it remains approximate. Your point is well taken. It is not exact if you begin with an approximate model. But it has nothing to do with the formulation.

REANALYSIS OF CONTINUOUS DYNAMIC SYSTEMS WITH CONTINUOUS MODIFICATIONS

Bo Ping Wang
Associate Professor
Dept. of Mechanical Engineering
University of Texas at Arlington
Box 19023
Arlington, Texas 76019

Yohji Okada
Associate Professor
Department of Mechanical Engineering
Ibaraki University
Hitachi, JAPAN 316

Walter D. Pilkey
Professor
Dept. of Mechanical & Aerospace Engineering
University of Virginia
Charlottesville, VA 22901

Formulations are presented for the efficient analysis of dynamic systems with discrete and continuous local modifications. It is assumed that the original (unmodified) system has been analyzed by a transfer matrix method with appropriate response information saved. The effect of introducing modifications can then be determined efficiently using a reanalysis procedure. The proposed technique is applied to a beam type structure.

INTRODUCTION

Continuous and discrete elements such as distributed inserts, intermediate supports, and vibration absorbers are frequently introduced to structures to control and improve their dynamic responses. The problem of discrete models with discrete modifications has been addressed often in the literature, e.g. [1,2]. Although continuous modifications such as a change in cross-sectional geometry or mass density are important in achieving desired dynamic responses, few analytical studies have been devoted to this subject. A reanalysis solution procedure encompassing both discrete and continuous modifications is presented here.

The purpose of a reanalysis formulation is to provide an analysis capability for a

modified system for which the complexity depends on the number of modifications rather than on the degrees of freedom of the original system. A reanalysis capability permits efficient parametric studies to be performed in which the effect of variations in portions of a structure is determined, as well as synthesis studies in which the structure is redesigned to achieve desired responses. The reanalysis approach employed here incorporates modifications as "pseudo-loads".

This paper deals primarily with the modification of line-like continuous dynamic systems. The system matrices are expressed in transfer matrix (\underline{U}), form, although a conversion to stiffness matrices is introduced to assure that no numerical instabilities occur in the analysis.

NOMENCLATURE

- A : region to the right of the segment being modified
- [A] : modification effect matrix = $[U_{ku}]^{-1} [U_k]$
- B : modification region
- [B] : reanalysis matrix = $\begin{bmatrix} U_{uu}^C \\ U_{ku}^C \end{bmatrix} [U_{ku}]^{-1} [\Delta k]$
- C : region to the left of the segment being modified
- $F^R = (F^R)$: 4x1 force vector for region R
- F_w, F_ϕ, F_M, F_V : displacement, angle, moment and shear force effects due to applied loading
- [I] : unit matrix
- K : stiffness
- $K_G = [K_G]$: global stiffness matrix
- $K_e = [K_e]$: element stiffness matrix
- ΔK : modification of stiffness matrix
- M^i : bending moment at station i
- [P] : frontal transfer matrix
- [Q] : frontal forcing term
- [R] : mobility or receptance matrix
- $\underline{s} = (s)$: extended state vector $\begin{bmatrix} s^i \\ 1 \end{bmatrix}$
- $\underline{s}^i = (s^i)$: 4x1 state vector at station i
- $\underline{U} = [U]$: extended transfer matrix $\begin{bmatrix} U^R & F^R \\ \dots & \dots \\ 0 & 1 \end{bmatrix}$
- $\underline{U}^R = (U^R)$: 4x4 transfer matrix for region R
- $\Delta \underline{U}^B = (\Delta U^B)$: change in transfer matrix for region B
- v^i : shear force at station i
- w^i : displacement at station i
- Z : impedance
- θ^i : angle at station i
- ω : frequency

Problem Formulation

Consider the system of Fig. 1, in which the structure with a line-like topology is divided into three segments A, B, and C. The substructures in regions A and C are fixed, while that in region B is subject to modification, including continuous changes as well as discrete modifications at the ends of the segment.

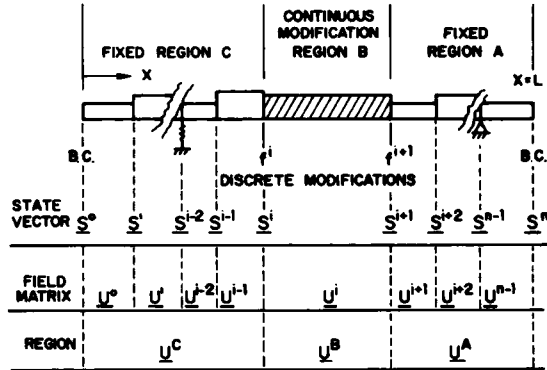


Fig. 1 A Line-like Structure with Continuous and Discrete Modification

The modification is related to the state variables \underline{s}^i and \underline{s}^{i+1} using the transfer matrix \underline{U}^B . The boundary conditions are set forth in \underline{s}^0 and \underline{s}^n . Point variables can be eliminated with the standard transfer matrix calculations and condensed to three matrices \underline{U}^C , \underline{U}^B , and \underline{U}^A .

Suppose the structure is a beam. According to transfer matrix theory [3,4], the state variables

$$\underline{s} = \{ w \quad \theta \quad M \quad V \}^T \tag{1}$$

are related at stations l and l+1 by

$$\underline{s}^{l+1} = \underline{U}^R \underline{s}^l \tag{2}$$

For the original system, the overall transfer matrix relationship would be

$$\underline{s}^n = \underline{U}^A \underline{U}^B \underline{U}^C \underline{s}^0 \tag{3}$$

Using the known boundary conditions, \underline{s}^0 of the original system can be evaluated. Responses along the structure can then be calculated with the standard transfer matrix procedure. In expanded form, Eq. (3) can be written as

$$\begin{bmatrix} \underline{s}^n \\ \dots \\ 1 \end{bmatrix} = \begin{bmatrix} \underline{U}^A \underline{U}^B \underline{U}^C & \dots \\ \dots & \dots \\ 0 & 1 \end{bmatrix} \begin{bmatrix} \underline{s}^0 \\ \dots \\ 1 \end{bmatrix} \tag{4}$$

where \underline{s}^0 is the vector of initial parameters of the original system. Now, assume the structure in region B is modified so that

$$\underline{U}^{B*} = \underline{U}^B + \Delta \underline{U}^B \quad (5)$$

Substitute equation (5) into (3) to obtain the modified system equation

$$\underline{s}^n = \underline{U}^A (\underline{U}^B + \Delta \underline{U}^B) \underline{U}^C \underline{s}^0 \quad (6)$$

For the region B, \underline{U}^{B*} appears as

$$\underline{s}^{i+1} = \underline{U}^{B*} \underline{s}^i$$

or

$$\begin{bmatrix} \underline{s}^{i+1} \\ \vdots \\ 1 \end{bmatrix} = \begin{bmatrix} \underline{U}^B + \Delta \underline{U}^B & \vdots & \underline{F}^B \\ \vdots & \ddots & \vdots \\ \underline{0} & \vdots & 1 \end{bmatrix} \begin{bmatrix} \underline{s}^i \\ \vdots \\ 1 \end{bmatrix} \quad (7)$$

Assume that the modification does not alter the forcing terms, which is usually the case. Then treat the matrix change $\Delta \underline{U}^B$ as a "pseudo-load" so that Eq. (7) appears as

$$\begin{bmatrix} \underline{s}^{i+1} \\ \vdots \\ 1 \end{bmatrix} = \begin{bmatrix} \underline{U}^B & \vdots & \underline{F}^B + \Delta \underline{U}^B \underline{s}^i \\ \vdots & \ddots & \vdots \\ \underline{0} & \vdots & 1 \end{bmatrix} \begin{bmatrix} \underline{s}^i \\ \vdots \\ 1 \end{bmatrix} \quad (8)$$

where $\Delta \underline{U}^B \underline{s}^i$ is the "pseudo-load" vector that depends on the state variables of the modified system.

Using equation (8), the transfer matrix relationship for the modified system becomes

$$\begin{bmatrix} \underline{s}^n \\ \vdots \\ 1 \end{bmatrix} = \begin{bmatrix} \underline{U}^A & \vdots & \underline{F}^A \\ \vdots & \ddots & \vdots \\ \underline{0} & \vdots & 1 \end{bmatrix} \begin{bmatrix} \underline{U}^B & \vdots & \underline{F}^B + \Delta \underline{U}^B \underline{s}^i \\ \vdots & \ddots & \vdots \\ \underline{0} & \vdots & 1 \end{bmatrix} \begin{bmatrix} \underline{U}^C & \vdots & \underline{F}^C \\ \vdots & \ddots & \vdots \\ \underline{0} & \vdots & 1 \end{bmatrix} \begin{bmatrix} \underline{s}^0 \\ \vdots \\ 1 \end{bmatrix} \quad (9)$$

or

$$\underline{s}^n = (\underline{U}^A \underline{U}^B \underline{U}^C \underline{s}^0 + (\underline{U}^A \underline{U}^B \underline{F}^C + \underline{U}^A \underline{F}^B + \underline{F}^A)) + \underline{U}^A \Delta \underline{U}^B \underline{s}^i \quad (10)$$

Define

$$\underline{U} = \underline{U}^A \underline{U}^B \underline{U}^C \quad (\text{the original overall transfer matrix})$$

$$\underline{F} = \underline{U}^A \underline{U}^B \underline{F}^C + \underline{U}^A \underline{F}^B + \underline{F}^A \quad (\text{the total effect of the external loading})$$

$$\Delta \underline{U} = \underline{U}^A \Delta \underline{U}^B \quad (\text{the modified effect})$$

$$\underline{s}^i = \begin{bmatrix} \underline{s}^i \\ \vdots \\ \underline{s}^i \\ \vdots \\ \underline{s}^i \end{bmatrix} = \begin{bmatrix} \text{unknown} \\ \text{known} \end{bmatrix} \quad \text{variables of } \underline{s}$$

Then Eq. (10) can be written as

$$\begin{bmatrix} \underline{s}^n \\ \vdots \\ \underline{s}^n \\ \vdots \\ \underline{s}^n \end{bmatrix} = \begin{bmatrix} U_{nn} & U_{nk} \\ U_{ku} & U_{kk} \end{bmatrix} \begin{bmatrix} \underline{s}_u^0 \\ \underline{s}_k^0 \end{bmatrix} + \begin{bmatrix} \underline{F}_u \\ \underline{F}_k \end{bmatrix} + \begin{bmatrix} \Delta U_u \\ \Delta U_k \end{bmatrix} \underline{s}^i \quad (12)$$

where submatrices are 2x2 and the state vectors are 2x1 corresponding to the unknown and known boundary variables. Suppose the known boundary variables are zero, i.e., $(\underline{s}_k^n) = (\underline{s}_k^0) = \underline{0}$. Then the lower half of Eq. (12) becomes

$$\underline{s}_k^n = \underline{0} = [U_{ku}] \underline{s}_u^0 + \underline{F}_k + [\Delta U_k] \underline{s}^i \quad (13)$$

so that

$$\underline{s}_u^{0*} = -[U_{ku}]^{-1} \underline{F}_k - [U_{ku}]^{-1} [U_k] \underline{s}^{i*} = \underline{s}_u^0 - [A] \underline{s}^{i*} \quad (14)$$

where the superscript * is used to identify the modified variables. The unmodified variable $(\underline{s}_u^0) = -[U_{ku}]^{-1} \underline{F}_k$ contains the original system initial parameters and

$$[A] = [U_{ku}]^{-1} [\Delta U_k] \quad (15)$$

The vector \underline{s}^{i*} can be calculated using the matrix $[U]$

$$\underline{s}^{i*} = [U^C] \underline{s}^{0*} + \underline{F}^C = \begin{bmatrix} U_{uu}^C & U_{uk}^C \\ U_{ku}^C & U_{kk}^C \end{bmatrix} \begin{bmatrix} \underline{s}_u^{0*} \\ \underline{s}_k^{0*} \end{bmatrix} + \underline{F}^C$$

Introduce Eq. (14) into the above equation

$$\begin{aligned} \underline{s}^{i*} &= \begin{bmatrix} U_{uu}^C \\ U_{ku}^C \end{bmatrix} \{ \underline{s}_u^0 - [A] \underline{s}^{i*} \} + \underline{F}^C \\ &= \underline{s}^i - [B] \underline{s}^{i*} \end{aligned}$$

Then,

$$\underline{s}^{i*} = ([I] + [B])^{-1} \underline{s}^i \quad (16)$$

where \underline{s}^i is the state variable vector of original system of station i and

$$[B] = \begin{bmatrix} U_{uu}^C \\ U_{ku}^C \end{bmatrix} [U_{ku}]^{-1} [\Delta U_k] \quad (17)$$

Once \underline{s}^{i*} is known, \underline{s}^{0*} can be calculated using Eq. (14)

$$\underline{s}_u^{0*} = \underline{s}_u^0 - [A] ([I] + [B])^{-1} \underline{s}^i \quad (18)$$

Finally, the responses of the modified system can be computed.

This formulation can be used efficiently to perform a synthesis problem such as one wherein the resonant frequency of the modified system is prescribed and the characteristics of the modifications necessary to achieve the desired frequency are to be calculated. This is accomplished by solving the characteristics equation

$$\det([I] + [B]) = 0 \quad (19)$$

for the required modification which is contained in $[B]$.

For a steady-state reanalysis problem, Eq. (18) can be employed to determine the initial state variables s_u^0 . Several point transfer matrices should be stored in order to calculate the corresponding point responses. This would require relatively large storage memories, but for reanalysis, the response calculations would be very efficient. See the point modification formulation of [5].

Numerical Stability of Transfer Matrix Calculations

It has long been recognized that the transfer matrix method sometimes encounters numerical difficulties which prevent it from wide application. To avoid this difficulty, several modified methods have been proposed [3,4]. Among them, the frontal transfer matrix method and the stiffness matrix (displacement) method have relatively stable and efficient numerical characteristics.

The Frontal Transfer Matrix Method In general, half of the state variables are known (usually zero) at the boundaries. Let (s_u^k) be unknown and (s_k^l) be known variable at the station l . When there is an in-span rigid support or in-span release, (s_u) and (s_k) should be re-arranged such that discontinuous state variables are included in (s_u) .

At the initial station 0,

$$\begin{pmatrix} s_u^0 \\ s_k^0 \end{pmatrix} = \begin{pmatrix} 0 \\ s_u^0 \\ 0 \\ s_k^0 \end{pmatrix} = \begin{bmatrix} I \\ 0 \end{bmatrix} \begin{pmatrix} s_u^0 \\ s_k^0 \end{pmatrix} \quad (20)$$

To cross the first segment, use

$$\begin{aligned} s^1 &= \begin{pmatrix} s_u^1 \\ s_k^1 \end{pmatrix} = \begin{bmatrix} U_{uu}^0 & U_{uk}^0 \\ U_{ku}^0 & U_{kk}^0 \end{bmatrix} \begin{pmatrix} s_u^0 \\ s_k^0 \end{pmatrix} + \begin{pmatrix} F_u^0 \\ F_k^0 \end{pmatrix} \\ &= \begin{bmatrix} U_{uu}^0 & 0 \\ 0 & U_{kk}^0 \end{bmatrix} \begin{pmatrix} s_u^0 \\ s_k^0 \end{pmatrix} + \begin{pmatrix} F_u^0 \\ F_k^0 \end{pmatrix} = \begin{bmatrix} P_u^0 & 0 \\ 0 & P_k^0 \end{bmatrix} \begin{pmatrix} s_u^0 \\ s_k^0 \end{pmatrix} + \begin{pmatrix} Q_u^0 \\ Q_k^0 \end{pmatrix} \end{aligned} \quad (21)$$

where the general form of P and Q will be defined later. From the upper relationship of Eq. (21),

$$\begin{pmatrix} s_u^0 \\ s_k^0 \end{pmatrix} = [P_u^0]^{-1} \begin{pmatrix} s_u^1 \\ s_k^1 \end{pmatrix} - [P_u^0]^{-1} \begin{pmatrix} Q_u^0 \\ Q_k^0 \end{pmatrix}$$

Introduce this equation into the lower relationship of Eqs. (21),

$$\begin{pmatrix} s_u^1 \\ s_k^1 \end{pmatrix} = [P_k^0] [P_u^0]^{-1} \begin{pmatrix} s_u^1 \\ s_k^1 \end{pmatrix} + \{ [Q_k^0] - [P_k^0] [P_u^0]^{-1} [Q_u^0] \}$$

Hence, the following equation is obtained

$$\begin{pmatrix} s_u^1 \\ s_k^1 \end{pmatrix} = \begin{bmatrix} [I] \\ [P_k^0] [P_u^0]^{-1} \end{bmatrix} \begin{pmatrix} s_u^1 \\ s_k^1 \end{pmatrix} + \begin{pmatrix} 0 \\ \{ [Q_k^0] - [P_k^0] [P_u^0]^{-1} [Q_u^0] \} \end{pmatrix} \quad (22)$$

To cross the next segment,

$$\begin{pmatrix} s_u^2 \\ s_k^2 \end{pmatrix} = \begin{pmatrix} s_u^1 \\ s_k^1 \end{pmatrix} = \begin{bmatrix} U_{uu}^1 & U_{uk}^1 \\ U_{ku}^1 & U_{kk}^1 \end{bmatrix} \begin{pmatrix} s_u^1 \\ s_k^1 \end{pmatrix} + \begin{pmatrix} F_u^1 \\ F_k^1 \end{pmatrix} \quad (23)$$

Substitute Eq. (21) into Eq. (22)

$$\begin{aligned} \begin{pmatrix} s_u^2 \\ s_k^2 \end{pmatrix} &= \begin{bmatrix} U_{uu}^1 & U_{uk}^1 \\ U_{ku}^1 & U_{kk}^1 \end{bmatrix} \left(\begin{bmatrix} [I] \\ [P_k^0] [P_u^0]^{-1} \end{bmatrix} \begin{pmatrix} s_u^1 \\ s_k^1 \end{pmatrix} \right. \\ &\quad \left. + \begin{pmatrix} 0 \\ \{ [Q_k^0] - [P_k^0] [P_u^0]^{-1} [Q_u^0] \} \end{pmatrix} \right) + \begin{pmatrix} F_u^1 \\ F_k^1 \end{pmatrix} \\ &= \begin{bmatrix} [U_{uu}^1] + [U_{uk}^1] [P_k^0] [P_u^0]^{-1} \\ [U_{ku}^1] + [U_{kk}^1] [P_k^0] [P_u^0]^{-1} \end{bmatrix} \begin{pmatrix} s_u^1 \\ s_k^1 \end{pmatrix} \\ &\quad + \begin{pmatrix} [U_{ku}^1] \{ [Q_k^0] - [P_k^0] [P_u^0]^{-1} [Q_u^0] \} + \{ F_u^1 \} \\ [U_{kk}^1] \{ [Q_k^0] - [P_k^0] [P_u^0]^{-1} [Q_u^0] \} + \{ F_k^1 \} \end{pmatrix} \end{aligned} \quad (24)$$

Now, define the general form of P and Q as

$$\begin{aligned} [P_u^l] &= [U_{uu}^l] + [U_{uk}^l] [P_k^{l-1}] [P_u^{l-1}]^{-1} \\ [P_k^l] &= [U_{ku}^l] + [U_{kk}^l] [P_k^{l-1}] [P_u^{l-1}]^{-1} \\ [Q_u^l] &= [F_u^l] + [U_{uk}^l] \{ [Q_k^{l-1}] - [P_k^{l-1}] [P_u^{l-1}]^{-1} [Q_u^{l-1}] \} \\ [Q_k^l] &= [F_k^l] + [U_{kk}^l] \{ [Q_k^{l-1}] - [P_k^{l-1}] [P_u^{l-1}]^{-1} [Q_u^{l-1}] \} \end{aligned} \quad (25)$$

If these relationships are used to proceed to the $n-1$ station (Fig. 1), then

$$\begin{pmatrix} s_u^n \\ s_k^n \end{pmatrix} = \begin{bmatrix} P_u^{n-1} \\ P_k^{n-1} \end{bmatrix} \begin{pmatrix} s_u^{n-1} \\ s_k^{n-1} \end{pmatrix} + \begin{pmatrix} Q_u^{n-1} \\ Q_k^{n-1} \end{pmatrix} \quad (26)$$

If the rows of (s^n) , $[P^{n-1}]$, and (Q^{n-1}) are interchanged properly so that the right-end known variables are included in (s_u) (usually zero), the following response is obtained

$$\begin{pmatrix} s_u^{n-1} \\ s_k^{n-1} \end{pmatrix} = -[P_k^{n-1}] [Q_k^{n-1}] \quad (27)$$

Continued backward substitution yields the entire beam response.

Consider now the modification. Suppose only the i th ($=B$) section is modified as in Eq. (8)

$$\begin{pmatrix} s_{i+1}^* \\ s_i^* \\ 1 \end{pmatrix} = \begin{bmatrix} U^i & F^i + \Delta U^i s_i^* \\ 0 & 1 \end{bmatrix} \begin{pmatrix} s_i^* \\ 1 \end{pmatrix}$$

From Eqs. (16) and (17), the reanalysis equation is obtained

$$\{s^{i+1}\} = \{[I] + [B]\}^{-1} \{s^i\} \quad (28)$$

Here the reanalysis matrix [B] can be calculated from the \underline{P} matrix

$$[B] = \begin{bmatrix} U_{cc}^C \\ \dots \\ U_{ku}^C \end{bmatrix} [U_{ju}]^{-1} [\Delta k] \quad (29)$$

$$\begin{bmatrix} U_{cc}^C \\ \dots \\ U_{ku}^C \end{bmatrix} = \begin{bmatrix} P_u^{i-1} \\ \dots \\ P_k^{i-1} \end{bmatrix} [P_u^{i-2}] \dots [P_u^0] \quad (30)$$

$$[U_{ku}] = [P_k^{n-1}] [P_u^{n-2}] \dots [P_u^1] \dots [P_u^0] \quad (31)$$

The frontal transfer matrix method is one of the most efficient numerical techniques available to solve the transfer relationship. The primary drawback is the complexity of its formulation, especially if reanalysis is involved.

Dynamic Stiffness Matrix Method The frontal transfer matrix method is computationally attractive. But the formulation is somewhat unfamiliar to most people and, also, it requires some inconvenient adjustments, depending on the selection of known variables and unknown variables on the boundaries and at certain in-span conditions.

In contrast, the stiffness method superimposed on the transfer matrices has the advantage of familiarity and of being able to use standard matrix solution routines. Additionally, it does not suffer the numerical instabilities associated with the pure transfer matrix method.

A generalized transfer matrix for a beam segment has the form [4]

$$\begin{Bmatrix} \omega \\ \theta \\ V \\ M \\ 1 \end{Bmatrix} = \begin{bmatrix} [U_{aa}] & [U_{ab}] & F_\omega \\ \dots & \dots & F_\theta \\ [U_{ba}] & [U_{bb}] & F_V \\ \dots & \dots & F_M \\ 0 & 0 & 0 & 0 & 1 \end{bmatrix} \begin{Bmatrix} \omega \\ \theta \\ V \\ M \\ 1 \end{Bmatrix}^i \quad (32)$$

This is readily converted to a dynamic stiffness matrix by first writing Eq. (32) as

$$\begin{Bmatrix} \omega \\ \theta \end{Bmatrix}^{i+1} = [U_{aa}] \begin{Bmatrix} \omega \\ \theta \end{Bmatrix}^i + [U_{ab}] \begin{Bmatrix} V \\ M \end{Bmatrix}^i + \begin{Bmatrix} F_\omega \\ F_\theta \end{Bmatrix} \quad (33)$$

$$\begin{Bmatrix} V \\ M \end{Bmatrix}^i = [U_{ba}] \begin{Bmatrix} \omega \\ \theta \end{Bmatrix}^i + [U_{bb}] \begin{Bmatrix} V \\ M \end{Bmatrix}^i + \begin{Bmatrix} F_V \\ F_M \end{Bmatrix} \quad (34)$$

Then solve Eq. (33) in terms of $\begin{Bmatrix} V \\ M \end{Bmatrix}^i$

$$\begin{Bmatrix} V \\ M \end{Bmatrix}^{i+1} = -[U_{ab}]^{-1} [U_{aa}] \begin{Bmatrix} \omega \\ \theta \end{Bmatrix}^i + [U_{ab}]^{-1} \begin{Bmatrix} \omega \\ \theta \end{Bmatrix}^{i+1} - [U_{ab}]^{-1} \begin{Bmatrix} F_\omega \\ F_\theta \end{Bmatrix} \quad (35)$$

Substitute Eq. (35) into Eq. (34) to get

$$\begin{Bmatrix} V \\ M \end{Bmatrix}^{i+1} = [U_{ba}] \begin{Bmatrix} \omega \\ \theta \end{Bmatrix}^i + [U_{bb}] \begin{Bmatrix} V \\ M \end{Bmatrix}^i - [U_{ab}]^{-1} [U_{aa}] \begin{Bmatrix} \omega \\ \theta \end{Bmatrix}^i + [U_{ab}]^{-1} \begin{Bmatrix} \omega \\ \theta \end{Bmatrix}^{i+1} - [U_{ab}]^{-1} \begin{Bmatrix} F_\omega \\ F_\theta \end{Bmatrix} + \begin{Bmatrix} F_V \\ F_M \end{Bmatrix} \quad (36)$$

At this point it is necessary to introduce a change in sign convention, since in the transfer matrix method, the positive direction of internal forces (shear and bending moment) is not the same as the displacements (deflection and rotation) at both ends of the segment (see Fig. 2), while in the dynamic stiffness matrix, the positive direction of internal forces is the same as the positive direction of the displacements at both ends of the beam segment. Considering this sign convention change, the following stiffness matrix is obtained.

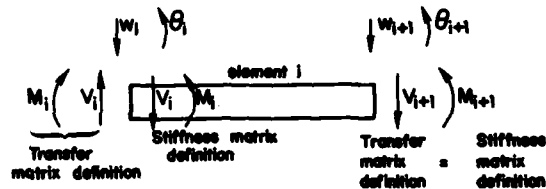


Fig. 2 Sign Change of Transfer Matrix to Stiffness Matrix

$$\begin{Bmatrix} V \\ M \\ 1 \end{Bmatrix}^{i+1} = \begin{bmatrix} [U_{ba}]^{-1} [U_{aa}] & -[U_{ab}]^{-1} & [U_{ab}]^{-1} \begin{Bmatrix} F_\omega \\ F_\theta \end{Bmatrix} \\ [U_{ba}] - [U_{bb}] [U_{ab}]^{-1} [U_{aa}] & [U_{bb}] [U_{ab}]^{-1} & -[U_{bb}] [U_{ab}]^{-1} \begin{Bmatrix} F_\omega \\ F_\theta \end{Bmatrix} + \begin{Bmatrix} F_V \\ F_M \end{Bmatrix} \\ 0 & 0 & 1 \end{bmatrix} \begin{Bmatrix} V \\ M \\ 1 \end{Bmatrix}^i \quad (37)$$

or

$$\begin{pmatrix} \left\{ \begin{matrix} v^i \\ \vdots \\ v^i \\ \vdots \\ v^{i+1} \end{matrix} \right\} - [u_{ab}]^{-1} \left\{ \begin{matrix} F_a \\ \vdots \\ F_a \\ \vdots \\ F_a \end{matrix} \right\} \\ \left\{ \begin{matrix} v^{i+1} \\ \vdots \\ v^{i+1} \\ \vdots \\ v^{i+1} \end{matrix} \right\} - [F_M] + [u_{bb}] [u_{ab}]^{-1} \left\{ \begin{matrix} F_a \\ \vdots \\ F_a \\ \vdots \\ F_a \end{matrix} \right\} \end{pmatrix} = \begin{pmatrix} [u_{aa}]^{-1} [u_{aa}] & - [u_{ab}]^{-1} \\ [u_{ba}] - [u_{bb}] [u_{ab}]^{-1} [u_{aa}] & [u_{bb}] [u_{ab}]^{-1} \end{pmatrix} \begin{pmatrix} u^i \\ \vdots \\ u^i \\ \vdots \\ u^{i+1} \end{pmatrix} \quad (38)$$

This is a "dynamic" stiffness matrix of the sort discussed in Ref. [6]. The elements are functions of the forcing frequency.

The element stiffness matrices can be superimposed in the usual fashion to form the global stiffness equations.

$$\{F\} = [K_G]\{u\} \quad (39)$$

The stiffness matrix K_G is symmetric and band limited. Usually the bandwidth is four for a beam in plane bending. If there are some inspan supports or point modifications, appropriate impedances Z_i can be added to the proper diagonal element of the K_G matrix:

$$K_{ii} \quad K_{ii} + Z_i \quad (40)$$

In the case of displacement constraints, including boundary conditions, corresponding force elements and nondiagonal stiffness elements should be zero, that is, if u_i is prescribed to be zero; set $F_i = 0$ and $K_{ij} = 0, K_{ji} = 0 (j \neq i)$

$$\begin{pmatrix} 0 & \vdots & 0 \\ \vdots & \ddots & \vdots \\ 0 & \dots & 0 \\ 0 & \dots & 0 \\ \vdots & \ddots & \vdots \\ 0 & \dots & 0 \end{pmatrix} \begin{pmatrix} u_i \\ \vdots \\ u_i \\ \vdots \\ u_i \\ \vdots \\ u_i \end{pmatrix} = \begin{pmatrix} \vdots \\ \vdots \\ F_i = 0 \\ \vdots \\ \vdots \\ \vdots \\ \vdots \end{pmatrix} \quad (41)$$

This is equivalent to setting u_i equal to zero.

After assembling and modifying the global stiffness matrix, steady-state response can be obtained using a solution technique such as Gauss elimination.

Define the inverse matrix (mobility or receptance matrix) as by

$$\{R\} = [K_G]^{-1} \quad (42)$$

so that

$$\{u\} = [K_G]^{-1}\{F\} = \{R\}\{F\} \quad (43)$$

Consider now the incorporation of modifications. The dynamic stiffness matrix method can accept not only point modifications but also continuous modifications. Suppose

that for one segment there are a continuous parameter modification spanning the segment and two point modifications, one on each end of the segment. The continuous parameter modification causes the stiffness matrix change of that element and discrete parameter modification should be added to the diagonal term of ΔK_G

$$[K_G^*] = [K_G] + [\Delta K_G]$$

where the ΔK_G matrix appears as

$$[K_G] = \begin{pmatrix} 0 & \dots & 0 & \dots & 0 \\ \vdots & \ddots & \vdots & \ddots & \vdots \\ 0 & \dots & \Delta K & \dots & 0 \\ \vdots & \ddots & \vdots & \ddots & \vdots \\ 0 & \dots & 0 & \dots & 0 \end{pmatrix} \begin{matrix} C \\ \vdots \\ B \\ \vdots \\ A \end{matrix} \quad (45) \quad (45)$$

Here, the segment has been divided into the three regions of Fig. 1. The original solution u can be partitioned as

$$\{u\} = \begin{pmatrix} U_C \\ \vdots \\ U_B \\ \vdots \\ U_A \end{pmatrix} \quad (46)$$

and the modified stiffness equation becomes

$$\{F\} = \begin{pmatrix} F_C \\ \vdots \\ F_B \\ \vdots \\ F_A \end{pmatrix} = [K_G] \begin{pmatrix} U_C \\ \vdots \\ U_B \\ \vdots \\ U_A \end{pmatrix} + [\Delta K]\{U_B^*\} \quad (47)$$

By partitioning the mobility matrix into the three segments

$$\{R\} = [K_G]^{-1} = \begin{pmatrix} \hat{R}_C & \dots & \dots \\ \vdots & \ddots & \vdots \\ \hat{R}_B & \dots & \dots \\ \vdots & \ddots & \vdots \\ \hat{R}_A & \dots & \dots \end{pmatrix} \quad (48)$$

It then follows that

$$\begin{pmatrix} U_C^* \\ \vdots \\ U_B^* \\ \vdots \\ U_A^* \end{pmatrix} = \begin{pmatrix} U_C \\ \vdots \\ U_B \\ \vdots \\ U_A \end{pmatrix} - \begin{pmatrix} \hat{R}_C \\ \vdots \\ \hat{R}_B \\ \vdots \\ \hat{R}_A \end{pmatrix} [\Delta K]\{U_B^*\} \quad (49)$$

The modification portion of the reanalysis equation is given by

$$\{U_B^*\} = [[I] + [\hat{R}_B][\Delta K]]^{-1}\{U_B^*\} \quad (50)$$

Substitution of $\{u_B^*\}$ into the rest of Eq. (49) gives

$$\{U_B^*\} = \{U_C\} - [R_C][\Delta K]\{U_B^*\} \quad (51)$$

$$\{U_A^*\} = \{U_A\} - [R_A][\Delta K]\{U_B^*\}$$

Note that Eq. (50) is similar to the reanalysis relation of Eq. (16).

This can also be used to perform a synthesis problem such as one wherein the resonant frequency is prescribed and the characteristics of modification necessary to achieve the desired frequency are to be calculated. This is accomplished using the characteristic equation similar to Eq. (19).

$$\det([\mathbf{I}] + [R_B][\Delta K]) = 0$$

For a steady-state reanalysis problem, the partitioned mobility matrix $[R_A]$, $[R_B]$ and $[R_C]$ should be calculated and stored. Then the modified response is calculated efficiently by using equations (50) and (51).

The dynamic stiffness method is not quite as efficient as the frontal transfer matrix method. However, the treatment is very similar to the usual finite element method. This means that this method can be coupled to a standard structural analysis capability or can use standard linear equation solution techniques.

Numerical Examples

This formulation will be illustrated using the simple three-sectioned beam of Fig. 3. Although this reanalysis approach can accept modification of both continuous and discrete parameters, the only modification considered here is the distributed mass change $\Delta\rho$ in section B. In this example, the point stiffness k_2 is fixed at its value 0.2 MN/m. Other numerical values are shown in Table 1.

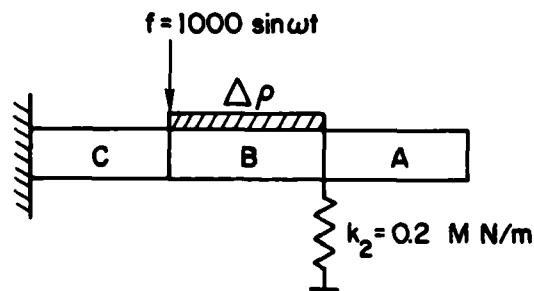


Fig. 3 Numerical Example

Table 1 Physical Properties for the Beam of the Example Problem

Section	C	B	A	unit
EI	0.5	0.5	0.5	kNm^2
ρ (density)	.0005	.0005 .0014 .0023	.0005	k/m
l (length)	.15	.20	.15	m

The steady-state responses of the original and modified beam are illustrated in Fig. 4. Of course, increasing the distributed mass causes a decrease of resonant frequency. However, the second resonant frequency undergoes a larger change than the other resonancies.

These responses were calculated using the three methods; the usual transfer matrix reanalysis formula, frontal reanalysis, and stiffness matrix reanalysis. The three results are the same, but as is to be expected the calculation time of the frontal method is slightly better than the stiffness method. Both of these methods are significantly more efficient than the pure transfer matrix method.

CONCLUSIONS

An efficient reanalysis procedure has been formulated for studying the dynamic effects of discrete and continuous local modifications to a continuous systems. In particular, the formulation applies to systems with a line-like geometry which are readily analyzed with the transfer matrix method. A conversion to frontal transfer and stiffness matrices is introduced to assure that no numerical instability occurs in the analysis. Numerically, these stable methods are more efficient than transfer matrices. The numerical examples illustrate the effectiveness of this approach. This formulation is appropriate for application to many engineering systems that are properly modeled as line type structures.

ACKNOWLEDGMENT

This work was supported by the U.S. Army Research Office, Research Triangle Park, North Carolina. W. Pilkey's effort was supported by the NAVSEA Research Chair at the Naval Postgraduate School, Monterey.

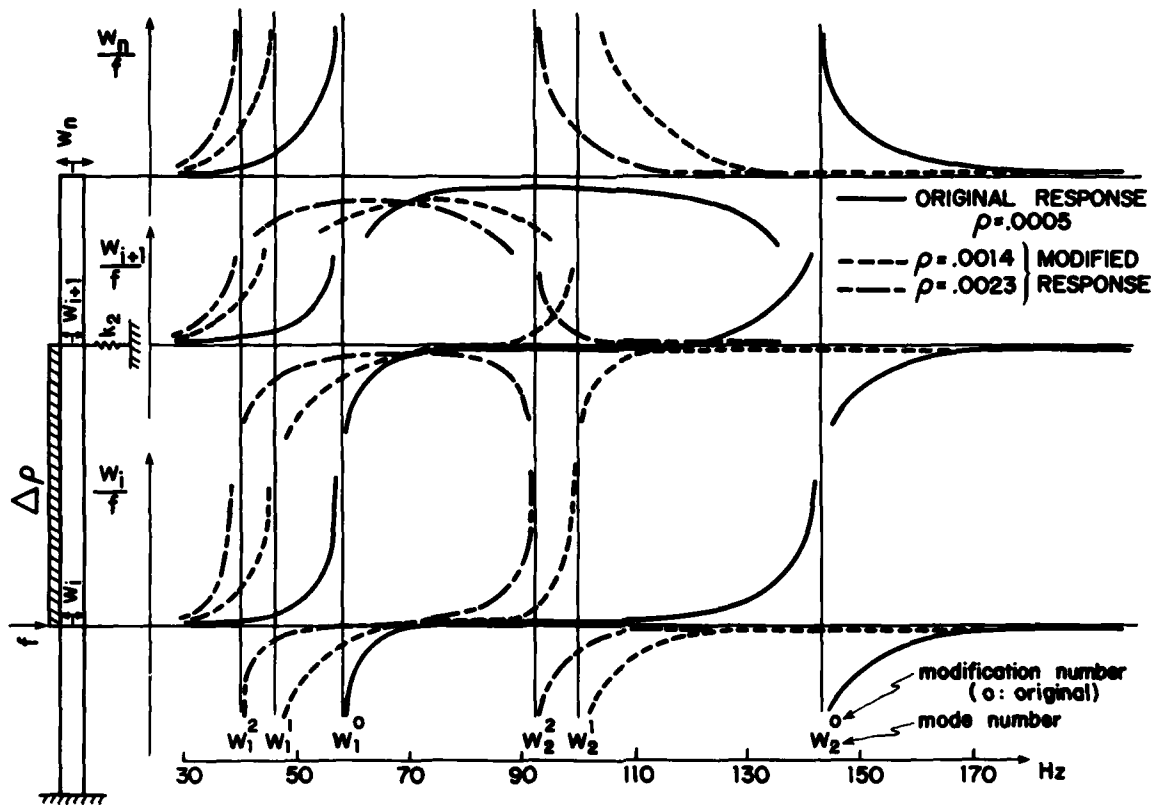


Fig. 4 Numerical Results

REFERENCES

1. Wang, P.B., Palazzolo, A.B., and Pilkey, W.D., "Reanalysis, Modal Synthesis, and Dynamic Design," Chapter 8. State of the Art Review of Finite Element Methods, edited by Noor, A., and Pilkey, W.D., ASME, 1983.
2. King, S.P., "The Modal Approach to Structural Modification," Journal of the American Helicopter Society, Vol. 28, No. 2, April 1983, pp. 30-36.
3. Pestel, E.C., and Leckie, F.A., Matrix Methods in Elastomechanics, McGraw Hill, 1963.
4. Pilkey, W.D., and Chang, P.Y., Modern Formulas for Statics and Dynamics, McGraw Hill, 1978.
5. Okada, Y., Wang, B.P., and Pilkey, W.D., "Discrete Modifications to Continuous Dynamic Systems," Shock and Vibration Bulletin, Vol. 54, 1983.
6. Lunden, R., and Akesson, B., "Damped Second-Order Rayleigh-Timoshenko Beam Vibration in Space - An Exact Complex Dynamic Member Stiffness Matrix," Int. Journal for Numerical Methods in Engineering, Vol. 19, 1983, pp. 431-449.

A POLE-FREE REDUCED-ORDER CHARACTERISTIC DETERMINANT
METHOD FOR LINEAR VIBRATION ANALYSIS BASED ON SUB-STRUCTURING

B. Dawson
Polytechnic of Central London
London, England

and

M. Davies
University of Surrey
Guildford, Surrey, England

A general method of solution for the linear vibration analysis of structures is presented. The method is based on sub-structuring and the formation of a reduced-order characteristic determinant whose zeros yield all the natural vibration frequencies of the system. The concept of the method and its application is illustrated via the determination of the torsional natural frequencies of engine-driven systems involving both discrete and continuous components.

INTRODUCTION

In linear vibration analysis the problem of determining the natural vibration frequencies of a structure is usually solved as a linear algebraic eigenvalue problem for which powerful and efficient algorithms exist. These methods are, however, only applicable to discrete structures. Structures containing continuum elements are therefore first discretised by finite element methods. Since these necessarily introduce approximations for which error bounds may or may not be available, the number of degrees of freedom may have to be very large in order to achieve a sufficiently representative model of the structure. Any attempt to reduce the order of the system by eliminating co-ordinates by economisation techniques introduce further approximations unless exact Guyan reduction is used, and this has the undesirable effect of introducing poles.

When the continuum elements have simple geometric shapes and are composed of homogeneous materials the exact analytic forms of the dynamic stiffness matrices of each component, whose elements have a transcendental dependence on frequency, may be known. Assembly of these individual matrices to form an overall, non-linear, dynamic stiffness matrix for the structure has the merit of giving rise to a relatively small order matrix provided the internal coordinates of each component are eliminated. However, this formulation again gives rise to poles.

The ubiquitous intrusion of poles presents a major problem in an otherwise highly

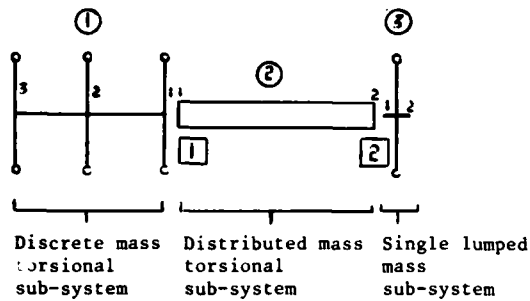
attractive method of vibration analysis. It makes an automatic root search well nigh impossible without previously locating the poles, and even then, close proximity of poles and zeros can make their resolution extremely difficult.

We have shown in a previous communication [1] that a pole-free formulation in the form of an asymmetric characteristic determinant whose zeros are the natural frequencies can be achieved for lumped-parameter branched marine drive systems. Subsequent consideration has confirmed that this method of analysis is possible for general structures provided no forced excitation frequency exists at which a sub-structure behaves as a decoupled system. However, as in general only specially designed mechanical components possess this latter property, a pole-free representation should be possible for all structures occurring in practice.

The pole-free method is based on a matrix transfer representation in which the coefficients of transfer matrices corresponding to individual system component substructures are assembled to form the elements of a reduced-order characteristic determinant. This method leads to a larger order determinant than that of the equivalent reduced-order dynamic stiffness matrix but it has the distinct advantage of being pole-free. The method is presented and illustrated by application to the determination of the natural frequencies of vibration of both straight and branched engine driven systems modelled as a combination of continuous and discrete components.

GENERATION OF REDUCED-ORDER CHARACTERISTIC DETERMINANT

To illustrate the principles of the method we consider the determination of the natural frequencies of torsional vibration of the system shown in Fig.1 which has been sub-structured into three sub-systems.



①, ② etc. denote sub-systems

1, 2 etc. denote local coordinates

Fig.1. - Sub-structured torsional vibration system.

These are indicated in the diagram by circles and in the text by bracketed superscripts (1), (2) etc. For any frequency, the reduced characteristic determinant is formed via consideration of the equilibrium equations at the junction points between sub-systems together with the satisfaction of the boundary conditions of the system. These equations are formed in terms of the elements of the transfer matrices of the individual sub-systems. Thus for each sub-system it is necessary to find the transfer matrix relating the state vectors at each end and these may be derived as follows.

Sub-system (1):

This consists of a set of individual discrete mass and stiffness components. However, in order to reduce the number of junction points and hence the order of the determinant it is considered as a single sub-system. The overall transfer matrix may be obtained via either

- (i) a matrix transfer formulation, or
- (ii) a Guyan reduction which reduces the number of co-ordinates to those corresponding to the end co-ordinates of the sub-structure, thus:

(i) Matrix transfer formulation :

The matrix transfer equation has the form

$$z_3^{(1)} = P_3 F_2 P_2 F_1 P_1 z_1^{(1)} = T^{(1)} z_1^{(1)} = \begin{bmatrix} t_{11} & t_{12} \\ t_{21} & t_{22} \end{bmatrix}^{(1)} z_1^{(1)} \quad (1)$$

where P_i, F_i are the respective point and field matrices along sub-system (1) and z_i denotes the state vector $\{\theta_i, Q_i\}$ at the point i . The generalized displacement θ_i and force Q_i are conventionally positive when acting in the direction of transfer, and respectively represent in this case the angular displacement and torque at the point. The elements of the associated transfer matrix $T^{(1)} = [t_{jk}^{(1)}]$ are obtained via the matrix multiplication operations set out in equation (1).

(ii) Guyan reduction:

The overall dynamic equations for sub-system (1) may be expressed in the form

$$\begin{bmatrix} D_{11} & D_{12} \\ D_{21} & D_{22} \end{bmatrix}^{(1)} \begin{bmatrix} \theta_2 \\ \theta_1 \\ \theta_3 \end{bmatrix}^{(1)} = \begin{bmatrix} 0 \\ -Q_1 \\ Q_3 \end{bmatrix}^{(1)} \quad (2)$$

where the 3x3 dynamic stiffness matrix $D^{(1)}$ of the sub-system is partitioned as shown and account is taken of the fact that the right hand vector in equation (2) represents the forces acting on the sub-system. Equation (2) is reduced by Guyan reduction to the condensed form

$$\tilde{D}^{(1)} \begin{bmatrix} \theta_1 \\ \theta_3 \end{bmatrix}^{(1)} = \begin{bmatrix} -Q_1 \\ Q_3 \end{bmatrix}^{(1)} \quad (3)$$

where the 2x2 dynamic stiffness matrix $\tilde{D}^{(1)}$ is given by

$$\tilde{D}^{(1)} = [D_{22} - D_{21} D_{11}^{-1} D_{12}]^{(1)} \quad (4)$$

In this particular case the calculation of the inverse of D_{11} is trivial since D_{11} is a scalar. In general, however, D_{11} will be a square matrix function of frequency ω . In that case its inverse may be determined via the spectral decomposition theorem [2] in terms of the natural frequencies of the sub-structure assuming rigid boundaries. These frequencies are obtained by finding the zeros of the determinant $|D_{11}|$.

Following the determination of the Guyan-reduced dynamic stiffness matrix, partitioned as

$$\tilde{D}^{(1)} = \begin{bmatrix} \tilde{D}_{11} & \tilde{D}_{12} \\ \tilde{D}_{21} & \tilde{D}_{22} \end{bmatrix} \quad (1)$$

with square sub-matrices, the transfer matrix $T^{(1)}$ is obtained from the following relationship established from equations (1), (3) and (5) that

$$T^{(1)} = \begin{bmatrix} -\tilde{D}_{12}^{-1} \tilde{D}_{11} & , & -\tilde{D}_{12}^{-1} \\ \tilde{D}_{21} - \tilde{D}_{22} \tilde{D}_{12}^{-1} \tilde{D}_{11} & , & -\tilde{D}_{22} \tilde{D}_{12}^{-1} \end{bmatrix} \quad (6)$$

In the present instance the matrix operations in (6) are trivial because the sub-matrices of matrix (5) are scalars. In general, however, since the object of the Guyan reduction process is to generate a matrix $\tilde{D}^{(1)}$ of small order, direct numerical inversion of the submatrix \tilde{D}_{12} is readily performed, and in view of the proviso made in the introduction that the system does not decouple, we must have $|\tilde{D}_{12}| \neq 0$ and therefore the inverse always exists.

Components (2) and (3):

The transfer matrices for these sub-systems are directly available in analytic form. Thus, for component (2), assumed to be a uniform circular cylinder of mass density ρ , length ℓ , modulus of rigidity G and polar second moment of area J :

$$z_2^{(2)} = \begin{bmatrix} t_{11} & t_{12} \\ t_{21} & t_{22} \end{bmatrix} z_1^{(2)} \quad (7)$$

with matrix elements

$$t_{11} = t_{22} = \cos \lambda \ell, \quad t_{12} = \sin \lambda \ell / GJ\lambda,$$

$$t_{21} = -GJ\lambda \sin \lambda \ell$$

where

$$\lambda = \omega / (\rho/G)$$

and ω represents frequency.

For component (3):

$$z_2^{(3)} = \begin{bmatrix} t_{11} & t_{12} \\ t_{21} & t_{22} \end{bmatrix} z_1^{(3)} \quad (8)$$

with matrix elements $t_{11} = t_{22} = 1$, $t_{12} = 0$ and $t_{21} = -I_1^{(3)} \omega^2$.

Assembly of reduced characteristic determinant

The elements of the reduced characteristic determinant are assembled by considering, in systematic order, first the force equilibrium equations and then the displacement compatibility conditions at sub-system interfaces, followed by the boundary conditions. Thus, in the present instance, we have:

Torque equilibrium:

$$Q_1^{(1)} + Q_1^{(2)} = 0 \quad (9)$$

$$-Q_2^{(2)} + Q_1^{(3)} = 0. \quad (10)$$

Displacement compatibility:

$$\theta_1^{(1)} = \theta_1^{(2)} \quad (11)$$

$$\theta_2^{(2)} = \theta_1^{(3)}. \quad (12)$$

Boundary conditions:

$$Q_3^{(1)} = 0 \quad (13)$$

$$Q_2^{(3)} = 0. \quad (14)$$

Using the matrix transfer equation of each sub-system, the set of equations (9) through (14) yield a linear homogeneous system in input state variables only. For this purpose it is convenient to assign the symbol α to the input displacement and β to the input force variables.

In this notation the transfer equations for the output state variables of the k th sub-system are

$$\theta_i^{(k)} = \alpha^{(k)} t_{i1}^{(k)} + \beta^{(k)} t_{i2}^{(k)} \quad (15)$$

$$Q_i^{(k)} = \alpha^{(k)} t_{21}^{(k)} + \beta^{(k)} t_{22}^{(k)}. \quad (16)$$

For sub-systems 1,2,3, we then have

$$\theta_1^{(1)} = \alpha^{(1)} = \theta_{[1]}; \quad Q_1^{(1)} = \beta^{(1)} \quad (17)$$

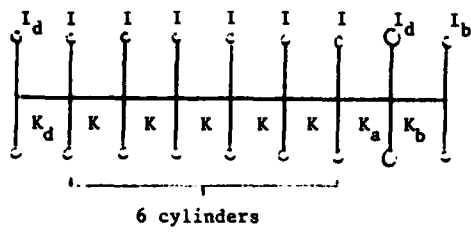
$$\theta_1^{(2)} = \alpha^{(2)} = \theta_{[1]}; \quad Q_1^{(2)} = \beta^{(2)} \quad (18)$$

$$\text{and } \theta_1^{(3)} = \alpha^{(3)} = \theta_{[2]}; \quad Q_1^{(3)} = \beta^{(3)}. \quad (19)$$

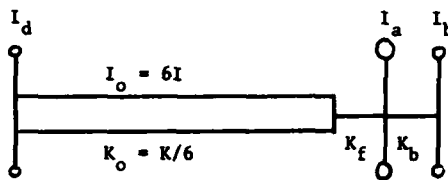
Also, by assigning a common variable to input displacements at the same interface the number of equations is further reduced. Thus on setting

$$\alpha^{(1)} = \alpha^{(2)} = \alpha_1, \quad \alpha^{(3)} = \alpha_2, \quad \beta^{(1)} = \beta_3,$$

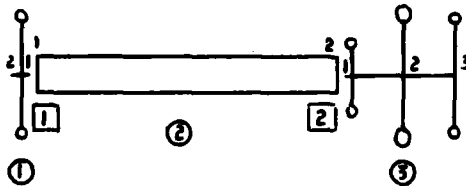
$$\beta^{(2)} = \beta_4, \quad \beta^{(3)} = \beta_5,$$



(a)



(b)

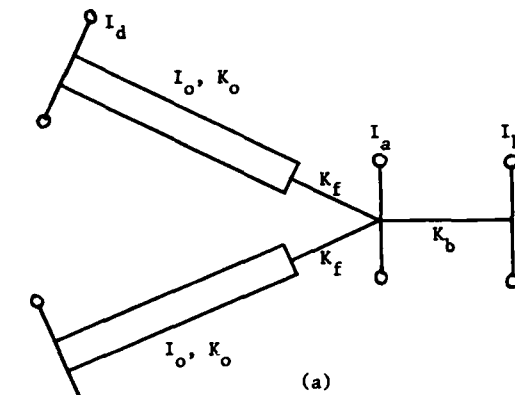


(c)

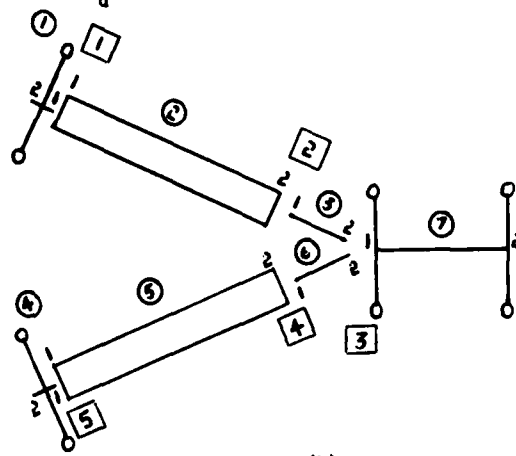
Fig.2. - Straight in-line engine/generator system.

treated as a discrete system and consisting of three sub-structures (see Fig.3(c)) were computed and the results are given in the table.

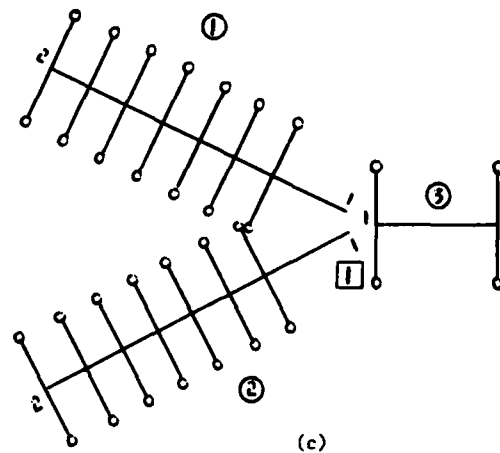
Some of the natural frequencies of the branched system occur with the identical engine branch arms vibrating in antiphase. These frequencies should equal the natural vibration frequencies of the individual engine arms with the branch point fixed. The latter frequencies were determined and are shown in Table 3.



(a)



(b)



(c)

Fig.3. - Branched system

TABLE 1

DATA FOR ENGINE/GENERATOR SYSTEM

I_d	I	I_a	I_b	I_o	
80 (708)	443 (3920)	15797 (139800)	2983 (26400)	2658 (23520)	kg m^2 (lb in s^2)
K_d	K	K_a	K_b	K_o	
233.9 (2070)	82.49 (730)	45.43 (402)	150.7 (1334)	13.75 (121.7)	$\times 10^6 \text{ N m}$ ($\times 10^6$) (lb in)

$$K_f = 2KK_a / (2K - K_a)$$

$$= 62.68 \times 10^6 \text{ N m}$$

$$(554.7 \times 10^6 \text{ lb in})$$

TABLE 2

NATURAL FREQUENCIES OF STRAIGHT IN-LINE ENGINE/GENERATOR SYSTEM

Mode No.	Natural Frequencies of Combined Discrete and Continuous System	Natural Frequencies of Discrete System
	(rad/s)	(rad/s)
1	0	0
2	96.43116	96.22528
3	244.60336	244.47902
4	282.13229	276.83540
5	481.29862	456.25927
6	689.88522	619.71590
7	903.10612	750.01238
8	1118.97961	834.03523
9	1336.55797	1866.41721
10	1555.347691	
11	1775.06451	
12	1995.52738	

TABLE 3
NATURAL FREQUENCIES OF BRANCHED SYSTEM

Mode No.	Natural Frequencies of combined discrete and continuous system (rad/s)	Natural Frequencies of combined engine branch arm fixed at junction point (rad/s)	Natural Frequencies of discrete system (rad/s)	Natural Frequencies of discrete engine branch arm fixed at junction point (rad/s)
1	0	-	0	-
2	90.8207	90.8207	90.6096	90.6096
3	101.5515		101.3524	
4	244.1567		243.9341	
5	279.7764	279.7764	274.3651	274.3651
6	284.4601		279.2546	
7	480.7409	480.7409	455.7482	455.7482
8	481.8671		456.7823	
9	689.6610	689.6610	619.5501	619.5501
10	690.1122		619.8844	
11	902.9976	902.9976	749.9604	749.9604
12	903.2155		750.0650	
13	1118.9199	1118.9199	834.0245	834.0245
14	1119.0396		834.0460	
15	1336.5220	1336.5220	1866.4172	1866.4172
16	1336.5941			
17	1555.3245	1555.3245		
18	1555.3710			
19	1775.0487	1775.0487		
20	1775.0804			

DISCUSSION OF RESULTS

The method yielded results accurate to the limiting precision of the computer. No numerical difficulties were experienced for either of these examples or for numerous other examples tested by the authors. The numerical stability of the method is confirmed by the exact agreement (to all significant digits) between the natural frequencies computed for each engine branch arm with the branch point fixed and the equivalent natural frequencies

of the branched system.

Whilst the object of the paper is essentially to present the method, it is of some interest to note the extreme sensitivity of the modelling on both the straight and branched systems with regard to the number of natural vibration frequencies in the range 0-1867 rad/s and to their values, especially after the 6th and 10th modes respectively.

CONCLUSIONS

A pole-free reduced-order determinant method has been presented for the computation of the natural vibration frequencies of systems comprising both discrete and continuous parameter components. Whilst the method has been described in terms of components executing torsional vibration only, its extension to the vibration analysis of general structures involves exactly the same principles.

REFERENCES

1. B. Dawson and M. Davies, "An improvement to Shaikh's method for the torsional vibration analysis of branched systems", Shock and Vibration Bulletin 51, Part 3, pp 1-10, 1981.
2. P. Lancaster, "Lambda Matrices and Vibrating Systems", Pergamon Press, Oxford, 1966.
3. B. Dawson, M. Davies and K. Bean, "A vibration analysis package for vibration courses", Proc. Fourth British Conference on the Teaching of Vibration and Noise, Sheffield Polytechnic, 1982.
4. W. Ker Wilson, "Practical Solution of Torsional Vibration Problems", Vol. 1, Chapman and Hall, 1963.

DETERMINATION OF SHEAR COEFFICIENT OF A GENERAL BEAM CROSS

SECTION BY FINITE ELEMENT METHOD

C. M. Friedrich and S. C. Lin
Westinghouse Electric Corporation
Bettis Atomic Power Laboratory
West Mifflin, Pennsylvania

A finite element method is formulated to determine the distribution of warping deflections of a general cross section of a beam under a shear load. Then, formulae for the shear stresses, shear strains, shear stiffness, and shear coefficient are obtained in terms of the warping deflections. Numerical values of the shear stresses and shear coefficients are computed for four beam cross sections and compared with values obtained by other writers or by approximate solutions.

INTRODUCTION

In the analysis of beam structures, deformation due to the transverse shear load is important for a beam whose length is comparable to a cross-section dimension. The shear deformation is usually measured by the beam shear coefficient [1]*, which is dimensionless and dependent upon the shape of the beam cross section. The primary purpose of this coefficient is to account for the fact that the warping of the cross section by shear load produces non-uniform shear stresses and shear strains.

Cowper [1] derived the beam equations from the theory of elasticity and obtained a formula for shear coefficients of cross sections. From this formula, he presented closed form solutions for five simple cross sections (circle, rectangle, ellipse, hollow circle, and semicircle) and approximate formulae for six thin-walled sections.

In practical applications, the cross section of the beam structures may not be simple or thin-walled. The formulae provided in [1] for calculating the shear coefficients may not be adequate for complicated cross sections, such as a blade of a helicopter. Thus, a finite element method, based on the theory of elasticity, is developed to solve the beam shear problem for any complex cross section. In the derivation of the shear distortion, the principle of virtual work is applied to determine the warping deflections of the cross section. Consequently, the distribution of the shear stress and shear strain over the cross section and the effective

shear stiffness are derived. A formula for the beam shear coefficient of the cross section is also derived. The numerical values of the shear coefficients for four cross sections, a circle, a square, a thin I-shaped section, and a honeycomb section, are computed using eight-node isoparametric quadrilateral elements. Values for the first three sections compare well with Cowper's [1] and Roark's [5] results. The shear coefficient for the honeycomb section is compared with the solid-section solution. Finally, the shear stress distribution for circular and square cross sections under shear loads are compared with their closed form solutions [2] and the shear stress distribution for the honeycomb section is compared with that from the elementary beam theory.

DERIVATION OF BEAM SHEAR DISTORTION

A finite element method is formulated to obtain the shear distortion of a beam under a shear load. The derivation of the shear distortion is arranged in four steps: (1) assume a set of nodal warping deflections on a small length Δz of the beam and establish equations of strains and stresses versus the nodal deflections; (2) from the external virtual work of these warping deflections, establish equilibrium equations of nodal forces versus beam shear load; (3) from internal virtual work of shear stresses, establish stiffness equations of nodal forces versus nodal deflections; and (4) calculate the shear coefficient after the stiffness equations are solved for the warping deflections. These four steps are discussed separately in the Appendix.

Note: Appropriate SI conversion units - 1 in. = 2.54 cm, 1 lb. = 0.4536 Kg,
1 ksi = 6.89 MPa.

*Numbers in brackets designate References at the end of paper.

Table 1

Shear Coefficients of Four Cross Sections

Shape	QUAD8	Roark [5]	Cowper [1]
Circle	0.882	0.900	0.882
Square	0.848	0.833	0.848
Thin I-Shaped Section	0.396	0.378	0.390
Honeycomb Section	0.603	--	--

NUMERICAL EXAMPLES

An in-house computer program was written for the BESTRAN system (Reference [3]) to solve the discussed beam shear problem with an eight-node isoparametric quadrilateral element called QUAD8. The configuration of the QUAD8 element is shown in Figure 1 and the associated shape functions for this element are

$$\begin{aligned}
 N_1 &= -(1 - \xi) (1 - \eta) (1 + \xi + \eta)/4 \\
 N_2 &= (1 - \xi^2) (1 - \eta)/2 \\
 N_3 &= (1 + \xi) (1 - \eta) (\xi - \eta - 1)/4 \\
 N_4 &= (1 - \xi) (1 - \eta^2)/2 \\
 N_5 &= (1 + \xi) (1 - \eta^2)/2 \\
 N_6 &= (1 - \xi) (1 + \eta) (\eta - \xi - 1)/4 \\
 N_7 &= (1 - \xi^2) (1 + \eta)/2 \\
 N_8 &= (1 + \xi) (1 + \eta) (\xi + \eta - 1)/4
 \end{aligned}$$

where ξ , η are the two local coordinate axes for the element, as discussed in Reference [4].

The cross sections to be investigated are a circle with radius of 1.0 inch, a 1.0 inch x 1.0 inch square, a thin I-shaped section (shown in Figure 2), and a honeycomb section (shown in Figure 3). The beam, subjected to a shear load of 10^4 lbs in the x-direction, is assumed to be homogeneous with the following material properties:

$$\begin{aligned}
 E &= 30 \times 10^6 \text{ psi} \\
 \nu &= (0.25).
 \end{aligned}$$

Since the sections are symmetric about the x- and y- axes, only one quarter of each section is modeled. The QUAD8 models for the circular,

thin I-shaped, and honeycomb sections are given in Figures 4, 5, and 6, and the model for the square is a square array of 36 QUAD8 elements. The shear coefficients defined in Equation (16) of Appendix are calculated by the in-house computer program and listed in Table 1. The corresponding values, except for the honeycomb section, are computed from the formulae of References [1] and [5] and are listed in Table 1 for comparison.

From Table 1, it can be seen that the results of the present method and [1] for the circle and square are identical. It can also be seen that the results of the three methods for a thin I-shaped section agree well even though the solution from Reference [1] assumes the stress distribution is uniform across the wall and Reference [5] uses elementary beam theory. For the honeycomb section, no solution is available. However, an upper bound of the shear coefficient is 0.833, the shear coefficient of a solid rectangle. The shear stresses for the circle and square obtained from the finite element method and from the closed form solutions (Reference [2]) are presented in Table 2 for comparison. The maximum difference between the two results is 1%. For the honeycomb section, the shear stresses along the y-axis obtained from the finite element method are listed in Table 3. The shear stresses are normalized by using a shear stress value of 256.5 psi which is computed from the elementary beam theory. From Table 3, it can be seen that the shear stress τ_{xz} is smaller at the center and becomes larger near the edge. The average value for the τ_{xz} along the y-axis is within 1% of the shear stress from the elementary beam theory. The values of τ_{yz} along the y-axis from the present method are basically zero.

Table 2

Shear Stresses (in ksi) of Circular and Square Cross Sections

Shape	Location (x, y)	QUAD8		Closed Form Solution	
		τ_{xz}	τ_{yz}	τ_{xz}	τ_{yz}
Circle	(0, 1)	3.84	0.0	3.82	0.0
	(0, 0.5)	4.31	0.0	4.29	0.0
	(0, 0)	4.47	0.0	4.46	0.0
	(0.5, 0)	3.36	0.0	3.34	0.0
	(1, 0)	0.0	0.0	0.0	0.0
	(0.5, 0.5)	3.20	-0.95	3.18	-0.96
	(0.707, 0.707)	1.91	-1.93	1.91	-1.91
Square	(0, 0.5)	16.95	0.0	16.89	0.0
	(0, 0)	14.16	0.0	14.10	0.0

Table 3

Shear Stress Distribution of Honeycomb Section

Location (x,y)	QUAD8		Elementary Beam Theory	
	$\tau_{xz}/256.5$	$\tau_{yz}/256.5$	$\tau_{xz}/256.5$	$\tau_{yz}/256.5$
0, 0.866	0.90	0.00	1.00	0.00
0, 1.250	0.89	0.00	1.00	0.00
0, 1.634	0.91	0.00	1.00	0.00
0, 3.366	0.95	0.00	1.00	0.00
0, 3.750	0.95	0.00	1.00	0.00
0, 4.134	0.98	0.00	1.00	0.00
0, 5.866	1.15	0.02	1.00	0.00
0, 6.122	1.15	0.01	1.00	0.00
0, 6.378	1.10	0.00	1.00	0.00
0, 6.634	1.10	0.00	1.00	0.00

CONCLUSION

From the theory and numerical results presented, it can be seen that this finite element method can accurately calculate not only the beam shear coefficient but also the distribution of the shear stresses and shear strains for any complex cross section under a shear load. Thus, it is believed that this method will provide a very useful approach in evaluating the warping deflections of shear loading on a beam and the shear stiffness of the beam in addition to the bending stiffness.

REFERENCES

1. R. G. Cowper, "The Shear Coefficient in Timoshenko's Beam Theory," Transactions, ASME, Vol. 33, Series E, No. 2, pp. 335-340, June 1966.

2. S. Timoshenko and J. N. Goodier, "Theory of Elasticity," Chapter 12, Second Edition, McGraw-Hill Book Company, Inc., New York, New York, 1951.

3. C. M. Friedrich, "BESTRAN - a Technique for Performing Structural Analysis," WAPD-TM-1140, Bettis Atomic Power Laboratory, February 1975.

4. O. C. Zienkiewicz, "The Finite Element in Engineering Science," Chapter 7, Equation (7.13), Second Edition, McGraw-Hill Publishing Company, Limited, London, 1971.

5. R. J. Roark, "Formulas for Stress and Strain," p. 129, Fourth Edition, McGraw-Hill Book Company, Inc., New York, New York, 1965.

6. A.E.H. Love, "A Treatise on the Mathematical Theory of Elasticity," Section 230, Fourth Edition, Dover Publications, New York, New York, 1944.

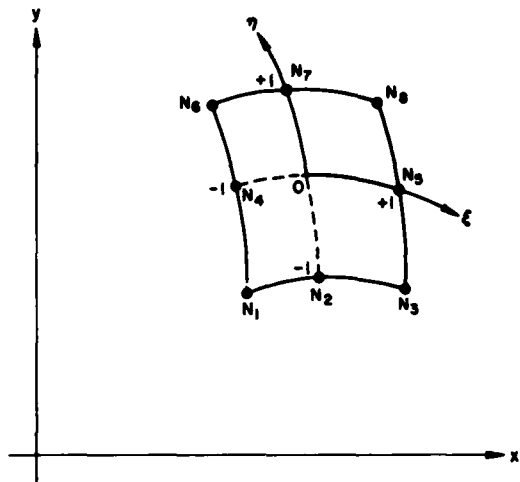


FIGURE 1. QUAD8 ELEMENT CONFIGURATION

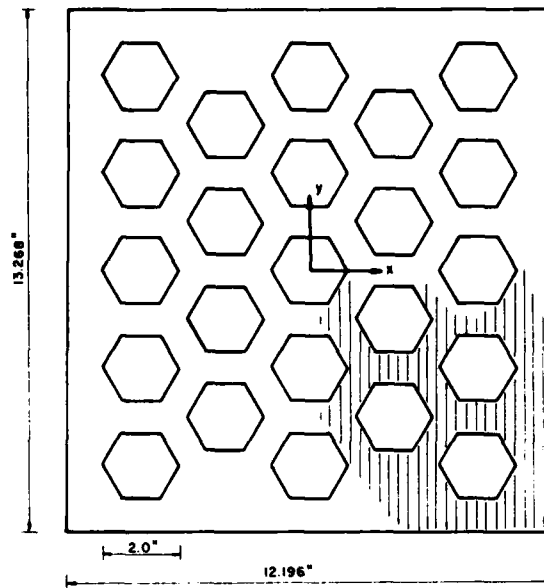


FIGURE 3. GEOMETRY OF HONEYCOMB SECTION

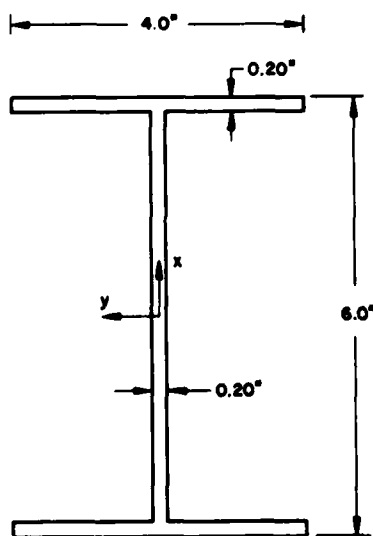


FIGURE 2. GEOMETRY OF THIN I-SHAPED SECTION

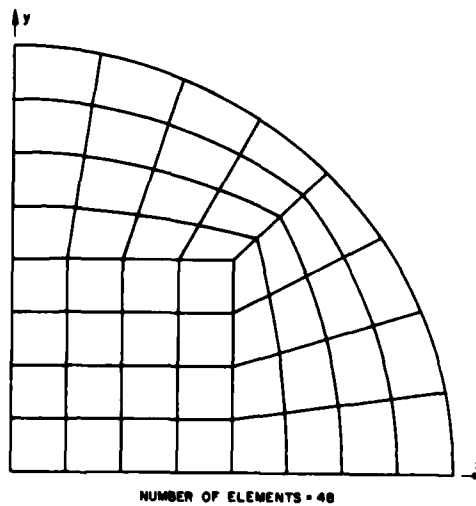


FIGURE 4. FINITE ELEMENT MODEL FOR ONE QUARTER OF A CIRCLE

APPENDIX:
DETAILS OF DERIVATION OF BEAM SHEAR DISTORTION

NOTATION

- (\cdot) = virtual change in () produced by the virtual deflections (\dot{w}_i).
- $A = \int dA = \iint dx dy$ = cross sectional area of beam.
- C_0 = coefficient for axial bending strain produced by the moment zF_x on the plane $z = \text{constant}$.
- D_x = working shear deflection per unit length along z , where $\dot{W} = F_x D_x$.
- $C_i = C_i(x,y)$ = shape function for node i , where $C_i = \delta_{ij}$ at node j .
- $E = E(x,y)$ = tensile modulus of elasticity.
- $F_i = \partial \dot{W} / \partial \dot{w}_i$ = shear load on node i as shown in Figure C.
- F_x = shear force, as shown in Figure A.
- $G = E / (2 + 2\nu)$ = shear modulus of elasticity.
- K = shear coefficient of the cross section.
- $K_b = \int Ex^2 dA$ = bending stiffness.
- i = index of a node. Note $i = 1$ to n .
- j = index of a node. Note $j = 1$ to n .
- n = number of nodes.
- N_i = Shape function for node i of an eight-node isoparametric quadrilateral element. If node i is common to m finite elements, the m shape functions of the elements at the node define the shape function $C_i(x,y)$ of the cross section for that node.
- u, v, w = deflections along the $x, y,$ and z axes, respectively.
- w_i = warping deflection, w , at node i .
- \dot{W} = virtual work per unit length.
- x, y, z = rectangular coordinates, with z along beam axis.
- $\epsilon_x, \epsilon_y, \epsilon_z$ = normal strains.
- $\gamma_{xy}, \gamma_{yz}, \gamma_{zx}$ = shear strains.
- $\sigma_x, \sigma_y, \sigma_z$ = normal stresses.
- $\tau_{xy}, \tau_{yz}, \tau_{zx}$ = shear stresses.
- ν = Poisson's ratio.
- $\delta_{ij} = 1$ if $i = j$, or $\delta_{ij} = 0$ if $i \neq j$.

1. Deflections, Strains, and Stresses

Let x - and y - axes be principal axes through the centroid of the beam cross section with area moments weighted by the elastic modulus E ; let z -axis be the beam axis with $z = 0$ at the cross section of interest; and let F_x

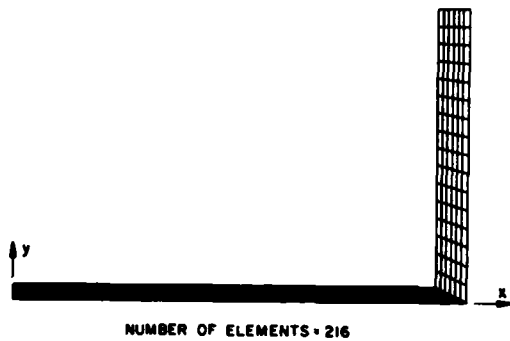


FIGURE 5. FINITE ELEMENT MODEL FOR ONE QUARTER OF A THIN I-SHAPED SECTION

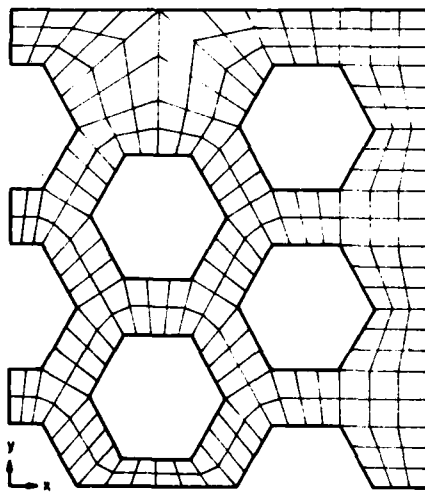


FIGURE 6. FINITE ELEMENT MODEL FOR ONE QUARTER OF A HONEYCOMB SECTION

be a shear force in the x direction on the cross section at $z = 0$, as shown in Figure A. The derivation of shear effects considers a small length, Δz , in which deflections are assumed in the following form

$$u = vC_0(-x^2 + y^2)z - C_0(\Delta z - z)^2 (2\Delta z + z)/3$$

$$v = -2vC_0xyz$$

$$w = -C_0x[(\Delta z)^2 - z^2] + \sum_{i=1}^n C_i(x,y)w_i \quad (1)$$

where all terms except the sums can be found from Section 230 of [6].

Coefficients C_0 and w_i , $i = 1$ to n , are to be determined from the standard beam conditions [2]

$$\begin{aligned} \sigma_x &= 0 \\ \sigma_y &= 0 \\ \tau_{xy} &= 0 \end{aligned} \quad (2)$$

and from the virtual-work condition

$$\dot{W} = \sum_{i=1}^n F_i \dot{w}_i = \int_0^{\Delta z} dz \int_0^A (\sigma_z \dot{\epsilon}_z + \tau_{yz} \dot{\gamma}_{yz} + \tau_{zx} \dot{\gamma}_{zx}) dA/\Delta z \quad (3)$$

under virtual deflections $\{\dot{w}_i\}$.

With the help of (1), the strain equations

$$\begin{aligned} \epsilon_x &= \partial u/\partial x \\ \epsilon_y &= \partial v/\partial y \\ \epsilon_z &= \partial w/\partial z \\ \gamma_{xy} &= \partial u/\partial y + \partial v/\partial x \\ \gamma_{yz} &= \partial v/\partial z + \partial w/\partial y \\ \gamma_{zx} &= \partial w/\partial x + \partial u/\partial z \end{aligned}$$

become

$$\begin{aligned} \epsilon_x &= -2vC_0xz = -v\epsilon_z \\ \epsilon_y &= -2vC_0xz = -v\epsilon_z \\ \epsilon_z &= 2C_0xz \\ \gamma_{xy} &= 0 \\ \gamma_{yz} &= -2vC_0xy + \sum_{i=1}^n (\partial C_i/\partial y)w_i \\ \gamma_{zx} &= vC_0(-x^2 + y^2) + \sum_{i=1}^n (\partial C_i/\partial x)w_i \end{aligned} \quad (4)$$

Note $\dot{\epsilon}_z = 0$ since ϵ_z is independent of $\{w_i\}$.

Next, with the help of (4), the stress-strain equations

$$\begin{aligned} \epsilon_x &= (\sigma_x - v\sigma_y - v\sigma_z)/E \\ \epsilon_y &= (\sigma_y - v\sigma_z - v\sigma_x)/E \\ \epsilon_z &= (\sigma_z - v\sigma_x - v\sigma_y)/E \\ \gamma_{xy} &= \tau_{xy}/G \\ \gamma_{yz} &= \tau_{yz}/G \\ \gamma_{zx} &= \tau_{zx}/G \end{aligned}$$

may be solved for the stresses

$$\begin{aligned} \sigma_x &= 0 \\ \sigma_y &= 0 \\ \sigma_z &= E\epsilon_z = 2EC_0xz \\ \tau_{xy} &= 0 \\ \tau_{yz} &= G[-2vC_0xy + \sum_{i=1}^n (\partial C_i/\partial y)w_i] \\ \tau_{zx} &= G[vC_0(-x^2 + y^2) + \sum_{i=1}^n (\partial C_i/\partial x)w_i] \end{aligned} \quad (5)$$

Since no axial load is applied to the beam, the normal stress σ_z in the range $0 < z < \Delta z$, as shown in Figure A, has to satisfy the following beam equilibrium conditions [2]

$$\begin{aligned} 0 &= \int \sigma_z dA \\ 0 &= \int y \sigma_z dA \\ zF_x &= \int x \sigma_z dA \end{aligned}$$

or, with the help of $\sigma_z = 2EC_0xz$ from (5),

$$\begin{aligned} 0 &= 2C_0z \int E(x,y) x dA \\ 0 &= 2C_0z \int E(x,y) xy dA \\ zF_x &= 2C_0z \int E(x,y) x^2 dA \end{aligned} \quad (6)$$

The x- and y- axes coincide with the principal axes of the cross section, as defined by the first two equations of (6). From the third equation of (6), we have

$$C_0 = F_x/(2K_b) \quad (7)$$

where the bending stiffness, K_b , is expressed by

$$K_b = \int x^2 E(x,y) dA.$$

As a result, the normal stress σ_z due to the bending moment zF_x is given as

$$\sigma_z(x,y,z) = (F_x/K_b) E(x,y)xz \quad (8)$$

and the stress distribution is shown in Figure B.

2. External Virtual Work

Consider arbitrary virtual deflections $\{\dot{w}_i\}$, $i = 1$ to n . Then the virtual warping deflection at (x, y, z) is

$$\dot{w} = \sum_{i=1}^n C_i(x,y) \dot{w}_i \quad (9)$$

and the external virtual work per unit length is

$$\dot{W} = [\int \sigma_z(x,y,\Delta z) \dot{w} dA] / \Delta z$$

or, with the help of (8) and (9),

$$\dot{W} = \sum_{i=1}^n [(F_x/K_b) \int EC_i x dA] \dot{w}_i. \quad (10)$$

The nodal force F_i , as shown in Figure C, is defined by

$$F_i = \partial \dot{W} / \partial \dot{w}_i$$

or, with the help of (10),

$$F_i = (F_x/K_b) \int EC_i x dA. \quad (11)$$

3. Internal Virtual Work

Note $\sigma_x = \sigma_y = \tau_{xy} = 0$ and $\dot{\epsilon}_z = 0$, so that evaluation of the virtual work \dot{W} from the internal strain energy gives

$$\dot{W} = [\int_0^{\Delta z} dz \int (\tau_{yz} \dot{\gamma}_{yz} + \tau_{zx} \dot{\gamma}_{zx}) dA] / \Delta z$$

or, with the help of (4) and (5),

$$\dot{W} = \int G \{ [C_0(-2vxy) + \sum_{j=1}^n (\partial C_j / \partial y) w_j] \}$$

$$\sum_{i=1}^n (\partial C_j / \partial y) \dot{w}_i + [vC_0(-x^2 + y^2)] \quad (12)$$

$$+ \sum_{j=1}^n (\partial C_j / \partial x) w_j \sum_{i=1}^n (\partial C_i / \partial x) \dot{w}_i \} dA.$$

Then by definition of F_i ,

$$F_i = \partial \dot{W} / \partial \dot{w}_i$$

or, with the help of (12),

$$F_i = K_{i0} + \sum_{j=1}^n K_{ij} w_j \quad (13)$$

where

$$K_{i0} = \int G C_0 [(-2vxy) (\partial C_i / \partial y) + v(-x^2 + y^2) (\partial C_i / \partial x)] dA$$

and

$$K_{ij} = \int G [(\partial C_j / \partial y) (\partial C_i / \partial y) + (\partial C_j / \partial x) (\partial C_i / \partial x)] dA.$$

Given the n values of F_i in (11), the n simultaneous equations of (13) may be solved for the n values of $\{w_i\}$, because the matrix $[K_{ij}]$ is symmetric and positive definite for a linearly independent set of n shapes, $\{C_i(x,y)\}$.

4. Shear Coefficient

The virtual shear deflection per unit length is

$$\dot{D}_x = (\sum_{i=1}^n F_i \dot{w}_i) / F_x = \sum_{i=1}^n (F_i / F_x) \dot{w}_i$$

whence the linear function of D_x versus warping deflection is

$$D_x = \sum_{i=1}^n (F_i / F_x) w_i. \quad (14)$$

Thus D_x is known after all n nodal deflections has been calculated, and the effective shear stiffness per unit length is

$$F_x / D_x = (F_x)^2 / \sum_{i=1}^n F_i w_i. \quad (15)$$

Also, the shear coefficient of the cross section is obtained as

$$K = F_x / (D_x AG) \quad (16)$$

where A is the cross section area and G is a reference shear modulus of elasticity. The definition of this shear coefficient is based on strain energy as in Reference [5], where approximations of elementary beam theory were made for stress distribution. Reference [1], on the other hand, finds the coefficient by integration of the equations of three-dimensional elasticity theory. The results of the three methods are compared in the numerical example section.

After C_0 and all n values of w_i have been calculated from (7) and (13), then at $z = 0$

(1) gives the warping deflections,

(4) gives the shear strains,

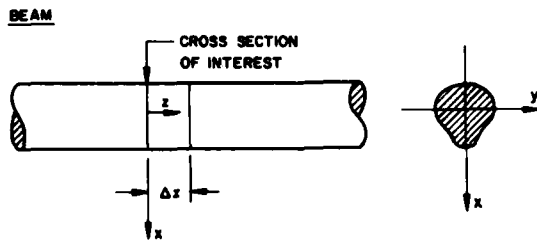
(5) gives the shear stresses,

(14) gives the effective shear deflection per unit length,

(15) gives the effective shear stiffness per unit length, and

(16) gives the shear coefficient of the cross section.

Thus, the problem due to the shear effect from a shear load on the beam cross section is now completely solved.



BEAM SEGMENT ($0 \leq z \leq \Delta z$)

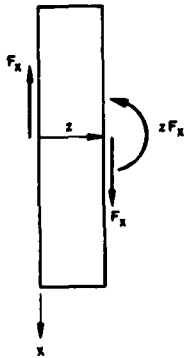
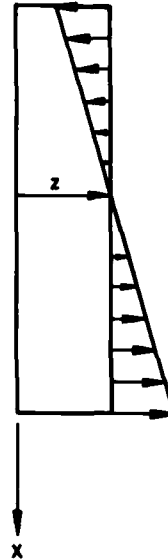


FIGURE A. SHEAR LOAD F_x ON BEAM SEGMENT



$$\sigma_z = E \epsilon_z$$

$$\text{WHERE } \epsilon_z = 2C_0 x z$$

FIGURE B. NORMAL STRESS OF MOMENT zF_x FOR $0 \leq z \leq \Delta z$

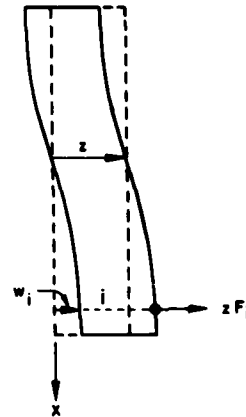


FIGURE C. NODAL FORCES EQUIVALENT TO MOMENT zF_x FOR $0 \leq z \leq \Delta z$

MACHINERY DYNAMICS

GEAR CASE VIBRATION ISOLATION IN A

GEARED TURBINE GENERATOR

Robert P. Andrews
Westinghouse Electric Corp.
Marine Division
Sunnyvale, California

The design and analysis of a flexible gear case mount system for a geared turbine generator is presented. The mount system isolates gear case vibration and allows the gear bearing loads to be equalized. The primary excitation frequencies to be isolated are the pinion rotational harmonics. Dynamic mathematical modeling was used to determine the proper mount flexibility relative to the inertia properties and flexibility of the system components. Damping is not considered in this analysis. Important design constraints discussed include mount stresses, system alignment requirements, and system vibration excitation frequencies. A snubber system was designed to limit vertical and athwartship deflections of the mount elements to prevent yielding under shock load conditions.

INTRODUCTION

The design and analysis of a flexible gear case mount system for isolation of gear case vibration in a geared turbine generator is presented (Figure 1). Isolation of vibrations at the pinion rotational harmonic frequencies is the objective.

The system analyzed consists of a flexibly mounted single reduction gear set, flexibly coupled to the turbine rotor and directly coupled to the generator rotor. The generator-gear shaft has three bearings, two in the gear case (gear bearings) and the other at the free end of the generator (generator bearing). The generator bearing is rigidly mounted. The entire turbine generator assembly is supported on a subbase (box beam structure) which is flexibly mounted in the ship's hull.

A two point gear case mount arrangement was selected, with one mount on each side of the gear case at the gear centerline elevation. Since the pinion and gear vibrations are transmitted radially through the bearings, the mounts are designed to be flexible in the radial directions (vertical and athwartship) and stiff in the axial direction (for/aft). The mounts are flexible in rotation about the athwartship axis of the gear case, this allows equalization of the gear bearing loads which promotes proper gear to pinion mesh alignment.

The mount flexibility required to achieve the desired vibration isolation is based on the theory for single degree of

freedom systems. The system natural frequencies are not allowed to coincide with any system vibration excitation frequencies. Stiffness equations for the proposed conceptual mount hardware design were derived. A set of dimensions were selected to produce the required stiffnesses, subject to constraints on mount stresses and deflections imposed by machinery weight, ship motions, thermal effects, and shock requirements. A snubber system was necessary to limit mount deflections due to shock.

Finite element analysis was used to include the effect of the generator gear shaft flexibility in refining the mount flexibility requirement. The mount hardware is included in the finite element model to determine how much rotation of the mounts is needed to fully equalize the gear bearing loads.

Mechanical alignment of the system is verified by measuring shaft bending moments using strain gauge techniques.

GEAR CASE ISOLATION SYSTEM

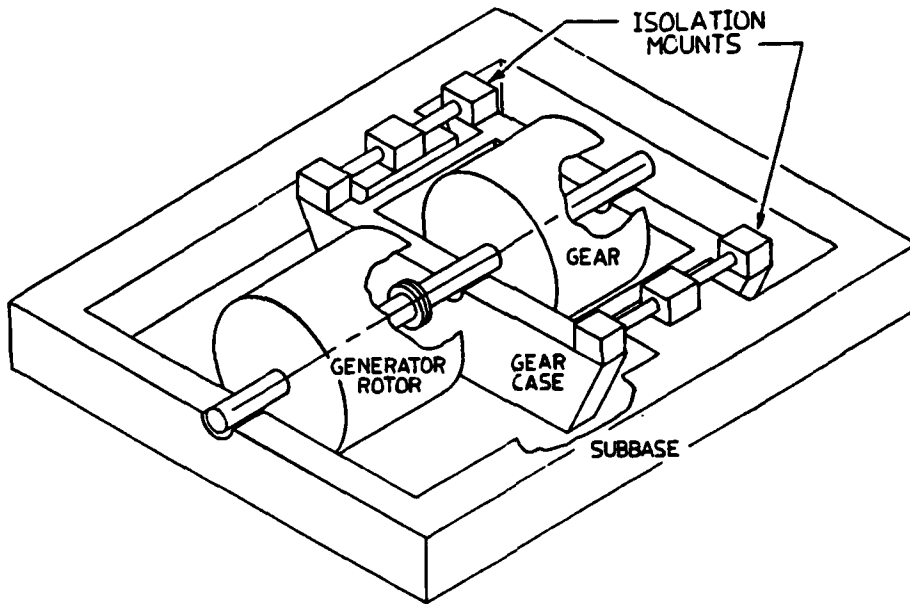


FIGURE 1

MODELING TECHNIQUES

The initial step in the design process is determination of the proper mount flexibility to achieve the design goals. This is accomplished by dynamic mathematical modeling of the proposed system. System damping is not considered in the model. A two point support arrangement with one mount on each side of the gear case at the gear centerline was chosen. The system includes the gear case and its mounts, the pinion, and the gear generator shaft. The coupling between the pinion and turbine is very flexible thus the turbine rotor is not considered as part of the system. The gear and generator are directly coupled, therefore the generator shaft must be considered since its weight and bending stiffness will be significant parameters in the dynamical model.

A first estimate of required mount vertical and athwartship stiffness is obtained by a greatly simplified two-dimensional model which only allows motions in a vertical plane through the two mount attachment loca-

tions. A preliminary mount stiffness requirement was established based on the desired modal frequencies. Candidate mount hardware configurations were designed and analyzed for stress at the resultant displacements under static loading.

The next step in the modeling process was to consider the bending stiffness of the gear-generator shaft while keeping the rigid model of the gear case. Finite element modeling was required. The gear case mounts may still be represented by linear springs (stiffness properties in all six directions may be required depending upon the constraints on gear case motion), or the mounts may be modeled by appropriate finite elements. Interactions between the gear and gear case and between the generator and ground at the journal bearings are modeled by linear springs representing the oil film with the appropriate stiffness properties. Calculation of bearing reactions is possible using the relative displacement at each bearing.

This model is useful for analysis of various static conditions that the system may be subjected to as well as system modal analysis.

A final step in the modeling process eliminates the rigid gear case assumption by extending the finite element model to include the gear case, this results in a rather large model. However, the modal frequencies calculated with the detailed gear case model were very close to those calculated with the rigid gear case model. Thus the detailed modeling was not required except to confirm the validity of the rigid gear case assumption. This is not surprising, since the mounts are designed to be much more flexible than the gear case structural elements.

A crude model was made to estimate the change in modal frequencies due to the sub-base mass and mount flexibility. This model treats the subbase as a rigid mass limited to vertical translational motion only.

VIBRATION EXCITATION

The fundamental vibration excitations present in the system are: high speed shaft (pinion) unbalance, slow speed shaft (gear, generator) unbalance, magnetic loads on the generator, and gear mesh forces. The excitation frequencies are:

1. Slow speed shaft rotation
2. High speed shaft rotation
3. Magnetic
4. Gear Mesh

Vibration data on existing geared ship service turbine generators of similar size reveals significant peaks in the frequency spectrum corresponding to the first three items on the above list. High vibration levels were also found at the lower harmonics of the pinion rotation frequency, particularly the fifth and sixth harmonics, presumably due to pinion "wear patterns".

Vibration excitation due to unbalance is minimized by carefully balancing the rotating parts at operating conditions. Isolation of the pinion harmonic vibrations is the primary goal of the gear case isolation system.

VIBRATION ISOLATION

The concept of vibration isolation is illustrated using a single degree of freedom system (Figure 2), which is simply a mass supported by a spring.

The transmission ratio (TR) is defined as the ratio of the transmitted force to the applied force. Transmission Ratio is a function of the forcing frequency and system natural frequency (Figure 3).

Vibration isolation is achieved by adjusting the system natural frequency relative to the known forcing frequency (or frequencies) such that the transmission ratio is minimized.

S.D.O.F. SYSTEM

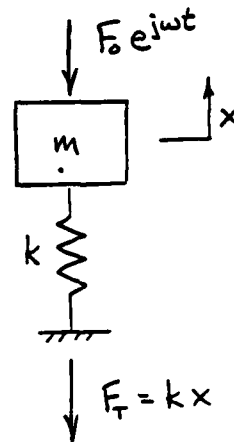


FIGURE 2

TRANSMISSION

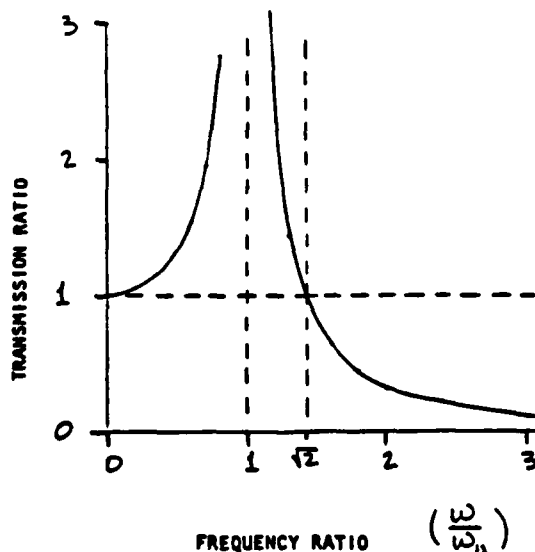


FIGURE 3

ISOLATION MOUNT

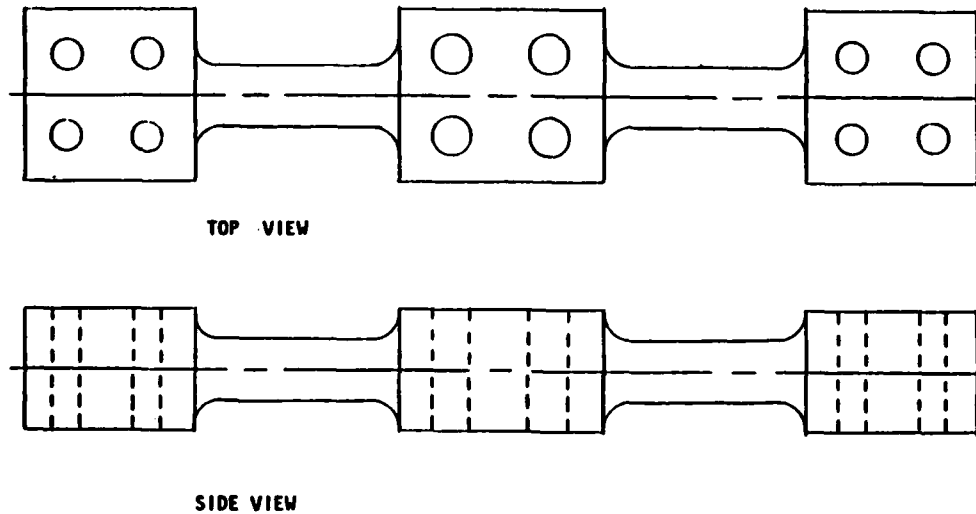


FIGURE 4

MOUNT DESIGN AND STIFFNESS CHARACTERISTICS

The mount design chosen consists of three rectangular blocks connected by two round rods as shown in Figure 4. The round rods are the spring elements. The center block and the two end blocks are used to secure the mount to the subbase and gear case, respectively.

The mounts are located on either side of the gear case at approximately the elevation of the gear axis, and oriented so that the axis of the spring element is parallel to the gear axis. This arrangement gives identical mount flexibility in the vertical and athwartship directions, with very little flexibility in the fore-aft direction. The mount arrangement also allows rotation of the gear case about an athwartship axis through the mount center blocks, thus promoting load equalization at the gear bearings.

Stiffness equations for the mount were developed based on a fixed-fixed beam model. The center block was not included in the model, but this has a significant effect only on the rotational stiffness normal to the mount axis. The mount stiffness is

controlled by the elastic modulus of the material and the length and radius of the spring elements. The overall length of the mount is set by the depth of the gear case, resulting in a limited range of lengths for the spring elements, thus the radius is the primary variable available to adjust the stiffness.

Bending stress in the spring elements is the primary constraint which determines an acceptable design. The mount must withstand all loads that may be present during normal operation of the turbine-generator unit. Stress analysis of the mounts will be discussed in detail later.

A special fillet design is used at the ends of the rods to minimize the stress concentration. It is an approximation to the ideal fillet given by Peterson (Reference 4). The fillet is neglected in the stiffness calculations.

MODAL ANALYSIS

The initial modal analysis was accomplished using the two dimensional model. Mount stiffness values were determined based on the target frequency for the first vertical and horizontal modes of vibration.

Three dimensional system models were needed to more accurately calculate the modal frequencies.

A comparison of modal frequencies obtained using the rigid versus the finite element gear case model shows the difference is less than six percent. Based on this result, all further analysis was done with the rigid model (to reduce computer codes).

The first two modes represent the lateral vibration modes of the generator - gear shaft. The third and fourth modes are gear case bounce modes on the mounts. The bounce modes result in transmission ratios of .06 and .12 for the second harmonic of pinion rotation frequency.

MOUNT DEFLECTION AND STRESS ANALYSIS

Mount material strength limits for yielding and fatigue determine the maximum steady state and alternating stresses which can be allowed under normal conditions. The mount is forged steel, heat treated to increase the yield strength.

Steady state loads are imposed by machinery weight, thermal expansion of the gear case, and gear torque output. Alternating loads will be generated by ship motions and load transients (e.g. start ups).

The maximum lateral displacement that the mount can be allowed to have under shock conditions is determined by yielding of the outer fiber of the spring element.

GEAR CASE SNUBBER SYSTEM

The mounts are required to survive severe shock input to the machinery without yielding, this is accomplished by limiting the mount displacement with a snubber system (Figure 5). The snubber system is a group of mechanical stops which limit the maximum vertical and athwartship displacements of the gear case (from its static position) to such an extent that the resulting mount displacements do not cause yielding. Snubbers are not required in the fore-aft direction.

The snubber system must be effective at all times. Since the machinery may be hot or cold, the thermal expansion of the gear case must not change the snubber gaps beyond their limits. The minimum snubber clearance must allow any mount displacements during normal operation without contacting the gear case.

Problems associated with thermal expansion are avoided by choosing snubber locations such that the gaps are not affected by the expansion. This dictates that the vertical snubbers be located at the same elevation as the mounts (gear horizontal centerline) and that the athwartship snubbers be located at the gear case vertical centerline. The arrangement chosen has four vertical snubbers just below the mounts and two athwartship snubbers on the bottom of the gear case.

ALIGNMENT

At assembly, the gear case must be positioned relative to the generator such that proper alignment of the slow speed shaft is obtained in both the vertical and horizontal planes. Horizontal alignment will eliminate any horizontal loads at the bearings due to shaft bending. Vertical alignment will equalize the vertical loads at the gear bearings.

Horizontal alignment is achieved by adjusting the location of the gear case mounts in the horizontal plane. Vertical alignment is achieved by adjusting the gear case mount elevation and rotation about the athwartship axis.

The alignment condition of the shaft can be determined by measuring the bending strains at a single location on the shaft. Bending moments in the vertical and horizontal planes can be calculated from the strain measurements. The alignment of the bearings can be uniquely determined for both the vertical and horizontal planes. Alignment corrections can be made based on calculated effects of gear case mount elevations and rotations.

SHOCK SNUBBERS

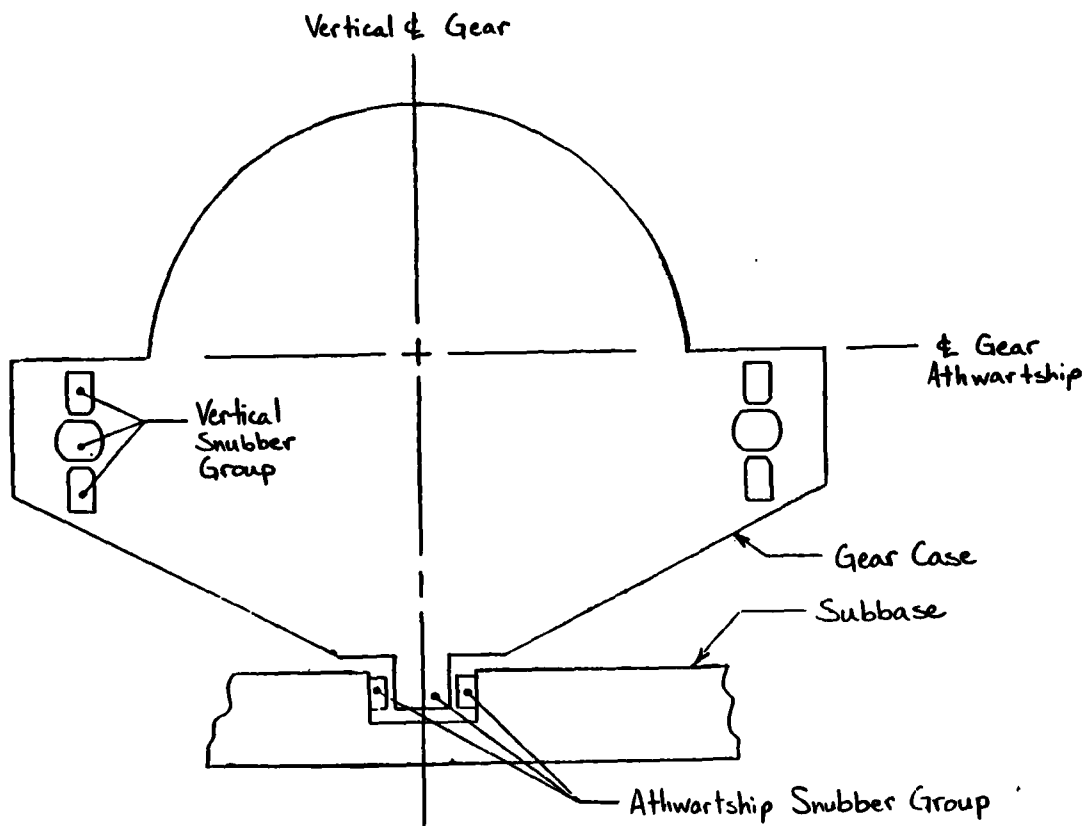


FIGURE 5

REFERENCES

1. An Introduction To Mechanical Vibration
Robert F. Steidel, Jr.
John Wiley & Sons, Inc., 1971
2. Dynamics of Mechanical and Electromechanical Systems
Crandall, Karnopp, Kurtz, Pridmore-Brown
McGraw Hill, 1968
3. Shaft Alignment Using Strain Gages
Albert W. Forrest, Jr. and Richard Labasky
Marine Technology, Vol 18, No. 3
July, 1981
4. Stress Concentration Factors
R. E. Peterson
Wiley - Interscience, 1974

DISCUSSION

Voice: What size generator is this?

Mr. Andrews: We are talking about a two-megawatt ship service turbine generator.

Mr. Sickmeier (General Motors): You said one of the fall-outs of your design was for better or equal loading on the bearings. What was the principal reason for isolating the gear box from the other two ends of the system?

Mr. Andrews: The gear box is not isolated from the generator. They are rigidly bolted together, so part of this generator is supported from the gear box.

Mr. Sickmeier: But, your paper was about an isolation system for the gear box?

Mr. Andrews: Yes.

Mr. Sickmeier: What was the principal reason for doing that?

Mr. Andrews: Due to the errors that develop in the gears, we pick up a strong single frequency vibration at a number of harmonics of the rotating speed of the pinion. Those vibrations can be measured on the mounting surfaces where the turbine generator interfaces with the ship. We are trying to isolate those vibrations from the ship, and we do that by putting the isolation system between the gear box and the sub base of the ship. The vibrations, then, are generated within the gear case, so we are trying to prevent them from eventually getting into the ship and becoming a structure-borne noise problem.

Mr. Eshleman (Vibration Institute): How much of the gear mesh vibration do you anticipate measuring at that outboard bearing of the generator?

Mr. Andrews: We don't really know. It is a rather difficult problem because the bearings are journal bearings, so there is an oil film which has some stiffness and damping. That will isolate the transmitted vibrations to a rather large degree. We do not expect a large amount of vibration to be transmitted through that shaft.

Mr. Eshleman: I assume you will measure that when you do the evaluation.

Mr. Andrews: Yes.

Mr. Eshleman: What mechanism are you using on the snubbers for your isolation?

Mr. Andrews: The snubbers are just mechanical stops.

Mr. Eshleman: Then you are not allowing any flexibility in the snubbers.

Mr. Andrews: No. They are very hard. We don't expect much deflection with those. They are there to limit the deflection of the mounts so they don't break.

EFFECT OF COUPLED TORSIONAL-FLEXURAL VIBRATION OF A GEARED
SHAFT SYSTEM ON THE DYNAMIC TOOTH LOAD

S.V. Neriya, R.B. Bhat and T.S. Sankar
Department of Mechanical Engineering
Concordia University
Montreal, Quebec, Canada H3G 1M8

The dynamic load on gear teeth is studied considering the coupling between the flexural and torsional vibrations in a simple geared shaft system. The flexibility of the mating teeth and the driving and driven shafts are included in the analysis. The coupled equations of motion for the geared shaft system are developed along with a constraint equation which ensures contact between the two mating teeth. The free vibration problem is solved to obtain the natural frequencies and mode shapes. Normal mode analysis is employed to obtain the dynamic response of the system to excitations arising from the mass unbalance and geometrical eccentricity in the gears. The effect of unbalance and geometrical eccentricity on the dynamic tooth load are studied.

NOMENCLATURE

c_{b1}	flexural damping of the driven shaft	U_2	mass unbalance in the driven gear
c_{b2}	flexural damping of the driving shaft	x_1	flexural displacement of the driving gear in the x-direction
c_t	average flexural damping of the gear tooth	x_2	flexural displacement of the driven gear in the x-direction
c_1	lumped torsional damping at the driving gear	y_1	flexural displacement of the driving gear in the y-direction
c_2	lumped torsional damping at the driven gear	y_2	flexural displacement of the driven gear in the y-direction
[C]	generalized damping matrix	y_{t1}	absolute displacement of the driving tooth
F	transmitted force	y_{t2}	absolute displacement of the driven tooth
{F}	generalized force vector	[γ]	diagonal damping matrix
I_1	moment of inertia of the driving gear	ϵ_1	geometrical eccentricity in the driving gear
I_2	moment of inertia of the driven gear	ϵ_2	geometrical eccentricity in the driven gear
J_1	moment of inertia of the motor	θ_1	rotational angle of the driving gear
J_2	moment of inertia of the dynamo	θ_2	rotational angle of the driven gear
k_{b1}	flexural stiffness of the driving shaft	θ_{f1}	angle between the directions of the eccentricity and unbalance for the driving gear
k_{b2}	flexural stiffness of the driven shaft	θ_{f2}	angle between the directions of the eccentricity and unbalance for the driven gear
k_t	average flexural stiffness of the gear tooth	[κ]	diagonal stiffness matrix
k_1	torsional stiffness of the driving shaft	λ_i	ith eigen value
k_2	torsional stiffness of the driven shaft	[μ]	diagonal mass matrix
[K]	generalized stiffness matrix	ϕ_1	rotational angle of the motor
m_1	mass of the driving gear	ϕ_2	rotational angle of the dynamo
m_2	mass of the driven gear	{ ψ_i }	ith eigen vector
m_{t1}	mass of the driving gear tooth		
m_{t2}	mass of the driven gear tooth		
[M]	generalized mass matrix		
{ P_s } _k , { P_c } _k	principal coordinates corresponding to the kth sine and cosine excitations		
c_m	lumped torsional damping at the motor		
c_d	lumped torsional damping at the dynamo		
{ q }	generalized displacement vector		
r_1	base circle radius of the driving gear		
r_2	base circle radius of the driven gear		
T_1	input torque		
T_2	output torque		
U_1	mass unbalance in the driving gear		

INTRODUCTION

An accurate determination of the dynamic load on a gear tooth is important for gear design. Due to the dynamic effects during operation, the actual load on the gear tooth

will be significantly higher than what it is intended to transmit. The factors causing the dynamic load are numerous, such as incorrect mounting of gears, variation of tooth stiffness during engagement, changes in tooth profile due to elastic distortion under load and errors of manufacture. The magnitude of the dynamic load depends upon the masses of the revolving gears, the extent of the effective errors and the speed of operation.

Dynamic tooth load due to torsional vibration of shafts was determined by Mahalingam and Bishop [1], considering the excitation to be due to a static transmission error, which encompassed all forms of errors in the geared system. The excitation was in the form of a periodic introduction of a wedge between the two perfect mating teeth.

The torsional vibration of a shaft is coupled to flexural vibration in a geared shaft system. Lund [2] considered such coupling in the torsional-flexural vibrations in a geared system of rotors. Here both forced vibrations, caused by mesh errors or by mass unbalance, and free damped vibrations whose complex eigen frequencies define the damped critical speeds and the stability of the rotor system are considered. Iida et al [3] studied a simple geared system including coupling in the torsional flexural vibration and calculated the response due to mass unbalance and geometrical eccentricity in the gears. They, however, did not study the system from the point of view of determining the dynamic tooth load. In their model, they considered only the driven shaft to be flexible in bending and the driving shaft to be rigid. The flexibility of the gear teeth was also not considered in the analysis. They showed that the system behavior is significantly affected by the coupled motion.

In this paper, the dynamic loading on gear teeth is studied considering the coupling between the flexural and torsional vibrations in a simple geared shaft system. The flexibility and damping of the mating teeth and the driving and driven shafts are included in the analysis. The frequency response of the geared shaft system and subsequently the dynamic tooth load are obtained by normal mode analysis. The influence of unbalance and geometrical eccentricity on the dynamic tooth load are studied.

ANALYSIS

A schematic representation of a simple geared shaft system is shown in Fig. 1. It shows a motor of moment of inertia J_1 driving a dynamo of moment of inertia J_2 through gears of moment of inertia I_1 and I_2 . The driving and driven gears and their relative positions are shown in Fig. 2. An equivalent spring mass representation for the same is shown in Fig. 3.

Assuming that the shafts are massless, the equations of motion for the system can be written as

$$m_1 \ddot{x}_1 + c_{b1} \dot{x}_1 + K_{b1} x_1 = U_1 \theta_1^2 \cos(\theta_1 + \theta_{f1}) \quad (1)$$

$$m_2 \ddot{x}_2 + c_{b2} \dot{x}_2 + K_{b2} x_2 = U_2 \theta_2^2 \cos(\theta_2 + \theta_{f2}) \quad (2)$$

$$m_1 \ddot{y}_1 + c_{b1} \dot{y}_1 + K_{b1} y_1 + \bar{c}_t (\dot{y}_1 + \epsilon_1 \omega_1 \cos \theta_1 + r_1 \dot{\theta}_1 - \dot{y}_{t1}) + \bar{K}_t (y_1 + \epsilon_1 \sin \theta_1 + r_1 \theta_1 - y_{t1}) = U_1 \theta_1^2 \sin(\theta_1 + \theta_{f1}) \quad (3)$$

$$m_2 \ddot{y}_2 + c_{b2} \dot{y}_2 + K_{b2} y_2 + \bar{c}_t (\dot{y}_2 + \epsilon_2 \omega_2 \cos \theta_2 + r_2 \dot{\theta}_2 - \dot{y}_{t2}) + \bar{K}_t (y_2 + \epsilon_2 \sin \theta_2 + r_2 \theta_2 - y_{t2}) = U_2 \theta_2^2 \sin(\theta_2 + \theta_{f2}) \quad (4)$$

$$m_{t1} \ddot{y}_{t1} + \bar{c}_t (\dot{y}_{t1} - \dot{y}_1 - \epsilon_1 \omega_1 \cos \theta_1 - r_1 \dot{\theta}_1) + \bar{K}_t (y_{t1} - y_1 - \epsilon_1 \sin \theta_1 - r_1 \theta_1) = -F \quad (5)$$

$$m_{t2} \ddot{y}_{t2} + \bar{c}_t (\dot{y}_{t2} - \dot{y}_2 - \epsilon_2 \omega_2 \cos \theta_2 - r_2 \dot{\theta}_2) + \bar{K}_t (y_{t2} - y_2 - \epsilon_2 \sin \theta_2 - r_2 \theta_2) = F \quad (6)$$

$$I_1 \ddot{\theta}_1 + K_1 (\theta_1 - \phi_1) + \bar{c}_t (\dot{y}_1 + \epsilon_1 \omega_1 \cos \theta_1 + r_1 \dot{\theta}_1 - \dot{y}_{t1}) (r_1 + \epsilon_1 \cos \theta_1) + \bar{K}_t (y_1 + \epsilon_1 \sin \theta_1 + r_1 \theta_1 - y_{t1}) (r_1 + \epsilon_1 \cos \theta_1) + c_1 \dot{\theta}_1 = 0 \quad (7)$$

$$I_2 \ddot{\theta}_2 + K_2 (\theta_2 - \phi_2) + \bar{c}_t (\dot{y}_2 + \epsilon_2 \omega_2 \cos \theta_2 + r_2 \dot{\theta}_2 - \dot{y}_{t2}) (r_2 + \epsilon_2 \cos \theta_2) + \bar{K}_t (y_2 + \epsilon_2 \sin \theta_2 + r_2 \theta_2 - y_{t2}) (r_2 + \epsilon_2 \cos \theta_2) + c_2 \dot{\theta}_2 = 0 \quad (8)$$

$$J_1 \ddot{\phi}_1 + K_1 (\phi_1 - \theta_1) - T_1 = 0 \quad (9)$$

$$J_2 \ddot{\phi}_2 + K_2 (\phi_2 - \theta_2) + T_2 = 0 \quad (10)$$

The condition for the mating teeth to remain in contact is

$$y_{t1} = y_{t2} \quad (11)$$

Expressing all the variables in terms of their respective mean values and variations about the mean,

$$\begin{aligned} y_1 &= y_{10} + \Delta y_1 & \theta_1 &= \theta_{10} + \omega_1 t + \Delta \theta_1 \\ y_2 &= y_{20} + \Delta y_2 & \theta_2 &= \theta_{20} + \omega_2 t + \Delta \theta_2 \\ y_t &= y_{t0} + \Delta y_t & \phi_1 &= \phi_{10} + \omega_1 t + \Delta \phi_1 \\ T_1 &= T_{10} - c_m \Delta \phi_1 & \phi_2 &= \phi_{20} + \omega_2 t + \Delta \phi_2 \\ T_2 &= T_{20} - c_d \Delta \phi_2 & F &= F_0 + \Delta F \end{aligned} \quad (12)$$

where θ_{10} , θ_{20} , ϕ_{10} and ϕ_{20} are initial angular positions.

Since only the flexural displacement in the y-direction is coupled with torsion, equations of motion in x-direction will not be considered in the subsequent analysis. Substituting the mean and variation about the mean of all the variables given in equation (12) into the equations of motion (3)-(10) and after considerable manipulation and simplification by ignoring terms involving squares and higher powers of small quantities, the equations of motion involving the quantities varying about the mean value can be written in the following matrix form:

$$[M]\{\ddot{q}\} + [C]\{\dot{q}\} + [K]\{q\} = \{F\} \quad (13)$$

where the generalized displacement vector $\{q\}$ is:

$$\{q\} = [\Delta y_1, \Delta y_2, \Delta y_t, \Delta \phi_1, \Delta \theta_1, \Delta \theta_2, \Delta \phi_2]^T \quad (14)$$

The matrices $[M]$, $[K]$, $[C]$ and $\{F\}$ are given by:

$$[M] = \begin{bmatrix} m_1 & 0 & 0 & 0 & 0 & 0 & 0 \\ 0 & m_2 & 0 & 0 & 0 & 0 & 0 \\ 0 & 0 & m_{t1} + m_{t2} & 0 & 0 & 0 & 0 \\ 0 & 0 & 0 & J_1 & 0 & 0 & 0 \\ 0 & 0 & 0 & 0 & I_1 & 0 & 0 \\ 0 & 0 & 0 & 0 & 0 & I_2 & 0 \\ 0 & 0 & 0 & 0 & 0 & 0 & J_2 \end{bmatrix}$$

$$[K] = \begin{bmatrix} K_{b1} + K_t & 0 & -\bar{K}_t & 0 & \bar{K}_t r_1 & 0 & 0 \\ 0 & K_{b2} + \bar{K}_t & -\bar{K}_t & 0 & 0 & K_t r_2 & 0 \\ -\bar{K}_t & -\bar{K}_t & 2K_t & 0 & -\bar{K}_t r_1 & -K_t r_2 & 0 \\ 0 & 0 & 0 & K_1 & -K_1 & 0 & 0 \\ \bar{K}_t r_1 & 0 & -\bar{K}_t r_1 & -K_1 & K_1 + \bar{K}_t r_1^2 & 0 & 0 \\ 0 & \bar{K}_t r_2 & -\bar{K}_t r_2 & 0 & 0 & \bar{K}_t r_2^2 + K_2 & -K_2 \\ 0 & 0 & 0 & 0 & 0 & -K_2 & K_2 \end{bmatrix}$$

$$[C] = \begin{bmatrix} c_{b1} + \bar{c}_t & 0 & -\bar{c}_t & 0 & \bar{c}_t r_1 & 0 & 0 \\ 0 & c_{b2} + \bar{c}_t & -\bar{c}_t & 0 & 0 & \bar{c}_t r_2 & 0 \\ -\bar{c}_t & -\bar{c}_t & 2c_t & 0 & \bar{c}_t r_1 & -\bar{c}_t r_2 & 0 \\ 0 & 0 & 0 & c_m & 0 & 0 & 0 \\ \bar{c}_t & 0 & -\bar{c}_t r_1 & 0 & c_1 + \bar{c}_t r_1^2 & \bar{c}_t r_2^2 + c_2 & 0 \\ 0 & \bar{c}_t r_2 & -\bar{c}_t r_2 & 0 & 0 & 0 & 0 \\ 0 & 0 & 0 & 0 & 0 & 0 & -c_d \end{bmatrix}$$

and

$$\{F\} = \begin{bmatrix} \bar{c}_t \epsilon_1 \omega_1 \cos(\omega_1 t + \theta_{10}) - \bar{K}_t \epsilon_1 \sin(\omega_1 t + \theta_{10}) \\ + U_1 \omega_1^2 \sin(\omega_1 t + \theta_{10} + \theta_{f1}) \\ -\bar{c}_t \epsilon_2 \omega_2 \cos(\omega_2 t + \theta_{20}) - \bar{K}_t \epsilon_2 \sin(\omega_2 t + \theta_{20}) \\ + U_2 \omega_2^2 \sin(\omega_2 t + \theta_{20} + \theta_{f2}) \\ \bar{c}_t [\epsilon_2 \omega_2 \cos(\omega_2 t + \theta_{20}) + \epsilon_1 \omega_1 \cos(\omega_1 t \\ + \theta_{10})] + \bar{K}_t [\epsilon_2 \sin(\omega_2 t + \theta_{20}) + \epsilon_1 \\ \sin(\omega_1 t + \theta_{10})] \\ 0 \\ \bar{c}_t r_1 \epsilon_1 \omega_1 \cos(\theta_{10} + \omega_1 t) - F_0 \epsilon_1 \cos(\theta_{10} \\ + \omega_1 t) - \bar{K}_t r_1 \epsilon_1 \sin(\theta_{10} + \omega_1 t) \\ \bar{c}_t r_2 \epsilon_2 \omega_2 \cos(\theta_{20} + \omega_2 t) + F_0 \epsilon_2 \cos(\theta_{20} \\ + \omega_2 t) - \bar{K}_t r_2 \epsilon_2 \sin(\theta_{20} + \omega_2 t) \\ 0 \end{bmatrix} \quad (15)$$

where θ_{f1} and θ_{f2} are angle between directions of mass unbalance and geometrical eccentricity.

The expression for the dynamic tooth load ΔF , is obtained as

$$\Delta F = m_{t1} \Delta \ddot{y}_t + \bar{c}_t (\Delta \dot{y}_t - \Delta \dot{y}_1 - \epsilon_1 \omega_1 \cos(\omega_1 t + \theta_{10})) \\ - r_1 \Delta \theta_1 + \bar{K}_t (\Delta y_t - \Delta y_1 - \epsilon_1 \sin(\omega_1 t + \theta_{10}) - r_1 \Delta \theta_1) \quad (16)$$

The homogeneous part of equation (13) neglecting damping, is given by,

$$[M]\{\ddot{q}\} + [K]\{q\} = \{0\} \quad (17)$$

is solved to obtain the eigen values λ_i and eigen-vectors $\{q_i\}$ of the system.

An inspection of the force vector $\{F\}$ in equation (15) shows that the excitation consists of frequencies ω_1 and ω_2 corresponding to the speeds of driving and driven gears. The force vector $\{F\}$ can be expressed as the sum of sine and cosine components, involving the two frequencies ω_1 and ω_2 as,

$$\{F\} = \{F_s\}_1 \sin \omega_1 t + \{F_s\}_2 \sin \omega_2 t \\ + \{F_c\}_1 \cos \omega_1 t + \{F_c\}_2 \cos \omega_2 t \quad (18)$$

where θ_{10} , θ_{20} , θ_{f1} and θ_{f2} have been assumed to be zero.

The corresponding response also can be expressed involving the two frequencies as

$$\{q\} = \{q_s\}_1 \sin \omega_1 t + \{q_s\}_2 \sin \omega_2 t \\ + \{q_c\}_1 \cos \omega_1 t + \{q_c\}_2 \cos \omega_2 t \quad (19)$$

Using equations (18) and (19), equation

(13) can be written as four separate equations.

$$\begin{aligned} [M]\{\ddot{q}_s\}_k + [C]\{\dot{q}_s\}_k + [K]\{q_s\}_k &= \{F_s\}_k \\ [M]\{\ddot{q}_c\}_k + [C]\{\dot{q}_c\}_k + [K]\{q_c\}_k &= \{F_c\}_k; k = 1,2 \end{aligned} \quad (20)$$

Expressing the response $\{q\}$ in terms of the modal coordinates $\{p\}$ as

$$\begin{aligned} \{q_s\}_k &= [\psi]\{p_s\}_k \\ \{q_c\}_k &= [\psi]\{p_c\}_k; k = 1,2 \end{aligned} \quad (21)$$

where $[\psi]$ is the modal matrix formed by using the eigen vectors $\{\psi_i\}$, and $\{p_s\}_k$ and $\{p_c\}_k$ are the principal coordinate vectors corresponding to the sine and cosine components. Using equations (21) in equation (20) and pre-multiplying by $[\psi]^T$ results in uncoupled equations in the modal coordinates of the form,

$$\begin{aligned} \mu_i \ddot{(p_{si})}_k + \gamma_i \dot{(p_{si})}_k + \kappa_i (p_{si})_k &= (\sigma_{si})_k \\ \mu_i \ddot{(p_{ci})}_k + \gamma_i \dot{(p_{ci})}_k + \kappa_i (p_{ci})_k &= (\sigma_{ci})_k \end{aligned} \quad (22)$$

where $k = 1,2$
 $i = 1,2,\dots,7$

where μ_i and κ_i are the elements of diagonal matrices $[\mu]$ and $[\kappa]$ given by

$$\begin{aligned} [\mu] &= [\psi]^T [M] [\psi] \\ [\kappa] &= [\psi]^T [K] [\psi] \end{aligned}$$

and γ_i is the equivalent damping coefficient in each mode. $(\sigma_{si})_k$ and $(\sigma_{ci})_k$ are the elements of the generalized force vectors $\{q_s\}_k$ and $\{q_c\}_k$, given by

$$\begin{aligned} \{q_s\}_k &= [\psi]^T \{F_s\}_k \\ \{q_c\}_k &= [\psi]^T \{F_c\}_k; k = 1,2 \end{aligned}$$

The solution of equation (22) yields,

$$\begin{aligned} (p_{si})_k &= \frac{(\sigma_{si})_k}{(-\omega_k^2 \mu_i + \kappa_i) + j(\gamma_i \omega_k)} \\ (p_{ci})_k &= \frac{(\sigma_{ci})_k}{(-\omega_k^2 \mu_i + \kappa_i) + j(\gamma_i \omega_k)}; \end{aligned} \quad (23)$$

$k = 1,2$
 $i = 1,2,\dots,7$

Using equations (23), (21) and (19) we obtain the system dynamic response $\{q\}$. The dynamic tooth load ΔF is calculated by using equation (16). Since the response involves two frequencies ω_1 and ω_2 , the total response has the form

$$\begin{aligned} q_j &= q_{1j} \sin(\omega_1 t + \psi_{1j}) + q_{2j} \sin(\omega_2 t + \psi_{2j}) \\ &= q_{1j} \sin \lambda_1 + q_{2j} \sin \lambda_2 \\ &= (q_{1j} + q_{2j}) \sin \left(\frac{\lambda_1 + \lambda_2}{2} \right) \cos \left(\frac{\lambda_1 - \lambda_2}{2} \right) \end{aligned}$$

$$+ (q_{1j} - q_{2j}) \cos \left(\frac{\lambda_1 + \lambda_2}{2} \right) \sin \left(\frac{\lambda_1 - \lambda_2}{2} \right) \quad (24)$$

Hence, the response is an amplitude modulated harmonic phenomenon. If ω_1 and ω_2 are close to each other, this will result in beats.

NUMERICAL RESULTS

The details of the geared shaft system used to obtain the numerical results are given in Table 1. The maximum value of the dynamic responses obtained from equation (24) are illustrated in Figs. 4 and 5 and the maximum dynamic tooth loads obtained from equation (16) are shown in Figs. 6 to 9. In the present investigation one percent of the critical damping is used in all the modes. The dynamic responses are plotted against the frequency of rotation of the driven shaft ω_2 . This representation also facilitates comparison of present results with those presented in [3]. Responses are presented up to 100 Hz which included only the first five natural frequencies of the system, since the other two natural frequencies are much higher in the range. The system natural frequencies are given in Table 2 where the natural frequencies of the system considered in [3] are also given for comparison.

The dynamic response of the driven shaft, Δy_2 , is plotted in Fig. 4 against the frequency of rotation of the driven shaft, for nominal values of ϵ_1 , U_1 and U_2 and for different values of ϵ_2 . A comparison of Δy_2 response with that presented in [3] was attempted. However, no information about damping in the system is given in [3] and in the frequency range for which the results are presented, there is only one response peak which compares satisfactorily with the present results. It is interesting to note in Fig. 4 that when the excitation frequency is related to the system natural frequency through the gear ratio, the system experiences resonance. This is the reason for the peaks occurring at 4.77 Hz, 29 Hz and 45.66 Hz. The Δy_2 response increases with increasing eccentricity of the driven gear, ϵ_2 . The response is very high at 25.37 Hz since the corresponding mode is predominantly the flexural mode of the driven shaft. The response is also significant at 45.66 Hz since, the driving side is exciting the system at its natural frequency of 25.37 Hz.

The flexural response of the driving shaft is shown in Fig. 5. The natural frequency corresponding to the flexure of the driving shaft is 16.14 Hz. The response is predominant at this frequency and at 29 Hz which are related by the gear ratio. The response at 29 Hz is higher compared to that at 16.14 Hz, since the plot is against the frequency of rotation of the driven shaft, ω_2 , and the driving shaft is subjected to excitation at 16.14 Hz when the driven shaft rotates at 29 Hz. For nominal value of ϵ_1 , U_1 and U_2 the response increases

with increasing eccentricity of the driven gear.

The dynamic tooth load ΔF , is plotted against the frequency of rotation of the driven shaft in Fig. 6. The unbalance U_1 and U_2 and the geometrical eccentricity in the driving gear ϵ_1 are kept at nominal values and the curves were plotted for different values of ϵ_2 .

It is seen that the dynamic response exhibits the most significant peak at 79 Hz, which corresponds to the fifth natural frequency.

The dynamic tooth load ΔF , is plotted against the frequency of rotation of the driven shaft in Fig. 7. The unbalance U_1 and geometrical eccentricities ϵ_1 and ϵ_2 are kept at nominal values and the curves were plotted for different values of U_2 . Again, the dynamic force exhibits a significant peak at 79 Hz.

The dynamic tooth load ΔF , is plotted against the frequency of rotation of the driven shaft in Fig. 8. The unbalances U_1 and U_2 and the geometrical eccentricity ϵ_2 , are kept at nominal values and the curves are plotted for different values of ϵ_1 . The dynamic force still exhibits a significant peak at 79 Hz.

The variation of dynamic tooth load against the frequency of rotation of the driven shaft is shown in Fig. 9 for nominal values of U_2 , ϵ_1 and ϵ_2 and for different values of U_1 . The peak dynamic tooth load occurs again at 79 Hz. The variation of the dynamic tooth load with U_1 is negligible.

In all the above cases, the dynamic tooth load has a maximum only at 79 Hz which is the system natural frequency corresponding to a predominantly torsional mode. However, the dynamic responses Δy_1 and Δy_2 exhibit maximum values at other system natural frequencies also. The torsional responses of the driving and driven shafts at the gear locations also exhibit peaks at all the system natural frequencies. One possible explanation for the dynamic tooth load having a peak at 79 Hz only is that the effect of dynamic responses at other natural frequencies are nullified due to their mutual phase relations. The dynamic tooth load is significant only at the torsional resonance in the system, and the coupling between the torsional and flexural vibrations does not change this behavior.

CONCLUSIONS

A geared shaft system is analyzed including the coupling between the torsional and flexural vibrations in the system. The analysis considers that there is no loss of contact between the mating teeth and the resulting dynamic tooth load is obtained. Based on the results presented it is observed that:

- 1) the dynamic responses have significant peaks not only at the system natural frequencies but also at frequencies which are related to the natural frequency through the gear ratio.

- 11) the dynamic tooth load is maximum at the torsional resonance in the system and the coupling between the torsional and flexural vibrations in the system does not change this behavior.

ACKNOWLEDGEMENTS

The work reported was partially supported by grants A7104 and A1375 from Natural Sciences and Engineering Research Council of Canada.

REFERENCES

1. Mahalingam, S. and Bishop, R.E.D., "Dynamic Loading of Gear Teeth", Journal of Sound and Vibration, 1974, pp. 179-189.
2. Lund, J.W., "Critical Speed, Stability and Response of a Geared Train of Rotors", Journal of Mechanical Design, July 1978, Vol. 100, pp. 535-539.
3. Iida, H., Tamura, A., Kikuch, K. and Agata, H., "Coupled Torsional-Flexural Vibration of a Shaft in a Geared System of Rotors", Bulletin of the JSME, Vol. 23, No. 186, December 1980, pp. 2111-2117.

I_1	3.12×10^{-4} Kgm ²
I_2	6.53×10^{-5} Kgm ²
J_1	4.78×10^{-3} Kgm ²
J_2	5.71×10^{-3} Kgm ²
K_{b1}, K_{b2}	2.04×10^3 N/m
K_t	2.55×10^7 N/m
K_1	1.17×10^4 Nm/rad
K_2	2.88×10^4 Nm/rad
m_1	16.96 kg
m_2	5.65 kg
m_{t1}, m_{t2}	4.9×10^{-3} kg
r_1	0.1015 m
r_2	0.0564 m
ϵ_1, ϵ_2	120 μ m (variable)
U_1, U_2	2.8×10^{-4} kgm (variable)

Mode No.	Present System	System of Ref. [3]
1	zero	zero
2	2.65	2.7
3	16.14	24.6
4	25.37	-
5	79	-
6	5806.43	-
7	1.13×10^5	-

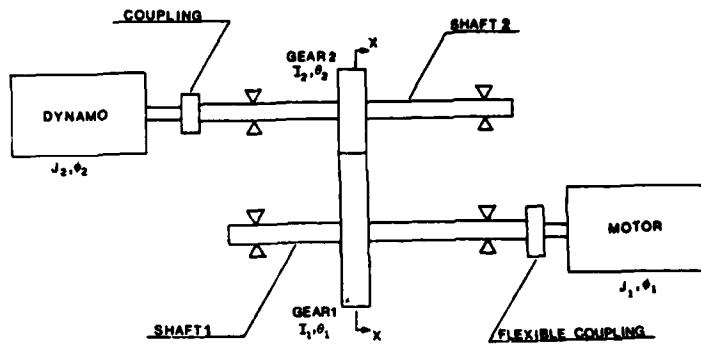
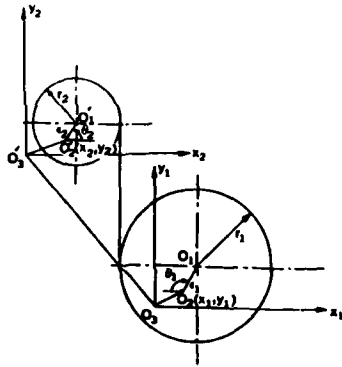


Fig. 1: Simple Geared Shaft System



- O_1 geometric center of the driving gear
- O_1' geometric center of the driven gear
- O_2 center of the driving shaft when it is rotating
- O_2' center of the driven shaft when it is rotating
- O_3 center of the driving shaft when it is stationary
- O_3' center of the driven shaft when it is stationary

Fig. 2: Sectional View at the Gear Location

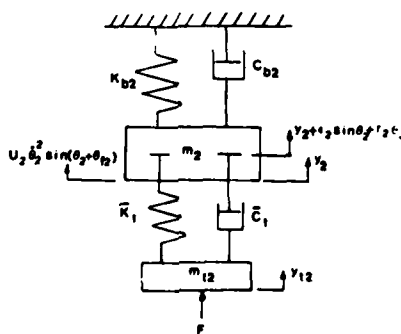


Fig. 3(a): Driven Gear Model

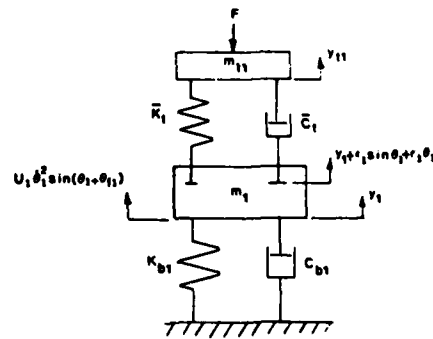


Fig. 3(b): Driving Gear Model

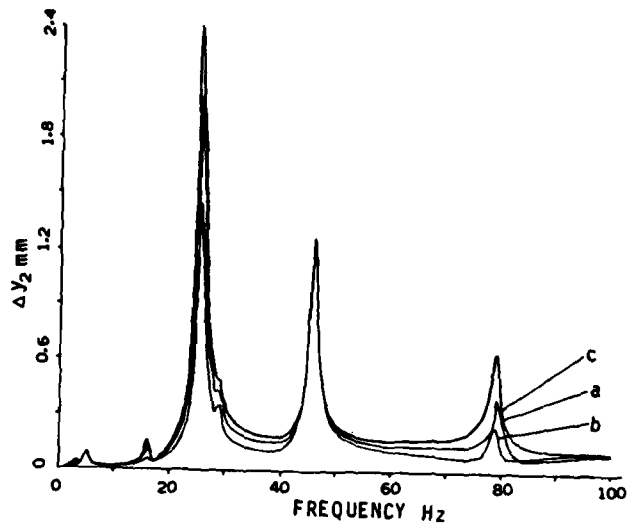


Fig. 4: Dynamic response of the driven shaft, Δy_2 , against frequency of rotation of the driven shaft.

($U_1 = 2.8 \times 10^{-4}$ kgm, $U_2 = 2.8 \times 10^{-4}$ kgm, $\epsilon_1 = 120 \mu\text{m}$,

(a) $\epsilon_2 = 20 \mu\text{m}$, (b) $\epsilon_2 = 80 \mu\text{m}$, (c) $\epsilon_2 = 120 \mu\text{m}$)

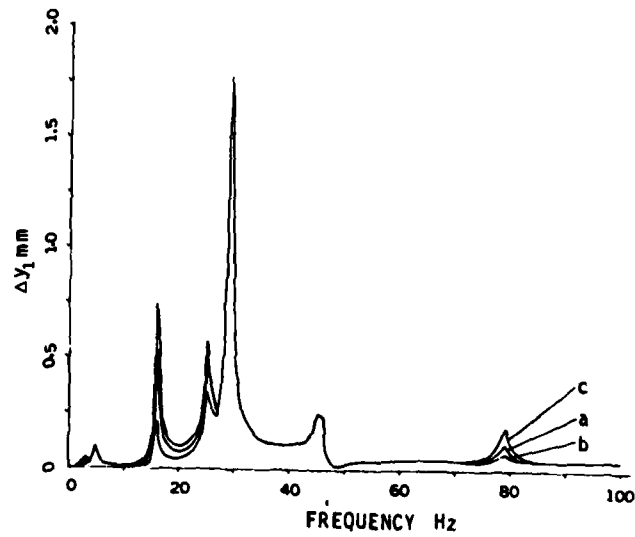


Fig. 5: Dynamic response of the driving shaft, Δy_1 , against frequency of rotation of the driven shaft.

($U_1 = 2.8 \times 10^{-4}$ kgm, $U_2 = 2.8 \times 10^{-4}$ kgm, $\epsilon_1 = 120 \mu\text{m}$,

(a) $\epsilon_2 = 20 \mu\text{m}$, (b) $\epsilon_2 = 80 \mu\text{m}$, (c) $\epsilon_2 = 120 \mu\text{m}$)

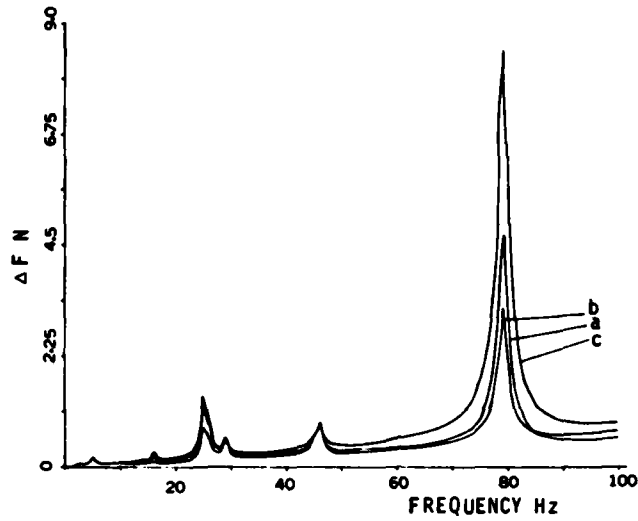


Fig. 6: Dynamic tooth load against frequency of rotation of the driven shaft.

($U_1 = 2.8 \times 10^{-4}$ kgm, $U_2 = 2.8 \times 10^{-4}$ kgm, $\epsilon_1 = 120 \mu\text{m}$,
 (a) $\epsilon_2 = 20 \mu\text{m}$, (b) $\epsilon_2 = 80 \mu\text{m}$, (c) $\epsilon_2 = 120 \mu\text{m}$)

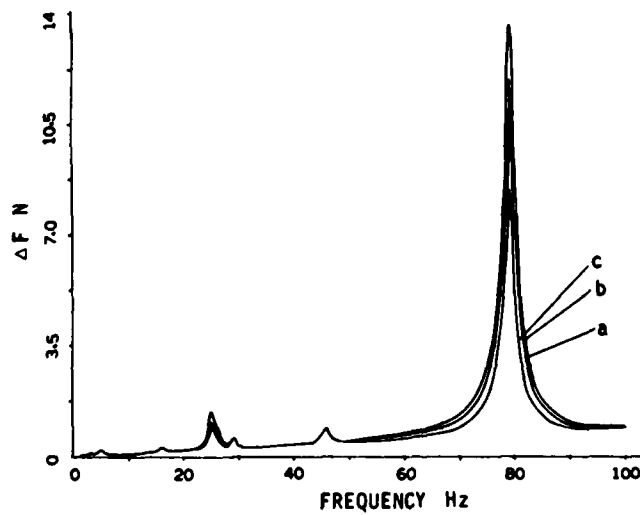


Fig. 7: Dynamic tooth load against frequency of rotation of the driven shaft.

($U_1 = 2.8 \times 10^{-4}$ kgm, $\epsilon_1 = 120 \mu\text{m}$, $\epsilon_2 = 120 \mu\text{m}$, (a) $U_2 = 0.78 \times 10^{-4}$ kgm
 (b) $U_2 = 1.47 \times 10^{-4}$ kgm, (c) $U_2 = 2.8 \times 10^{-4}$ kgm)

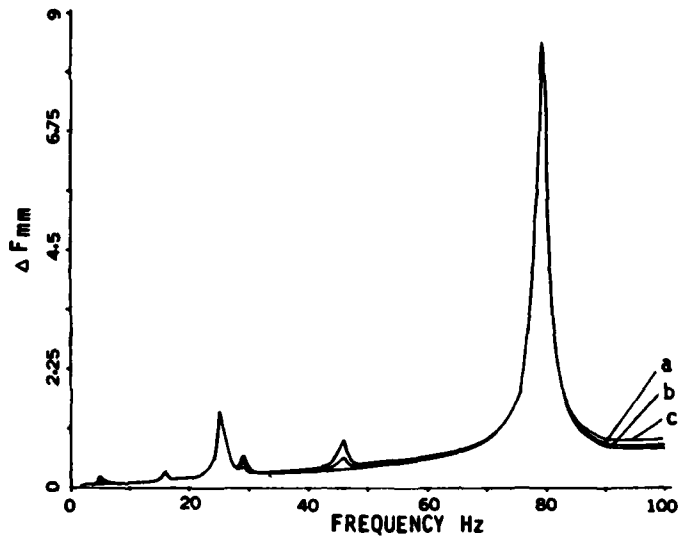


Fig. 8: Dynamic tooth load against the frequency of rotation of the driven shaft.

($U_2 = 2.8 \times 10^{-4}$ kgm, $U_2 = 2.8 \times 10^{-4}$ kgm, $\epsilon_2 = 120 \mu\text{m}$,
 (a) $\epsilon_1 = 20 \mu\text{m}$, (b) $\epsilon_1 = 80 \mu\text{m}$, (c) $\epsilon_1 = 120 \mu\text{m}$)

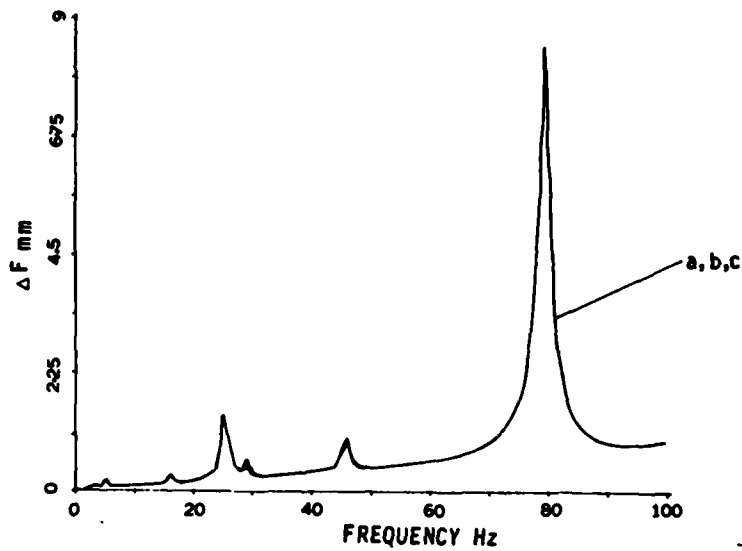


Fig. 9: Dynamic tooth load against the frequency of rotation of the driven shaft.

($U_2 = 2.8 \times 10^{-4}$ kgm, $\epsilon_1 = 120 \mu\text{m}$, $\epsilon_2 = 120 \mu\text{m}$, (a) $U_1 = 0.78 \times 10^{-4}$ kgm
 (b) $U_1 = 1.47 \times 10^{-4}$ kgm, (c) $U_1 = 2.8 \times 10^{-4}$ kgm)

PRECISION MEASUREMENT OF TORSIONAL
OSCILLATIONS INDUCED BY GEAR ERRORS

S. L. Shmutter
Research Staff
Ford Motor Company
Manufacturing Processes Laboratory
Dearborn, Michigan

This paper describes an original and practical measuring technique applicable to torsional and gear related systems. The technique incorporates a novel angular sensor with resolution of better than 1 part in 10,000 in velocity variations, which is based on commercially available components. A method of establishing dynamic response of a drive train is presented. The method depends on the internal excitation from a gear set itself, thus eliminating any external devices. The resulting response closely describes dynamic behavior of a real rotating system. An efficient and accurate algorithm to perform Fourier order analysis of the conjugate error is devised for the general case of "hunting tooth" geometry of the gear set.

INTRODUCTION

Gearing is a constant velocity method of transmitting motion. A gear performance error, referred to as conjugate deviation, is defined as a departure from a uniform instantaneous velocity ratio between two meshing gears. These angular variations cause the gear set to act as a generator of vibrations.

Among all the gear related vibrations, angular (torsional) oscillations are the most direct indicator of the conjugate deviation. Although a conjugate error is also reflected in a linear vibration pattern of the housing, this pattern is usually greatly masked by many other excitations from radially acting forces and/or from external sources. On the other hand, most of such sources (unbalance, for example) affect the torsional vibration only as a second order effect. Some of the applications, where the gear induced torsional oscillations become of prime concern are: a quality inspection of new gear sets; a baseline monitoring of potential gear failures; and also an evaluation of noise and vibration levels and/or sources of a rotating drive train.

Conjugate deviation of a gear set causes only minute variations in angular velocity of the rotating members. For example, in the case of pitchline runout, a measurable threshold may cover 0.0002" T.I.R. in a 2" diameter pinion, corresponding to a variation of one

part in 10,000 of mean rotational velocity. Consider a typical tooth-mesh frequency component in the 10 arc sec range of angular error, in the case of a 15 tooth pinion. The velocity variation is translated into 0.08%. Since the desired resolution is one order of magnitude higher than the typical error, the instrumental accuracy becomes 0.01% to 0.005%, which is again one part in 10 to 20 thousand.

The required high resolution makes it necessary that a system measuring the gear related torsional vibrations incorporates:

- an angular sensor sufficiently accurate in the broad frequency range,
- an adequately defined procedure of data reduction and identification,
- a quantitatively established source-to-sensor transmissibility of the drive train.

This paper addresses all of these matters in detail. The problem is that the inclusion of a gear set into a drive train causes substantial complications in applying conventional techniques. An original and practical solution is presented pertaining to each of the above issues.

A description of an accurate, reliable, easy to calibrate and easy to install angular sensor is given. The sensor is based on a

commercial optical shaft encoder and a recovery network. A reliably resolved signal to 0.005% in velocity variations can be obtained in the frequency range of 1 to 1000 Hz, at the minimum.

A method of calibration studies of a mechanical drive train is presented, one which depends on the natural excitation from a gear set itself. As a result, the transmissibility curve furnishes quantities which closely describe behavior of a real rotating system with the gear set included.

An efficient and accurate way to computerize spectral order analysis is discussed. It is based on the external sampling generator positionally locked to the rotating shaft. The algorithm for "leakage-free" conjugate gear error analysis is devised, which extends the scope of the method for a general case of "hunting tooth" geometry of the gear set.

All of the above newly developed techniques, as part of the larger package, are practically implemented in the on-line rear-axle diagnostic machine, which has been already described elsewhere [1,2]. This paper, however, extracts the most practical solution and presents it in a rather general fashion. The technique is expected to be profitably utilized in many applications of torsional and gear related systems.

desirable to provide reliably conditioned signals on the order of at least 0.1 mv, equivalent to 0.01% variation of 100 rad/sec or 1000 rpm.

Among other requirements, an on-site calibration check which eliminates the need for any precision calibrating fixture, and a pass-through configuration of the sensor which avoids interference to the drive train, are of significant importance. An optional requirement associated with the sensing device is to provide an additional output containing a pulse train for sampling and triggering. Such a train, otherwise generated by a separate encoder, will control sampling of the sensor signal to allow computer processing in precise synchronism with the shaft rotation.

Not much is commercially offered in precision sensors of angular motion. Available sensors fail to satisfy most of the requirements outlined before. Those devices, which measure the torque deviation, are much better developed and well available. However, the torque sensing approach is an indirect method of the conjugate error measurement. The degree of correlation between the torque and the error has to be additionally established and may vary.

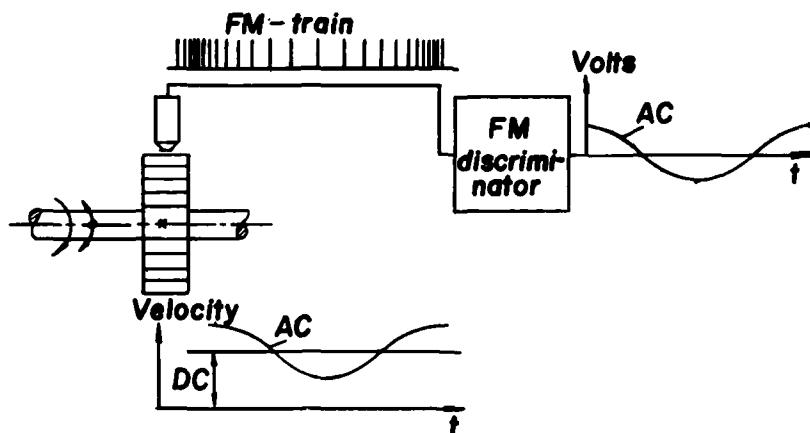


Fig. 1 - Principle of the Angular Velocimeter

ANGULAR VELOCIMETER

A measurement resolution of one part in 10 to 20 thousand of mean rotational velocity is required. This high resolution has to be furnished in the broad frequency range-from the possible ring gear fundamental to the tooth meshing components. A reasonable range of 5 to 1000 Hz would cover the most of applications. A sensitivity of the sensor equal or higher than 10 mv per rad/sec is

There is a practical solution, one which is part of the more sophisticated design [1]. It is believed that this simplified solution will suit many applications.

Encoder. A precision angular velocimeter is based on measurement of frequency modulation in the output pulse train of the optical incremental shaft encoder. The principle (Fig. 1) assumes a device which generates a pulse train at fixed angular increments of the

shaft rotation. Pulses arrive at uniform time intervals in case of perfectly steady speed of rotation, thus representing the carrier frequency. Whenever torsional vibration is present, it is superimposed upon the steady rotation, and the pulse time intervals vary. A frequency modulation (FM) occurs since the torsional vibration acts as a modulating signal. If such a pulse train is inputted into an FM discriminator circuit, the modulating signal is recovered if it exceeds the threshold of the circuit resolution.

The principle itself is well known. It is often used by positioning a magnetic transducer in close proximity to an existing gear wheel or to a toothed wheel attached to the drive line. Also used are photoelectric means in conjunction with a light-chopping disc. Commercially available torsional vibration measuring instruments use a 60 to 120 toothed chopper and expect larger than 0.2 rad/s amplitude of vibrational signal before any reading occurs. That is why they fail to meet the required 0.01% resolution in velocity variation (e.g. 0.01 rad/s at 1000 rpm). Test results obtained from the velocimeter developed here indicate that the velocity variations can be reliably resolved to a precision of 0.005% of mean value.

An encoder (Fig. 2) comprises a glass disc which is rigidly connected to the input shaft. The disc has a precision pattern that is photographically imprinted, containing areas that are clear and areas that are opaque. A light beam passing through the rotating disc will illuminate the pattern, and behind the disc a photo-sensor will produce a corresponding on-off output signal. By focusing light into a very narrow beam, a very high resolution of thousands of pulses per turn can be obtained.

In optical encoders one is concerned with two kinds of accuracy: bit-to-bit and absolute.

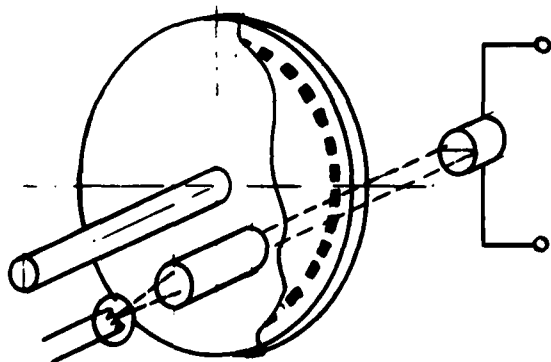


Fig. 2 - Schematic of an Optical Encoder

The first refers to the distance between adjacent bits, the latter refers to the actual shaft position. It is not unusual to obtain from some of the encoder series the following characteristics of accuracy:

- bit-to-bit arc sec RMS 2
- absolute arc sec RMS 4

Let us assume now, for the sake of simplicity, that the absolute error values taken over the entire circle of bits form a pure sinusoidal pattern with the integer number 'k' of complete cycles and with the magnitude of σ_k arc sec RMS. While steadily rotating, the encoder reading vs. actual shaft position would contain an erroneous sinusoidal component of $1.4\sigma_k$ amplitude of displacement and of ' kf_r ' frequency (where $f_r = \text{rpm}/60$ - rotational or fundamental frequency).

Since the actual error pattern of any shape is converted by a steady rotation to a periodic function ($T = 1/f_r$), the encoder reading error may be represented by a sum of its Fourier components $\Sigma(1.4\sigma_k \cdot \text{SIN } 2\pi k f_r t)$ with the total RMS level of the error equal to:

$$\sigma = \sqrt{\sum_{k=1}^{\infty} \sigma_k^2} \quad (1)$$

In order to comply with 0.01% (or 10^{-4}) accuracy in velocity variation, each of the error component σ_k (in RMS of displacement) has to satisfy the following self explanatory relationship:

$$\begin{aligned} \sigma_k &< \frac{1}{2} (10^4 \cdot \omega_r \cdot 57.3 \cdot 3600) / 2\pi k f_r \\ &= \frac{15}{k} \text{ arc sec} \end{aligned} \quad (2)$$

With this in mind let us have a look into the given absolute error of 4 arc sec RMS. Typically the error is spread among harmonics in a way in which the higher the order the lower the amplitude, and amplitudes of sufficiently high harmonics decay faster than in inverse proportion. Thus, a reasonable estimate for error components would be an expression

$$\sigma_k < \frac{4}{k} \text{ arc sec} \quad (3)$$

Since the estimated errors (3) are well below allowable values (2), such an encoder is expected to meet the accuracy requirements.

Another important characteristic is the resolution of the encoder or, in other words, the number of pulses produced per one turn. The resolution determines the highest frequency of vibration component which still can be sensed without distortion. A discretization procedure, such as employed in an encoder,

imposes a condition called the Nyquist-Kotelnikov rule. It means that the number of data points (pulses in our case) to be taken per one cycle of the highest frequency component of interest, must be larger than 2. Practically, it is recommended to keep the number at least equal to 4.

If 'n' is the order of the highest harmonic of interest, the resolution N of the proper encoder must be $N > 4n$. Thus, for a sensor with 10 to 1000 Hz frequency range, to the fundamental component of 10 Hz corresponds the upper possible order around 100. Then, $N > 400$. Some of the commercial encoder series offer wide ranges of counts per turn (typically up to $(5-12) \times 10^3$), that practically covers any of possible need.

Another fact about 'N' appears to be important. Computer algorithms of the Fast Fourier Transform (FFT) operate with blocks of data points equal to an integer power of 2. If the number of counts per turn of the encoder is also some integer power of 2, the computer will always acquire a signal length of integer number of complete turns. This synchronism permits averaging of readings through a number of revolutions, to yield accurate results at precise multiples of the fundamental frequency while rejecting other vibrations. Encoder manufacturers nowadays include such numbers as 256, 1024 and others of power of 2 to their standard specification of disc resolution.

An example of the encoder, which meets the foregoing requirements, is BEI 670-series optical incremental encoder with hollow shaft of 2" dia. The pass-through configuration eliminates any interference with the power train, and relieves the encoder from any torque load when installed in any intermediate part of the shaft. If a proper flexible coupling is employed, it also relieves the encoder from excessive radial and axial loads. By limiting the forces to 10 lb, a sufficient bearing life of 3×10^9 rev and an absolute accuracy of 4 arc sec RMS are achieved.

Converter. An FM discriminator is another important part of the velocimeter with regard to precision, stability and simplicity. Time intervals between encoder output pulses are to be measured with a resolution around 1 part per 10,000 and linearity must be on the same order.

A possible solution may be based on a digital timer-counter technique with sufficiently high base frequency (like 200 MHz for 20 kHz carrier) and with properly configured interface to a computer. A significantly less sophisticated solution has been proposed by employing an integrated circuit module for the frequency-to-voltage conversion along with a simple filtering network.

The DATEL VFV-100K universal voltage-to-frequency and frequency-to-voltage converter

is an example of a module with adequate performance. The VFV-converter has a resolution of better than 1 part in 10,000 and a non-linearity between 0.05 and 0.005%. The linearity holds down to zero input, resulting in wide dynamic range of 80 db. The wide carrier frequency range of 0 to 100 kHz covers practically any combination of encoder resolution and speed (like 1024 counts/turn at about 6000 rpm).

The output signal of the F/V converter contains three parts:

- DC component proportional to the mean carrier frequency (mean speed of rotation);
- AC component proportional to the FM-modulating signal (torsional vibration);
- carrier frequency output ripple.

Due to substantial differences between the AC (below 1 kHz) and ripple (above 5-10 kHz) frequencies, an enhancement of the AC part is only a matter of conventional filtering techniques.

Output ripple of the F/V converter can be made arbitrarily low by using an external filtering capacitor as a feedback (Fig. 3a). However, this also slows down the output response time (Fig. 3b) affecting the AC components of interest. A proper trade-off is achieved by employing a subsequent network.

An example of the signal recovery network, which has been incorporated into the velocimeter with 1024 counts/turn for 500-5000 rpm, is shown in Fig. 4. The preamplifier part takes care of the ripple-to-signal ratio reduction in order to ensure the required amplifier resolution. The amplified signal is subsequently transferred to the computer input through an antialiasing filter, where the ripple component is completely eliminated.

The VFV-100 with a conversion factor of 0.1 v/kHz will output, say, 2 v DC from an input train of 20 kHz (1200 rpm, 1024 counts). The external feedback capacitor of 0.01 μ F will output 500 mv of ripple (Fig. 3a) to be compared with only 0.2 mv of AC component to be resolved (remember 0.01% of 2 v DC). On the other hand, the time constant of 0.1 ms (Fig. 3b), or 1600 Hz cutoff, leaves room to employ more filtration.

The next cascade simply eliminates the DC part, and then the third cascade once again forms a low-pass filter with 1600 Hz cutoff, thus reducing the total bandwidth to about 1000 Hz level. On the other hand, the ripple amplitude now exceeds the signal at most by 40 db which is compatible with characteristics of a typical amplifier (say, linearity of 0.01%, common mode rejection of 120 db, input noise below 10 μ v).

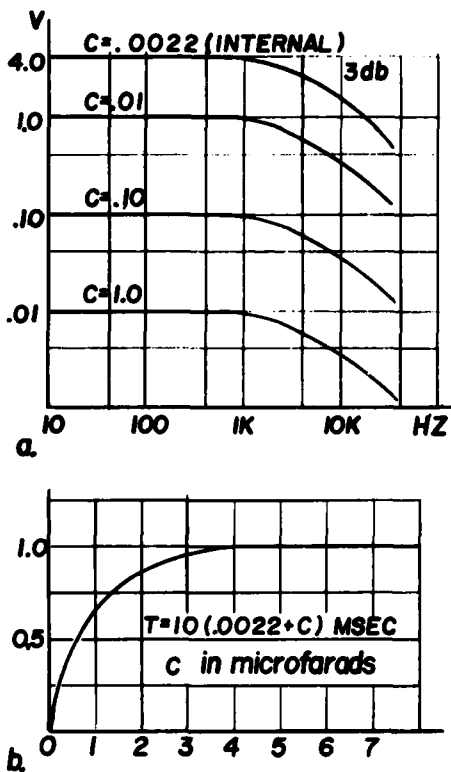


Fig. 3 - Characteristics of the F/V converter: a - peak-to-peak output ripple vs. input pulse rate, b - normalized output vs. time in multiples of the time constant

The remaining part of filtering is performed by the antialiasing filter. 48 db/octave slope and 2 kHz cutoff setup will finally provide for signal-to-ripple ratio to better than 80 db. The actual test proved that a signal as low as 1 part in 30,000 of DC component may be recovered by this network accurately to 5%.

It is worthwhile to note, that by branching the F/V output (prior to the first RC cascade in Fig. 4), and utilizing a low-pass network, the DC and low frequency signal can be easily obtained in addition to the three other outputs. This new output, if needed, can be used as a conventional tachometer.

Performance. Among several important advantages of the new velocimeter, one is its ease of calibration. Usually the more precise is a transducer, the more careful and tedious is its calibration procedure. Highly accurate external mechanisms and/or alternative reference devices are usually involved. This is not the case with the new velocimeter.

Indeed, the calibration factor 'k', as a ratio of the input velocity ' ω ' in rad/s to the output voltage 'V' can be expressed as a product of two factors:

$$k = \frac{\omega}{V} = \frac{\omega}{F} \cdot \frac{F}{V} \frac{\text{rad/s}}{V}$$

Where: $F = N \cdot f_r$ - carrier frequency
 N - encoder resolution in counts/turn
 $f_r = \omega/2\pi$ - frequency of rotation

The first is the encoder conversion constant which is readily seen to be equal to $2\pi/N$.

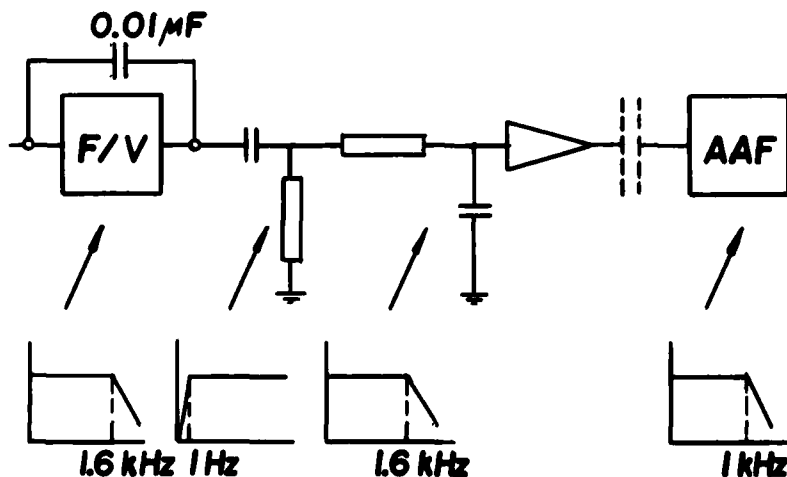


Fig. 4 - Schematic of the recovery network

It does not require any calibration since 'N' is known. The second multiplier represents a conversion constant of the recovery network. Electronic instruments are the only means required to establish and adjust this constant to any desired degree of accuracy. Hence, the calibration of the velocimeter is reduced to the procedure of tuning the electric circuitry, which is easily performed on site.

Accuracy of the new velocimeter has been intensively studied [1]. High linearity of the device is only violated at low signals, namely those comparable to the residual readings (so called null-errors) due to imperfections of the device. Studies have demonstrated that a null-error for any harmonic above the fundamental is well below 0.005% of mean rotation velocity. That confirms the anticipated performance evaluated above.

The null-error at the fundamental frequency is sensitive to excentric rotation of the encoder ball bearings. Improper means of encoder coupling increase the error to 0.2-0.3%. A sufficiently flexible coupling is one which reduces forces transferred to ball bearings to a level below 10 lb. On the other hand, the coupling must be torsionally stiff to avoid any resonance in the frequency range of interest caused by interaction with the inertia of the encoder rotor.

A coupling, configured to fit inside the 2" hollow shaft of the BEI-670 encoder, which flexibly couples this shaft to the 1-1/8" pass-through drive shaft, is shown in Fig. 5a. This coupling employs a diaphragm type principle. It is designed to compensate for relatively small residual angular misalignment, provided that fabrication tolerances of the assembly shown in Fig. 5a do not exceed .002-.003". With such a coupling the fundamental null-error has been reduced to 0.006-0.007% of mean rotation velocity, and no resonance within 900 Hz range was observed. The coupling is also important to ensure the specified ball bearing life.

Another method of coupling the sensor to a drive train is to use a rigid attachment to the shaft and a flexible suspension coupled to the base (Fig. 5b). Again, this suspension must be torsionally stiff, however this time much stiffer since it works against larger inertia of the entire housing.

Further improvement in accuracy is achieved by using a special encoder with an additional optical pickup station. The station is located 180 mechanical degrees away from the primary pickup and produces a secondary output. While the torsional signal appears precisely the same at any readout station, a null-error at every odd harmonic comes out from the primary and secondary outputs in counterphase. By simple summation of the two analog outputs a compensation for the largest (fundamental) null-error as well as for other odd harmonics

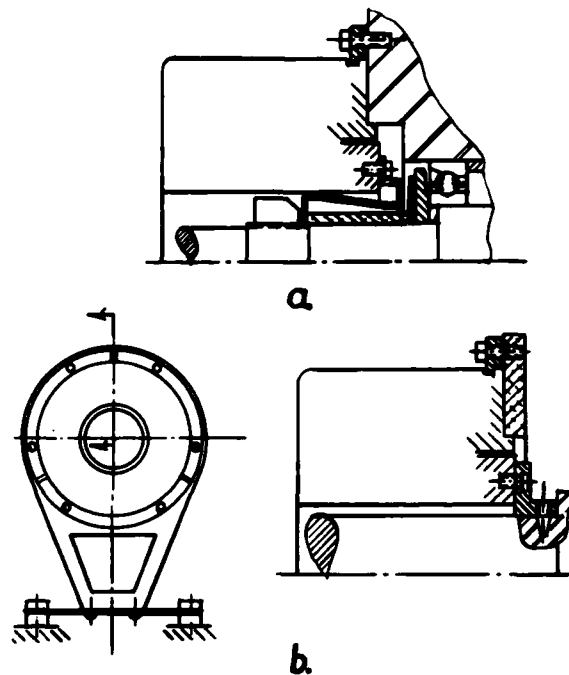


Fig. 5 - Installation of the Velocimeter with a Flexible: a) rotor coupling or b) housing suspension

is achieved. Accuracy of 180° shift is equal to less than half of one count. For the encoder of 1024 counts/turn the shift-error is less than 0.17° . For the harmonic order, say 101, the error becomes about 17° which is still good for compensation.

With the above improvements the threshold level of the velocimeter is within 0.005% of mean rotation velocity.

SIGNAL PROCESSING

Waveforms of the gear fault related torsional vibrations and their spectral representation are schematically shown in Fig. 6. Along with the fundamental pinion component (1P) and its harmonics (2P, 3P ...) there exists the corresponding series of ring gear harmonics or orders (1G, 2G ...) caused by pitchline runout. Some of the harmonics might be more pronounced due to special reasons. Examples are: - influence of the bolt holes in the ring gear body ($1G \times$ number of holes), - appearance of the "ghost" component embedded by the gear machining process ($1G \times$ index wheel teeth).

Tooth meshing components (1TM, 2TM ...) represent "mesh noise" and appear at frequen-

cies that are multiples of the number of teeth. Each of the TM components is surrounded by sidebands. Because of nonlinear interaction between excitations through the tooth loading, a modulation effect occurs and gives rise to a pair of sidebands [3]. Difference in orders between central (TM) and side components is exactly equal to the order of the low frequency error. If, say, the modulation is caused by the fundamental component (IP), the difference is one order, and the side components will be $TM + 1$, where TM is equal to number of pinion teeth. As a result, the energy induced by the tooth-meshing error is spread along the bandwidth, thus the error is no longer quantitatively represented by TM-orders alone [4]. Other related orders also have to be considered.

The prime objective of the data processing system is to identify the conjugate deviation components. The best diagnostic tool is to apply the pinion and gear order analysis. Sometimes, along with the FFT, it is also advantageous to reduce data in the time domain. Such is a case of sharp impacts referred to in Fig. 6 as "nicks". The energy of a sharp impulse is spread between a wide band of harmonics in the frequency domain, without leaving any distinct features of the "nick". One is better off by applying, say, convolution or other digital filtering techniques to the waveform signature, along with time domain averaging. This will allow enhancement and extraction of impact events of a periodic nature.

An efficient and accurate method to computerize order analysis is to digitize the analog signal at an external sampling rate, this rate being controlled by an encoder angularly locked to the rotating shaft of interest [5]. The encoder produces a number of pulses per revolution equal to some interger power of 2. Thus, a block of data which contains - a) a number of data points equal to an interger power of 2, and - b) an interger number of fundamental periods (or revolutions), can be easily acquired. These two conditions are sufficient to obtain a "leakage free" Discrete Fourier Transform, therefore harmonics caused by gearing action can be accurately identified.

Normally, one would acquire certain number of data blocks, each containing a number of data points satisfying the above two conditions. To eliminate random scatter, these blocks would be accumulated by averaging in time domain with subsequent FFT processing or, alternatively, would first undergo FFT and then be accumulated by averaging in the frequency domain.

However, substantial complications are encountered in the gear-related data processing of the frequently occurred cases of a so called "hunting tooth". The "hunting tooth" means that the gear teeth constitute a mutually

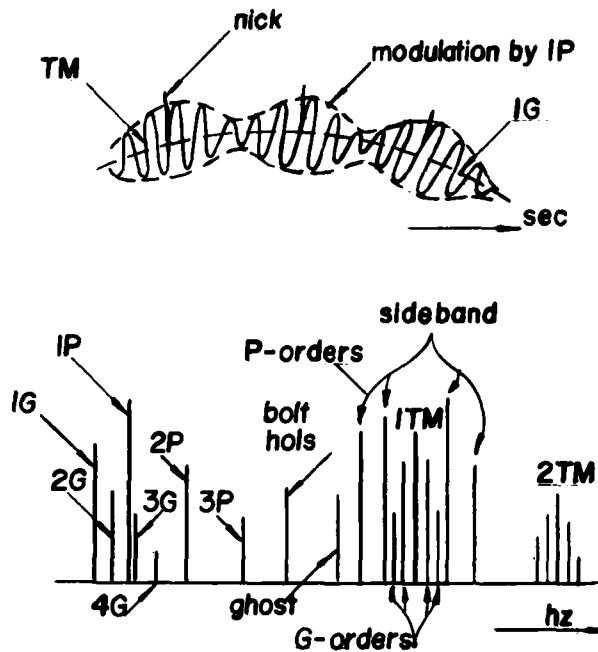


Fig. 6 - Typical components of conjugate error

prime set of numbers, for example 12 and 37, which implies that the same pair of teeth will contact again only in exactly 37 pinion, 12 ring gear revolutions. Whenever such an arrangement is kinematically allowable, it is also preferable because of a number of advantages.

A quieter gear set is obtained since part of the energy, induced by a conjugate error, is shifted toward low frequencies, practically out of the vibration range. Furthermore, through contacting virtually all of the mating teeth, wear tends to mitigate distortion introduced by a "bad" tooth. This is contrary to aggravating the distortion (imprinting) when only a few mating teeth are permanently in contact. Additional advantage is achieved from the fact that many of the pinion and gear spectral components do not coincide, thus indicating distinctly the source of the error (e.g. $1P \neq 3G$ in case of 12 & 37 teeth, contrary to the 12 & 36 teeth case).

Let us return now to the complications in the data processing caused by the "hunting tooth". The example of 12 & 37 teeth will again be used throughout the discussion.

First, in order to eliminate a possible influence of the periodicity inflicted by the same pair of mating teeth on harmonics of interest, data points must be acquired over

the time interval which contains an integer number of these periods (at least, one set of 37 pinion revolutions).

Second, a data block consisting of an integer number of pinion revolutions generally does not contain an integer number of ring gear revolutions. Remember that both conditions are of prime importance to obtain "leakage free" (accurate) Fourier transform. The shortest acceptable data block is one which covers 37 consecutive pinion revolutions: it also contains exactly 12 ring gear revolutions. Thus, real time data acquisition of a number of consecutive shaft revolutions is required.

Third, such a data block, directly acquired through a sampling rate synchronous with the shaft rotation, will contain a number of data points never equal to an integer power of 2. The reason for that is simple: 37 is not an integer power of 2. Therefore, the necessary condition for FFT is not satisfied.

There exists an algorithm (Fig. 7) which allows meeting all of the three above conditions.

A block size of 2^n data points is defined, 2^n also being the number of pulses per pinion revolution, generated by the external device. The analog conjugate gear error signal is sampled, digitized, and entered into the block only at every 37th pulse of the external pulse train. Therefore, it takes 37 rotations of the pinion to fill 2^n entries into the data block. It also takes exactly 12 complete revolutions of the gear.

The remainder of the procedure is obvious. FFT is applied to the whole 2^n -point block. The pinion order spectrum now consists of FFT components located at position 37 and multiplies thereof (74, 111, ...). Positions 12, 24, 36, ... in the FFT will form the gear order spectrum. The fundamental tooth mesh order (1TM) is common to pinion and gear orders, being the $37 \times 12 = 444$ th FFT component.

The only concern left is to select the resolution 2^n of the data block and, respectively, of the external encoder, sufficient to represent without distortion the highest harmonic of interest. According to the already mentioned Nyquist-Kotelnikov rule, the number of data points, taken per one cycle of the highest harmonic, is recommended to be at least equal to 4. If, for example, the spectrum of interest is limited to the second tooth-mesh component with the side band: $2TM + 3 = 27$ in terms of pinion orders, the total number of points acquired in 37 revolutions must exceed $37 \times 27 \times 4 = 3996$, and $2^n = 4096$ is the resolution suitable for this case.

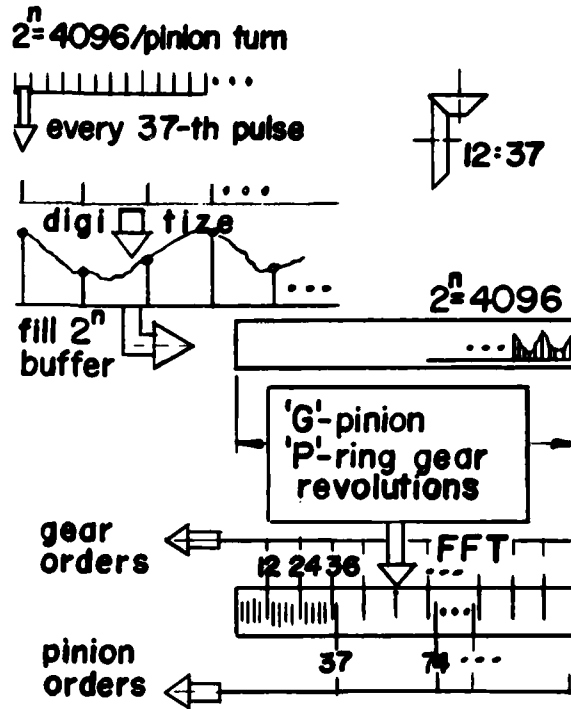


Fig. 7 - Algorithm of separate pinion and ring gear order analysis

DYNAMIC RESPONSE

The torsional signal, accurately transmitted and processed, is not yet directly related to the conjugate error. The relationship between the signal and the source is determined by the transfer function of the mechanical system, the encoder mounting fixture included. Therefore, the correction of the pinion and gear order components by the proper transmissibility factors is required.

In order to establish quantitative transmissibility characteristics of the mechanical system by conventional experimental methods, one would normally introduce the exciting force of a known level in the frequency range of interest. This becomes an exceedingly difficult task for the gear drive train. The gear set would have to be in place since the gear ratio determines the dynamic characteristics of the train. The forcing function would have to be applied in the vicinity of meshing gears and, preferably, during rotation, since the damping factors may be different.

A more natural method of excitation is devised, one which employs a conjugate error of the gear set itself. The method does not require any additional facilities, providing the speed of rotation can be varied. By measuring a few properly selected spectral

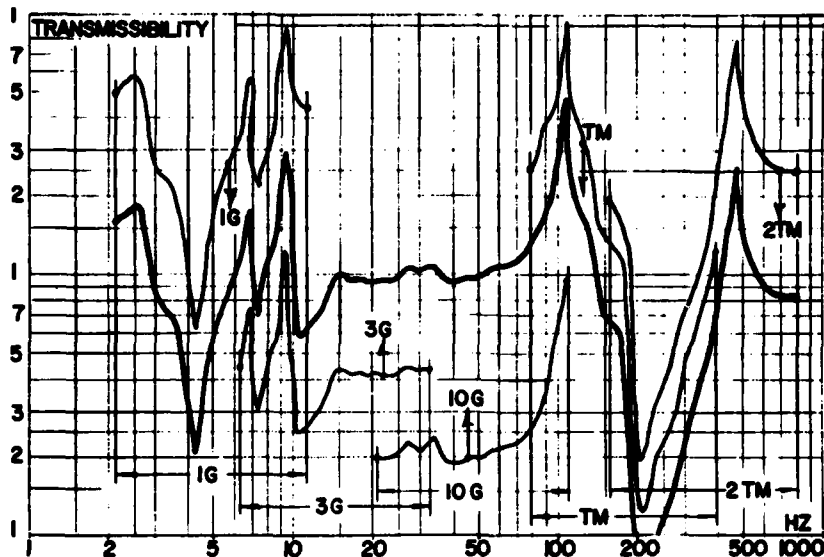


Fig. 8 - Calibration of dynamic response by matching of selected spectral components

components, while varying speed of rotation, and by sequential matching the overlapped parts of the response, the normalized transmissibility curve can be experimentally obtained. The quantities furnished by the curve directly relate both the error and the signal components to each other as a function of their frequency.

In more detail the method is illustrated in Fig. 8 in reference to the 12:37 gears assembled into some mechanical setup.

First, the range of variable pinion rpm from 400 to 2000 is selected suitable for running this particular system. Therefore, each single component will cover a frequency range of 5.

Next, a few prominent spectral components are selected to be spaced in frequency ratios of less than 5 (preferably, 3 to 4), thus the frequency ranges of adjacent components will overlap. The lowest is the gear fundamental component 1G, which at 400 rpm determines 2.2 Hz as the lowest frequency of the response curve ($400/60 \cdot 12/37 = 2.2$), and reaches 11 Hz at 2000 rpm. Other components and reasons for their selection are as follows:

- 3G, which is preferred here to the almost coinciding 1P as less susceptible to the drive motor noise at sensor location;
- 10G, which happens to be pronounced because of the 10 bolt holes in the ring gear body;

- TM, that is 37G, as being properly spaced (3.7 times) from the previous one;
- 2TM, which at 2000 rpm determines 800 Hz as the highest frequency of the response curve ($2000/60 \cdot 2 \cdot 12 = 800$).

Then, the system is tested over the speed range of interest, each of the selected components is measured as the angular displacement vs. frequency and plotted in logarithmic coordinates. An absolute value of the scale factor for each of the plots can be chosen arbitrarily. In Fig. 8, for example, both the 1G and the 2TM plots look quite similar but they cover very different ranges -- 60 to 900 and 0.4 to 8 arc sec, respectively. This simply reflects the fact that the various error components introduce different levels of excitation.

In order to reduce the result to a uniform level of excitation throughout the entire frequency range, all of the five plots are combined into one by matching the overlapped portions of information. In case of discrepancies between adjacent overlapped portions, any method of curve fitting would be helpful.

Finally, the combined response have to be normalized using a portion where transmissibility is known. Usually at frequencies below the first source-to-sensor resonance the response is merely determined by the inertia distribution between the pinion and gear shafts. In this example, the response at 15 to 50 Hz range (just above the isolation related low frequency resonance) was assigned to unity, since the opposite shaft inertia was

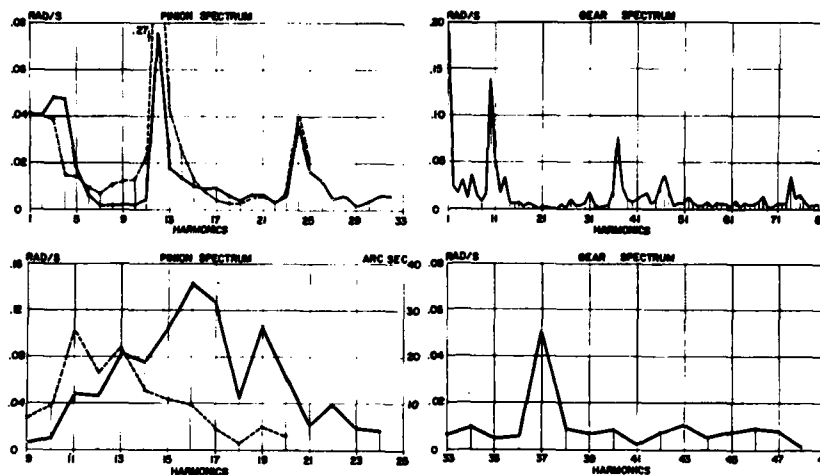


Fig. 9 - Case of 12:37 gear set studies

intentionally enlarged by a flywheel. Thus, 3G amplitude is taken as reference, 1G and 10G are obtained from it by overlap, from which TM and then 2TM are similarly matched.

ILLUSTRATION

Fig. 9 shows some output results with respect to the 12:37 gear and the setup which is characterized by the dynamic response as per Fig. 8. The results are selected to illustrate the above concepts of gear error measurement.

The pinion fundamental component occurs at 26.5 Hz, corresponding to the 166 rad/s of rotation velocity (1590 rpm). Since the level of 0.01 rad/s can be distinctly observed in the graphs, the resolution is containable within the goal of 1 part in 10,000. Both the pinion (Fig. 9a) and the gear (Fig. 9b) order spectra exhibit prominent characteristic components:

1P to 5P, TM, $TM \pm 1P$, 2TM, $2TM \pm 1P$ and

1G, 10G (bolt holes), TM, $TM \pm 1G$, $TM \pm 6G$, $TM \pm$ bolt holes (27 & 47), 2TM.

A dashed line in Fig. 9a relates the pinion spectrum to the source of the error as a result of applying the transmissibility factors. Some of the components undergo significant changes. Thus, the 12-th order (318 Hz) increases 3.7 times because of its proximity to the node around 210 Hz in Fig. 8. Contrary to that, the 4-th order decreases 3.5 times since it closely approaches the 108 Hz resonance.

After the correction is applied, it is easy to obtain any of the components in arc sec of angular displacement, if the conjugate error is of a prime concern. For instance,

the tooth-meshing component (12P) of .27 rad/s represents:

$$0.27 \cdot 57.3 \cdot 3600 / (2\pi \cdot 26.5 \cdot 12) = 28 \text{ arc sec - as related to the pinion shaft;}$$

or

$$28 \cdot 12/37 = 9 \text{ arc sec - as related to the gear shaft.}$$

Another case of 12:37 gear set is shown in Fig. 9c, d as partial view on the tooth-meshing order with the sidebands. The only prominent component of the gear order spectrum is the 37G (TM), whereas the pinion orders have rather peculiar form. However, the dashed line graph in Fig. 9c, which represents the corrected and also translated into seconds of arc spectrum, exhibits a typical picture of significant modulation. Indeed, the pinion fundamental component, which happened to be very pronounced in that case, gave rise to the sidebands. The 11-th and 13-th orders (that is $TM \pm 1P$) of 25 and 23 arc sec respectively, are especially strong. They exceed even the prime TM component, that is the 12-th order of 17 arc sec magnitude.

This case illustrates a very good separation of pinion and gear orders, and subsequently, separation of their respective causes. The case also confirms that the TM-orders alone may not be representative of the tooth-meshing error. Energy of the error may be drained to the sidebands, subject to how deep is the modulation.

CONCLUSIONS

A drive train whose dynamic response has been calibrated, a novel sensing device, and a signal processing algorithm described in this paper, form the basis of a powerful measuring technique applicable to gear trains. In measuring the conjugate error of a gear set, output data capable of separating pinion from gear order spectra are obtainable.

Mechanical implementation of this technique, including sensing instrumentation, is relatively simple, being based on commercially available components. No external devices are needed to provide excitation for purposes of establishing the dynamic response of the test system. All necessary information is obtained by varying the speed of rotation of the system.

While simple to implement, the technique is very effective in supplying accurate measurements. When used with a properly configured computing system, preferably with one which includes an array processor, data acquisition and processing time may be as short as 3 seconds. The technique is proven for on-line field application [2] with results that have shown 95-98% correlation with conventional laboratory measurements.

It should be pointed out that the newly developed angular velocimeter is not limited to gear related measurements. It may be profitably utilized in many applications concerned with torsional oscillations. The principle employed to calibrate the dynamic response on the basis of excitations internal to the system is likewise not limited to gears. Ball bearings, belt transmissions, turbine wheels, and the like may be utilized as natural sources of excitation for purposes of calibration of torsionally as well as linearly vibrating systems.

REFERENCES

1. Milenkovic, V. Shmutter, S., "An Angular Sensor for Transmission Error Inspection", Transactions 1982, Vol. 91, Section 1, pp. 202-220, SAE, 1983.
2. Milenkovic, V. Shmutter, S., Field, N., "On-Line Diagnostics of Rear-Axle Transmission Errors", Computer Integrated Manufacturing, H00288, pp. 101-109, ASME, 1983.
3. Brovman, J. S., Demirchian, K. S., Shmutter, S. L., "Diagnostic of Vibration Sources in Electric Motors", Electro-technica, No. 1, 1973 (in Russian).
4. Remmers, E. P., "Gear Mesh Spectra for Arbitrary Tooth Spacing Errors, Load and Design Contact Ratio", ASME Journal of Mechanical Design, Vol. 100, pp. 715-722, Oct. 1978.
5. Braun, S. G., Seth, B. B., "On the Extraction and Filtering of Signals Acquired from Rotating Machines," Journal of Sound and Vibration, 65(1), pp. 37-50, 1979.

ACKNOWLEDGEMENT

The author would like to thank Dennis Schafer, Michael Stolnicki, and Ming Loo of Ford Research Staff for their contribution to the experimental work.

DISCUSSION

Mr. Volin (Shock & Vibration Information Center): What was the source of the carrier ripple frequency in the measurements of the gear vibration?

Mr. Shmutter: By carrier, do you mean the carrier frequency fluctuation?

Mr. Volin: No. There was a ripple frequency. What was that due to?

Mr. Shmutter: It is the number of pulses per turn. You rotate the encoder, and if the velocity is steady, it just produces a two kHz pulse. You have 1,024 pulses per turn, and you may rotate it at 1,200 rpm. So, you have a frequency of 20 Hz multiplied by 1,000 pulses per turn, and you get a 20 kHz pulse rate. This produces the ripple. When you demodulate the signal, you recover your torsional vibration which is below one kHz. But, the 20 kHz is a carrier frequency, so you want to get rid of it. That is what I mean by carrier frequency ripple.

Mr. Volin: Could this system be used to detect gear meshing problems? Could it also be used for machinery health condition monitoring? This looks like it might be one very good application, particularly since you have a non-contacting measurement scheme. Trying to recover gear signatures from just monitoring or measuring the vibration at the bearing caps is difficult.

Mr. Shmutter: That is true. Yes, I share this with you. Although we use it for the diagnostic on the production floor, this technique can be used for machinery conditioning monitoring as well, especially in the way I presented it here. I extracted from our machine the simple solution and presented here to be used in other applications. One application is base-line monitoring or something like that which you just mentioned.

THE ANALYSIS BY THE LUMPED PARAMETER METHOD OF BLADE PLATFORM FRICTION DAMPERS USED
IN THE HIGH PRESSURE FUEL TURBOPUMP OF THE SPACE SHUTTLE MAIN ENGINE

R. J. Dominic
University of Dayton Research Institute
Dayton, Ohio

Premature cracking of the first stage turbine blades in the high pressure fuel turbopump of the space shuttle main engine could be alleviated by redesign of the platform friction dampers that are used to reduce the vibration response of the blades. Analytical studies, by the lumped mass method, of friction damper effectiveness have been performed. Methodologies used in the program are described. Results show that the effectiveness of the blade platform dampers can be increased if the operating parameters of the system can be defined.

NOMENCLATURE

- A, D - peak deflection amplitudes of the inboard and outboard modal masses, respectively, of the lumped parameter blade
- E - engine order of the excitation forcing function
- f_1, f_2, f_3 - resonant frequencies for the first three flexural modes
- k_1, k_2 - modal stiffnesses of the outboard and inboard flexural springs of the lumped parameter blade
- m_1, m_2 - modal masses of the lumped parameter blade
- N - normal force holding two surfaces together
- n - total number of blades in a bladed disk
- S - peak amplitude of the forcing function
- t - instantaneous value of time
- x, \dot{x}, \ddot{x} - instantaneous values of the deflection, velocity, and acceleration of a modal mass
- α, γ - phase angles associated with A and D, respectively
- δ - phase angle associated with S for a particular blade
- η - loss factor of the lumped parameter blade
- θ - relative blade to blade phase angle of a tuned system
- μ - coefficient of friction
- v - blade number
- ω - $2\pi f$, the angular velocity
- 1, 2 - subscripts for the outboard and inboard blade parameters, respectively

1. BACKGROUND

The space shuttle main engine (SSME) is a reusable, high performance, liquid-propellant rocket engine with variable thrust. Each of the three SSME's used on the orbiter vehicle is rated at 375,000 lb. thrust at sea level, 470,000 lb. thrust in vacuum, and is throttle controllable from 65 to 109 percent of rated thrust. Four accessory turbopumps feed the liquid hydrogen

fuel and liquid oxygen oxidizer at high pressure to the injectors of the main burner. The two high pressure turbopumps are driven by steam mixed with hydrogen which is produced by combustion of an over-rich fuel mixture in each of two preburners, one in the fuel and one in the oxidizer supply system. The liquid hydrogen fuel is circulated as a coolant through tubes in the main nozzle and combustion chamber walls, and over the turbine blade necks and through the bearings of the high pressure turbopumps. The SSME's are rated for 7.5 hours of operational life and 55 starts. The standard mission consists of 520 seconds of operation.

The SSME has been very reliable to date except for premature cracking of first stage turbine blades in the high pressure fuel turbopump (HPFTP). The HPFTP consists of a two stage high speed turbine driving a three stage centrifugal pump through a common shaft (See Fig. 1). The shaft is supported at the turbine inlet by a roller bearing constrained by 13 struts attached to the turbine housing. The aft support is provided by a thrust bearing assembly attached to the pump housing. The HPFTP turbine operates at high-speed (28,000 to 38,000 rpm), high-pressure (4,000 to 5,500 psi inlet pressure), high-temperature (2,000°R at inlet), and is rated at 70,000 hp. The two stage turbine assembly is approximately 12 inches in diameter and 12 inches long.

The first stage turbine of the HPFTP consists of a fixed 41 vane nozzle assembly feeding a 63 blade turbine wheel. A schematic of the flow path is shown in Figure 2. The solid blades of the turbine are cast from a superalloy (Mar M 246) and are directionally solidified. The blades attach to the disk with a four-element firtree. They have a short neck, a platform, and a curved airfoil that measures approximately 0.85 inch in both the spanwise and chordwise directions. Interblade friction dampers are constrained in slots below the platform to provide both; (1) a platform seal between the hot driving gas and the blade neck coolant; and (2) damping of blade vibrations through the application of friction forces to the lower sur-

face of the blade platform. The friction dampers are held loosely in the slots below the platforms until turbine spin up occurs. Thereafter they are held tightly against the lower surface of the platforms by the combination of centrifugal force and by the pressure differential between the driving and coolant gases. A photo of two HPFTP first stage turbine blades and friction dampers is shown in Fig. 3.

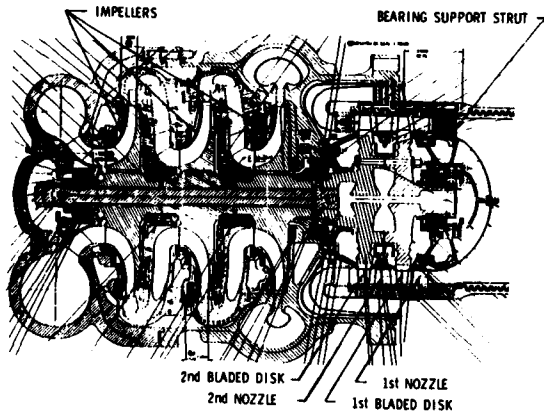


FIG. 1 SECTION, SSME HIGH PRESSURE FUEL TURBOPUMP

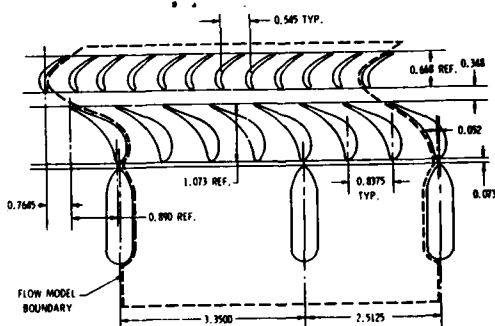


FIG. 2 HPFTP FLOW PATH SHOWING STRUTS, NOZZLES AND TURBINE BLADES, $R = 5.465$

The HPFTP failures have consisted of cracks in the first stage turbine blade airfoils just above the platform, primarily in the leading and trailing edges of the airfoils. Three failures that occurred very early in the engine development program were the most severe and were attributed to:

1. An overtemperature run that welded dampers to some of the platforms, causing platform lockup;
2. An overtemperature run that caused a nickel plate anti-friction coating on the dampers to extrude between platforms, again causing platform lockup;
3. Platform lockup caused by insufficient

clearance between adjacent blade platforms for one turbine build.

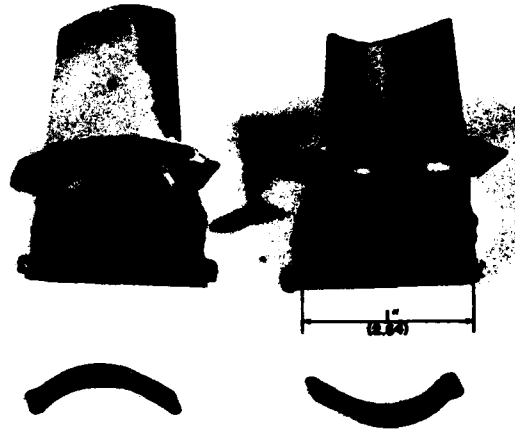


FIG. 3 HPFTP 1st STAGE BLADES AND DAMPERS

Additional slowly growing cracks have been noted in other test stand turbine runs, and have been attributed to lockup of adjacent platforms by overeffectiveness of the interblade friction dampers. This problem has been reduced considerably through a test and development program which has led to reduction of the mass of the friction dampers by a factor of three and also has led to streamlining of the turbopump front bearing support struts.

However, test and analytical studies have been inconclusive in defining the fatigue life of this turbine blade because neither the vibration excitation forcing function nor the blade response, as affected by the platform friction dampers, could be clearly or completely described. The turbopumps therefore have been used for only one or two flights of the SSME.

The critical mode of the HPFTP first stage turbine blade is judged to be the first flex mode of the overall blade with the root firmly clamped at the firtree. Modal analyses have been performed on several blades and show this mode occurs at $4,500 \pm 200$ Hz. The platform dampers installed in this turbine stage have always damped this mode effectively. However, if these dampers lockup adjacent platforms a new flex bending mode of only the airfoil section of the blade occurs at approximately 8,500 Hz. If the platforms become rigidly locked this mode is very lightly damped. As mentioned, previous blade failures have been attributed to just such occurrences. Successful operation of this platform damper thus requires sufficient damping to alleviate the first flex mode resonance condition without inducing an undamped or very lightly damped airfoil alone resonance mode. Both of these modes show maximum alternating stresses at the leading and trailing edge corners of the airfoil just above the platform-to-airfoil fillet radius, the locations where most failures have occurred.

The primary excitation source for blade vibration is the drive gas stream perturbations caused by the wakes from the 13 front bearing support struts and the 41 first stage nozzle vanes. These wakes provide fairly broadband excitation of the turbine blades to an upper frequency of at least 50 KHz. The 13 support struts are each aligned with a nozzle vane and increase the wake effects for 13 of the 41 vanes, as shown in Figure 4. Since the strut spacing is necessarily non-symmetrical a large number of fourier components appear in the flow perturbation pattern frequency analysis. The strongest component occurs at 41 x revolutions per second (41E) which covers the range from 19 to 26 KHz for the operational speed range of the turbopump. This frequency range includes some of the higher modes of the blade. Other components occur at 9E, 11E, 13E, and 15E, which would excite the 4500 and 8500 flex modes of the blade within the operational speed range. The 8500 Hz flex mode of the airfoil alone is excited over a wider speed range and at a higher energy level than the 4500 Hz flex mode of the whole blade. The very low blade damping at rigid platform lockup makes the 8500 Hz mode a potentially high damage mode. The configuration of the front struts has been redesigned to a near optimal streamline to reduce the excitation of the lower vibration modes of the blade but these modes are still judged to be the major causes of blade fatigue damage, with the 8500 Hz mode judged most damaging. However, the level of the excitation has not been well defined and this causes a problem in designing an optimum damper, as will be seen later in the analysis data.

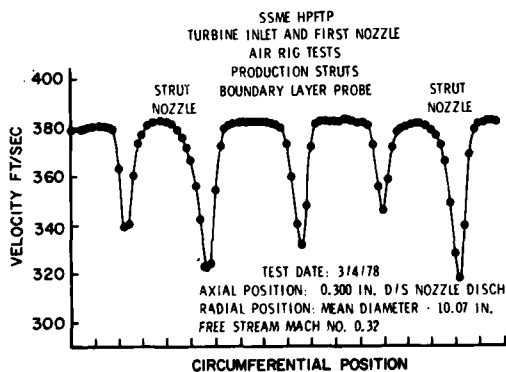


FIG. 4 WAKE PERTURBATIONS CAUSED BY NOZZLES AND STRUTS

2. THE LUMPED PARAMETER (LUMPED MASS) ANALYSIS

The lumped mass program analyzes the blade only in its lower order flexural modes and only for the steady state solution. The blade is represented by two concentrated masses (m_1, m_2) supported in series by two flexural springs (k_1, k_2) with a hysteretic loss factor (η) associated with the springs. The hysteretic loss factor represents the combination of root damping, aerodynamic damping, and material damping in the operating blade. The concentrated masses and flexural springs represent the modal param-

eters of the blade in the flexural plane. The modal parameters for the SSME HPFTP first stage blade can be determined from the resonance equations of the blade in three flexural resonance conditions, as shown in Fig. 5. The resonance frequencies f_1, f_2, f_3 have been measured in test programs as follows: f_1 has been measured by Rocketdyne Division of Rockwell International (RD) in siren tests and by the University of Dayton Research Institute (UDRI) in impact tests; f_2 has been measured by RD in siren tests; f_3 was shown in the RD whirligig test data (Reference 1) on blades with welded platforms and on blades with friction dampers when the dampers greatly limited platform motion. These values are average values for several blades.

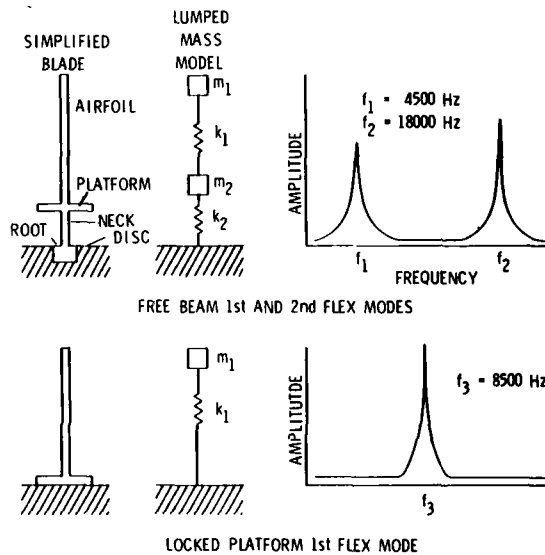


FIG. 5 HPFTP 1st STAGE BLADE FLEX MODES

Three resonance equations can be derived, two for the free blade and one for the platform locked blade, as below.

$$\frac{k_1 k_2}{m_1 m_2} = (4\pi^2 f_1 f_2)^2 \quad (1)$$

$$\frac{k_1 + k_2}{m_2} + \frac{k_1}{m_1} = 4\pi^2 (f_1^2 + f_2^2) \quad (2)$$

$$\frac{k_1}{m_1} = (2\pi f_3)^2 \quad (3)$$

These three equations can be simplified algebraically to state three of the unknown parameters in terms of the fourth as:

$$k_1 = (2\pi f_3)^2 m_1 \quad (4)$$

$$k_2 = \frac{(2 f_1 f_2 f_3)^2}{(f_2^2 - f_3^2)(f_3^2 - f_1^2)} m_1 \quad (5)$$

$$m_2 = \frac{f_3}{(f_2^2 - f_3^2)(f_3^2 - f_1^2)} m_1 \quad (6)$$

Then if m_1 is assigned a value the other three parameters are defined. We assigned $m_1 = 0.027$ pound, then $m_2 = 0.007975$ pound, $k_1 = 5.705 \times 10^7$ pounds/inch, and $k_2 = 2.859 \times 10^7$ pounds/inch. The dimensionless hysteretic loss factor, η , has been assigned values of 0.002 and 0.008 in various computer analysis runs conducted to date.

If a series of these blades are installed in a rigid disk with platform friction dampers between the blades and with airfoil excitation forces imposed, the discrete bladed disk model shown in Figure 6 is evolved. This system is a modal analog of the HPFTP first stage blade disk in the frequency range of 0 to perhaps 20,000 Hz.

The equations of motion for the v th blade in Fig. 6 are:

$$m_{1v} \ddot{x}_{1v} + k_{1v}(x_{1v} - x_{2v}) + \frac{k_{1v}\eta}{\omega} (\dot{x}_{1v} - \dot{x}_{2v}) = S_v \cos(\omega t + \delta_v) \quad (7)$$

$$m_{2v} \ddot{x}_{2v} - k_{1v}x_{1v} + \frac{k_{1v}\eta}{\omega} (\dot{x}_{2v} - \dot{x}_{1v}) + \frac{k_{2v}\eta}{\omega} \dot{x}_{2v} + \mu N_v R \text{ sign}(\dot{x}_{2v} - \dot{x}_{2,v+1}) + \mu N_{v-1} R \text{ sign}(\dot{x}_{2v} - \dot{x}_{2,v-1}) + (k_{1v} + k_{2v})x_{2v} = 0 \quad (8)$$

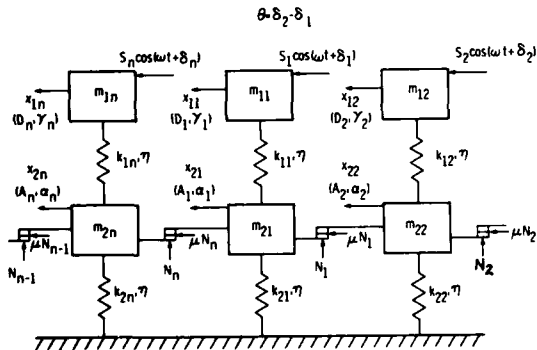


FIG. 6 LUMPED MASS MODEL OF BLADED DISK SYSTEM for $v = 1, 2, \dots, n$, where n is the number of blades in the system. These are a set of nonlinear equations of the second order, the only nonlinear terms representing a Coulomb model of the friction forces on the platform. The previously undefined terms in these equations are the harmonic excitation force, $S_v \cos(\omega t + \delta_v)$, the coefficient of friction, μ , the normal force on the friction surface, N_v , and R is a correction coefficient. The phase angle, δ_v , represents the time lag of a traveling wave excitation around the disk system. This is representative of the spinning blade system passing through pressure disturbances caused by the inlet vanes and shaft front support struts.

This system of equations is solved using the method of harmonic balance. A nonlinear matrix iteration is used to obtain numerical solution (see Reference 3). The solution, obtained by computer, consists of the amplitudes D_v , A_v , and the phase angles γ_v , ϵ_v , for the outboard

(airfoil) and inboard (platform and neck) modal masses of each blade as a function of the system parameters m_{1v} , m_{2v} , k_{1v} , k_{2v} , N_v , S_v , μ , η , and

ω . Since most of the system parameters are input to the computer as arrays, i.e., all the subscripted parameters, many types of mistuned systems can be evaluated. Only solutions for a tuned system have been evaluated to date in this study, specifically, a tuned system with the HPFTP average blade. To vary N , S , μ , or η a series of runs must be made. Analyses have been made with $\eta = 0.008$ or 0.002 , $\mu = 0.19$ or 0.38 , $S = 1, 10$ or 100 pounds, and N equal various values from 0 (the undamped case) to 50,000 pounds (with N appropriate to the other parameters selected).

The usual analysis is a series of computer runs with η , μ , and S constant and N varying from 0 to a selected upper limit in about ten steps. In each run solutions are obtained from a lower starting frequency to an upper ending frequency at fixed increments of the frequency range. The range from 3,000 to 12,000 Hz has been evaluated in 100 Hz increments in most runs since failures at the 8500 Hz mode when platform lockup occurs are of major interest. A few runs from 3,000 to 20,000 Hz have been processed and show that the friction damping is as effective at the second flexural mode of the free blade (18,000 Hz) as it is at the first flexural mode (4500 Hz).

Another controlling parameter of the friction damper performance is the blade to adjacent blade phasing. One would expect that when adjacent blades are in phase no damping by the interplatform friction dampers would occur. Conversely, maximum damping would be expected when the blades are out of phase. The interblade phase angle is controlled by δ_v , the phase shift of the harmonic forcing function $S_v \cos(\omega t + \delta_v)$, and is input to each run as an array. The value of δ_v , the phase angle of the v th blade for a phase tuned system is defined as:

$$\delta_v = \frac{2\pi E(v-1)}{n} \quad (9)$$

where E is the engine order of the vibration mode and n is the total number of blades in the disk. For simplification $n=64$, the number of blades in a synthetic system has been used rather than $n=63$, the number of blades in the actual HPFTP first stage disk system. This allows for considerable simplification and consequent cost savings in the computer runs. The blade to blade phase shift is called phase angle θ . θ is defined as:

$$\theta = \frac{2\pi E}{n} = \delta_v - \delta_{v-1} \quad (10)$$

$$\text{Thus } \theta = \pi = \frac{2\pi 32}{64} = \frac{2\pi}{2} \quad (11)$$

and $n = 2$, a closed two-bladed tuned disk system. Similarly,

$$\theta = \frac{\pi}{2} = \frac{2\pi 16}{64} = \frac{2\pi}{4} \quad (12)$$

a four-bladed disk system and

$$\theta = \frac{\pi}{4} = \frac{2\pi 8}{64} = \frac{2\pi}{8} \quad (13)$$

leads to an eight-bladed disk system. These systems have been analyzed. Future plans include runs of 16 and 32 bladed tuned systems ($E = 4$ and 2 , and $\theta = \pi/8$ and $\pi/16$, respectively). In these tuned systems all blades experience identical deflections at the modal masses (D, A for m_1, m_2) and identical phasing (γ, α).

3. ANALYSIS RESULTS

A sample of program output data for the outboard modal mass is presented in Fig. 7 as a plot of amplitude D versus frequency and a similar set of data for the inboard modal mass (amplitude A) is presented in Figure 8 for the same computer runs. These data sets arise from successive runs of the lumped mass program with the program N array set successively to the values shown in the tables on the figures. The other system parameters for these runs were:

$$\theta = \pi/4 \text{ (8 bladed disk)}$$

$$S = 1.0 \text{ lb.} \cos \left(\omega t + \frac{2\pi(\nu-1)}{8} \right)$$

$$\mu = 0.19$$

$$\eta = 0.002$$

and m_1, m_2, k_1, k_2 , = HPFTP average blade modal values for the tuned first stage disk system.

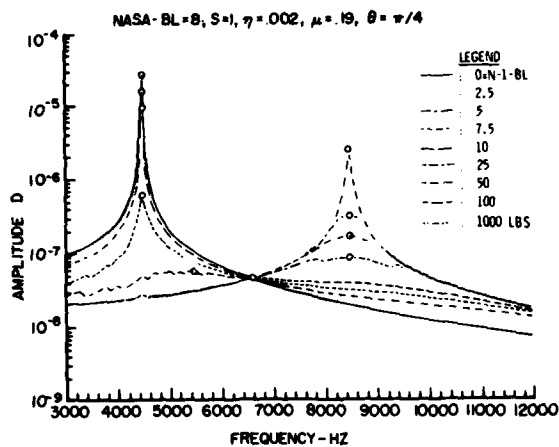


FIG. 7 AMPLITUDE OF HPFTP BLADE MODAL MASS m_1 VERSUS FREQUENCY OF EXCITATION

Figure 7 shows that amplitude D is reduced nearly three orders of magnitude when optimum damping occurs and that it is quite highly damped at 8500 Hz, even for large values of N , the damper normal force. In Figure 8, it can be seen that amplitude A tends to a value at 8500 Hz that is more than three orders of magnitude below the value for the free blade at 4500 Hz. This indicates that the Coulomb friction force is supplying a substantial amount of damping, even for very low amplitude platform motion. This will be discussed in more detail later.

Figure 9 shows the plot of the maximum amplitude of D (airfoil modal mass deflection)

versus the ratio $\mu N/S$, the ratio of the friction force amplitude opposing platform motion to the blade forcing function amplitude. The data points selected for the Figure 9 plot are circled and annotated on Figure 7. Figures 7 and 8 show that the blade vibration amplitude is reduced very quickly by friction damping at relatively low values of N . This fact is depicted very graphically on the D versus $\mu N/S$ plot. Figures 7 and 8 show also that the blade transitions very quickly from the 4500 Hz mode to the 8500 Hz mode at low values of N or $\mu N/S$ and that the minimum response of the blade occurs in this transition region at very near the midfrequency of the region.

$$\text{NASA-BL-8, } S=1, \eta=0.002, \mu=.19, \theta=\pi/4$$

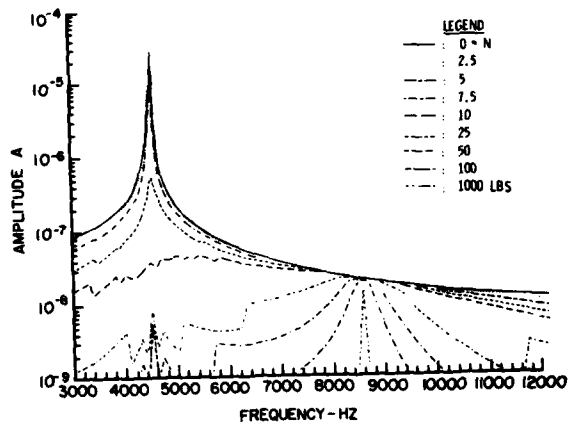


FIG. 8 AMPLITUDE OF HPFTP MODAL MASS m_2 VERSUS FREQUENCY OF EXCITATION

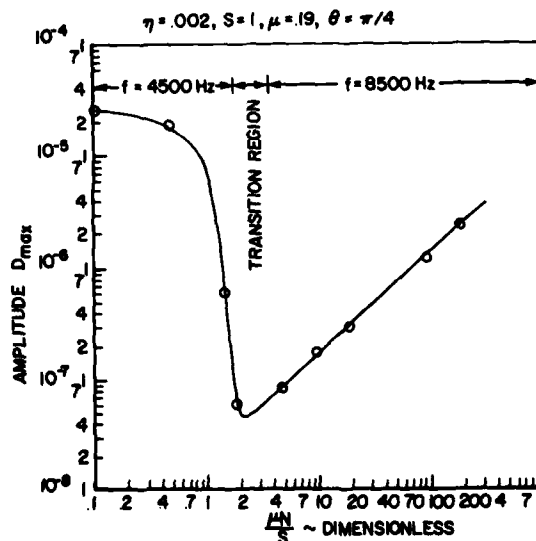


FIG. 9 MAXIMUM AMPLITUDE OF m_1 VERSUS $\frac{\mu N}{S}$

Figure 10 shows the effect of quadrupling η , the hysteretic loss factor, from 0.002 to 0.008 while all other parameters remain unchanged. Figure 10 shows that hysteretic damping is linearly effective in combination with the friction damping at the 4500 Hz modal frequency. After the friction damping forces the frequency into the transition region, however, the effect of the hysteretic damping becomes negligible.

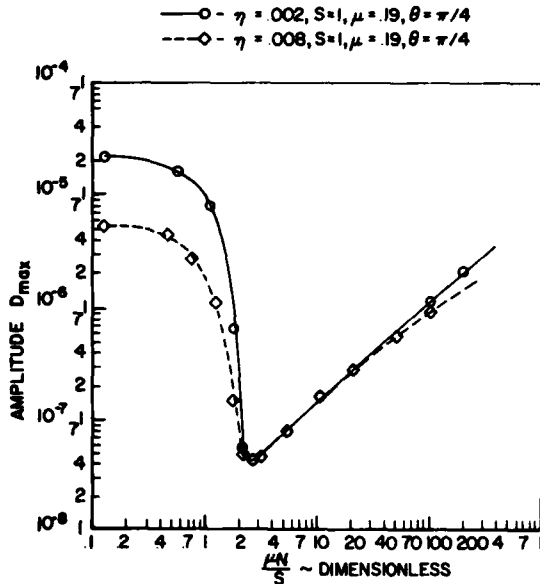


FIG. 10 MAXIMUM AMPLITUDE OF m_1 VERSUS $\frac{\mu N}{S}$, VARIATION IN η

Figure 11 shows the effect of variation of θ , the blade to blade phase angle. It is seen that a larger phase shift between blades up to an equivalent engine order (E) of vibration of $n/2$, produces a higher level of Coulomb friction damping, as expected. However, this is not usually a controllable parameter in an operational turbine, as may be true of most of the other parameters. The figure does show the characteristics of the curves for various engine orders of excitation, and consequently provides useful design or evaluation information. It should be noted that the amplitude reduction possible is the same for all values of θ but at different values of $\mu N/S$.

Figure 12 shows the effect of variation of S , the forcing function amplitude. It should be noted that the three curves shown have identical shapes, but that for an order of magnitude increase in S the D (and A) response amplitudes increase by an order of magnitude. This shows the system to be linear with S and indicates that a unit curve ($S=1$) can be used to define a system. Then, the response amplitude can be scaled by the value of S at any $\frac{\mu N}{S}$ for any operating system having otherwise identical operating parameters.

All the previous data sets represents systems

having a μ (the damper to platform coefficient of friction) of 0.19, a strictly arbitrary value used by UDRI in some analyses for a previous program. A set of computer data was generated for a system having μ of 0.38, double the previous value. However, when a data point for $\mu N/S$ values $\frac{0.38 \times 5}{1}$ was plotted, the amplitude fell identically on $\frac{0.19 \times 10}{1}$, and similarly for all values of 0.19 XN equivalent to 0.38XN. This shows that μ and N are not independent variables, which should be expected as it is a basic tenet of Coulomb friction. This does not mean that it is not necessary to know the values of μ and N and their characteristics throughout the operating temperature-pressure speed regime of the turbine. Instead, the converse is true because they may be amenable to some modification if design problems are encountered, or if, later, operational fatigue problems are encountered that make modification of the system mandatory.

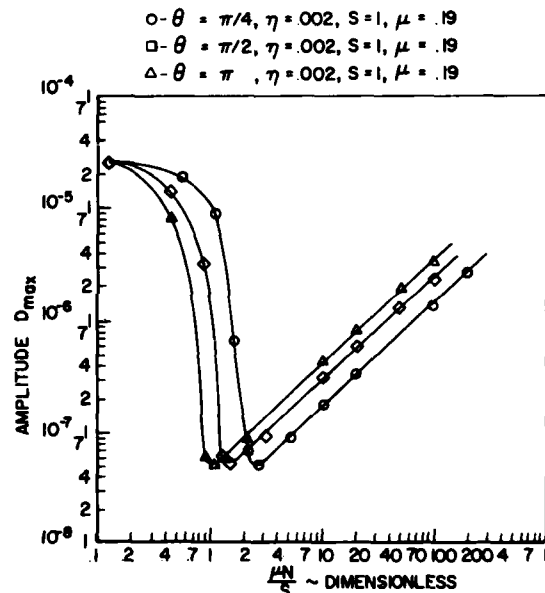


FIG. 11 MAXIMUM AMPLITUDE OF m_1 VERSUS $\frac{\mu N}{S}$, VARIATION OF θ

A weakness of this dynamic analysis is that the Coulomb friction model applies only over a limited lower part of the $\mu N/S$ range. The extent of Coulomb friction damping in the $\mu N/S$ range is affected by the friction surface parameters, the normal forces, and the vibration frequency and amplitude. At some magnitude of $\mu N/S$ Coulomb friction ends and the regime of stick-slip friction begins. The stick-slip regime is followed by the end of slip, the lockup regime, where friction ends and the surfaces are locked firmly together. Important questions for any friction damping system are:

1. Where do stick-slip begin and end? and
2. What are the effects of the stick-slip mode?

The consequence of platform lockup has been

shown to be quite severe for the system under study, being almost immediate failure of the turbine blade. The effect of lockup is not only the loss of friction damping but also the loss of the normally very effective blade root damping. Thereafter, airfoil vibration amplitude at excited resonance modes is limited only by the very low blade material hysteretic loss factor combined with whatever aerodynamic viscous damping is imparted to the blade by the flow of the driving fluid. The outboard blade section effective loss factor is quite likely to be at least an order of magnitude less than that of the inboard blade section.

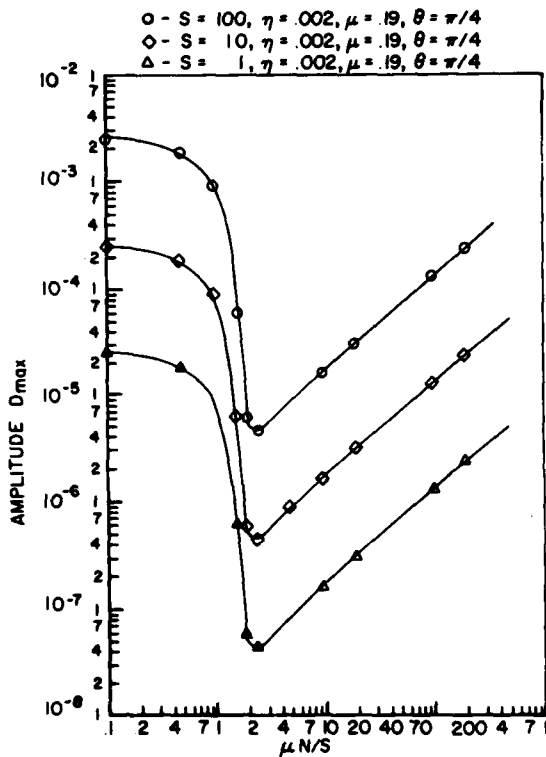


FIG. 12 MAXIMUM AMPLITUDE OF m_1 VERSUS $\mu N/S$, VARIATION OF S

The consequences of stick-slip and lockup have been sketched on a copy of the Figure 9 graph as shown in Figure 13. The Figure 13 data was replotted with linear scales in Figure 14 to emphasize its significance. The location of stick-slip onset and the breadth of the stick-slip range may be very critical to system survival. They are likely to be indeterminable without a careful and costly test program. Such a program may yield only marginally satisfactory results. What is needed is instrumentation data readings during system operation. Acquisition of such data is still beyond the state of the art for some high performance systems, particularly small ones operating at high rotational speeds.

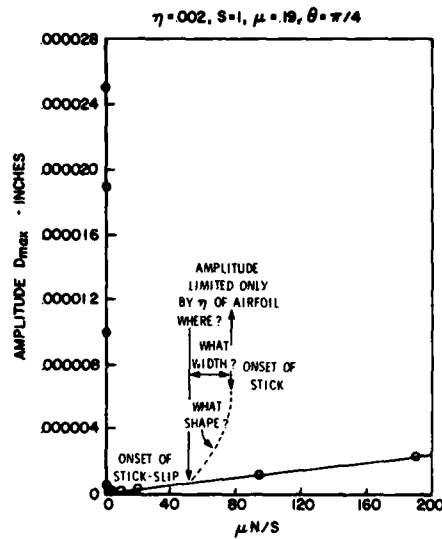


FIG. 13 MAXIMUM DEFLECTION OF m_1 VERSUS $\mu N/S$, EFFECTS OF STICK-SLIP AND STICK

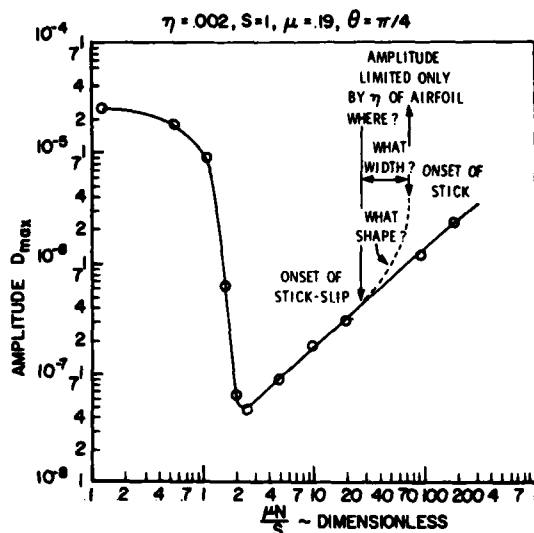


FIG. 14 MAXIMUM AMPLITUDE OF m_1 VERSUS $\mu N/S$ - LINEAR PLOT, EFFECTS OF STICK-SLIP AND STICK

The computer program for the lumped mass analysis of the HPFTP blade has been modified recently to separate the loss factor η into two separate parameters, η_1 and η_2 , to be associated with the flexural springs k_1 and k_2 , respectively. The program results now will reflect the absence of root damping in the blade airfoil section vibration. Additional analysis is in work to evaluate the effects of this change. A follow on paper will be written describing the new analysis and its results.

4. CONCLUSIONS

The following conclusions are drawn concerning the application of the lumped parameter (or lumped mass) analysis to the HPFTP 1st stage blade failure problem.

1. The lumped mass analysis shows the qualitative effects of the platform friction dampers on the flexural resonance response modes of the blade in the frequency range of 0 to 20,000 Hz.

2. Good quantitative analysis (amplitude, strain) is dependent on reliable knowledge of the parameters upon which the analysis is based, i.e., m_1 , m_2 , k_1 , k_2 , μ , η , N , S , and θ or δ , these latter being functions of the excitation frequency and the number of blades in the disc.

3. The analysis shows that very effective friction damping is achieved in the range of the parameter $\mu N/S$ from the values of 2 to the value where $\mu N/S$ causes the onset of stick-slip friction, and later stick (no friction). In the range of $\mu N/S$ from 2 to 100, for instance, the amplitude response of the blade is reduced more than 90 percent.

4. The root damping of the blade does not appreciably affect the airfoil response after the friction damping becomes effective.

5. The response amplitude of the airfoil is reduced more than two orders of magnitude (more than 99 percent) in the minimum response frequency transition region ($\mu N/S$ range approximately 2 to 5, dependent on θ).

6. The response amplitude curves shown in Figure 10 through 12 define the effects of variation of η , θ , and S on the response of the HPFTP 1st stage blade in the lower $\mu N/S$ region where stick-slip and stick are not encountered.

7. Figure 12 shows that the response curves for $S=1$ can be used for design or redesign of the blade-damper system since the amplitude response scales linearly as a function of S at any value of $\mu N/S$.

8. The values of $\mu N/S$ that cause onset of stick-slip and stick are critical to the damper system design. If these regions can be avoided the Coulomb friction damping is very effective.

9. The airfoil amplitude response during stick-slip is undefined and if stick is encountered the airfoil amplitude will be controlled only by the damping of the airfoil section of the blade.

It can be stated further that the HPFTP 1st stage blade/damper lumped mass analysis provides guidance for the design of any similar blade system. It is emphasized that the stick-slip and stick regimes must be avoided and that quantitative evaluation is dependent on the accuracy of the data set input to the analysis.

ACKNOWLEDGEMENTS:

This work was performed for Marshall Space Flight Center (MSFC) of NASA under contract NAS8-34682. Mr. Larry Kiefling, the project technical monitor, of the Structural Dynamics Division of MSFC, was very helpful in providing data and guidance for the work. Mr. Tom W. Held, Dr. B. Basava Raju, and Dr. Mohan L. Soni of UDRI performed the computer program revisions, processing system development, and generation of the analysis program output data. Pam Brown typed the text and Donna Percy performed the

drafting. Their efforts were greatly appreciated. Also, the development of the lumped parameter analysis, over the past several years, by Dr. A. Muszynska, now of Bently Nevada Corporation, Dr. D.I.G. Jones of AFWAL/MLLN, Wright-Patterson Air Force Base, Dayton, Ohio, and their co-workers must be acknowledged.

REFERENCES

1. Sutton, R.F., "NASA, High Speed Rotating Diagnostic Laboratory Testing, SSME High-Pressure Fuel Turbopump Blade/Damper Evaluation," Rocketdyne Division of Rockwell International Report RSS-8626, November 1978.
2. Scott, L.P., J.E. Pond, C.C. Myers, G.A. Teal, G.F. Lewis, and J.K. Robinson, "Assessment of HPFTP Turbine Blade Environment and Fatigue Life Study on the SSME, Volumes I and II," Lockheed Missiles and Space Company Inc. Huntsville Research and Engineering Center Report LMSC-HREC TR D784198, May 1981.
3. Muszynska, A., D.I.G. Jones, T. Lagnese, and L. Whitford, "On Nonlinear Response of Multiple Blade Systems," Paper presented at 51st Shock and Vibration Symposium, San Diego CA, October 1980, and published in Shock and Vibration Bulletin 51, Part 3, May 1981.
4. Jones, David I.G., "Vibrations of a Compressor Blade with Slip at the Root," AFWAL-TR-80-4003, April 1980.
5. Dominic, R.J., Philip A. Graf, and B. Basava Raju, "Analytical and Experimental Investigation of Turbine Blade Damping-Final Report" University of Dayton Research Institute Report UDR-TR-82-39, August 1982. (AD-A120470, AFOSR-82-0911TR, or NTIS HC A04/MF A01).
6. Dickerson, E.O., "Turbine Blade Structural Dynamic Analysis," AIAA Paper 80-0782, 1980.
7. Raju, B.B., R.J. Dominic, T.W. Held, "Friction Damping Studies in Multiple Turbine Blade Systems by the Lumped Mass Method," Proceedings of AIAA Dayton-Cincinnati Section 9th Annual Mini-Symposium on Aerospace Science and Technology, March 22, 1983.

DISCUSSION

Mr. Sickmeier (General Motors): Since friction produces wear, based on your testing, did you predict how long this damper would last before it would wear out and lose its effectiveness?

Mr. Dominic: I made no predictions. Friction studies, in most cases, are quite expensive and difficult, in my experience.

Mr. Sickmeier: At this point, how long were the runs that you have made that have proven satisfactory in time?

Mr. Dominic: I don't have that information. But, the little bit that I have picked up in going through my data sets is really quite fascinating. A number of the engines have flown several missions, and as far as I know, there have been no problems with friction dampers. Those are super alloy blades and dampers, MAR-M-246 directionally solidified blades, and the same material is in the dampers. There is some lubrication by gas flow from the cooling system on the roots, up through the dampers and into the turbine drive gas stream. I would really like to know what the coefficient of friction is myself. I don't think it is possible to get that information.

Mr. Lee (Ohio State University): Do you have any experimental measurements showing what is actually going on at the interface of the disk and the root of the blade, such as friction and relative motion?

Mr. Dominic: No. David Jones wrote an extensive paper on root damping in turbine blades. It is referenced in my paper.

Mr. Lee: Also, there was some theoretical work done about ten years ago by Jim McBain, at the Aero Propulsion Laboratory, on the effect of root constraint on the vibration of a blade. So, I am very interested in this subject myself. How do you model something which obviously looks like a discrete model having a mass and spring damper? It wouldn't be able to take care of the initial stresses due to temperature, and perhaps the stress induced by rotation at the root. It may not behave as a coulomb friction low damper. So, I wonder if a more complete model should consider the deformation of the interface between the blade and the disk, and also the initial stress due to the temperature rise and the rotation of the machinery? I believe they must be considered for a more complete analysis. How do you feel?

Mr. Dominic: I think that is true. Of course, you are talking about one of the very tough problems. There was a very extensive finite element analysis of this blade by Lockheed. Many people spent a lot of time on it, and they developed a very detailed model. But, they did not even pick up the 8,500 Hz mode, which is the failure mode of the blade. So, I think the more

complicated the finite element models get, the more fineness you get in your answers. But you get less resolution because you don't know your input parameters or the input effects that closely.

Mr. Lee: Since you mentioned the finite element method, I don't know whether the existing finite element model can really handle such a complicated problem including, perhaps, frictional contact, impact, and slip stick. These are very, very complicated problems. Second, about the root; in your experimental results, I believe you said that if it is welded, you did not see any vibration above 4,500 Hz. But, if it is slotted, you saw a spanwise bending mode, or was it a torsional mode?

Mr. Dominic: It was a spanwise bending mode, but you also get a torsional mode. There is a very strong torsional mode on the blade at about 11,000 Hz.

Mr. Lee: In that set of experimental data, I was wondering whether there was a switch in the mode from spanwise bending to a torsional vibration that depended on the speed of rotation?

Mr. Dominic: This is the welded blade, and here is the 4,500 Hz region. There is a very small indication of it, and that is about all. The data are in the transition region up to the 8,500 Hz mode which sets in at a very high amplitude. This is the failure mode of the blade. The torsional mode is also very strong, but it is primarily the 8,500 Hz mode that causes the problem. This was the first run made on this particular test program from which these data were taken. The interruptions in the data are due to problems with the high speed slip rings. They shut down the test (they were going to 38,000 rpm on this test) at 28,000 rpm because of outer limit response at one of their safety parameters that they monitored. They made later runs where they had 13 E excitation which they knew was an exciting parameter for the blades. But by the time they got there, most of the strain gauges were gone. They lost a good many of their strain gauges in this run, and that is why I presented a set of data from this run. All of the strain gauges on the welded together blades went out on this run. There are no data on the constrained blades on any of the other runs. There are some data on the blades with no dampers and on the blades having three different types of friction dampers. So, that is a problem. They tested a blade with three different types of dampers. The masses of those dampers were .5 gram, .65 gram, and one gram. They got almost equal response from the .5 gram and the .65 gram dampers. I think they called this their precision damper. They had some lands built on the end of the damper to try to restrict the torsion mode because they would have more friction on the lands. You would only have

sporadic contact between those lands. But you can see, there is a little bit in the 4,500 Hz mode, and this is primarily unbalanced data. That is the first torsion, and that is the first airfoil bending.

VIBRATION PROBLEMS

TRANSIENT VIBRATION TEST CRITERIA

FOR SPACECRAFT HARDWARE

D. L. Kern and C. D. Hayes
Jet Propulsion Laboratory
California Institute of Technology
Pasadena, California

Transient vibration test criteria have been developed for spacecraft hardware. The test criteria provide a test rationale to verify the capability of the hardware to withstand the low and mid frequency transient vibration environments induced by launch vehicle events. The traditional test method employed to simulate transient vibration environments, the slow swept sine, results in excessive resonant response buildup and an excessive number of vibration cycles as compared to the actual transient flight environment. A unique test method, consisting of a series of discrete frequency, limited cycle, modulated sine wave pulses, was developed to avoid the slow swept sine drawbacks, yet provide a repeatable test that would excite all frequencies. The shape of the waveform is that of the classic response of the mass of a one degree of freedom system when it is base-excited by an exponentially decayed sine wave transient. Criteria were developed to define pulse amplitudes, shapes, and center frequencies from spacecraft loads analyses. Test tolerance criteria were also developed and specified. The transient vibration test criteria were implemented on spacecraft flight hardware both at the Jet Propulsion Laboratory and at contractor facilities. The test criteria achieved their objective of providing a more realistic test simulation (i.e., less conservative) for qualification of spacecraft hardware without risk of undertest.

BACKGROUND

The Jet Propulsion Laboratory has been assigned by NASA the task of managing the Galileo program, a planetary exploration spacecraft with a Jupiter orbit and probe deployment mission scheduled for launch via Shuttle/Wide Body Centaur in 1986. Loads predictions for Galileo show that the spacecraft and its hardware will be subjected to significant low (below 35 Hz) and mid (between 35 and approximately 100 Hz) frequency transient vibration environments during launch vehicle events. To ensure mission success, it is necessary to verify that the spacecraft and hardware can withstand these transient launch environments. The traditional test method to simulate transient vibration environments for spacecraft hardware (electronic equipment, mechanical devices, science instruments, etc.) is the slow swept sine vibration test. However, this test method has the drawbacks of inducing excessive resonant response buildup

and an excessive number of vibration cycles as compared to the actual transient flight environment. Two Galileo spacecraft hardware items, both predicted to experience high transient vibration loads during Shuttle launch, were anticipated to be particularly susceptible to the slow swept sine vibration test. In support of the Galileo program, special transient vibration tests have been developed and implemented for these hardware: the Radioisotope Thermoelectric Generators (RTG's) and the Magnetometer Boom Assembly. The RTG's were identified early in the Galileo program as being sensitive to slow swept sine vibration testing, based on previous test experience with a similar design that flew on the Voyager and the Lincoln Labs Experimental Satellite (LES) 8 and 9 spacecrafts. The two boom mounted RTG's, which weigh 122 pounds each, provide the electrical power for the spacecraft. An RTG will also fly on the

International Solar Polar Mission (ISPM) spacecraft, which is also launched on a Shuttle/Wide Body Centaur. The Magnetometer Boom Assembly consists of sensor elements on the end of a long collapsible boom stowed in a canister for launch. This item was identified, later in the program, as being sensitive to low frequency vibration and slightly different transient vibration test criteria were developed for its qualification.

TRANSIENT VIBRATION ENVIRONMENTS

The low and mid frequency transient vibration environments that the Galileo spacecraft will experience are induced by Shuttle/Wide Body Centaur launch vehicle transient events such as liftoff ignition, nonsymmetric ignition of the Solid Rocket Boosters (SRB's), SRB thrust buildup, stage separations, engine cutoff gusts, transonic and maximum Q flight, and landing. These transient events provide the dominant vibration source for the Galileo spacecraft in the low frequencies. The high frequencies are dominated by the acoustically induced random vibration environment. The cross over frequency range for Shuttle payloads where the random vibration environment begins to dominate over the transient environment is not well defined. However, current Galileo loads predictions show significant transient environments out to 80 Hz. The predicted Galileo transient vibration responses are based on a shock spectra and impedance method to determine an upper bound for spacecraft loads, Reference 1. Below 35 Hz, Galileo responses are predicted using transient forcing functions supplied by the STS contractor. Final loads verification will be accomplished by a full Space Transportation System (STS)/Galileo coupled loads analysis. STS payload transient forcing functions are defined only to 35 Hz due to STS Finite Element Model (F.E.M.) size and other limitations. Between 35 Hz and 80 Hz, Galileo transient responses are predicted using a "synthetic" forcing function. This "synthetic" forcing function is based on Shuttle flight data and on a generalized extrapolation of loads analyses below 35 Hz to the higher frequencies. The Galileo loads analyses are restricted to an upper frequency of 80 Hz due to the spacecraft F.E.M. accuracy limitations.

Based upon uncertainties in the definition of the Shuttle dynamic environments prior to the availability of STS-1 flight data, Galileo RTG and Magnetometer Boom Assembly transient vibration environments were specified to 100 Hz and 200 Hz respectively. The magnitude of the environments were derived from the load analyses and from response data from the Voyager spacecraft forced vibration tests. Both the RTG and the Magnetometer Boom Assembly are represented in the Galileo F.E.M. by single point masses at their c.g.s. Each point has six degrees of freedom. Results of the

spacecraft loads analyses are in the form of maximum acceleration or force for each spacecraft mode. Eighty spacecraft modes are calculated, which cover the frequency range from about 12 Hz to 80 Hz. Spacecraft loads are developed by calculating the square root of the sum of the squares (RSS) of the acceleration or force levels for each mode.

TRANSIENT TEST SIMULATION METHODS

There are a number of factors which must be considered in selecting a method to simulate the launch transient vibration environment for qualification of spacecraft hardware, such as,

- 1) accuracy of the test method relative to desired test level, frequency, waveform, etc.
- 2) repeatability of the test for the same or different qualification hardware and test facilities,
- 3) potential risk of inadvertent overtest,
- 4) number of vibration cycles imposed on the hardware relative to the predicted flight environment,
- 5) magnitude of the hardware responses relative to the predicted flight responses,
- 6) loading history (acceleration versus time) on the hardware relative to predicted flight environment,
- 7) manpower, materials, test time, and facilities required to conduct the qualification tests, and
- 8) contractor capabilities to implement the test.

Various test methods for simulating the launch transient vibration environments were considered. The above factors served as the criteria for evaluating these methods. The major advantages and disadvantages of the test simulation methods considered are as follows.

Slow Swept Sine

By far the most common method for simulating low frequency transient vibration environments is the slow swept sine. The conventional slow swept sine vibration test is well understood, easy to implement and control, and is repeatable. However, it has several disadvantages. The responses of hardware to swept sine tests are frequently considerably greater than to the actual flight transient environment due to resonance buildup. The resonance buildup can be compensated for by reducing the sine test level to provide the same hardware response as predicted in flight.

However, this requires knowledge of the Q for the critical hardware resonance and may result in overttest or undertest for other resonances with different Q values. Also, the slow swept sine test produces many more peak response cycles than does the actual flight transient environment. The increased number of cycles may be significant relative to material fatigue, wear on internal components that rub or impact, and fracture control requirements for Shuttle payloads. Another disadvantage is that the sine test excites resonances individually, while the flight pulse contains a relatively broad band of excitation and will excite several response modes simultaneously. Thus, potential failure mechanisms related to simultaneous modal excitation are not simulated.

Narrow Band Random

In this test method narrow band random vibration excitation is applied to the hardware at one or more frequencies at a time, Reference 2. This method has the advantages that the resonance buildup is reduced relative to the slow swept sine and the number of vibration cycles exceeding a preselected level can be reduced. Simultaneous excitation of two or more hardware response modes may also be accomplished. However, direct control over input amplitudes and number of cycles is limited, as is test repeatability. This method may provide some simulation improvement for transient events that occur repeatedly over a period of time, such as maximum Q flight, but has much less promise for simulating the dominant Shuttle transient events, associated with liftoff ignition and landing.

Classical Pulses

This method applies a classical transient pulse to the spacecraft hardware, such as a terminal sawtooth or half sine. These waveforms are easy to generate on a shaker and excite a broad frequency range. However, such pulses are a poor simulation of oscillatory type flight transient environments. Also, the method relies on shock spectra to define the magnitude.

Direct Transient Reproduction

A complex transient pulse based on the spacecraft loads analysis is applied to the hardware in this case, References 2 and 3. This is theoretically the most realistic test method. However, the complex waveform is difficult to generate and implement on a shaker. Modifications to the spacecraft structure or inaccuracies in the model can make the test nonconservative even if the shock spectrum of the transient does not change significantly. Also, the complex transient would be difficult to notch if it were desirable to limit the responses of the hardware at certain frequencies.

Fast Swept Sine

The fast swept sine wave transient test method has been employed with some success, Reference 4. The waveform is apparently easy to generate on electrodynamic shakers and amplitudes are reasonably controllable, although it would be difficult to generate a narrowband notch at specific frequencies to limit hardware resonant response. Amplitudes and sweep rates for the fast swept sine are usually defined to match a shock spectrum response requirement. It would be possible, however, to define the sweep rate based on a specified number of cycles per modal bandwidth. As with the slow swept sine, the fast swept sine excites only one frequency at a time.

Modulated Sine Pulse

A series of individually applied, discrete frequency, limited cycle, modulated sine wave pulses was the test method selected to simulate vibration environments for susceptible Galileo spacecraft hardware. The shape of the waveform is the acceleration versus time response of the mass of a one degree of freedom system when it is base-excited by an exponentially decayed sine wave transient. The normalized waveform, shown in Figure 1, can be approximated by the following equation:

$$G_p(f_1, t) = B e^{-\zeta \omega_1 t} \sin(\omega_1 t) \quad \text{for } t \geq 0 \quad (\text{Peak Gs}) \quad (1)$$

where $t =$ time (seconds) (2)

$f_1 =$ frequency of the 1th pulse (Hz) (3)

$\omega_1 = 2\pi f_1$ (radians/sec) (4)

$B = \omega_1 \zeta G_1$ (Peak Gs/sec) (5)

$\zeta =$ damping ratio = 0.04897 (6)

$G_1 =$ Peak Gs input at the 1th frequency (7)

$e =$ Base of natural logarithms (8)

NOTE #1 For the amplitude duration B , defined by equation (5), G_1 is equal to the amplitude of the maximum peak of the particular modulated sine pulse.

NOTE #2 The precise value of the damping ratio ζ used for these pulses was chosen to satisfy the following requirements:

1. The primary requirement for this value ($\zeta = 0.04897$) was that it be approximately equal to 0.05, which is a typical magnitude for ζ for complex structure
2. Its precise value also satisfied the additional requirement that the peak of the envelope of any pulse (i.e., the maximum of the equation for $G_p(f_i, t)$) occurs during the peak of the maximum sine wave oscillation for that pulse.

These requirements provide a particular expression for $G_p(f_i, t)$ which can be accurately compared to the maximum excursion of the actual modulated sine test pulses.

The modulated sine pulse waveform was chosen to simulate the transient environment because it is the basic waveform observed, for widely separated modes, from Galileo loads analysis responses. Figure 2 shows the response waveform for the RTG in the vertical axis, resulting from the spacecraft loads analysis, which can be compared to the normalized test pulse in Figure 1. Figure 2 shows the response waveforms, from the spacecraft loads analysis, of a spacecraft element with two dominant modes. The corresponding filtered waveform for each mode would be similar to that of Figure 1.

Analytically, this waveform can be approximately derived by making simplifying assumptions regarding the source pulse, the transfer function from the source to the Shuttle/spacecraft interface and the transfer function from the Shuttle/spacecraft interface to the spacecraft hardware. This is illustrated in Figure 3. The transient source waveform is assumed to be a delta function. Assuming the Shuttle can be represented as a single degree of freedom system, the response at the Shuttle/spacecraft interface to a base delta function input is an exponentially decayed sine wave transient, shown in Figure 3. The same approximate waveform will also result for more complex systems and for more realistic transient waveforms than the delta function waveform if the modes are widely separated. Assuming that the forcing function at the Shuttle/spacecraft interface is the exponentially decaying sine wave transient, and that the spacecraft can be represented by a single degree of freedom system, the response

of the spacecraft at hardware locations (such as the RTG c.g.) is the modulated sine wave shown at the bottom of Figure 3. Again, for widely separated modes, the response will still resemble, even for more complex systems, a modulated sine wave.

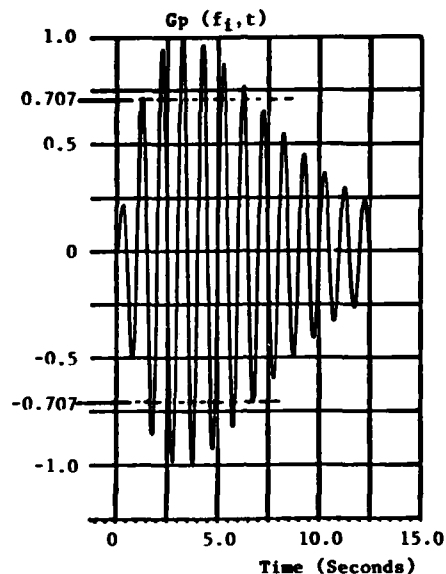


Fig. 1 Normalized Modulated Sine Pulse Time-History

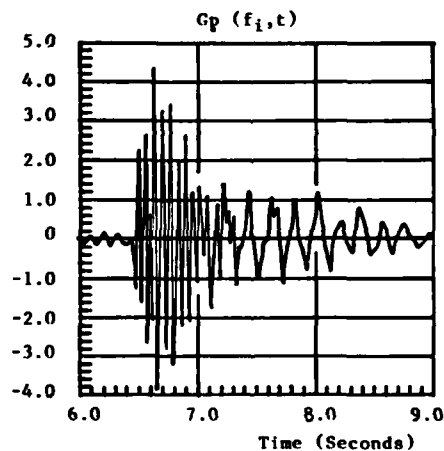
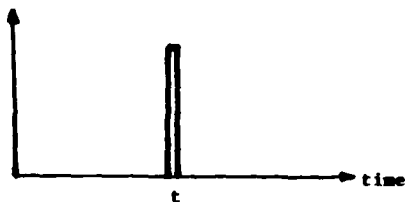
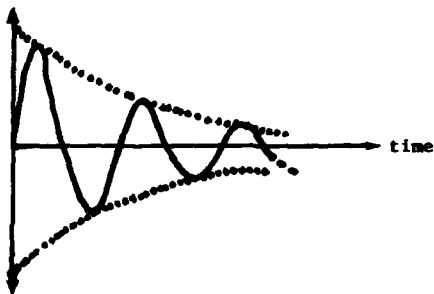


Fig. 2 Typical Spacecraft Hardware Response from Loads Analysis

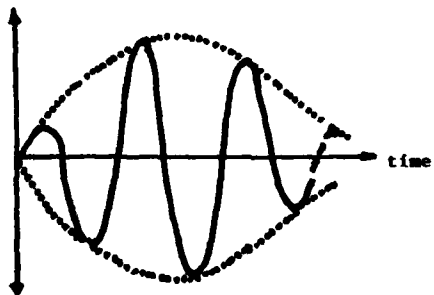
$$F_1(t) = A \delta(t)$$



$$F_2(t) = D e^{-\zeta \omega_n t} \sin \omega_n t$$



$$F_3(t) = B t e^{-\zeta \omega_n t} \sin \omega_n t$$



$F_1(t)$ = Input Pulse ("Source")

$F_2(t)$ = Pulse at Shuttle/Spacecraft Interface

$F_3(t)$ = Response Pulse at RTG center-of-gravity

Fig. 3 Input/Response Pulse History

The principal disadvantage of this modulated sine test pulse is the same as the fast swept sine test method-it does not simulate the loads at all frequencies simultaneously. However, there are a number of advantages:

- 1) The modulated sine wave pulses approximate the shape of the Galileo structural response as determined by the loads analysis.
- 2) The test pulse can be easily correlated to the Galileo loads analysis transients. Since the result of the loads analysis is the peak acceleration level for each spacecraft mode, the analysis result can be used directly to determine the peak level of the test pulse. The number of cycles in the test pulse can be adjusted easily to match the loads analysis pulse cycles. It is not necessary to artificially adjust the test pulse to achieve a response shock spectra criteria.
- 3) The test pulses are not difficult to generate, implement, and control. In the event that the spacecraft hardware test response needs to be limited at certain resonant frequencies, the entire amplitude of the test pulses at the corresponding frequencies can be appropriately reduced, based on low level test results.
- 4) The test pulse provides test accuracy and repeatability which is comparable to the slow swept sine. Since the waveforms are generic in nature, only the amplitudes and possibly the number of cycles would have to be changed in the event of a revised loads analysis.

RTG TEST CRITERIA

Only conventional rigid fixture shaker vibration test methods with input control on the fixture were considered. Although RTG accelerations determined by the loads analyses are defined at the RTG c.g., installation of the control accelerometer on the flight hardware was not feasible. This was not an insurmountable problem since at most frequencies within the test range, the major mass of the RTG acts as a rigid body. That is, the response at the c.g. equals the input. The major concern for the RTGs relative to the transient environments was lightweight internal components sensitive to accelerations at lower frequencies. At major resonances of the RTG on the rigid fixture, input levels were reduced so that c.g. responses corresponded to loads predictions.

In order to evaluate the practicability of the modulated sine pulse test method, a series of shaker vibration tests were conducted using the simplified one and two mass models idealized in Figure 4. Each mass weighed approximately 60 pounds - the weights of the RTG case and heat

source. The pulses were generated by utilizing the Time Data software program normally used to produce decaying sinusoidal waveforms for pyrotechnic shock simulation. Modulated waveforms of various amplitudes, discrete frequencies, and number of cycles were used. Test results were compared to results of swept sine tests. Waveform distortion was minimal except when the excitation pulse frequency matched the RTG model first resonance. Since similar distortion occurred during the swept sine vibration tests, this was attributed to shaker fixture/model interactions due to the model weight, low damping, and c.g. offset.

Analytical and test comparisons of the slow swept sine wave and the modulated sine pulse showed similar results. Resonant response from the modulated sine pulse excitation was significantly less than the slow swept sine. Table I compares the resonant response of a single degree of freedom system to sine dwell, slow swept sine, and the modulated sine pulse. The number of cycles imposed within the half power points of a response was more than an order of magnitude less with the modulated sine pulse as compared to the slow swept sine. A review of the Galileo loads analysis waveforms indicated that spacecraft hardware responses did not contain more than five high amplitude cycles for any significant launch vehicle event. Therefore the RTG test pulse waveforms were limited to five cycles that exceeded .707 times the highest amplitude cycle, as shown in Figure 1. Table II compares the number of cycles within a resonance for sine dwell, swept sine excitation and modulated sine pulse excitation.

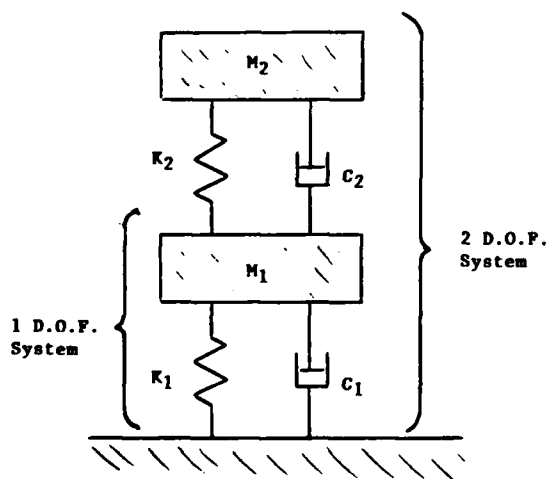


Fig. 4. One and Two Degree-of-Freedom Test Models

Since the RTGs will fly on both the Galileo and International Solar Polar Mission (ISPM) spacecrafts, transient test requirements were developed which envelope the predicted vibration environments for both spacecrafts. The approach taken was to define a frequency spectrum which conservatively enveloped predicted RTG accelerations for both spacecrafts and to apply the pulses at equal frequency increments to encompass the full spectrum. Pulse frequencies and spacings were based on response spectrums. A criteria was specified that the crossover point for adjacent response shock spectrums (using $Q = 10$) shall be not more than 3 dB (half power point) below the peak level of the shock spectrums. A Q of 10 was chosen as a typical experimentally observed response ratio for complex structures. It was determined that a pulse spacing of one third octave satisfied this criteria. This is illustrated in Figure 5.

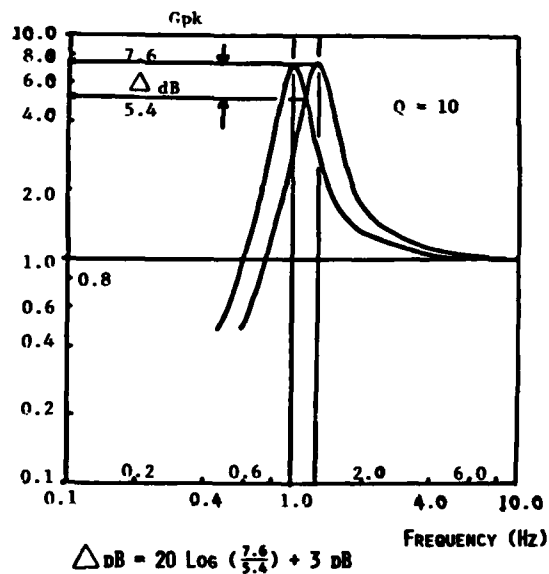


Fig. 5. Typical Shock Spectrum Overlap Between Two Adjacent Test Spectrums

The Galileo loads analysis for the RTG is in terms of the Root Sum Square (RSS) acceleration level and the acceleration level for each spacecraft mode. Since the test is applied only one frequency at the time, setting the test pulse levels equal to the acceleration of each mode would be nonconservative. To develop a conservative test spectrum, the acceleration level for each mode was multiplied by the ratio

Table I

Response at Resonance for 3 Test Methods

Test		System Q	Input G'spk	Response G's pk		
Method	Condition			F _n =10 Hz	F _n =25 Hz	F _n =50 Hz
Sine	10 seconds	10	1.0	10	10	10
Dwell	30 seconds	10	1.0	10	10	10
Sine	2 oct/min	10	1.0	9.7	9.5	9.4
Sweep	6 oct/min	10	1.0	9.5	9.3	9.0
Modulated Sine Pulses	5 cycles (≥ 0.707 max pulse amplitude)	10	1.0	7.5	7.5	7.5

Table II

Number of Response Cycles for 3 Test Methods

Test		System Q	Number of Cycles (≥ 0.707 * max response)		
Method	Condition		Resonant Frequency		
			10 Hz	25 Hz	50 Hz
Sine	10 seconds	10	100	250	500
Dwell	30 seconds	10	300	750	1500
Sine	2 oct/min	10	43	108	216
Sweep	6 oct/min	10	14	36	72
Modulated Sine Pulses	5 cycles (≥ 0.707 * max pulse amplitude)	10	5	5	5

of the RSS acceleration level to the acceleration level of the highest mode. This approach added only about 40% to the acceleration levels of the individual modes when only a few modes dominated, but was probably overly conservative for directions in which there were no modes that greatly exceeded the other modes. The ISPM RTG loads analysis, performed by General Dynamics, was in terms of time histories and shock spectrums. The highest peak level from each time history was multiplied by a factor of 1.3 to obtain an approximate RSS level. The shock spectrums were then scaled such that the highest peak of the shock spectrum equaled the appropriate RSS level. Table III shows the RTG composite test spectrum. These pulses are input one at a time.

Transient vibration test tolerance requirements were also developed for the RTG tests. The tolerances and their derivation are described below:

- 1) Amplitude Tolerance: Amplitude of each pulse shall be within the tolerance band of Figure 6.

These amplitude tolerances were defined based on conventional sine test tolerances ($\pm 10\%$ for peak levels) and test control practicability as established by early developmental testing.

- 2) Frequency Shift Tolerance: The fundamental frequency of each pulse shall be within $\pm 2\%$ of the specified 1/3 octave center frequency.

A Monte Carlo statistical analysis, using shock spectrums, was used to establish the adequacy of the $\pm 2\%$ frequency shift tolerance and the 1/3 octave center frequency spacing of the pulses. In particular, the following criteria was implemented:

The notch generated by the intersection of the shock spectra of pulses having equal amplitudes and fundamentals equal to the "worst case" center frequencies of two adjacent 1/3 octave bands, is required to be

TABLE III

RTG Composite Test Spectrum

Fundamental Pulse Frequency	Test Acceleration Level (Flight Acceptance Level)		
	Lateral (X axis)	Lateral (Y axis)	Longitudinal (Z axis)
Hz	Gpk	Gpk	Gpk
12.5	4.0	4.0	4.0
16.0	16.0	6.5	6.5
20.0	8.0	8.0	10.0
25.0	8.0	8.0	12.0
31.5	8.0	8.0	6.0
40.0	15.0	15.0	6.0
50.0	15.0	15.0	6.0
63.0	6.0	6.0	6.0
80.0	6.0	6.0	6.0
100.0	6.0	6.0	6.0

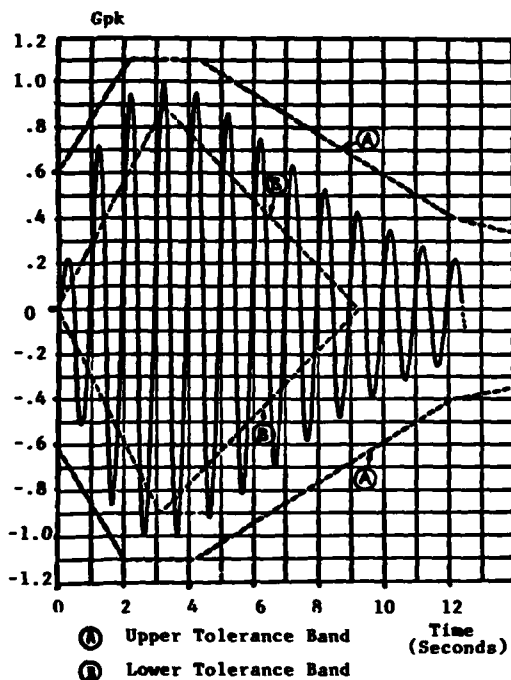


Fig. 6 Normalized Modulated Sine Pulse with Test Tolerance Bands

n... more than 4 dB below the shock spectrum magnitude ($Q = 10$) at the fundamental frequency. ("Worst case" fundamentals consisted of a -2% shift of the lower fundamental frequency and a +2% shift of the upper fundamental frequency at any two adjacent pulses. This condition resulted in the maximum frequency spacing between the two pulses, consistent with the tolerance limits, and a corresponding maximum in the depth of above-described notch.)

- 3) Harmonic Distortion Tolerance: The Shock Spectrum Amplitude (with $Q = 10$) of each pulse at any harmonic above the fundamental shall be at least 6 dB below the Shock Spectrum amplitude at the fundamental.

This criteria, based on a Monte Carlo shock spectra analysis, requires that the shock spectrum peak of any harmonic be at least 6 dB lower than

the shock spectrum peak of the fundamental. This criteria was imposed even in the extreme case where all of the harmonic energy of the pulse is concentrated in a single frequency component.

The above criteria assured a measure of test article excitation throughout the entire frequency spectrum of interest. In particular, it assured excitation at any frequency within 4 dB of the maximum excitation which occurred at each of the pulse's fundamental frequency.

MAGNETOMETER BOOM ASSEMBLY TEST CRITERIA

The Magnetometer Boom Assembly test criteria were similar to those employed for the RTGs, with some minor variations. Test criteria for the Magnetometer Boom Assembly were developed much later in the Galileo program, when the spacecraft design configuration had been frozen and all loads analysis cycles, except the final verification analysis, had been completed. Since the prediction of the magnitude and frequency content of the Magnetometer Boom Assembly transient vibration environment could be expected not to undergo further changes, a more specific test representation of the environment was specified. However, since the shock spectrum loads analysis method does not provide a unique complex waveform, a direct transient waveform reproduction test method was not considered. The Magnetometer Boom Assembly test criteria was derived from the test method developed for the RTGs. Rather than encompass the full frequency range by equally spacing pulses every one third octave, test pulses were specified only at the precise modal frequencies of the higher level transients. In this case, pulses were specified for all predicted transients of 2.7 Gpk or higher. The test pulse frequencies are shown on Table IV. To account for the lower level transient at other spacecraft modes, a 2.0 Gpk sine sweep was imposed on the hardware from 10 to 200 Hz. Additionally, the more recent loads analysis showed that the number of significant cycles for the dominant transient events was fewer than five. A shortened test pulse, shown in Figure 7 was used for the Magnetometer Boom Assembly.

TEST RESULTS

The RTGs are being furnished to NASA by the Department of Energy (D.O.E.). The contractor for D.O.E., responsible for the RTGs, is General Electric (G.E.), Valley Forge, Pennsylvania. G.E. has tested an RTG dynamic model, which consists of a dynamically simulated case and heat source, but with a thermopile which is only mass-simulated. They have also tested an engineering model, which

TABLE IV
Magnetometer Boom Assembly Test Spectrum

Lateral (X axis)		Lateral (Y axis)		Longitudinal (Z Axis)	
Fundamental Pulse Frequency	Test Acceleration (Flight Level)	Fundamental Pulse Frequency	Test Acceleration (Flight Level)	Fundamental Pulse Frequency	Test Acceleration (Flight Level)
Hz	G _p	Hz	G _p	Hz	G _p
16.6	6.4	29.5	4.6	19.4	9.5
37.5	2.7	34.6	7.4	22.9	16.0
40.2	2.7	40.2	4.6	33.4	3.1
		43.5	2.7	45.2	3.3
		65.1	10.3	53.9	5.0
		71.0	4.6	56.0	11.7
		76.1	5.2	65.1	4.7
		80.2	5.7	69.0	6.6
				80.2	4.2

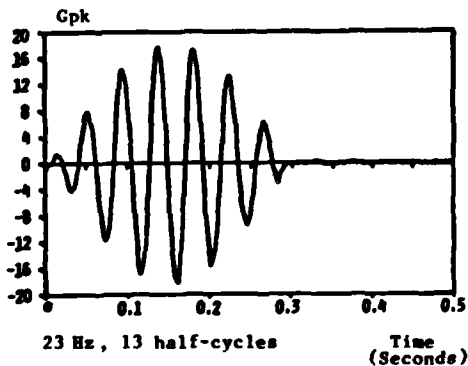


Fig. 7. Typical Test Pulse for Magnetometer Boom Transient Testing

consists of a flight-like RTG case and thermopile, but with a dynamically non similar electric heat source. The test transient waveforms were generated by modifying the shape of a segment of a very slowly swept sine wave by means of a tracking filter and high and low

pass filters. The RTG dynamic simulator successfully passed the transient vibration qualification level tests, but the engineering model suffered broken thermocouples due to the dynamic displacement of a lightweight internal frame which impacted the hot shoes. The failure was considered significant, based on the realistic flight-like test conditions; the frame was redesigned and the engineering model successfully passed retest. The qualification RTG is scheduled to undergo transient vibration testing, in early 1984, at a D.O.E. facility which is certified to handle nuclear materials. Software modifications to the facilities control system will allow the transient waveforms to be generated digitally.

The Magnetometer Boom Assembly was transient vibration test qualified at JPL. The pulses were generated by a software program which is normally used to produce decaying sinusoidal waveforms for pyrotechnic shock simulation. The Magnetometer Boom Assembly successfully passed the qualification tests. The waveforms were found to be easy to generate and to control. Response limiting was accomplished by measuring responses from low level pulse test inputs and adjusting the peak level of the qualification pulse to obtain the desired response.

CONCLUSIONS AND RECOMMENDATIONS

Two sensitive spacecraft hardware items were subjected to limited cycle, discrete frequency, modulated sine wave pulses, which verified their capability to withstand the launch vehicle induced transient vibration environments. The transient vibration test method avoided unrealistic hardware failures which were anticipated to occur if the conventional slow swept sine vibration test method had been utilized. The transient pulse tests were found to be reasonably simple to implement and control. The time required to perform the transient tests could be made comparable to the slow swept sine test time if the discrete frequency pulses were combined into a single wave train. Based on the above described test experiences, it is recommended that transient vibration test methods be employed to replace slow swept sine tests in order to more realistically simulate the effects of transient vibration environments.

ACKNOWLEDGMENTS

The authors wish to thank George Ambrose of the General Electric Company, Valley Forge, PA, for his support in implementing the transient vibration test criteria for the RTGs and Dr. Marc Trubert of the Jet Propulsion Laboratory for his support in defining the transient waveform characteristics.

The work described in this paper was carried out by the Jet Propulsion Laboratory, California Institute of Technology, under contract with the National Aeronautics and Space Administration.

References

1. A Generalized Shock Spectra Method for Spacecraft Loads Analysis, M. Trubert and M. Salama, JPL Publication 79-2 (TM 038), March 15, 1979.
2. Spacecraft Structural Dynamics Test Improvements - Final Report, Space and Communications Group, Hughes Aircraft Company, March 1977.
3. "Methodology of Uniaxial Transient Vibration Test for Satellites", from Recent Advances in Space Structure Design Verification Techniques, Page 35, B. Boissin, A Girard and J. F. Imbert, European Space Agency, April 27-28, 1981.
4. "A Simulated Method of Transient Environment---The Fast Swept Sine Method", from 1981 PROCEEDINGS - Institute of Environmental Sciences, Page 94, Huang You Xian, 27th Annual Technical Meeting.

VIBRATIONAL LOADING MECHANISM OF UNITIZED CORRUGATED CONTAINERS
WITH CUSHIONS AND NON-LOAD-BEARING CONTENTS

Thomas J. Urbanik, Research General Engineer
Forest Products Laboratory,* Forest Service
U.S. Department of Agriculture

The use of hardwood and recycled fiber will no doubt increase as specifications for corrugated fiberboard containers change from material to performance standards. This report shows another way to accelerate this use by reducing the strength requirements of containers shipped in unitized loads. The rate of container deformation with top loading and the compliance of internal packing material or cushions are newly identified variables governing the compression of bottom containers.

Unitized containers need strength beyond the warehouse stacking requirements to support dynamic loads during shipping. The spring rates of top-loaded containers and internal cushions amplify the weight force of a unitized load during transportation. The progressive deformation with top-loading of corrugated containers causes increasingly higher spring rates with a subsequent effect on dynamic loads. Cushions or internal packing provide a natural ability to absorb vibrations to a degree, depending on their spring rates relative to the containers'.

Over-the-road shipping vibrations encompass the natural frequencies of most unitized loads and dynamically load the bottom containers. A worst case assessment calculates the maximum load on the bottom tier, expected during truck transportation. The cushion-to-container spring ratio and the rate of increasing container spring rates with top-loading are the primary variables determining dynamic loads.

NOMENCLATURE

C_t	Total compressive loading factor	K_n	Container spring rate in tier n
c_{ci}	Critical damping coefficient of element i	K_p	Container spring rate with top load P
c_i	Damping coefficient of element i	K_w	Container spring rate with top load W
[D]	Damping matrix	K_1	Container spring rate with unit top load
$[D_{ij}]$	Partition of damping matrix	k_i	Stiffness coefficient of element i
F	Cushion-to-container spring ratio	[M]	Mass matrix
f	Natural frequency factor	m	Unit mass
f_1	Lowest natural frequency factor	m_i	Mass of element i
G	Gravitational constant	N	Number of mass elements
[I]	Identity matrix	n	Tier number
i	Element number in spring-mass model	P	Top load
j	Imaginary unit	P_d	Dynamic compressive load
K_c	Cushion spring rate	[R]	A matrix of stiffness coefficients
K_N	Bottom container spring rate	$[\sqrt{R}]$	A matrix of stiffness coefficients
		r	Exponent in spring rate formula
		[S]	Stiffness matrix
		$[S_c]$	Condensed stiffness matrix
		$[S_{ij}]$	Partition of stiffness matrix
		W	Unit weight per container
		{X}	Response vector

*Maintained at Madison, Wis., in cooperation with the University of Wisconsin.

X_{N+1}	Displacement of element N+1
\ddot{X}_{N+1}	Acceleration of element N+1
{Y}	Disturbance vector
{Y'}	Partition of disturbance vector
Y	Displacement disturbance
\ddot{Y}	Acceleration disturbance
ρ	Damping ratio
ω	Natural frequency
ω_1	Lowest natural frequency
{0}	Zero matrix
{0,0}	Zero vector

INTRODUCTION

One problem with designing corrugated fiberboard containers is determining an adequate load carrying ability. The top-to-bottom compressive strength measured in a laboratory test is the upper limit of strength expected under only the most favorable conditions. The problem of comparing this strength to the anticipated dynamic load becomes particularly relevant when containers are shipped in unitized loads. While the additive weight of the upper containers is obvious, it is not always apparent how to treat the effects of over-the-road vibrations.

Unitized containers need extra strength beyond the warehouse stacking requirements to support dynamic loads during shipping. One of the surest methods for assessing adequate strength is the ASTM Vibration Test [1]. However, being empirical, its application is a trial and error search for a unitized load that survives the test.

An analysis can speed up the search, and one of the earliest is that by Godshall [2]. Godshall treated corrugated containers as spring-mass systems, and determined which characteristics would predict their response to transportation vibrations. He used repeated loading compression tests to measure the spring rates of top-loaded containers. Later vibration experiments by Godshall [3] confirmed the effectiveness of these tests. A primary finding was that corrugated-container systems will likely resonate during shipping with destructive compressive forces limited primarily by material damping, empirically determined to be 0.115 times the critical damping value.

With machines where changing damping is impracticable, engineers have attached vibration absorbers to stabilize their motion. Analogously, it makes sense that cushions within containers can reduce unit load vibrations. Hatae [4] gives a comprehensive treatment of the mechanics of package cushions. Godshall [5] applied these concepts to corrugated pads and compared spring rates determined from repeated loading tests with values calculated from resonant frequencies determined in vibration tests. The vibration test is more

accurate, especially when the loading condition between a product and cushion may be uncertain.

While Godshall studied only single degree of freedom systems, my earlier work [6,7] proposed a new theory and a computer program for multiple degree of freedom systems. Calculations with representative spring rates and damping characteristics of corrugated containers explained why disturbances at only the lowest of multiple natural frequencies inherent to a unitized load cause problems. One example trial of my computer program evaluated a unitizing arrangement in a theoretical shipping environment for dynamic compression of the bottom containers.

The investigation by Ostrem and Godshall [8] quantified the actual shipping environment for unitized loads. Figure 7 in their report summarizes the envelope of truck vibrations and suggests that calculating the response of unitized loads for a 0.5 G acceleration disturbance predicts the hazards associated with this mode of shipping.

This previous research thus established the following principles leading to this study: (1) Repeated loading tests predict the spring rates of corrugated containers; (2) spring rates of cushions are determinable from vibration tests; (3) corrugated fiberboard systems are damped at about 0.115 times the critical damping value; (4) the first natural frequency is of primary concern, and the truck transportation environment normally excites that frequency; and (5) vibration disturbances in trucks are typically about 0.5 G in magnitude.

OBJECTIVE AND SCOPE

The objective of this report is to explain how the spring rates of cushions and containers amplify the compressive weight force of a unitized load during truck transportation. This study starts by measuring spring rates of combinations of corrugated containers and plastic bottles. The experiments lead to a formula for predicting the spring rates of containers in different tiers of a stack. A theory proposes the behavior of a unitized load having definable ratios among its components' spring rates. The spring rates of cushions enter the theory as a means of reducing the dynamic response of a stack. A spring-mass model of a unitized load guides the theory through a matrix analysis for which a set of dimensionless parameters greatly reduces the number of variables.

While transportation vibrations can disarrange a unitized load or resonate the contents, the primary mode of damage considered in this report is compression of the bottom containers. The theory treats a specific type of package wherein the innermost contents carry no load, although the interior package might share the load with the box. Moreover, these contents

act like lumped masses suspended on cushions resulting from actual cushions within the boxes, the compliance of interior packages, or when the contents are soft, their own compliance.

The general principles of vibration isolation discussed in [9] indicate the significance of material damping. Although arbitrary cushioning materials may encompass wide variations in damping characteristics, this study considers only one damping ratio typical of corrugated fiberboard. An application of the theory calculates compressive loads for combinations of spring rates and numbers of unitized tiers. The results suggest ways to reduce the strength requirement of boxes used in unitized loads.

TEST MATERIAL AND PROCEDURE

A repeated loading test top-loads a container to an equilibrium value equal to the static load it normally supports then repeatedly raises and lowers the load to simulate vibrations and establish a linear section of the load deformation trace. A series of repeated loading tests for this study measured the spring rates of corrugated containers and plastic water bottles. The bottles were nominal 1-gallon, commercial plastic bottles for distributing distilled water. The boxes were nominal 200-pound C-flute commercial, regular-slotted containers intended for the bottles.

To test the effect of load sharing between the bottles and the box, 16 test units were separated into four arrangements. Units 1-9 were tested in the normal arrangement of a box containing six bottles filled with water. Tests of units 10-13 used a box with six sand filled bottles having cut-down tops. Each bottle contained 3.8 kg of sand. This arrangement concentrated the top load in the box while providing the normal lateral pressure.

The reverse arrangement whereby the bottles carried all of the load was used for testing units 14 and 15. The midsection about the perimeter of each box was cut away and the box contained six water-filled bottles. Unit 16 consisted of six water-filled bottles with no box.

To test the effect of environmental conditions, the tests were conducted at three different temperatures and relative humidities (RH). Units 1-3 and 16 were tested at 73°F and 50 percent RH; units 4-6, at 80°F and 30 percent RH; and units 7-15, at 80°F and 90 percent RH. Container preparation followed the normal preconditioning in a dry environment according to ASTM D 685-73 [10] with subsequent conditioning at the prescribed testing environment. Conditioning times were long enough to ensure an equilibrium moisture content of the material.

A check was made for vibrational work hardening. While other units were unused prior to compression tests, units 10-12 consisted of containers used in previous vibration tests performed at 30 and 90 percent RH for another study.

Each unit underwent 16 repeated loading tests. Each test first compressed the container between two parallel platens at a rate of 42.3 $\mu\text{m/s}$ up to an equilibrium load (EL) followed by repeatedly raising and lowering the load with an amplitude determined as a percentage of the EL. The 16 tests consisted of all combinations of 4 EL's and 4 percentages of EL.

Equilibrium loads of 25, 50, 75, and 100 kg duplicated the static top load per container due to the upper four tiers of a stack. Repeated loading and unloading between amplitudes of 25, 50, 75, and 100 percent of each EL simulated different vibration magnitudes.

Load was measured with an electronic transducer attached to the bottom platen and deformation with a drum recorder whose rotation was mechanically proportional to the displacement of the upper platen. Five cycles of loading were enough to produce a repeating load deformation trace.

DATA AND ANALYSIS

The spring rate of a container equals the slope of a tangent drawn at the EL to the trace produced by the final increasing load. The spring rate data appear in Table I.

Spring rates of the containers in units 1-15 follow the empirical formula

$$K_p = K_w (P/W)^r \quad (1)$$

P is the EL and K_p is the spring rate at that load. W is a reference load and K_w the corresponding spring rate. r is an empirical constant. A modified formula represents conditions in a unit load by considering only values of P and K_p identified with each tier. Let the reference load, W , equal the unit weight per container and number the tiers 1, 2, ... N as shown in Figure 1 beginning with the second tier from the top. If $n = P/W$, equation (1) reduces to

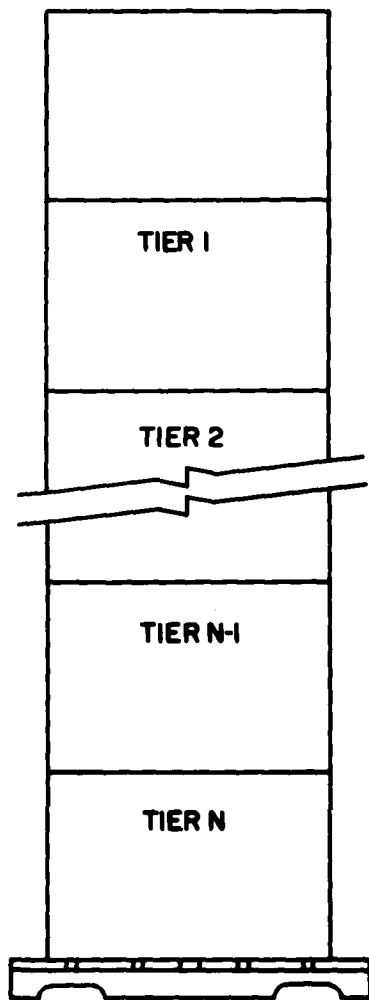
$$K_n = K_1 n^r ; n = 1, N \quad (2)$$

where K_n is the spring rate at tier n .

Table I.--Container spring rates

Repeated loading amplitude		Container arrangement and unit number															
		Box with six water-filled bottles															
		73°F, 50% R.H.			80°F, 30% R.H.			80°F, 90% R.H.			Box with six sand-filled bottles having cut-down tops			Box with cut-away mid-section and six water-filled bottles			
Pct of EL	Equilibrium load	1	2	3	4	5	6	7	8	9	10 ^{1/}	11 ^{1/}	12 ^{1/}	13	14	15	16
		kN/m															
25	25	376	214	339	341	350	362	196	269	178	333	208	239	210	214	201	584
	50	500	362	600	501	477	420	568	618	466	584	412	447	477	256	226	618
	75	778	725	750	724	750	656	913	995	808	1,070	1,170	890	914	404	362	656
50	100	955	913	913	955	913	808	955	1,050	913	1,690	1,110	1,750	1,630	553	512	636
	25	202	194	339	258	277	244	291	328	178	256	191	223	196	194	178	512
	50	477	362	525	438	429	396	584	656	477	664	477	429	411	253	242	568
75	100	677	656	725	618	538	618	725	913	750	1,110	913	913	840	388	323	618
	25	808	808	840	750	677	700	875	1,105	875	1,880	808	1,280	1,500	447	500	538
	50	184	178	300	242	234	223	202	280	142	210	170	187	196	166	163	466
100	75	457	339	477	382	382	362	500	538	368	553	362	389	333	259	219	525
	50	584	584	636	500	500	553	618	808	584	955	761	778	700	344	284	525
	100	700	725	700	636	600	618	700	954	636	1,400	--	1,030	1,170	375	382	438
25	25	156	159	309	228	223	215	187	244	137	187	116	160	163	149	150	429
	50	404	298	447	389	350	307	412	429	328	466	305	313	291	193	189	525
	75	553	584	558	457	457	501	457	656	447	750	636	636	584	246	242	500
100	100	600	636	648	553	512	583	584	700	500	1,050	--	--	914	313	339	368

^{1/} Boxes were used in vibration tests performed at 30% and 90% R.H. prior to compression testing.



ML83 5399

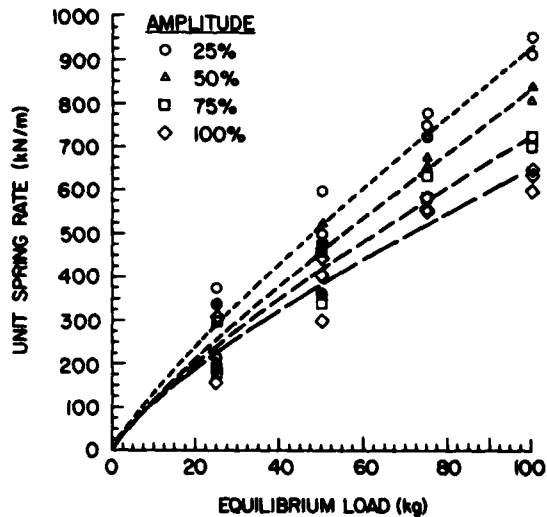
Figure 1.--Representation of a unitized load. The tiers are numbered to match the static loading condition.

Equation (2) reduces the measured spring rates K_1 , K_2 , K_3 , and K_4 to predicted parameters in terms of K_1 and r for each repeated loading amplitude of each group of data. The values of K_1 and r fitting the data appear in Table II.

Table II.--Parameters K_1 and r determined from repeated loading data

Repeated Loading amplitude	Unit number					
	1-3	4-6	7-9	10-12	13	14,15
<u>Pct of EL</u>						
K_1 (kN/m)						
25	291	307	282	202	142	159
50	255	258	305	228	120	160
75	239	233	250	173	115	160
100	226	224	219	134	114	136
r						
25	.838	.757	.937	1.46	1.74	.838
50	.856	.734	.840	1.28	1.81	.759
75	.801	.710	.835	1.41	1.66	.618
100	.765	.655	.746	1.48	1.49	.620

Figures 2 and 3 show some representative plots of the data and average characteristics. As evidenced in Figure 2, higher repeated loading amplitudes cause lower spring rates. Table II, however, suggests that the effect of amplitude on the predicted r 's is not serious.



ML83 5401

Figure 2.--Spring rate versus equilibrium load for top-loaded corrugated containers and plastic bottles of units 1-3. The points represent the data. The curves fit equation (1) to data obtained with 25, 50, 75, and 100 percent repeated loading amplitudes.

Figure 3 shows the effects of the different arrangements, environments, and prior use. A comparison among units 1-3, 4-6, and 7-9 shows the combined effects of temperature and humidity. The contribution of load sharing by the bottles becomes evident by comparing units 7-9 with unit 13 and units 14, 15. Work hardening permanently deforms the paperboard material and increases the spring rates of lightly loaded containers. Comparing units 10-12 with unit 13 shows this effect.

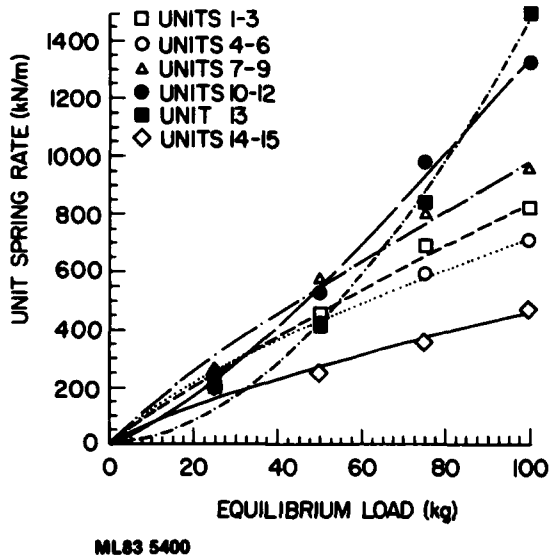


Figure 3.--Spring rate versus equilibrium load with a repeated loading amplitude of 50 percent of the equilibrium load. The points represent the average data. The curves fit equation (1) to the data.

A series of repeated loading tests can be abbreviated by testing only two containers. Determine spring rates, K_1 and K_N for the second and bottom tiers in a unit load and calculate r from

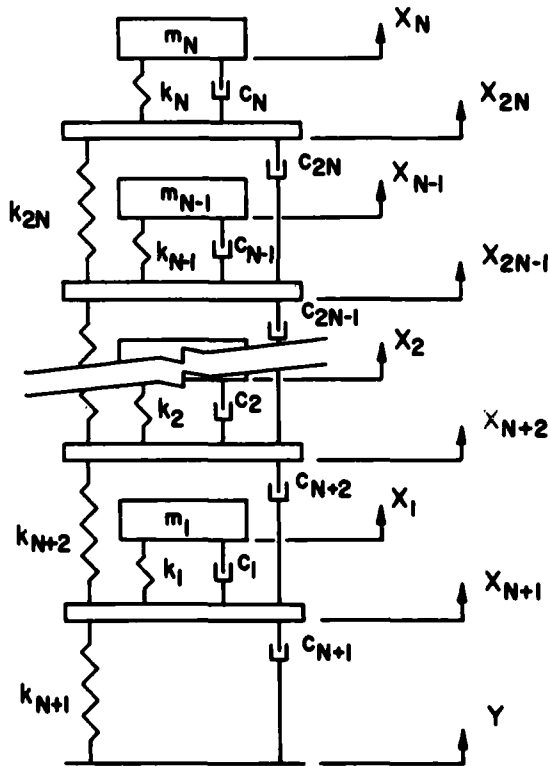
$$r = \frac{\ln(K_N/K_1)}{\ln N} \quad (3)$$

Of course extra tests check the variability.

THEORY

The diagram in Figure 4 represents a unitized load with cushioned, non-load-bearing masses. A model with N masses has $2N$ degrees of freedom corresponding to a unit load with $N + 1$ tiers. My step by step analysis of a similar model appears in [6,7]. This theory

follows the same steps where, after associating equations of equilibrium with the degrees of freedom, it arranges the equations for a matrix solution. To simplify the analysis the theory introduces six dimensionless parameters, of which N and r have already been mentioned.



ML83 5398

Figure 4.--Representation of a unitized load as a spring-mass system. The degrees of freedom are numbered for calculating the dynamic loading condition.

The weight of the contents of each container is lumped into a mass m . All masses being equal gives

$$m_i = m = W/G ; i = 1, N \quad (4)$$

The interior springs represent cushions and remain equal provided the container compression does not interfere with the mass vibration. Call the spring rate of the cushions K_c and let the dimensionless parameter F be the cushion-to-container spring ratio.

$$F = K_c / K_1 \quad (5)$$

The corresponding stiffness values become

$$k_i = FK_1 \quad ; \quad i = 1, N \quad (6)$$

The outer springs follow the behavior of top-loaded containers becoming increasingly stiffer progressing down the stack. Starting with element k_{2N} identified with tier 1, and being careful to note the difference between tier numbers in Figure 1 and spring numbers in Figure 4, the stiffness values are

$$k_{2N+1-i} = K_1 i^r \quad ; \quad i = 1, N \quad (7)$$

The assumption of viscous damping explained Godshall's data [3] reasonably well and is extended here to a unitized load. If the critical damping associated with each dashpot is

$$c_{ci} = 2 \sqrt{mk_i} \quad ; \quad i = 1, 2N \quad (8)$$

and all elements have equal damping ratios, ρ , they take on damping values given by

$$c_i = \rho c_{ci} = 2 \rho \sqrt{mk_i} \quad ; \quad i = 1, 2N \quad (9)$$

The mass matrix [M] of size $2N \times 2N$ is constructed from the identity submatrix [I] and the zero submatrix [0] both of size $N \times N$.

$$[M] = m \begin{bmatrix} I & 0 \\ 0 & 0 \end{bmatrix} \quad (10)$$

The stiffness matrix [S] of size $2N \times 2N$ is partitioned into submatrices $[S_{11}]$, $[S_{12}]$, $[S_{21}]$, and $[S_{22}]$ all of size $N \times N$. The partitions are constructed according to equations

$$\left. \begin{aligned} [S_{11}] &= K_1 F [I] \\ [S_{12}] &= [S_{21}] = -[S_{11}] \\ [S_{22}] &= K_1 [R] \end{aligned} \right\} \quad (11)$$

where [R] appears in Table III. The complete form of [S] is finally

$$[S] = \begin{bmatrix} S_{11} & \dots & S_{12} \\ \vdots & \ddots & \vdots \\ S_{21} & \dots & S_{22} \end{bmatrix} \quad (12)$$

The damping matrix [D] is partitioned as [S] was according to

$$[D] = \begin{bmatrix} D_{11} & \dots & D_{12} \\ \vdots & \ddots & \vdots \\ D_{21} & \dots & D_{22} \end{bmatrix} \quad (13)$$

Its construction follows a similar pattern given by equations

$$\left. \begin{aligned} [D_{11}] &= 2 \rho \sqrt{mK_1} \cdot \sqrt{F} [I] \\ [D_{12}] &= [D_{21}] = -[D_{11}] \\ [D_{22}] &= 2 \rho \sqrt{mK_1} [\sqrt{R}] \end{aligned} \right\} \quad (14)$$

where an element of $[\sqrt{R}]$ is equal to the sum of the square roots of each term in the corresponding element of [R]. See Table III.

To exclude degrees of freedom having no mass, the condensed stiffness matrix $[S_c]$ is determined by the static condensation method discussed by Clough and Penzler [11]. $[S_c]$ of size $N \times N$ is calculated from

$$[S_c] = [S_{11}] - [S_{12}] [S_{22}]^{-1} [S_{21}] \quad (15)$$

which reduces to

$$[S_c] = K_1 (F [I] - F^2 [R]^{-1}) \quad (16)$$

The natural frequencies of the system are determinable by solving for the frequencies ω that make the determinant

$$\left| [S_c] - \omega^2 [M] \right| = 0 \quad (17)$$

This formula is made dimensionless by introducing the natural frequency factor f to define

$$\omega = f \sqrt{K_1 / m} \quad (18)$$

Table III.--Construction of matrices [R] and [\sqrt{R}]

$$\begin{aligned}
 [R] &= \\
 &\begin{bmatrix}
 N^r + (N-1)^r + F & ; & -(N-1)^r & & ; & 0 & \cdots \\
 -(N-1)^r & & ; & (N-1)^r + (N-2)^r + F & ; & -(N-2)^r & & ; & 0 & \cdots \\
 0 & & ; & -(N-2)^r & & ; & (N-2)^r + (N-3)^r + F & ; & -(N-2)^r & ; & 0 & \cdots \\
 & & & & & & \cdots & 0 & ; & -2^r & ; & 2^r + 1 + F & ; & -1 \\
 & & & & & & & & & \cdots & 0 & ; & -1 & & ; & 1^r + 0 + F
 \end{bmatrix} \\
 [\sqrt{R}] &= \\
 &\begin{bmatrix}
 \sqrt{N^r} + \sqrt{(N-1)^r} + \sqrt{F} & ; & -\sqrt{(N-1)^r} & & ; & 0 & \cdots \\
 -\sqrt{(N-1)^r} & & ; & \sqrt{(N-1)^r} + \sqrt{(N-2)^r} + \sqrt{F} & ; & -\sqrt{(N-2)^r} & & ; & 0 & \cdots \\
 & & & & & & \cdots & 0 & ; & -\sqrt{1} & ; & \sqrt{1^r} + \sqrt{0} + \sqrt{F}
 \end{bmatrix}
 \end{aligned}$$

Substituting equations (10), (16), and (18) into (17) gives

$$(F [I] - F^2 [R]^{-1}) - f^2 [I] = 0 \quad (19)$$

of which the smallest solution f_1 yields the first natural frequency ω_1 .

The disturbance vector {Y} of size $2N \times 1$ is constructed from real and imaginary components of a sinusoidal displacement of infinite duration. The disturbance occurring only at the bottom makes all except one of the elements in {Y} equal zero. {Y} is partitioned into the complex zero vector {0,0} and a complex sub-vector {Y'} both of size $N \times 1$ with

$$\{Y'\} = \begin{Bmatrix} 1,0 \\ 0,0 \\ \vdots \\ 0,0 \end{Bmatrix} \quad (20)$$

where the displacement amplitude is normalized to unity. The complete form of {Y} is

$$\{Y\} = \begin{Bmatrix} 0,0 \\ \vdots \\ Y' \end{Bmatrix} \quad (21)$$

The response vector {X} is the set of complex numbers representing sinusoids associated

with the steady state motion of the degrees of freedom and ultimately results from {Y}. {X} has size $2N \times 1$ and is calculated from

$$\begin{aligned}
 \{X\} &= ([S] - \omega^2 [M] + j\omega [D])^{-1} \\
 &\cdot (N^r K_1 + j\omega 2 \rho \sqrt{m} K_1 \sqrt{N^r}) \{Y\} \quad (22)
 \end{aligned}$$

where j is the imaginary unit. This formula is made dimensionless by combining previous equations to get

$$\begin{aligned}
 \{X\} &= \left(\begin{bmatrix} FI & \cdots & -FI \\ -FI & & R \end{bmatrix} - f^2 \begin{bmatrix} I & \cdots & 0 \\ 0 & & 0 \end{bmatrix} \right. \\
 &+ j f 2 \rho \begin{bmatrix} \sqrt{F} I & \cdots & -\sqrt{F} I \\ -\sqrt{F} I & & \sqrt{R} \end{bmatrix} \left. \right)^{-1} \\
 &\cdot (N^r + j f 2 \rho \sqrt{N^r}) \begin{Bmatrix} 0,0 \\ \vdots \\ Y' \end{Bmatrix} \quad (23)
 \end{aligned}$$

where expressions FI and $\sqrt{F} I$ represent matrices $F [I]$ and $\sqrt{F} [I]$.

APPLICATION

Overcompression of the bottom container causes stack failure. The maximum compression equals the amplitude of the difference between

sinusoids X_{N+1} and Y occurring at ω_1 as given by $|X_{N+1} - Y|$. Repeating the previous analysis leading to equation (23) with units of acceleration instead of displacement yields the maximum compression $|\ddot{X}_{N+1} - \ddot{Y}|/\omega_1^2$. Multiplying this maximum by the spring rate of the bottom container gives the dynamic compressive load

$$P_d = |\ddot{X}_{N+1} - \ddot{Y}| K_1 N^r / \omega_1^2 \quad (24)$$

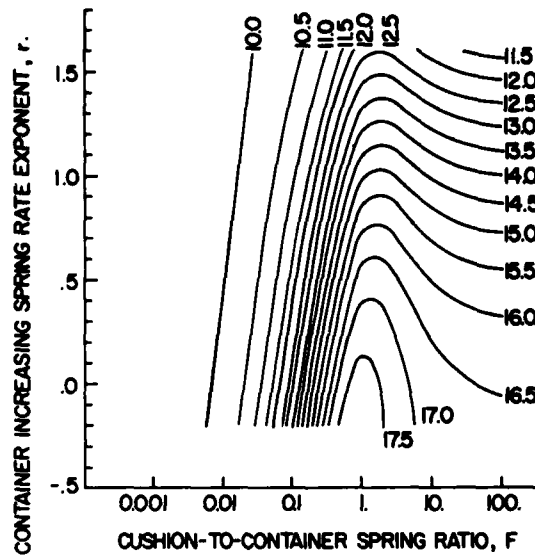
The total load on the box due to statics and dynamics is $P_d + W \cdot N$. The following is an assessment of a worst-case condition for loading based on the information of Ostrem and Godshall [8] that the envelope of truck vibrations includes the natural frequencies of most unitized loads, and exerts acceleration levels on the order of 0.5 G. The results give the total multiplication of unit weight the bottom container is likely to experience in terms of the dimensionless total compressive loading factor C_t .

$$C_t = \frac{P_d + W \cdot N}{W} = .5 \frac{|\ddot{X}_{N+1} - \ddot{Y}| N^r}{f_1^2 G} + N \quad (25)$$

Values of C_t were calculated for various unit loads with different combinations of r , F , and N . The values $-0.2 \leq r \leq 1.6$ encompass typical values indicated by the repeated loading data. The values $0.001 \leq F \leq 100$ check the effects of relatively very soft to relatively very hard cushions. All calculations assumed $\rho = 0.115$.

Figure 5 shows the effects of r and F on C_t for a four-tier stack. Static conditions would normally load the bottom container to three times its weight. The results show that the maximum total load during shipping can attain about 16 times the unit weight for the lowest r value found in this study. The cause of dynamic compression shifts around $F = 1$. When $K_c > K_1$ the system is "hard" with the cushions becoming increasingly less effective with higher spring rates. Ultimately, the cushions act as though they were rigid. While changing K_1 or K_c (and thus F) has little effect on C_t , increasing r reduces C_t . With effectively rigid cushions the rate of container deformation with increasing top loads governs the magnitude of dynamic loading.

When $K_c < K_1$ the system is "soft" with the cushions becoming more effective as their



ML63 5306

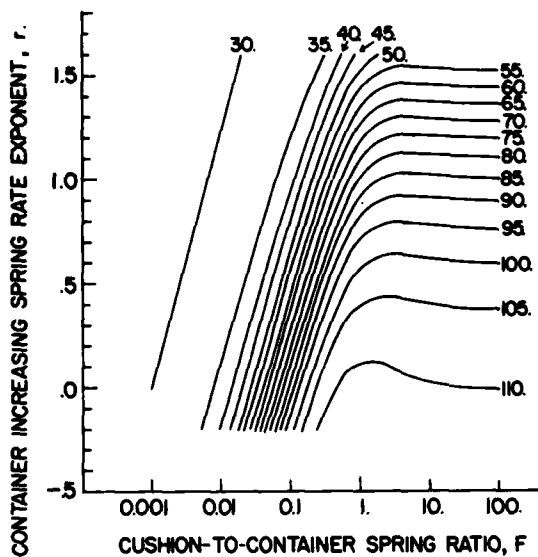
Figure 5.--Contours of constant load multiplication factors C_t calculated for combinations of r and F in a four-tier unitized load. The calculations assume $\rho = 0.115$.

spring rates decrease. While increasing K_1 or reducing K_c reduces C_t , changing r has little effect on C_t . If the cushions have spring rates lower than the containers', the magnitude of loading results primarily from the spring rate of the cushion relative to that of the container.

The shift in the mechanism of dynamic compression makes sense considering how vibration energy gets absorbed throughout the stack. If the system is "hard", the response of each tier is effectively added until the bottom container resists all the action. If the system is "soft", each container absorbs some energy thereby reducing the cumulative response.

The effect of stack height is determinable by comparing previous values of C_t to values calculated for a ten-tier stack (Fig. 6). The shift between a hard and soft system is again evident and rigid cushions are now possible at lower spring rates. If the unit weight remains unchanged, static conditions would load the bottom tier of a ten-tier stack three times that of a four-tier stack. A representative $C_t = 90$ corresponds to about $C_t = 15$ in

Figure 5, indicating that the expected total load is actually six times more than that of a four-tier stack. Additional tiers are thus more severe not only because they weigh more,



ML83 5397

Figure 6.--Contours of constant load multiplication factors C_t calculated for combinations of r and F in a ten-tier unitized load. The calculations assume $\rho = 0.115$.

but because their weight gets increasingly amplified during shipping.

CONCLUSIONS

The top-to-bottom strength requirements of unitized corrugated containers may exceed the normal static strength requirement depending on the compressive loads caused by transportation vibrations. The spring rates of top-loaded containers and cushions are primary properties determining dynamic loads.

This report proposes new ideas about the progressive deformation of corrugated containers with loading, using a set of dimensionless parameters, r , F , N , ρ , f , and C_t , which reduces the numbers of variables involved with calculating the response. The permanent yielding of material around the top of the box increases its spring rate and superior boxes yield gradually with lower tier position. Inferior boxes that deform excessively during initial loading cause high dynamic loads by equalizing the spring rates of the lower tiers.

Repeated loading experiments provided data on typical spring rates of corrugated containers and plastic bottles. The spring rates increased with greater equilibrium loads due to yielding of material. Flattening the horizontal scoreline, and pressing the bottle caps into the box flaps are primary causes of higher

spring rates with increased loading. As containers are stacked, the spring rate of each tier progressively decreases from the bottom tier to the top tier. Thus, by increasing the rate of changing stiffness in the various tiers using inserts, scoreline stiffness, interior package, etc. the dynamic load can be reduced.

This report also shows how the spring rates of cushions can affect the dynamic loading of containers. Cushions having spring rates lower than those of the containers absorb vibrations and significantly reduce the compressive loads. Extending the concept of a cushion implies that interior packages could be arranged to take advantage of their inherent cushioning ability.

The effects of progressive deformation and of cushions become more pronounced with more tiers. To reduce the dynamic load on the bottom tier you should therefore minimize the number of tiers, make containers that hold their shape with top loading, and softly support the contents using cushions or an effective arrangement of interior packages. It should be noted that excessively soft cushions could bottom-out and result in a damaged product.

ACKNOWLEDGMENT

W. D. Godshall provided data from his own unpublished exploratory investigations.

REFERENCES

1. American Society For Testing and Materials. 1975. Standard methods for vibration testing of shipping containers. D999-75.
2. Godshall, W. D. 1968. Effects of vertical dynamic loading on corrugated fiberboard containers. USDA, For. Serv. Res. Pap. FPL 94, For. Prod. Lab., Madison, Wis.
3. Godshall, W. D. 1971. Frequency response, damping and transmissibility characteristics of top-loaded corrugated containers. USDA For. Serv. Res. Pap. FPL 160, For. Prod. Lab., Madison, Wis.
4. Hatae, M. T. 1976. Packaging design. Shock and Vibration Handbook. McGraw-Hill.
5. Godshall, W. D. 1973. Vibration transmissibility characteristics of corrugated fiberboard. USDA For. Serv. Res. Pap. FPL 211, For. Prod. Lab., Madison, Wis.
6. Urbanik, T. J. 1978. Transportation vibration effects on unitized corrugated containers. USDA For. Serv. Res. Pap. FPL 322, For. Prod. Lab., Madison, Wis.

7. Urbanik, T. J. 1981. A method for determining the effect of transportation vibration on unitized corrugated containers. *The Shock and Vibration Bulletin*. pp. 213-224, May.
8. Ostrem, F. E., and W. D. Godshall. 1978. An assessment of the common carrier shipping environment. *USDA For. Serv. Gen. Tech. Rep. FPL 22, For. Prod. Lab., Madison, Wis.*
9. Crede, C. E., and J. E. Ruzicka. 1976. *Theory of vibration isolation. Shock and Vibration Handbook.* McGraw-Hill.
10. American Society For Testing and Materials. 1980. Standard method of conditioning paperboard, fiberboard, and paperboard containers for testing. D685-73.
11. Clough, R. W. and J. Penzler. 1975. *Dynamics of Structure.* McGraw-Hill.

DISCUSSION

Mr. Reed (Naval Surface Weapons Center, Session Chairman): I noticed that your data on the truck and train vibration went up to 100 Hz. That seems contrary to what is more or less standard practice.

Mr. Urbanik: The data are based on a compilation of about four major studies of the rail and truck transportation environments. It is based on the maximum expected acceleration level. There are some more statistically sophisticated presentations of the data, but the approach I used was a simplification that has been documented to smooth out the existing data.

LEAKAGE-FLOW INDUCED VIBRATIONS OF A CHIMNEY

STRUCTURE SUSPENDED IN A LIQUID FLOW

H. Chung
Components Technology Division
Argonne National Laboratory
Argonne, IL 60439

This paper presents the results of flow-induced vibration tests conducted to assess the vibration characteristics of a chimney structure suspended in a liquid flow. The test article is a full-scale model of a flow chimney used in a nuclear reactor as a part of reactor upper internals. Tests were performed by simulating all pertinent prototype conditions achievable in a laboratory environment. The test results show that the chimney experiences an unstable, motion-limited vibration which has a distinct lock-in phenomenon with respect to the flowrate. This unstable vibration is associated with the leakage-flow-modulated excitation through the small clearances between the chimney and its supports.

INTRODUCTION

Many nuclear reactor internal components have complex geometries and are subjected to high-speed coolant flow. On evaluating the flow-induced vibration characteristics of such components, experimental studies are generally required as analytical methods may not provide practically useful information.

Chimney-type structures are often used as a part of the upper-internal structures of a nuclear reactor. They are typically designed to conduct the coolant flow from the reactor core assembly to the upper plenum in order to prevent the control rods from experiencing cross-flow-induced vibrations and to minimize thermal striping on the upper-internal-structure (UIS) components. The flow chimney considered in this paper has complex geometry and is supported in a rather complicated manner.

This paper presents an experimental study of the flow-induced-vibration characteristics of a chimney structure suspended in a high-Reynolds-number liquid flow. The study includes an examination of the chimney's potential to rattle at its supports due to the potential leakage-flow excitation through the small clearances at the chimney supports.

CHIMNEY ASSEMBLY

Figure 1 shows a simplified schematic of the chimney and its support arrangement considered in this paper. The chimney assembly consists of a cylindrical chimney shell with its ends fitted with diaphragm rings and a control-rod shroud tube attached to the inner diameter of the diaphragm rings: essentially

two cylinders concentrically attached together. The inner and the outer rings are connected together by three tangential spokes.

There are two types of chimneys used in the reactor: Chimney A with the coolant flow from the core is constricted by the presence of the control rod drive line (CRDL) and Chimney B without such flow constriction. To allow expansion and shrinkage during thermal cycles of reactor operations, either chimney assembly is loosely fitted between the holes of the lower and the upper support plates of the UIS. The total weight of the chimney is solely supported at the lower support plate. The diametrical clearances between the chimney ends and the support slots are designed to be 0.013-0.041 cm (5-16 mils) taking into account manufacturing tolerances. However, these clearances would allow the chimneys to move within the constraints of the clearances.

The chimney is mostly made of Inconel 718. The chimney shell is approximately 218-cm (86-in.) long and has a 27-cm (10.75-in.) inner diameter with a 0.635-cm (0.25-in.) wall. The shroud tube is approximately 326-cm (129-in.) long. The cross-sectional dimensions of the shroud tubes are: 11.4-cm (4.5-in.) ID and 0.635-cm (0.25-in.) wall thickness. The weight of chimney is approximately 189 kg (418 lb). The prototype chimney operates under normal conditions of 537.8°C (1000°F) and 12.8 kPa (1.8 psi) pressure drop. The flow through the chimney is estimated to be 143.6 kg/s (1.14 x 10⁶ lb/hr or 2760 gpm), which corresponds to an average flow velocity of 3.75 m/s (12.29 ft/s).

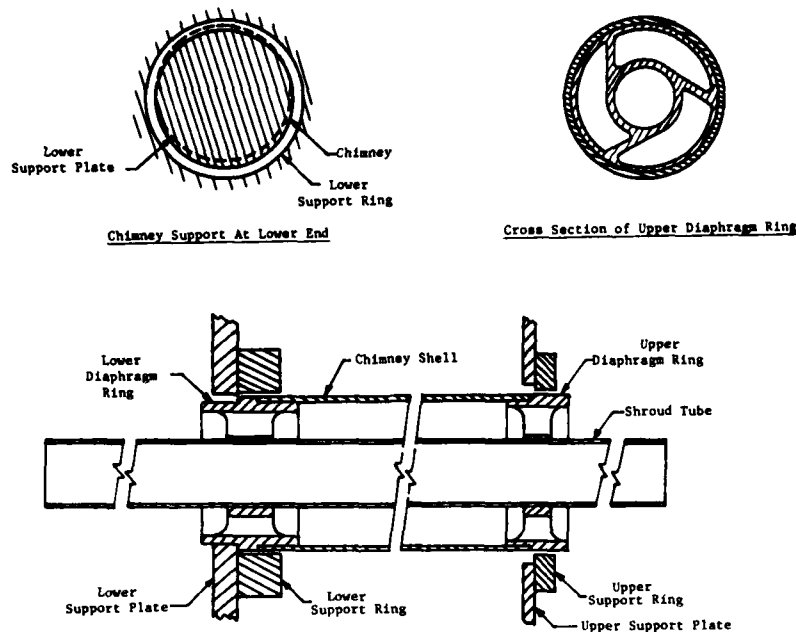


Fig. 1 - Simplified schematic of central chimney and supports

FLOW-INDUCED VIBRATIONS

There are three types of flow-induced-vibration mechanisms potentially involved in exciting the chimney.

(1) Leakage-flow-modulated excitation mechanism resulting from flow through the support clearances.

(2) Vortex-shedding excitation mechanism resulting from flow across the three spokes of the diaphragm rings.

(3) Turbulent random-pressure fluctuation on the surface of the chimney.

Since the chimney is subjected to high-Reynolds-number flow, well-defined vortex-shedding excitation may not occur. Turbulence flow and leakage-flow-modulated excitations are more important ones to consider. The leakage-flow-induced vibrations are strongly system-dependent and may not be easily predicted by analytical methods or by scale-model testing [1-3]. The geometry of the leakage-flow path, the pressure drop through the path, the fluid-film damping in the path, and the drag force are all important governing parameters. Turbulence flow excitation is another complicating factor on the chimney vibration. Therefore, a full-scale testing is necessary to obtain the vibration characteristics and to ensure that the chimney response, which, if significant, could result in excessive wear over the design life, is acceptable.

SIMILITUDE REQUIREMENTS

In order to accurately assess the vibration characteristics of the chimney, the

testing has to be performed with careful consideration of similitude parameters between the test and the prototype conditions. The pertinent similitude parameters are geometric parameters, material and fluid properties, flow velocities, and fluid-structure interaction parameters [4-5]. The fluid-structure interaction parameters include the Reynolds number, the Strouhal number, the Euler number, and the fluid damping factor.

Geometric similarity is achieved by designing the test model in full scale and retaining the geometrical features pertinent to flow-induced vibrations. Flow restrictions in Chimney A due to CRDL was modeled by blocking the top of the shroud tube. This modification is considered to be acceptable as it can lead to more conservative test results. The test model is made of Type 304 stainless steel, whose mechanical properties closely simulate Inconel 718 used in the prototype.

The ratio of the material and the fluid density is an important parameter on simulating the susceptibility of structure to flow-induced vibrations. This density ratio is approximately 20% larger for the prototype than the model, as the water density is approximately 20% larger than the sodium density.

The tests were performed with room-temperature water at flowrates up to 176% of the prototype design flowrate. At full scale, design flow, with water near room temperature, the Reynolds number is about 1/4 the prototypic Reynolds number, as the kinematic viscosity of water is about four times larger

than that of liquid sodium. However, Reynolds numbers with respect to the inner diameter of the chimney shell at the design flowrate are in the range of 10^6 for the prototype and the test model. In the high-Reynolds-number region ($>10^6$), flow-induced-vibration is usually independent of Reynolds number, thus the chimney vibrations will be well simulated in the model test with respect to vortex shedding and turbulence excitations.

The Reynolds numbers with respect to the support clearances are much smaller ($\sim 10^3$) than that for the chimney-shell inner diameter. The leakage-flow-modulated excitation mechanism has two important similitude parameters, among others, of Reynolds number and fluid damping factor. The Reynolds-number similarity invokes the larger clearance for the test model. However, the fluid damping drastically decreases as the gap size increases [6-7]. Consequently, variation in the clearance size and flowrates was selected as 0.0381-0.0635 cm (15 and 25 mils) in order to closely simulate the Reynolds number with respect to the width of the support clearances.

The Strouhal number is an essential parameter to achieve similarity of well-defined vortex-shedding excitation. Other flow-induced-vibration phenomena such as turbulent buffeting and fluidelastic instability may also require the similarity of Strouhal-number [4-5]. Therefore the potentially important Strouhal number was simulated by testing the model up to 176% of design flow.

The Euler number similarity requires

$$\left(\frac{\Delta p}{\rho_f V^2}\right)_p = \left(\frac{\Delta p}{\rho_f V^2}\right)_m$$

For the prototype flowrate in the model (v_m) and in the prototype (v_p), the pressure drop for the model with the prototypic support clearances is determined by

$$\begin{aligned} (\Delta p)_m &= \left(\frac{\rho_f}{\rho_p}\right)_m (\Delta p)_p = 1.21(\Delta p)_p \\ &= 15.2 \text{ kPa (2.2 psi)} \end{aligned}$$

and this similarity is achieved in the test.

The vibration response is largely governed by the system damping, including the structural and fluid-dynamic damping. Because of the uncertainty and difficulty in characterizing damping in the prototype, a generally used approach is to minimize structural damping in the model to thereby achieve a conservative test.

For the chimney configuration, the fluid-dynamic damping is expected to be much larger than the structural damping, due to narrow fluid gaps between the chimney ends and its supports. With the same support clearance

sizes, the fluid damping will be larger for the model than for the prototype as water has higher viscosity than liquid sodium. However, the selection of larger support clearances for the test model will offset this increase in fluid damping as fluid damping decreases with larger clearances. Consequently, the fluid-damping similarity is approximately achieved. However, because of uncertainties on quantifying the fluid damping, conservative modeling of the overall system damping is not fully ensured.

CHIMNEY TEST MODEL

The arrangement of the test assembly is shown in Fig. 2. A photograph of the test article is shown in Fig. 3. The test assembly consists of a chimney assembly, an upper and a lower support rings, and necessary vessel and pipings. The chimney shell was fabricated by rolling a Type 304 stainless steel plate and seam-welding it to form a cylindrical shell. The shroud tube was also made of Type 304 stainless steel seamless tube. The upper and lower diaphragm rings were sand-casted Type 304 stainless steel, and their outer and inner surfaces were machined to a close tolerance. The diaphragm rings were welded to the shroud tube at the upstream side and were fitted into the chimney shell with interference up to 76 microns (3 mils).

The main bodies of the support rings were made of Muntz metal with Type 304 stainless steel sleeve inserts. Thus the interface conditions between the chimney and the support rings were simulated to those of the prototype. Two pairs of support rings were

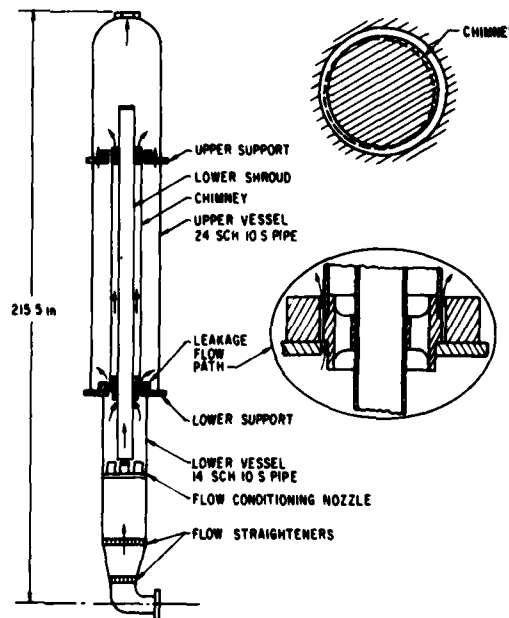


Fig. 2 - Chimney model test assembly



Fig. 3 - Cross-sectional view of chimney model assembly

fabricated; incurring 0.0381- and 0.0635-cm (15- and 25-mils) diametrical clearances. The pressure vessels accommodating the chimney assembly and its support clearance rings were fabricated from two segments of 24-in. ASA Schedule 10S welded pipe, three 24-in. ASA 150# forged flanges, and an elliptic head.

Vertical orientation of the test section and space limitation of the test facility precluded the direct connection of long runs of straight pipe to the immediate inlet of the test section. Consequently, it was necessary to use pipe bends and an area enlarged prior to the chimney inlet pipe. Two steps of flow straighteners were placed at the upstream of the test section to remove major distortions of the axial velocity profile and to simulate the fully developed flow expected in the prototype.

For the Chimney A test, flow through the central nozzle of the seven flow conditioning nozzles (Fig. 2) was blocked by a cap, while flow through the shroud tube was blocked by a plug at the top of the shroud tube (Fig. 3). However, neither of these flow restrictions were made for the Chimney B test.

The test section was connected to the Flow-Induced-Vibration Test Facility (FIVTF) at Argonne National Laboratory. The FIVTF is capable of providing up to 8000 gpm of room-temperature water and equipped with extensive flow control and measurement instruments.

INSTRUMENTATION

Two types of vibratory motion were anticipated: (1) chimney vibration due to flow-induced internal excitations and (2) external vibratory motion transmitted to the chimney from the test loop.

Requirements for the internal vibration-measuring transducers are that the transducers avoid disturbing the flow regime and are protected from the water-contamination. For internal vibration transducers, two pairs of

non-contacting displacement transducers (Kaman Science Model KD-2300-1S) and three pairs of miniature accelerometers (four Endevco Model 2220C and two Endevco PICOMIN Model 22) were selected and encased in small water-proofed containers and mounted inside the test section. Figures 4 and 5 show general layout of the test instrumentation and data-acquisition system. A pair of displacement transducers was mounted on each diaphragm rings, positioned 90° apart (D1 and D2 on the lower, and D3 and D4 on the upper ring) (see Fig. 6). Two pairs of accelerometers were also installed on the lower (A1 and A2) and the upper (A3 and A4) end of the chimney with the same sensing orientation as the displacement transducers. Accelerometers A5 and A6 were located on the chimney-shell surface about 96.5-cm (38-in.) above its lower end. To measure the global vibratory motion of the test section, triaxial accelerometers (Endevco Model 2228C) were mounted to the upper and lower flanges of the pressure vessel. The signals from all sensors were recorded on an FM tape recorder and analyzed by a Hewlett-Packard 5451C Fast Fourier Transform (FFT) analyzer.

The pressure drop across the chimney assembly were measured via two differential pressure transducers (Viatran Model 209). The absolute pressure at the top of the test section was also measured by a Bourdon gauge. The flowrates were measured by turbine flowmeters installed in the test loop (FIVTF). The loop water temperature was kept near 20°C

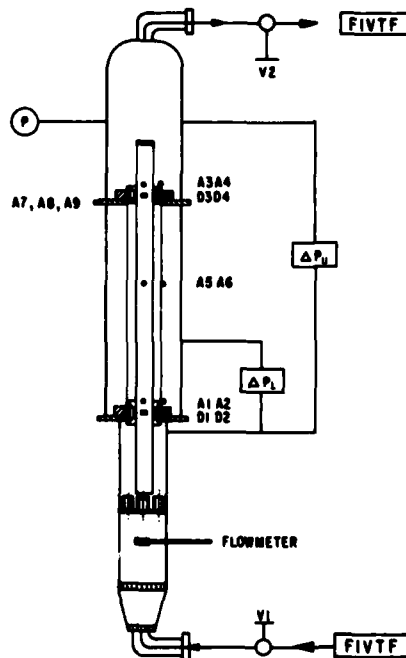


Fig. 4 - Chimney model test instrumentation

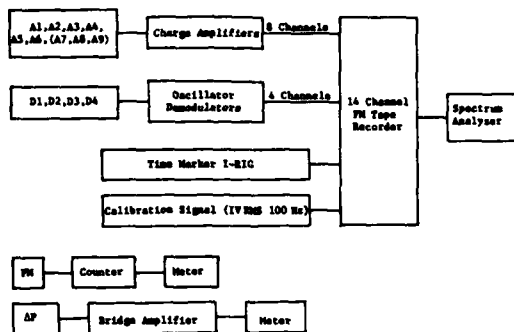


Fig. 5 - Schematic of data acquisition system



Fig. 6 - Upper support region with instrumentation

throughout the test performance. To verify the uniformity of the inlet flow velocity profile, a turbine flowmeter (Flow Technology Model FTP-GJS (S)) was placed immediately upstream of the inlet flow nozzles.

FREE VIBRATION TESTS

Prior to the flow tests, three phases of free vibration tests were performed to determine the free vibration characteristics of the chimney in air and in water, and thus to aid the interpretation of the flow-induced-vibration test results. Initially, the modal analysis testing with a Fourier analyzer system was performed to investigate the natural frequencies and the mode shapes of the chimney shell in air. Second, the chimney assembly was installed into the test rig and an impact test was performed. The transient-response signal was captured and processed by the Fourier analyzer to provide frequency spectra. In the third phase of testing, the test rig was filled with water and the same procedure as the second phase was repeated to identify the peak frequencies of the chimney assembly in water.

Natural frequencies of the chimney shell are high, greater than 180 Hz in air and 122 Hz in water. Analytical solutions [8] based

on the classical-shell theory were also used to substantiate the test results.

During the impact tests, the shell natural frequencies were well monitored from accelerometers A5 and A6. In-water impact test shows that the shell natural frequencies are substantially reduced due to the inertia effect of added water mass.

Accelerometers A1-A4, installed into the upper and lower supports of the chimney, revealed some additional resonance peaks other than the shell frequencies. These resonance peaks may be associated with the free vibration of the chimney-containing vessel, the test-assembly support frame, or the piping connected to the test section. However, these frequencies were considered not important for the present test program as we are primarily concerned with the chimney movement with respect to its support rings.

Displacement transducers D1-D4, mounted in pairs at the upper and lower support rings, measured the displacement of the chimney relative to the rings. Transducers D3 and D4, mounted at the upper ring, showed low-level frequency peaks at 19 and 14 Hz in air and in water, respectively. However, D1 and D2, mounted at the lower support ring, showed no predominant peak; the impact force exerted on the chimney was not large enough to shake the chimney. Based on these impact-test results, one can conclude that the chimney may rattle within the upper support ring at a frequency of 14 Hz during the flow-induced-vibration test. The impact tests also indicated that the damping of the chimney is small: <0.3% in air and <2% in water.

FLOW-INDUCED-VIBRATION TESTS

After the free-vibration tests, the test section was subjected up to 176% of the prototype design flowrate of 2759 gpm. The flow-induced-vibration tests were performed to characterize the dynamic behavior of the chimney as a function of flowrates for various support clearances configurations and to identify any dominant flow excitation mechanism associated with chimney vibrations.

A total of eight test configurations were tested: four different combinations of the upper and lower support clearances for Chimney A and B. Each test configuration was identified by three codes; for example, A-15-25 is Chimney A test with 15- and 25-mils clearances at the upper and the lower support, respectively. For each test configuration, the parameters varied were flowrate and loop static pressure. Measurements of displacements, accelerations, and pressures were made at the flowrates ranging from 12.5% to 176% of the prototype design flowrate and the flowrate for which any instability occurs. During the lower-flowrate (below 2500 gpm) testing, the static pressure in the test section was raised by throttling the downstream butterfly valve in order to maintain the minimum of 104 kPa

(15 psia). At higher flowrates, the upstream and downstream valves were left wide open. This effort was necessary to eliminate air bubbles in the flow, and thus minimize any two-phase flow effects and the possibility of cavitation.

During the tests the two displacement transducers measuring the lateral motion of the chimney at the upper and the lower support ring were displayed on an oscilloscope screen for continuous visual monitoring, and thus to identify the critical flowrate associated with any dominant flow-induced vibration. Because the frequency response of the taped recordings rolled off at ~1000 Hz, the accelerometer signals were scanned periodically and inspected on an oscilloscope screen for any visual sign of impacting.

Data tapes containing transducer signals were processed to provide displacement and acceleration PSD for the frequency range of 0-100 Hz; frequency components above 80% of the upper range limit were filtered out to minimize aliasing errors in the analog-to-digital converter. In the analysis range of 0-100 Hz, the spectrum was the results of ensemble averaging of 10 consecutive samples with a resolution of 0.195 Hz. The RMS displacement of the chimney at its upper and lower supports were calculated by integrating the displacement PSD. The RMS amplitudes based on accelerometer data were calculated by doubly integrating the acceleration PSD over the frequency bandwidth containing the vibration frequency of interest.

DISCUSSION OF RESULTS

Data-analysis results and visual observation during the tests revealed that Chimney A experienced an unstable, motion-limited vibration starting at ~120% of the prototype design flowrate. However, this vibration did not prevail with Chimney B where the flow through the shroud tube was allowed.

The vibration response of Chimney A at the lower support became unstable at ~3320 gpm and reached its total instability at ~3440 gpm; these are ~120% and ~125% of the design flowrate, respectively. This unstable vibration was concentrated at frequencies below 15 Hz as shown in Fig. 8, and persisted at higher flowrates without much changing its amplitudes and spectral contents. As the flowrate decreased, the response became restabilized at ~3135 gpm that is lower than the flowrate associated with the onset of instability; indicating the vibration has the hysteretic behavior with respect to the flowrate.

Inspection of the accelerometer signals during testing showed no recognizable evidence of impacting. The vibratory motion was limited by the support clearances and their associated squeeze-film fluid damping, with the result that amplitudes are smaller than the size of the clearances; the chimney was not impacting the support clearance rings.

However, the vibration amplitude at the upper support increased steadily with the flowrate; no apparent jump phenomenon was observed.

The observed flow-induced vibration is associated with the leakage-flow-modulated excitation mechanism controlled by the chimney weight, the flow lift force, and the asymmetry of the leakage-flow path. As the flowrate increases, the lift force exerting on the chimney rises. When the lift force becomes large enough to overcome the chimney weight, the chimney starts to levitate, incurring the change of leakage-flow paths and lateral fluid forces to the chimney (see Fig. 7). Lateral movements of the chimney and resulting changes in the leakage-flow paths are modulated to sustain the vibratory motions. As the chimney levitated with increasing flowrate, the leakage-flow paths became enlarged and the lift force exerting on the chimney stabilized; resulting the height of levitation settled became and did not increase with the flowrate.

Figure 9 presents RMS vibration amplitudes for a Chimney A configuration. The RMS displacements at the lower support jumped to higher values by an order of magnitude at ~125% of the design flowrate. However, they showed a gradual increase at the upper support. For the Chimney A configuration, D1 and D2 showed consistent patterns of jumps for all clearance configurations. On the contrary, D3 and D4 were somewhat inconsistent for different clearances.

The observed leakage-flow induced vibrations are also clearly demonstrated by the horizontal trajectory plots of the chimney movements as shown in Fig. 10. Starting with the onset of instability, the lower end showed a random pattern without a directional preference. However, the upper end initially showed a random pattern and, as the flowrate reached 3830 gpm (~138% of the design flowrate), it vibrated in a distinctly preferred direction which is perpendicular to the axis of the bottom support eccentricity. These vibration patterns are consistent for all clearance configurations of Chimney A.

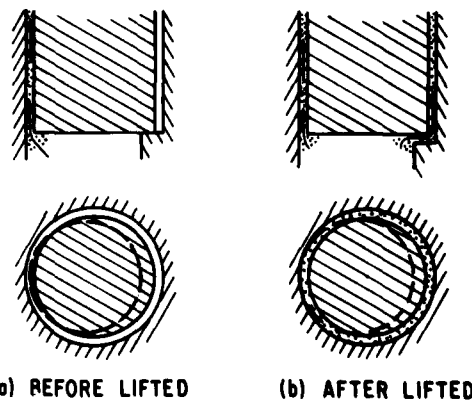


Fig. 7 - Leakage flow paths

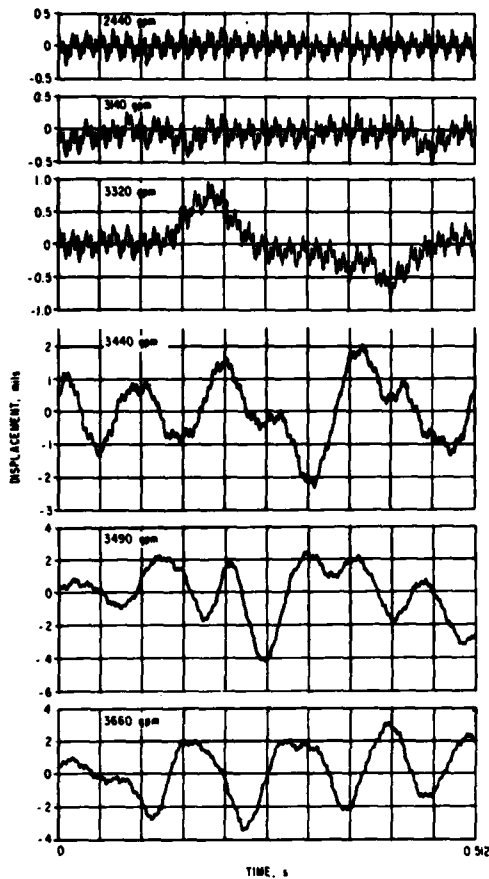


Fig. 8 - Displacement (D1) signals for Chimney A model (A-15-25) at various flowrates

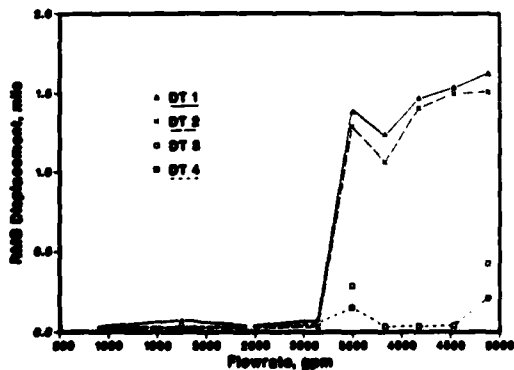


Fig. 9 - RMS displacements of Chimney A model for A-15-25

Spectral analyses of the displacement transducer measurements show that the observed flow-induced vibration is a band-limited random vibration in the frequency range of

5-15 Hz at the lower support and 2-10 Hz at the upper support. As discussed earlier for the time-history signals, the predominant frequencies of the vibration signals slightly increase with flowrate. PSD curves of the transducer signals (see Figs. 11-12) show these trends for the upper and lower end movements. PSD curves of accelerometers A5 and A6, showed a predominance of energy peaks near the natural frequencies of the chimney shell, 122, 364 Hz, etc. The PSD curves for external accelerometers showed quite different spectra from the internal accelerometer spectra; the chimney vibration and the loop piping motion were not coupled. On some PSD curves, electrical noises of 60 Hz are shown. In the calculation of the RMS displacement, the influence of these noises was neglected.

The maximum peak-to-peak displacements were also obtained from the time-history analysis of the displacement transducer signals. For all test configurations, the peak-to-peak amplitudes were smaller than the clearances at the upper and lower supports; attesting that the chimney was not impacting the support clearance rings. On the basis of idealized model-test criteria, the vibration amplitudes of the prototype chimney at the supports can be somewhat larger than the present test model due to the following reason. The kinematic viscosity of the prototype fluid, liquid sodium, is four times lower than that of room-temperature water. Therefore, a smaller fluid damping in the prototype may increase the vibration amplitudes. However, the conservatism is already built into the test results, as the test model was less restrictively designed for its vibrational movements at the supports and the test parameters were conservatively selected. This conservatism would more than offset the likely increase of vibration amplitudes due to the decrease of fluid damping in the prototype; the present test results are considered to be conservative with respect to the prototype case.

The pressure drops across the chimney (Δp_u) and across the lower support plate (Δp_l) were measured for each test configuration (Fig. 13). Very little pressure drop was expected across the upper support plate, because large cutouts were provided to simulate the conditions of the reactor's upper plenum. Consequently, Δp_u and Δp_l are expected to be similar; this was confirmed (see Fig. 13).

Based on the test specifications, the pressure drops were determined by dividing the total flow through the upper internal structures by the total number of chimneys. Consequently, the expected pressure drop (2.2 psi) calculated earlier for the chimney model testing is an average value for two different types of chimneys: Chimney A and Chimney B. Test results show that the total pressure drop (Δp_u) at the specified design flowrate (2760 gpm) are respectively ~4.0 and

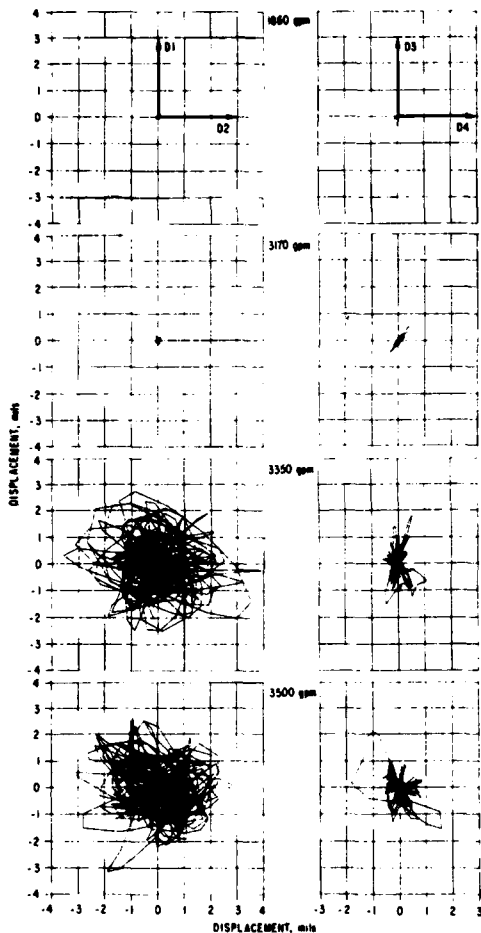


Fig. 10 - Vibration patterns of Chimney A model (A-15-15) at various flowrates

~1.9 psi for Chimney A and Chimney B. It is also contemplated that the actual flowrates would be different for Chimney A and Chimney B when they are subjected to the common pressure drop. At a pressure drop of 2.2 psi, the actual normal operating flow through Chimney A and Chimney B would be ~1900 and ~2950 gpm, respectively.

The vibration characteristics of Chimney B were distinctively different from those of Chimney A. Chimney B underwent low-amplitude random vibration; its amplitude was an order-of-magnitude smaller than for Chimney A for the same flowrates. As the shroud tube was not blocked, the lift force was not large enough to levitate the chimney. Consequently, the leakage-flow-modulated vibration could not occur in Chimney B. The flow turbulence was only attributed to its low-amplitude random vibrations.

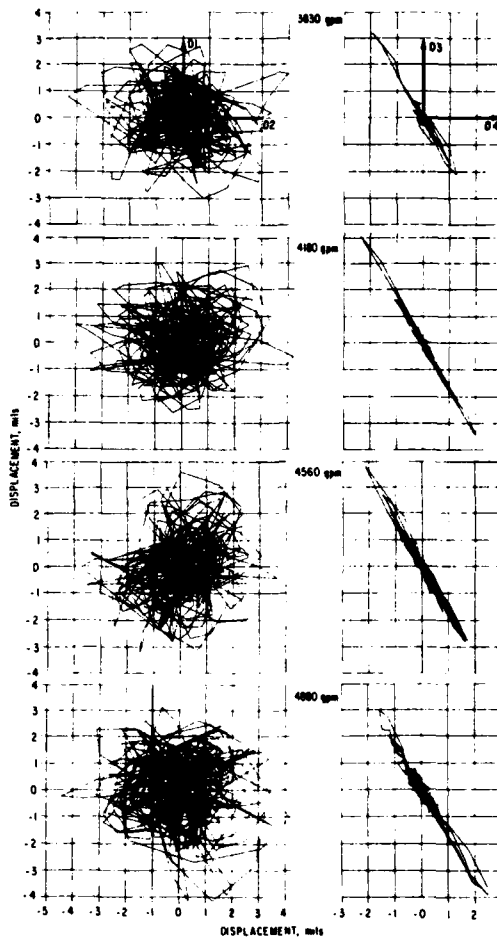


Fig. 10 (Contd.)

CONCLUSIONS

The flow-induced vibration characteristics of a chimney structure were investigated by testing a full-scale model subjected to simulated prototype conditions. Test results show that an unstable vibration occurred with Chimney A, however, not with Chimney B. The chimney levitated and underwent an unstable vibration starting at ~125% of the prototype design flow and a pressure drop of 5.5 psi. Before levitation of the chimney, it experienced a random vibration at the upper support in a narrow frequency band below 10 Hz with a small amplitude.

The chimney vibration after levitation is associated with a leakage-flow-modulated excitation mechanism that has controlling parameters of the chimney weight, the flow lift force, and the eccentricity of the leakage-flow path. While the chimney was undergoing an unstable vibration, its motion was being limited by narrow support clearances

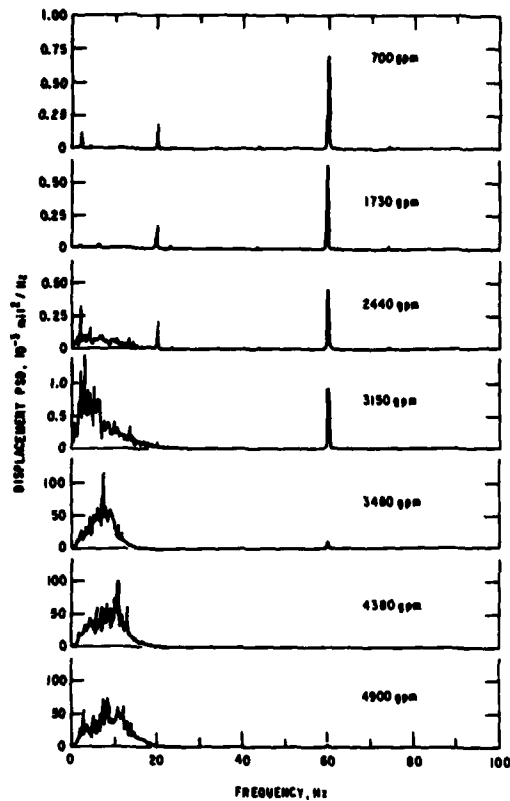


Fig. 11 - Displacement (D1) PSD for Chimney A model (A-25-25) at various flowrates

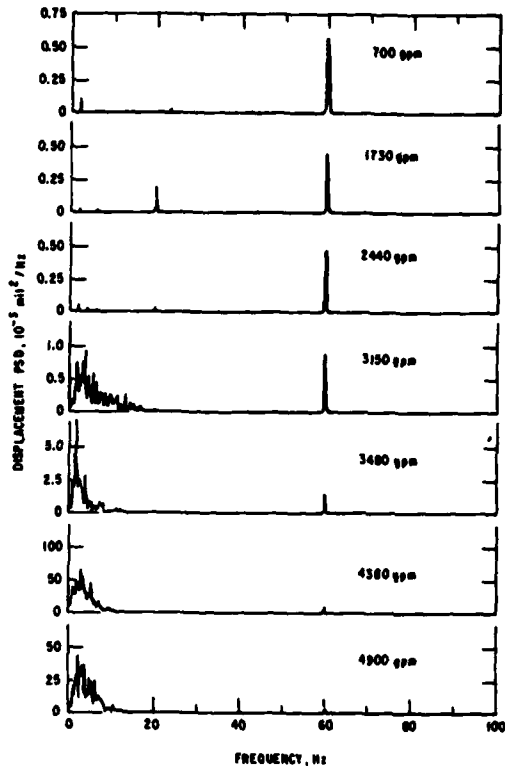


Fig. 12 - Displacement (D3) PSD for Chimney A model (A-25-25) at various flowrates

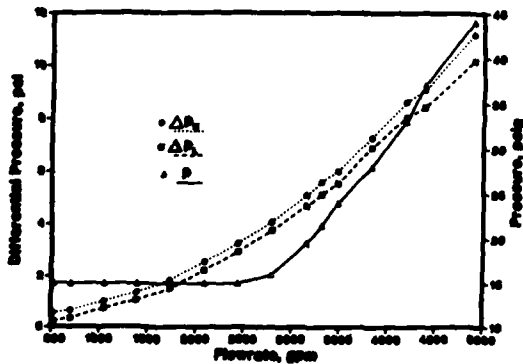


Fig. 13 - Pressure and pressure drop for Chimney A model (A-25-25) at various flowrates

and their associated squeeze-film damping, with the result that amplitudes are smaller than the sizes of the clearances. Consequently, these results and the observation of accelerometer signals during the tests lead to a conclusion that the chimney was not impacting the support clearance rings.

The prototype design flowrate (2760 gpm) is ~80% below the critical flowrate (3440 gpm) associated with the unstable vibration. Based on the pressure drop consideration, the actual normal operating flowrate through Chimney A would be ~1900 gpm, that is ~55% below the critical flowrate. Consequently, the observed leakage-flow-induced vibration would not occur with the prototype chimney under the normal operating condition. If an even higher margin of safety is desired, either the chimney weight should be increased or the flow path through the chimney should be redesigned to shift the balance point of the chimney weight and the lift force.

ACKNOWLEDGMENT

This work was performed under the sponsorship of the U.S. Department of Energy.

REFERENCES

1. M. R. Torres, "Flow-Induced Vibration of BWR Feedwater Spargers," ASME Spec. Publ. PVP-41, Flow-Induced Vibrations of Power Plant Components, presented at the ASME Pressure Vessel and Piping Conference, San Francisco (Aug 13-15, 1980).
2. J. E. Corr, "Big Rock Point Vibration Analysis," ANL-7685, Proceedings of the Conference on Flow-Induced Vibrations in Reactor System Components, Argonne National Laboratory, pp. 272-289, 1970.
3. D. E. Hobson, "Fluid-Elastic Instabilities Caused by Flow in an Annulus," presented at the 3rd Conference on Vibration in Nuclear Plant, May 11-14, 1982, Keswick, English Lakes, U.K.
4. G. S. Beavers and R. Plunkett, "Modeling of Flow-Induced Vibration in Heat Exchangers and Nuclear Reactors," Trans. ASME, J. Fluids Eng., pp. 358-364, Dec 1974.
5. A. Fortier, "General Considerations of the Problems of Aero- and Hydroelasticity," L. Houille Blanche, Vol. 5, 383-390, 1971.
6. T. T. Yeh and S. S. Chen, "The Effect of Fluid Viscosity on Coupled Tube/Fluid Vibrations," J. Sound Vib., Vol. 59, No. 3, pp. 1-24, 1978.
7. T. M. Mulcahy, "Fluid Forces on Rods Vibrating in Finite Length Annular Regions," Trans. ASME, J. Appl. Mech., Vol. 47, pp. 234-240, June 1980.
8. H. Chung, "Free Vibration Analysis of Circular Cylindrical Shells," J. Sound Vib., Vol. 74, No. 3, pp. 331-350, 1981.

DISCUSSION

Mr. Pinson (NASA Langley Research Center): You said you measured the flow rate. Did you measure the steady flow, or did you measure the unsteady flow?

Mr. Chung: I measured the steady flow, it was a steady flow problem.

Mr. Pinson: Do you have an analysis that quantitatively predicts the instability for this?

Mr. Chung: Yes. It was quantitative in the sense that we could measure the amplitude of vibration, and the data were obtained for a critical flow rate.

THE EXPERIMENTAL PERFORMANCE OF AN OFF-ROAD
VEHICLE UTILIZING A SEMI-ACTIVE SUSPENSION

E. J. KRASNICKI
LORD CORPORATION
ERIE, PENNSYLVANIA

The transition of the semi-active suspension system from an operating laboratory prototype into an operational off-road vehicle prototype, which utilizes a self contained semi-active suspension system, is presented. The modified vehicle and a stock vehicle, with a conventional passive suspension system, are compared on a designated test course. The experimental performance results of the "On-Off" semi-active system and the conventional system are compared and discussed. The improved performance of the semi-active system, predicted by analytical models, is experimentally verified.

INTRODUCTION

Semi-active vibration isolation was first disclosed in Reference [1]. This led to the original patent on the concept. Since then the analytical investigation and experimental verification of semi-active isolation systems has been well documented. References [2], [3], and [4] document both analytical and experimental verification of two variations of semi-active damping systems conducted at Lord Corporation. A brief presentation of the concept of a semi-active suspension system, its operation and performance advantages, as well as a discussion of the two semi-active concepts are included in this section.

Figure 1 represents 3 different types of simple single degree-of-freedom isolation systems which are used for discussion purposes. Figure 1a represents a conventional, totally passive suspension system. The linear frequency response of this system is illustrated in Figure 2 for a damping ratio, ζ , of 0.7.

The second schematic, Figure 1b, is representative of a fully active suspension system. These systems utilize a force generator connecting the ground input $V_{in}(t)$ and the sprung mass, m . This force generator can ideally produce any size force, in any direction, instantaneously. The typical realization of this force generator is a hydraulic actuator powered by a high pressure source. The feedback law utilizes a measure of the system state (the absolute velocity of

the mass in this case) obtained from a sensor located on the mass. This signal is then processed by the control algorithm to produce a desired control force, F . Various control algorithms may be used to obtain desired system performance.

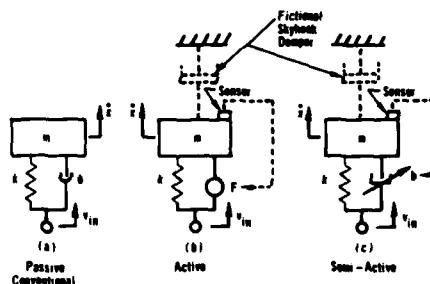


FIGURE 1
PASSIVE, ACTIVE, & SEMI-ACTIVE VERSIONS
OF A SINGLE d-o-f GROUND VEHICLE

A typical control strategy, which provides excellent resonance control coupled with excellent high frequency isolation, is to have the force actuator behave like a damper connected between the sprung mass and inertial ground. The force applied to the mass would be proportional to the absolute velocity of the mass. A passive device which would provide the identical control force is the theoretical "skyhook" damper. It is a

fictitious device for vehicle applications due to the absence of a true inertial reference. The position of the "skyhook" damper is illustrated in Figure 1. The frequency response of the totally active system is also illustrated in Figure 2. Fully active systems were investigated in the 1960's and were found to be costly, complex, and require significant amounts of external power. These systems are not very practical for suspending large heavy vehicles due to the large power requirements.

In contrast, semi-active control, shown schematically in Figure 1(c), provides improved ride quality in ground vehicles that approaches the performance of fully active systems while requiring no hydraulic power supply. This performance is accomplished using only low level electrical power needed for signal processing and valve actuation. The implementation of this hardware is significantly simpler and less costly than that of a fully active suspension system. The semi-active suspension is basically a passive suspension in which the damping forces can be instantaneously modulated. Reference [1] documents the introduction of semi-active control, while References [2], [3], and [4] show some of the development work that has occurred in the area of semi-active vibration isolation. The semi-active damper or force generator can be most easily conceptualized as a conventional hydraulic shock absorber in which the resistance in the fluid flow path can be instantaneously varied. In this way, the damper forces (although generated totally passively) can be controlled through application of a very small control effort. Therefore, a semi-active system would consist of a damper with characteristics that may be modulated, used in combination with a passive, conventional spring suspension. Since this is essentially a passive system, the actual damper force can be set equal to the desired control force only when the sign of the actual damper force is the same as that of the desired force. When this is the case, only a small amount of power is required to control very large damper forces. Through analysis and experimentation with many different dynamic systems, it has been found that this type of semi-active control can produce system behavior approaching that of a fully active system. Semi-active control is particularly well suited for shock and vibration control. This fact is clearly seen in Figure 2 where the frequency response of the semi-active system almost matches that of the fully active system with relatively insignificant amounts of power being used. Since semi-active systems are inherently nonlinear (or bilinear), the frequency response is actually interpreted from computer simulation of the system subject to harmonic input.

The control policy used by a semi-active suspension is essentially the same as that discussed for the fully active system. The

damper force, generated passively, is set to equal the desired force that would be generated by a passive "skyhook" damper whenever the sign of the actual and desired forces are the same. The major difference between the fully and semi-active system is the semi-active system sets the passively generated damper force to zero (more realistically, some flow area is set to its maximum value) when the desired and actual forces are of opposite sign. In this way the system minimizes the amount of energy put into the mass due to the base motion.

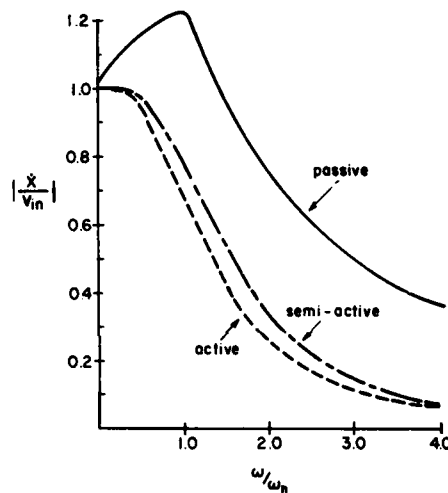


FIGURE 2
FREQUENCY RESPONSE FOR PASSIVE & ACTIVE
SINGLE d-o-f VEHICLES

The experimental prototype of the continuously variable "skyhook" semi-active system performed exceedingly well as shown in Ref. [2]. A much simpler version of the semi-active control policy consists of using an approach coined "on-off" control. In this system the logical decisions to have the damper "on" or "off" is made based on the "skyhook" policy just discussed for the continuously variable system, but the control force is not modulated in the "on" state. When the damper is on, a fixed flow area is provided. The theory and experimental performance of the device is discussed in Ref. [3]. The on-off, semi-active system has the advantage of not requiring continuously variable area modulation nor the associated microprocessor control. Since the on-off active damper is not generating the theoretical skyhook force, when it can, the system does not perform quite as well as the continuous force modulating system. However,

as shown in Ref. [3], the performance approaches that of the continuous semi-active system and is superior to conventional passive systems when enough damping is added to sufficiently reduce system resonance. Therefore, the on-off semi-active system trades off some system performance against reduced system cost and complexity.

The research efforts at Lord Corporation and the University of California have demonstrated analytically and experimentally that semi-active suspension systems achieve ground input isolation performance approaching that of hydraulically powered, totally active suspension systems ([2], [3], [4]). This paper documents the transition of the semi-active system from an operating laboratory prototype into an operational off-road vehicle prototype which utilizes a self contained semi-active suspension system. The modified vehicle and a stock vehicle, with a conventional passive suspension system, are compared on a designated test course. The performance results of the semi-active system and the conventional system are compared and discussed.

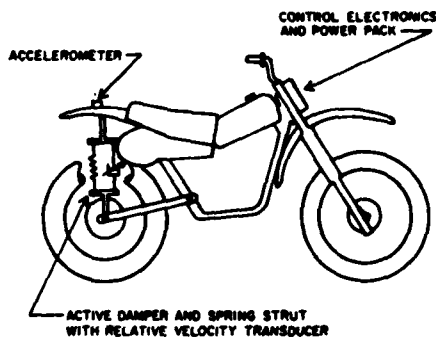


FIGURE 3
SCHEMATIC OF THE VEHICLE PROTOTYPE

THE HARDWARE PROTOTYPE

The vehicle that was used for the suspension modification and testing was a commercially available off-road motorcycle. The semi-active suspension hardware replaced the conventional suspension at the rear of the motorcycle only. The front fork assembly was not altered. Figure 3 schematically illustrates the hardware configuration. For simplicity, this schematic depicts the modified spring and damper assembly attached in a vertical orientation between the rear wheel and the suspended frame. The rear suspension used in most of the current

off-road motorcycles is a single spring and damper assembly, connected in various configurations, between the swing arm and the suspended frame. This arrangement expedited the implementation of a semi-active rear suspension.

The prototype motorcycle is a self contained system. The "On-Off" semi-active rear suspension, the required measurement transducers, the control electronics, and the electronic power supply were all contained within the motorcycle envelope. In this prototype, the power supply required by the control electronics and the control valve actuation device is a battery pack located on the motorcycle. In the future vehicle prototypes the power will be taken directly from the vehicle.

The absolute velocity of the rear of the suspended frame was obtained through integration of an acceleration signal. The relative velocity between the rear wheel and the suspended frame was measured directly. These two signals were used as inputs to the control algorithm.

The experimental performance of the conventional suspension system was obtained by replacing the "On-Off" semi-active system with the stock spring and damper strut. In this way, the changes in the vehicle dynamics due to the added weight and location of the control electronics and battery pack would be encountered by both suspension systems.

Both motorcycles were tested over the same test track, affording us the opportunity of directly comparing the two set of performance results.

DESCRIPTION OF THE TEST SETUP

The bump course used for this test consisted of 4 inch by 4 inch wooden beams spaced 15 feet apart, securely attached to the pavement. Eight beams were used; each beam was 48 inches long. These beams were securely fastened to a smooth, asphalt paved road. A chase vehicle (a pickup truck) was used to carry the instrumentation necessary for recording the motorcycle performance data. The testing was carried out at the Thomas Lord Research Facility in Cary, North Carolina.

The chase truck carried a Racal 4-channel FM tape recorder with which to record the necessary data, being the acceleration of the mass, the absolute velocity of the mass, the relative velocity between the wheel and the mass, and the relative displacement between the wheel and the frame, as well as other necessary diagnostic information. The instrumentation on the motorcycle was connected to the truck through breakaway cabling. No electronics, or measurement transducers, required for actively controlling

the suspension, were carried in the truck. Everything was on the motorcycle. All of the current test runs were made at one speed, 15 mph. Each run began approximately 500 feet before the first bump. This allowed adequate time for the motorcycle and the instrumentation truck to accelerate and enter the bump course at the desired speed. This speed was maintained throughout the entire bump course.

These tests were run with two different rider positions. The first set was conducted with the rider seated, and another set with the rider standing on the pegs. The latter is the position in which most motocross riding takes place. A direct comparison of isolation system performance was conducted by first testing all configurations of the Lord damper system, both semi-active and passive. Then, the stock conventional suspension system was installed and the same tests were conducted for various damping rate settings. The performance data collected during these tests allowed us to observe and verify the proper operation of the self contained "On-Off" damper prototype.

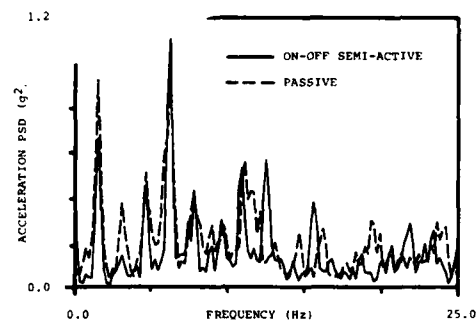
DISCUSSION OF THE RESULTS

The criteria used for evaluating performance of the suspension system are, acceleration of the rear of the suspended motorcycle frame and the relative displacement between the frame and the rear wheel (rattle space). These data were measured, recorded, and utilized as the comparative measure of suspension system performance. The taped information was then played back into a Hewlett Packard 5420 digital signal analyzer for an FFT (fast fourier transform) analysis. These results are presented in Figures 4 through 6. The acceleration data is presented in the form of standard power spectral density (PSD) plots. The acceleration PSD plots are always presented as part "a" of figures 4, 5, and 6. The solid traces always represent the acceleration response of the Lord damper under semi-active control. The dashed trace always represents the acceleration response of a passive damping system, whether it be the stock conventional damper strut or the Lord damper used in a passive mode. Both passive dampers were tested in a highly damped state and a lightly damped state.

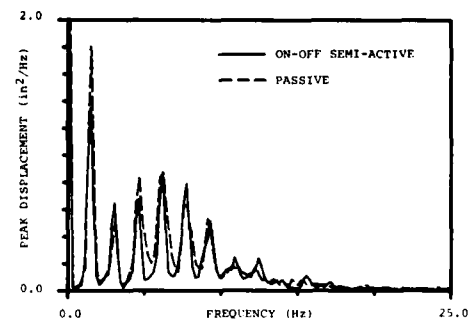
The relative displacement (rattle space) data were also analyzed by a fast fourier transform (FFT) analysis. These results are more meaningfully presented in the form of peak signal amplitude versus frequency plots. These data are presented as part "b" of figures 4, 5, and 6. The solid trace again always represents the relative displacement response of the Lord damper under semi-active control. The dashed trace always represents the displacement response of one of the passive damping systems. Again, both dampers

were tested in the passive mode with a highly damped and a lightly damped setting.

The acceleration PSD plots, as well as the peak relative displacement versus frequency plots, are calibrated. It is possible to read directly from each plot either the magnitude of the displacement per Hz. or $(g_{rms})^2/Hz$. The comparative nature of these plots show the relative performance between two damping systems. Comparisons of performance traces between different plots are also valid due to the consistency of recording technique and instrument calibration technique. In all cases, the X and Y axis of all plots are linear; therefore, relative performance differences are easily and accurately identified.



a. Acceleration PSD



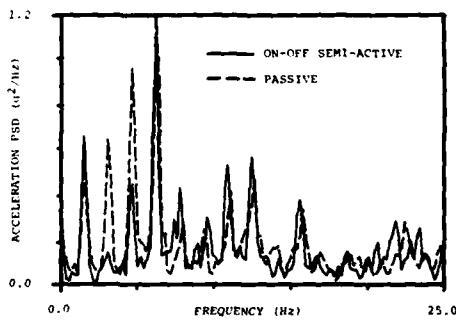
b. Relative Displacement (Rattle Space)

FIGURE 4
COMPARING THE ON-OFF SEMI-ACTIVE DAMPER
AND A LIGHTLY DAMPED PASSIVE DAMPER

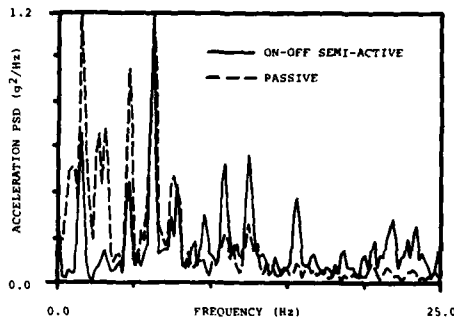
Figures 4, 5, and 6 represent test runs at 15 mph with the rider seated on the motorcycle. The results obtained from the test runs with the rider standing on the pegs are consistent with the illustrated results and are therefore not included in this paper.

The enormous amount of information in these plots, revealing particular suspension system performance in limited frequency regions, makes it impossible to discuss specific details in a paper of this kind. Therefore, only general interpretations of the results will be presented here. This leaves the reader the opportunity to investigate any or all regions of the data plots and form their own conclusions as to the performance advantages of the semi-active suspension system.

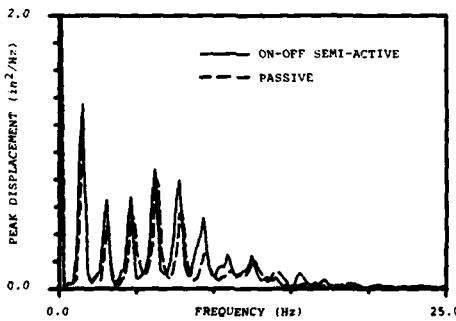
frequency gives us a relative performance reading between hardware systems. It is the author's opinion that large acceleration peaks at the low frequency, below approximately 10 Hz., are indicative of the large acceleration forces that would be felt by a rider, resulting in a harsh ride. Higher frequency accelerations tend to be isolated through structural and particularly seat compliance. The rider may not feel these accelerations, even though they look quite prominent in the PSD plot.



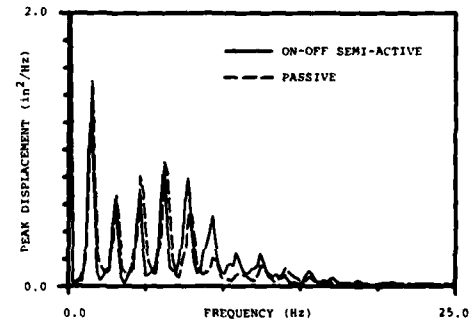
a. Acceleration PSD



a. Acceleration PSD



b. Relative Displacement (Rattle Space)



b. Relative Displacement (Rattle Space)

FIGURE 5
COMPARING THE ON-OFF SEMI-ACTIVE DAMPER
AND A HEAVILY DAMPED PASSIVE DAMPER

Generally speaking, the magnitude of the peaks in the acceleration PSD plot are a measure of the harshness of the ride as experienced by the rider. The magnitude of the peaks in the peak relative displacement plot are a measure of the amount of wheel travel. Comparing these peak magnitudes at a particular

FIGURE 6
COMPARING THE ON-OFF SEMI-ACTIVE DAMPER
AND THE STOCK PASSIVE DAMPER

The performance results presented in the acceleration PSD plots clearly illustrate that the acceleration peaks in the lower frequency regions (0 Hz to 10 Hz) are significantly and at times substantially smaller in magnitude than any of the passive damper configurations tested, whether the Lord damper or the stock

system had required no more rattle space than any of the passive systems, except the Lord damper in the highly damped setting.

These results demonstrate that when the self contained semi-actively suspended motorcycle is subjected to the described bump track, the acceleration levels to which the rider is subjected are significantly reduced without increasing the amount of wheel travel required to achieve such isolation. These test results experimentally verify that the self contained "On-Off" active damper is operating properly and demonstrates the performance advantages predicted analytically. These test results also are consistent with the test riders evaluation of reduced ride harshness and improved motorcycle controllability when the semi-active suspension is used in comparison to the passive suspension systems tested.

CONCLUSIONS

An off-road vehicle utilizing a self-contained, "On-Off" semi-active rear suspension has been successfully developed and tested. This vehicle prototype is a conventional off-road motorcycle which has been modified by replacing the existing rear suspension with an "On-Off" semi-active system. The vehicle system contains within its envelope all the necessary control system components and is, therefore, designated as self-contained.

The main purpose of this series of performance tests was to experimentally verify that a self contained "On-Off" semi-active system used in

suspension performance by minimizing acceleration of the motorcycle frame in the frequency region below 10 Hz, without increasing the required rattle space. The performance test results, included in this paper, document the fact that the semi-active rear wheel suspension of the test motorcycle does accomplish this objective. Because higher frequency vibrations are isolated through structural and seat compliance, the improved low frequency acceleration isolation leads to improved motorcycle controllability and reduced ride harshness for the rider.

REFERENCES

1. Karnopp, D.C., Crosby, M.J., Harwood, R.A., "Vibration Control Using Semi-Active Force Generators," ASME Paper No. 73-DET-122, June 1974.
2. Krasnicki, E.J., "Comparison of Analytical and Experimental Results for a Semi-Active Vibration Isolator," Proceedings of the 50th Shock and Vibration Symposium, October 1979.
3. Krasnicki, E.J., "The Experimental Performance of an "On-Off" Active Damper," Proceedings of the 51st Shock and Vibration Symposium, San Diego, October 1980.
4. Margolis, D.L., "Semi-Active Heave and Pitch Control for Ground Vehicles," Journal of Vehicle System Dynamics, Vol. II, No. 1, February 1982.

DISCUSSION

Voice: What is the primary frequency due to the spacing of the two by fours?

Mr. Krasnicki: 2 Hz.

Voice: Only 2 Hz?

Mr. Krasnicki: Yes. We hit one four by four about every half second at 15 miles per hour.

EFFECT OF AIR CAVITY ON THE VIBRATION
ANALYSIS OF LOADED DRUMS

SASADHAR DE
National Research Institute
P.O. Bankisol, Bankura
W.Bengal (INDIA)

The paper is concerned with the free vibration analysis of loaded circular and annular drums with an enclosed air cavity. The effect of the compressibility of the entrapped air on the vibration characteristics has been studied. The membrane over the drum is supposed to be composed of any number of parts with different materials and small loads are applied at the junctions. The modification of the frequency spectrum due to such loading has been mathematically analyzed and some particular cases have been discussed. It has been pointed out that both drums essentially follow the same rules in the study of the altered frequencies by the application of small loads at the junctions of the membranes. The possibility of construction of an annular drum-head like kettledrum may be suggested.

1. INTRODUCTION

The effect of air cavity on the vibration characteristics of circular [a-k] and annular [l] drums have been discussed. The vibration characteristics of Japanese drums, consisting of two membranes at either end of a curved cylindrical body, have been investigated [m]. The vibrations of loaded kettledrums [n-q] have been further analyzed and the early works have been reviewed [r,s]. It has been shown that some of the allowed values of frequency of a vibrating kettledrum can be made essentially harmonic because of the interaction with the air

inside the kettle [d], by careful adjustment of the tension [t] and by the application of small load on the membrane [n,o]. The present study deals with the free vibration analysis of circular and annular drums when the membranes are composite as well as loaded at the junctions. The harmonic relationships of loaded drums have been examined to give some information for the design of drums.

2. FUNDAMENTAL EQUATIONS

We consider a membrane composed of n parts

$$r_{k-1} \leq r \leq r_k$$

$k = 1, 2, \dots, n$; $\gamma_0 = 0$,
for the circular boundary. The mass
per unit area of the k -th membrane
is denoted by σ_k . The membrane is
stretched over one end of an airtight
vessel. The vibration displacements
 $w_k = w_k(r, \theta, t)$, $k = 1, 2, \dots, n$,
must satisfy the equation of motion
[a, q]

$$\frac{1}{c_k^2} \frac{\partial^2 w_k}{\partial t^2} = \nabla^2 w_k - \left(\frac{\rho_0 c_a^2}{V_0 \tau} \right) \sum_{k=1}^n \int_{r_{k-1}}^{r'_k} r' dr' \int_0^{2\pi} d\theta' w_k'(r', \theta'), \quad (1)$$

$$k = 1, 2, \dots, n, \quad c_k \ll c_a$$

where c_k is the speed of waves in the
membrane, $c_k^2 = \tau_k / \sigma_k$ (τ_k =
tension (force per unit length) in the
 k th membrane), V_0 is the equilibrium
volume of the enclosed cavity, ρ_0 is
the equilibrium density of air and c_a
is the velocity of sound waves in air
at the equilibrium pressure and temp-
erature in the vessel ($\equiv \sqrt{\gamma P_0 / \rho_0}$, γ
is the ratio of specific heats at
constant pressure to constant volume
of the entrapped air with equilibrium
pressure P_0).

Assuming $v_{ks} = R_k(r) T(s)$
 $\cos s\theta$ ($s = 0, +1, +2, \dots$), we find
that the θ -integral vanishes for
 $s \neq 0$. For the symmetrical vibrations
($s=0$), the above equation is rewritten
as

$$\frac{d^2 w_k}{dr^2} + \frac{1}{r} \frac{dw_k}{dr} + \beta_k^2 w_k = \left(\frac{2\pi \rho_0 c_a^2}{V_0 \tau} \right) \int_{r_{k-1}}^{r'_k} w_k'(r') r' dr', \quad (1a)$$

$$\beta_k^2 = \omega^2 / c_k^2, \quad k = 1, 2, \dots, n, \quad (2)$$

ω is the angular frequency of
vibration.

For a homogeneous circular mem-
brane of outer radius r_n stretched
over the drum, the frequency equation
is written as [a, x]

$$h J_0(\beta_n r_n) + \beta_n J_0'(\beta_n r_n) = 0$$

$$\text{i.e., } J_0(\beta_n r_n) + \lambda_n / \beta_n^2 J_2(\beta_n r_n) = 0, \quad (3)$$

where

$$h = \frac{(\lambda_n - \beta_n^2) r_n \beta_n^2}{2 \lambda_n}, \quad \beta_n = \omega / c_n,$$

$$\lambda_n = \pi \rho_0 c_a^2 r_n^2 / V_0 \tau.$$

For an annular drum (the membrane is
fastened rigidly at both the inner
edge of radius r_0 and the outer edge
of radius r_n), the possible values
of frequency are obtained from the
equation (1a) [1]

$$\begin{aligned} & [x_n^2 + \lambda'_n (1 - \Gamma^2)] [J_0(x_n) Y_0(\Gamma x_n) \\ & - J_0(\Gamma x_n) Y_0(x_n)] - \frac{2 \lambda'_n}{x_n} \{ \Gamma [Y_0(x_n) \\ & Y_1(\Gamma x_n) - J_0(x_n) Y_1(\Gamma x_n)] + \\ & [Y_0(x_n) J_1(x_n) - J_0(\Gamma x_n) Y_1(x_n)] \} \\ & + \frac{8 \lambda'_n}{\pi x_n^2} = 0, \quad (4) \end{aligned}$$

where $x_n = \beta_n r_0$, $\Gamma = r_n / r_0 > 1$,

$$\lambda'_n = r_0^4 \lambda_n / r_n^2$$

The equation (4) can be written as

$$\begin{aligned} & [x_n^2 + \lambda'_n (1 - \Gamma^2)] [J_0(x_n) Y_0(\Gamma x_n) \\ & - J_0(\Gamma x_n) Y_0(x_n)] + \frac{2 \lambda'_n}{x_n} \\ & \left\{ \frac{J_0^2(x_n) + J_0^2(\Gamma x_n)}{J_0(x_n) J_0(\Gamma x_n)} \right\} \\ & + \frac{8 \lambda'_n}{\pi x_n^2} = 0, \quad (5) \end{aligned}$$

where we have used the relation [y]

$$\begin{aligned} & J'_\mu(\xi_i b) Y_\mu(\xi_i a) - Y'_\mu(\xi_i b) J_\mu(\xi_i a) \\ & = \frac{1}{\xi_i b} \frac{J_\mu(\xi_i a)}{J_\mu(\xi_i b)} \quad (6) \end{aligned}$$

As $\lambda'_n \rightarrow 0$, the equation (5) reduces to

$$\begin{aligned} & J_0(x_n) Y_0(\Gamma x_n) - J_0(\Gamma x_n) Y_0(x_n) \\ & = 0, \quad (7) \end{aligned}$$

the frequency equation of an annular
membrane without the air cavity [v].

The fixed edges of radii r_0 and r_n impose restrictions on the allowed values of β_n . The presence of the vessel tends to raise the allowed values of frequency [a]. In the case of a circular drum, as the air cavity parameter, λ_n increases, the allowed values of frequency will increase, the fundamental being much more affected than the higher frequencies. In the case of an annular drum, the fundamental is the most affected frequency and thus the ratios of higher modal frequencies to first-mode frequency are decreased [1]. This lowering becomes more pronounced as λ_n increases.

3. INITIAL AND BOUNDARY CONDITIONS

The initial conditions of the problem are given, the same functions $f(r)$ and $g(r)$ being used throughout the membrane, by

$$w_k(r, 0) = f(r)$$

$$\left. \frac{\partial w_k}{\partial t} \right|_{t=0} = g(r), \quad k=1, 2, \dots, n. \quad (8)$$

The conditions of continuity and the boundary conditions are as follows [a, u]:

$$w_1(r_0, t) = 0, \quad t > 0 \text{ (for an annular drum)} \quad (9)$$

$$w_1(0, t) \text{ finite for any } t > 0 \text{ (for a circular drum)} \quad (10)$$

$$w_k(r_{k-1}, t) = w_{k-1}(r_{k-1}, t),$$

$$k = 2, 3, \dots, n, \quad t > 0$$

$$m_{k-1} \frac{\partial^2 w_{k-1}}{\partial t^2} = \tau_k \left(\frac{\partial w_k}{\partial r} \right) - \tau_{k-1} \left(\frac{\partial w_{k-1}}{\partial r} \right), \quad (11)$$

$$r = r_{k-1}, \quad k = 2, 3, \dots, n, \quad t > 0$$

m_{k-1} are the small loads per unit length of the membrane [a].

$$w_n(r_n, t) = 0, \quad t > 0 \quad (12)$$

4. CHARACTERISTIC MODE SOLUTION

The integrals $w_k = w_k(r, t)$ of equation (1a) are assumed to be of the form

$$w_k = R_k(r) T(t),$$

$$R_k(r) = A_k J_0(\beta_k r) + B_k Y_0(\beta_k r), \quad (13)$$

and

$$T(t) = C \cos \omega t + D \sin \omega t, \quad (14)$$

$$k = 1, 2, \dots, n,$$

β_k is defined in Sec. 2.

The conditions (9)-(12) are written as

$$R_1(r_0) = 0 \quad (15)$$

$$R_1(0) \text{ finite} \quad (16)$$

$$R_k(r_{k-1}) = R_{k-1}(r_{k-1})$$

$$m_{k-1} \frac{\partial^2 w_{k-1}}{\partial t^2} = \tau_k \frac{\partial w_k}{\partial r}(r_{k-1})$$

$$- \tau_{k-1} \frac{\partial w_{k-1}}{\partial r}(r_{k-1}), \quad k=2, 3, \dots, n, \quad (17)$$

$$R_n(r_n) = 0. \quad (18)$$

Using condition (16), we get

$$B_1 = 0 \quad (19)$$

and from conditions (15) and (18), we get

$$A_1 J_0(\beta_1 r_0) + B_1 Y_0(\beta_1 r_0) = 0 \quad (20)$$

$$A_n J_0(\beta_n r_n) + B_n Y_0(\beta_n r_n) = 0. \quad (21)$$

From equations (17), we get

$$A_k = \frac{\tau_{k-1}}{\tau_k} r_{k-1} (a_{k-1} A_{k-1} + \alpha_{k-1} B_{k-1})$$

$$B_k = \frac{\tau_{k-1}}{\tau_k} r_{k-1} (b_{k-1} A_{k-1} + \gamma_{k-1} B_{k-1}), \quad (22)$$

$$a_{k-1} = a_{k-1}(\omega, \lambda) = \left\{ -\beta_{k-1} J_0'(\beta_{k-1} r_{k-1}) \right.$$

$$\left. + \frac{m_{k-1} \omega^2}{\tau_{k-1}} J_0(\beta_{k-1} r_{k-1}) \right\} Y_0(\beta_k r_{k-1})$$

$$\begin{aligned}
& + \beta_k J_0(\beta_k \tau_{k-1}) Y_0'(\beta_k \tau_{k-1}) \\
\alpha_{k-1} = \alpha_{k-1}(\omega, \lambda) &= \left\{ -\beta_{k-1} Y_0'(\beta_{k-1} \tau_{k-1}) Y_0(\beta_{k-1} \tau_{k-1}) \right. \\
& + \frac{\tau_{k-1}^2}{2} Y_0(\beta_{k-1} \tau_{k-1}) \left. \right\} Y_0(\beta_k \tau_{k-1}) + \beta_k Y_0(\beta_{k-1} \tau_{k-1}) \\
& Y_0'(\beta_k \tau_{k-1}) \\
b_{k-1} = b_{k-1}(\omega, \lambda) &= \left\{ \beta_{k-1} J_0'(\beta_{k-1} \tau_{k-1}) - \frac{\tau_{k-1}^2 \omega^2}{2} \right. \\
& J_0(\beta_{k-1} \tau_{k-1}) \left. \right\} J_0(\beta_k \tau_{k-1}) - \beta_k J_0(\beta_{k-1} \tau_{k-1}) \quad (23) \\
& J_0'(\beta_k \tau_{k-1}) \\
\gamma_{k-1} = \gamma_{k-1}(\omega, \lambda) &= \left\{ \beta_{k-1} J_0'(\beta_{k-1} \tau_{k-1}) - \frac{\tau_{k-1}^2 \omega^2}{2} \right. \\
& Y_0(\beta_{k-1} \tau_{k-1}) \left. \right\} J_0(\beta_k \tau_{k-1}) - \beta_k J_0(\beta_{k-1} \tau_{k-1}) \\
& J_0'(\beta_k \tau_{k-1}),
\end{aligned}$$

the tension is supposed to be uniform in the present study.

5. EIGENFUNCTIONS

Equation (23) may be expressed in the matrix forms $[w, x, z]$

$$K_k = \pi/2 \tau_{k-1} M_{k-1}(\omega) K_{k-1}, \quad k = 2, 3, \dots, n$$

$$K_k = \begin{pmatrix} A_k \\ B_k \end{pmatrix}, \quad k = 1, 2, \dots, n$$

$$M_k(\omega, \lambda) = \begin{pmatrix} a_k(\omega, \lambda) & \alpha_k(\omega, \lambda) \\ b_k(\omega, \lambda) & \gamma_k(\omega, \lambda) \end{pmatrix} \quad (24)$$

$$k = 1, 2, \dots, (n-1).$$

From the above equations,

$$K_k = (\pi/2)^{k-1} \tau_1 \tau_2 \dots \tau_{k-1} P_{k-1}(\omega, \lambda) \begin{pmatrix} A_1 \\ B_1 \end{pmatrix} \quad k = 2, 3, \dots, n$$

(for the annular drum-head)

$$= (\pi/2)^{k-1} \tau_1 \tau_2 \dots \tau_{k-1} P_{k-1}(\omega, \lambda) \begin{pmatrix} A_1 \\ 0 \end{pmatrix} \quad k = 2, 3, \dots, n$$

(for the circular drum-head)

$$P_k(\omega, \lambda) = M_k(\omega, \lambda) M_{k-1}(\omega, \lambda) \dots M_2(\omega, \lambda) M_1(\omega, \lambda) \quad (25)$$

$$k = 1, 2, \dots, (n-1)$$

Let $\tau_1 \tau_2 \dots \tau_k = \tau^{(k)}$,

$$k = 1, 2, \dots, (n-1)$$

and hence the unknown constants A_k and B_k may be expressed in terms of A_k and B_k when $k = 1$. Putting

$$P_k(\omega, \lambda) = \begin{bmatrix} p_k^{[\mu, \nu]}(\omega, \lambda) \\ p_k^{[\mu, \nu]}(\omega, \lambda) \end{bmatrix}, \quad \mu, \nu = 1, 2, \quad k = 1, 2, \dots, (n-1)$$

we get from equations (24) and (25)

$$A_k = (\pi/2)^{k-1} \tau^{k-1} \left\{ p_{k-1}^{[1,1]}(\omega, \lambda) A_1 + p_{k-1}^{[2,2]}(\omega, \lambda) B_1 \right\} \quad (26)$$

$$B_k = (\pi/2)^{k-1} \tau^{k-1} \left\{ p_{k-1}^{[2,1]}(\omega, \lambda) A_1 + p_{k-1}^{[2,2]}(\omega, \lambda) B_1 \right\}$$

(for the annular drum)

$$k = 2, 3, \dots, n$$

and the same expressions for the circular boundary are obtained when $B_1 = 0$.

Substituting equation (26) in equation (20), we obtain

$$\begin{aligned}
A_k &= (\pi/2)^{k-1} \tau^{k-1} \left\{ p_{k-1}^{[1,1]}(\omega, \lambda) - p_{k-1}^{[1,2]}(\omega, \lambda) \right. \\
& \left. J_0(\beta_1 \tau_0) / Y_0(\beta_1 \tau_0) \right\} A_1 \\
B_k &= (\pi/2)^{k-1} \tau^{k-1} \left\{ p_{k-1}^{[2,1]}(\omega, \lambda) - p_{k-1}^{[2,2]}(\omega, \lambda) \right. \\
& \left. J_0(\beta_1 \tau_0) / Y_0(\beta_1 \tau_0) \right\} A_1 \quad (27)
\end{aligned}$$

Substitution of equation (27) into equations (21) gives

$$\sum_{m=0}^{\infty} A_m^{(1)} Q_m(\omega, \lambda) = 0, \quad (28)$$

where

$$\begin{aligned}
Q_m(\omega, \lambda) &= J_0(\beta_n \tau_n) \left\{ p_{n-1}^{[1,1]}(\omega, \lambda) - p_{n-1}^{[1,2]}(\omega, \lambda) \frac{J_0(\beta_1 \tau_0)}{Y_0(\beta_1 \tau_0)} \right\} + Y_0(\beta_n \tau_n) \\
& \left\{ p_{n-1}^{[2,1]}(\omega, \lambda) - p_{n-1}^{[2,2]}(\omega, \lambda) \frac{J_0(\beta_1 \tau_0)}{Y_0(\beta_1 \tau_0)} \right\}.
\end{aligned}$$

The system of equations (28) can yield non-vanishing solutions for $\lambda_m^{(1)}$, if the determinant of the coefficient vanishes. Thus the characteristic equation of the present problem is given by

$$\begin{aligned} & J_0(\beta_n \tau_n) \left\{ b_{n-1}^{[1,1]}(\omega, \lambda) Y_0(\beta_1 \tau_0) \right. \\ & - b_{n-1}^{[1,2]}(\omega, \lambda) J_0(\beta_1 \tau_0) \left. \right\} + Y_0(\beta_n \tau_n) \\ & \left\{ b_{n-1}^{[2,1]}(\omega, \lambda) Y_0(\beta_1 \tau_0) - b_{n-1}^{[2,2]}(\omega, \lambda) \right. \\ & \left. J_0(\beta_1 \tau_0) \right\} = 0, \end{aligned} \quad (29)$$

where β_n is a positive root of the equation (4).

For a circular drum, we obtain

$$\begin{aligned} & b_{n-1}^{[1,1]}(\omega, \lambda) J_0(\beta_n \tau_n) + b_{n-1}^{[2,1]}(\omega, \lambda) \\ & Y_0(\beta_n \tau_n) = 0. \end{aligned} \quad (30)$$

In this case, β_n is a positive root of the transcendental equation given by (3).

At a certain eigenvalue, ω_m , the set of coefficients is expressed from equations (27) as

$$\begin{aligned} A_m^{(k)} &= (\pi/2)^{k-1} \tau^{(k-1)} A_m^{(1)} \left[b_{k-1}^{[1,1]}(\omega_m, \lambda) \right. \\ & - b_{k-1}^{[1,2]}(\omega_m, \lambda) \left. \left\{ J_0(\beta_m^{(1)} \tau_0) / Y_0(\beta_m^{(1)} \tau_0) \right\} \right] \\ B_m^{(k)} &= (\pi/2)^{k-1} \tau^{k-1} A_m^{(1)} \left[b_{k-1}^{[2,1]}(\omega_m, \lambda) \right. \\ & - b_{k-1}^{[2,2]}(\omega_m, \lambda) \left. \left\{ J_0(\beta_m^{(1)} \tau_0) / Y_0(\beta_m^{(1)} \tau_0) \right\} \right]. \end{aligned} \quad (31)$$

Equation (2) gives the system of quantities

$$\beta_m^{(k)} = \omega_m / c_k, \quad k = 1, 2, \dots, n. \quad (32)$$

Substituting equations (31) into the expression (14) and using the expressions (32), we get, corresponding to the eigenvalue ω_m ,

$$\begin{aligned} U_m^{(k)}(\tau, t) &= (\pi/2)^{k-1} \tau^{k-1} U_m^{(k)}(\tau) V_m(t) \\ & \quad k = 1, 2, \dots, n \end{aligned} \quad (33)$$

where

$$\begin{aligned} U_m^{(1)}(\tau) &= J_0(\beta_m^{(1)} \tau) - \left\{ J_0(\beta_m^{(1)} \tau_0) / \right. \\ & \quad \left. Y_0(\beta_m^{(1)} \tau_0) \right\} Y_0(\beta_m^{(1)} \tau) \\ U_m^{(k)}(\tau) &= J_0(\beta_m^{(k)} \tau) \left[b_{k-1}^{[1,1]}(\omega_m, \lambda) \right. \\ & - b_{k-1}^{[1,2]}(\omega_m, \lambda) J_0(\beta_m^{(1)} \tau_0) / Y_0(\beta_m^{(1)} \tau_0) \\ & + Y_0(\beta_m^{(1)} \tau) \left[b_{k-1}^{[2,1]}(\omega_m, \lambda) \right. \\ & - b_{k-1}^{[2,2]}(\omega_m, \lambda) J_0(\beta_m^{(1)} \tau_0) / Y_0(\beta_m^{(1)} \tau_0) \left. \right] \left. \right] \end{aligned} \quad (34)$$

$k = 2, 3, \dots, n$

$$V_m(t) = A_m^{(1)} (C \cos \omega_m t + D \sin \omega_m t).$$

The expressions (34) define the eigenfunctions U .

In the case of a circular drum, the eigenfunctions are defined as $[x]$

$$U_m^{(1)}(\tau) = J_0(\beta_m^{(1)} \tau), \quad \tau^{(0)} = 1$$

$$\begin{aligned} U_m^{(k)}(\tau) &= b_{k-1}^{[1,1]}(\omega_m, \lambda) J_0(\beta_m^{(k)} \tau) \\ & + b_{k-1}^{[2,1]}(\omega_m, \lambda) Y_0(\beta_m^{(k)} \tau), \end{aligned} \quad (35)$$

$k = 2, 3, \dots, n$,

$$V_m(t) = A_m^{(1)} (C \cos \omega_m t + D \sin \omega_m t)$$

6. ORTHOGONALITY RELATIONS

The orthogonality relations of the eigenfunctions, U , can be derived as given in refs. $[w, x, z]$. The relations are

$$\sum_{k=1}^n \left(\frac{\pi^{(k)} \tau^{(k-1)}}{2^k c_k} \right)^2 \int_{\tau_{k-1}}^{\tau_k} \tau U_m^{(k)}(\tau) \times U_q^{(k)}(\tau) d\tau = 0 \quad (36)$$

$$m \neq q, \quad m, q = 1, 2, 3, \dots$$

7. SOLUTION OF THE PROBLEM

We can write the required solution of the problem in the form

$$\begin{aligned} W_k(\tau, t) &= \sum_{m=1}^{\infty} v_m^{(k)}(\tau, t) \\ & \quad \tau_{k-1} \leq \tau \leq \tau_k \\ & \quad k = 1, 2, \dots, n, \end{aligned} \quad (37)$$

where the expression $U_m^{(k)}(r, t)$ is determined by the expressions (33) and (34) in the case of an annular drum or by (33) and (35) in the case of a circular drum.

The two unsatisfied conditions (8) appear in the forms

$$C(\eta/2)^{k-1} r^{(k-1)} \sum_{m=1}^{\infty} A_m^{(1)} U_m^{(k)}(r) = f(r)$$

$$D(\eta/2)^{k-1} r^{(k-1)} \sum_{m=1}^{\infty} \omega_m A_m^{(1)} U_m^{(k)}(r) = g(r), \quad (38)$$

from which we can determine the quantities CA_{1m} , DA_{1m} .

Thus we find

$$CA_{1m} = f_m / N_m \quad (39)$$

and $DA_{1m} = g_m / \omega_m N_m$,

where

$$f_m = \sum_{k=1}^n \frac{\pi^{k+1} r^{(k-1)}}{2^{k+1} c_k^2} \int_{r_{k-1}}^{r_k} f(r) r U_m^{(k)}(r) g_m = \sum_{k=1}^n \frac{\pi^{k+1} r^{(k-1)}}{2^{k+1} c_k^2} \int_{r_{k-1}}^{r_k} g(r) r U_m^{(k)}(r) x dr$$

$$N_m = \sum_{k=1}^n \left(\frac{\pi^k r^{(k-1)}}{2^k c_k} \right)^2 \int_{r_{k-1}}^{r_k} r \{U_m^{(k)}(r)\}^2 dr$$

$m = 1, 2, 3, \dots$

The expressions (40) in the case of asymmetrical vibrations of the membrane ($s \neq 0$) are found to be

$$f_{ms} = \sum_{k=1}^n \frac{\pi^k r^{(k-1)}}{2^{k+1} c_k^2} \int_{r_{k-1}}^{r_k} f(r, \theta) r U_{ms}^{(k)}(r) \times g_{ms} = \sum_{k=1}^n \frac{\pi^k r^{(k-1)}}{2^{k+1} c_k^2} \int_{r_{k-1}}^{r_k} g(r, \theta) r U_{ms}^{(k)}(r) \times e^{-i s \theta} d\tau d\theta, \quad (40a)$$

$$N_{ms} = \sum_{k=1}^n \left(\frac{\pi^k r^{(k-1)}}{2^k c_k} \right)^2 \int_{r_{k-1}}^{r_k} r \{U_{ms}^{(k)}(r)\}^2$$

$s = 0, \pm 1, \pm 2, \dots$

Using these constants, we can write

the final solution (37) as

$$W_k(r, t) = (\eta/2)^{k-1} r^{(k-1)} \sum_{m=1}^{\infty} \frac{1}{N_m} U_m^{(k)}(r) \left[f_m \cos c_k \beta_m t + \left(\frac{g_m}{c_k \beta_m} \right) \sin c_k \beta_m t \right], \quad (41)$$

$$r_{k-1} \leq r \leq r_k, \quad k = 1, 2, \dots, n,$$

where the sum is taken over all the positive roots of equation (3) in case of a circular drum and of equation (5)

in case of an annular drum.

8. HOMOGENEOUS DRUM MEMBRANE

When a membrane is homogeneous, $\sigma_k = \sigma$ and $c_k^2 = c^2 = r/\sigma$, $\beta_k = \omega/c$, $k = 1, 2, \dots, n$ and

$$a_k(\omega, \lambda) = \gamma_k(\omega, \lambda) = 2/\pi r_k \quad (42)$$

$$\alpha_k(\omega, \lambda) = b_k(\omega, \lambda) = 0, \quad k = 1, 2, \dots, (n-1).$$

So, from equations (24) and (25), we get

$$M_k(\omega, \lambda) = \frac{2}{\pi r_k} \begin{bmatrix} 1 & 0 \\ 0 & 1 \end{bmatrix} \quad k = 1, 2, \dots, (n-1)$$

$$P_k(\omega, \lambda) = \frac{2^k}{\pi^k r^k} \begin{bmatrix} 1 & 0 \\ 0 & 1 \end{bmatrix} \quad (43)$$

$$\beta_m = \omega_m / c.$$

Upon using the expressions (40), (41),

(42) and (43), the solution for a

vibrating circular drum is finally

written in the form $[x]$

$$W(r, t) = \sum_{m=1}^{\infty} \frac{J_0(\beta_m r)}{\int_{r_0}^{r_n} r J_0^2(\beta_m r) dr} \times \int_0^{r_n} r J_0(\beta_m r) \left[f(r) \cos c \beta_m t + \frac{g(r)}{c \beta_m} \sin c \beta_m t \right] dr, \quad (44)$$

where the sum is taken over all the positive roots of equation (3).

The expression (44) in the case of an annular drum, will be of the form $[W]$

$$W(r, t) = \sum_{m=1}^{\infty} \frac{J_0(\beta_m r) Y_0(\beta_m r_0) - Y_0(\beta_m r) J_0(\beta_m r_0)}{\int_{r_0}^{r_n} \{J_0(\beta_m r) Y_0(\beta_m r_0) - Y_0(\beta_m r) J_0(\beta_m r_0)\} r dr} \times \int_{r_0}^{r_n} \{J_0(\beta_m r) Y_0(\beta_m r_0) - Y_0(\beta_m r) J_0(\beta_m r_0)\} \times \left[f(r) \cos(c \beta_m t) + \frac{g(r)}{c \beta_m} \sin(c \beta_m t) \right] r dr, \quad (45)$$

where β_m is a positive root of equation (5).

It is to be noted that in the case of asymmetrical free vibrations of an annular membrane (without the air cavity), the final form of the expression (45) is $[W]$

$$u(r, t) = \frac{1}{4} \sum_{s=1}^{\infty} \sum_{m=1}^{\infty} \left[\frac{\beta_{ms}^2 J_s^2(\beta_{ms} r_n)}{\{J_s^2(\beta_{ms} r_0) - J_s^2(\beta_{ms} r_n)\}^{1/2}} \int_0^{r_n} u_{ms}(\beta_{ms} r) \{f(r, \theta) \cos \beta_{ms} t + \frac{1}{c} \frac{\partial f(r, \theta)}{\partial t} \sin c \beta_{ms} t\} e^{-i s \theta} r^d + d \theta \right] u_{ms}(\beta_{ms} r), \quad (46)$$

$$u_{ms}(\beta_{ms} r) \equiv J_s(\beta_{ms} r) Y_s(\beta_{ms} r_0) - J_s(\beta_{ms} r_0) Y_s(\beta_{ms} r),$$

β_{ms} is a root of the equation (7).

9. TWO PART ANNULAR DRUM MEMBRANE

For an annular membrane consisting of two parts ($k = 2$), we get

$$\beta_1^{[1,1]} \equiv a_1(\omega, \lambda) = [-\beta_1 Y_0'(\beta_1 r_1) + \frac{m_1 \omega^2}{c} J_0(\beta_1 r_1)] Y_0(\beta_2 r_1) + \beta_2 J_0(\beta_1 r_1) Y_0'(\beta_2 r_1)$$

$$\beta_1^{[1,2]} \equiv a_1(\omega, \lambda) = \{-\beta_1 Y_0'(\beta_1 r_1) Y_0(\beta_1 r_1) + \frac{m_1 \omega^2}{c} Y_0(\beta_1 r_1)\} Y_0(\beta_2 r_1) + \beta_2 Y_0(\beta_1 r_1) Y_0'(\beta_2 r_1) \quad (47)$$

$$\beta_1^{[2,1]} \equiv b_1(\omega, \lambda) = [\beta_1 J_0'(\beta_1 r_1) - \frac{m_1 \omega^2}{c} J_0(\beta_1 r_1)] J_0(\beta_2 r_1) - \beta_2 J_0(\beta_1 r_1) J_0'(\beta_2 r_1)$$

$$\beta_1^{[2,2]} \equiv b_1(\omega, \lambda) = [\beta_1 J_0'(\beta_1 r_1) - \frac{m_1 \omega^2}{c} Y_0(\beta_1 r_1)] J_0(\beta_2 r_1) - \beta_2 J_0(\beta_1 r_1) J_0'(\beta_2 r_1).$$

The frequency equation obtained from (29) is written as

$$\frac{Y_0(\beta_1 r_1) J_0(\beta_1 r_0) - J_0(\beta_1 r_1) Y_0(\beta_1 r_0)}{Y_0(\beta_2 r_1) J_0(\beta_2 r_2) - J_0(\beta_2 r_1) Y_0(\beta_2 r_2)} =$$

$$\left[-\frac{m_1 \omega^2}{c} \{Y_0(\beta_1 r_1) J_0(\beta_1 r_0) - J_0(\beta_1 r_1) Y_0(\beta_1 r_0)\} + \beta_1 \{Y_0'(\beta_1 r_1) J_0(\beta_1 r_0) - J_0'(\beta_1 r_1) Y_0(\beta_1 r_0)\} \right] / \left[\beta_2 \{Y_0'(\beta_2 r_1) J_0(\beta_2 r_2) - J_0'(\beta_2 r_1) Y_0(\beta_2 r_2)\} \right]. \quad (48)$$

In the absence of the load, we get the corresponding equation from (48) by simply putting $m_1 = 0$. The right hand side of equation (48) can be written in a simplified form as

$$\left[\frac{m_1 r_1 \omega^2}{c} \{J_0(\beta_1 r_0) Y_0(\beta_1 r_1) - Y_0(\beta_1 r_0) J_0(\beta_1 r_1)\} + J_0(\beta_1 r_1) J_0(\beta_2 r_1) + J_0(\beta_1 r_0) J_0(\beta_2 r_1) \right] / J_0(\beta_1 r_1) J_0(\beta_2 r_2).$$

Here β_2 is a root of the equation given by (5)

For a nonhomogeneous composite membrane of the annular drum, we assume

$$\sigma_1 = \sigma_0 \quad \text{and} \quad \sigma_2 = \sigma_0 r_1^2 / r_2^2, \quad (49)$$

assuming the density distribution is continuous. (Density is supposed to be maximum for the first part and gradually decreases towards the boundary).

In this case, the frequency equation is written as

$$-\frac{m_1 \omega^2}{\beta_1 c} - J_0(\beta_1 r_0) / [\beta_1 r_1 J_0(\beta_1 r_1)] + \{Y_0(\beta_1 r_1) J_0(\beta_1 r_0) - J_0(\beta_1 r_1) Y_0(\beta_1 r_0)\}^{(50)}$$

$$= \cot(r_1 \beta_1 \ln \frac{r_1}{r_2}).$$

Let $\beta_{on}(0)$ and $\beta_{on}(m)$ represent respectively the frequencies in cps ($\beta_{on} = c/2\pi \beta_{on} = c x_{on}/2\pi r_0$) of an unloaded and loaded annular drum. Avoiding mathematical complexity, it can simply be written as an approximation

$$\beta_{on}^2(0) / \beta_{on}^2(m) = 1 + \frac{m_1}{\sigma_0 r_2} \left(\frac{r_1}{r_0}\right) \left(\frac{r_1}{r_0}\right) (x_{on})^2 \left\{ \frac{J_0(x_{on} \frac{r_1}{r_0}) Y_0(x_{on} \frac{r_1}{r_0}) - J_0^2(x_{on} \frac{r_1}{r_0})}{J_0(x_{on})} Y_0(x_{on}) \right\}, \quad (51)$$

$(m_1 / \sigma_0 r_2 \ll 1)$

where x_{on} can be obtained from equation (5) for different values of λ'_n [4].

As $r_1 \rightarrow r_0$, the radius of the inner edge, $\beta_{on}(0) \rightarrow \beta_{on}(m)$. The equation (51) (with equation (5)) shows that the possible values of frequency are functions of eccentric load m , λ'_n , r_1/r_0 and Γ . The variation of $\beta_{on}(m)$ with $m_1 / \sigma_0 r_2$ is shown in Tables 1 and 2 for $\lambda'_n = 0$ and 2 respectively.

Table - 1

(Frequencies vs. mass load for $\lambda'_n = 0$, $\tau_1/\tau_0 = 1.15$,
 $\tau_2/\tau_0 (\equiv \Gamma) = 1.25$)

$m_1/\sigma_0 \tau_2$	$x_{0n}(m)$			
	1	2	3	4
0.0	12.559	25.129	37.697	50.264
0.01	12.182	28.647	36.943	54.787
0.02	11.805	34.175	36.189	60.819
0.03	11.428	44.981	35.812	69.364
0.04	11.177	87.951	35.058	82.432

Table - 2

(Frequencies vs. mass load for $\lambda'_n = 2$, $\tau_1/\tau_0 = 1.15$,
 $\tau_2/\tau_0 = 1.25$)

$m_1/\sigma_0 \tau_2$	$x_{0n}(m)$			
	1	2	3	4
0.0	12.595	25.129	37.698	50.264
0.01	11.335	28.647	36.944	54.787
0.02	10.454	34.175	36.190	60.819
0.03	9.698	44.981	35.813	69.364
0.04	9.068	87.951	35.059	82.432

In the case of a circular drum, we have an approximate expression [q]

$$\frac{\gamma_{0n}^2(0)}{\gamma_{0n}^2(m)} = 1 + \frac{m_1 \beta_{0n}}{\sigma_0} \left[\frac{J_0(\beta_{0n} \tau_1)}{J_1(\beta_{0n} \tau_1)} \right], \quad (52)$$

$$m_1/\sigma_0 \tau_2 \ll 1$$

where β_{0n} can be obtained from equation (3). The values of β_{0n} ($\equiv \pi \gamma_{0n}/\tau_2$) can be obtained from Morse (1948) [a] for different values of $x_n (\equiv \lambda_n \tau_1)$. The frequencies in cps are $\gamma_{0n} = \beta_{0n} c/2\pi = \gamma_{0n} c/2 \tau_2$. The equation (52) has been analyzed in detail [q] to study the frequency spectrum of a loaded kettledrum. The variation of $\gamma_{0n}(m)$ with different values of $m_1/\sigma_0 \tau_2$ for $x_n = 0$ and

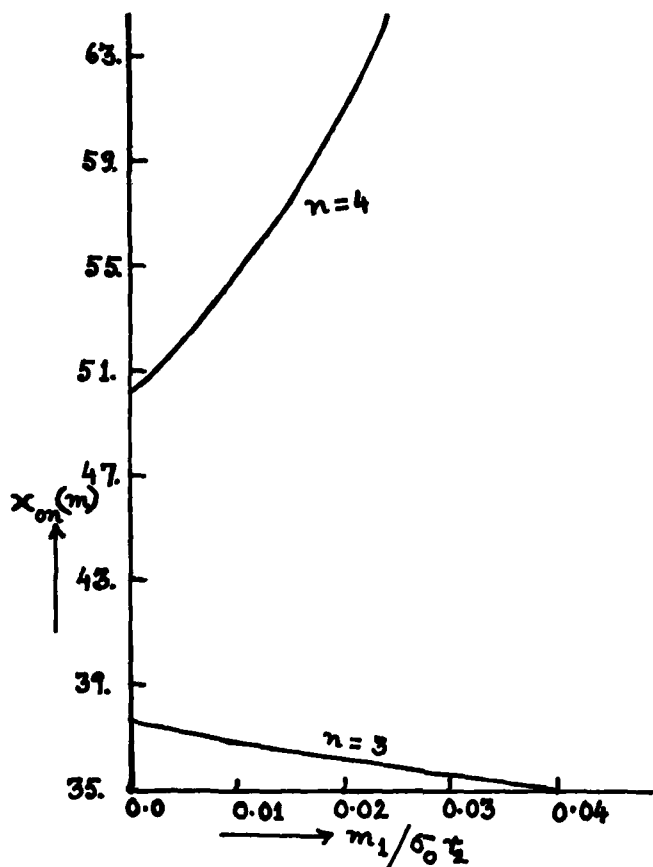


Fig. 1. Plot of $x_{on}(m)$ vs. $m_1/\sigma_0 r_2$ for $\lambda'_n = 2$ (annular drum)

2 is shown in Tables 3 and 4 respectively.

Table - 3
(Frequencies vs. mass load for $\alpha_n = 0, r_1/r_2 = 0.5$)

$m_1/\sigma_0 r_2$	$f_{on}(m)$			
	1	2	3	4
0.0	0.766	1.757	2.755	3.754
0.01	0.750	1.767	2.534	3.866
0.02	0.743	1.775	2.369	3.941
0.03	0.727	1.788	2.204	4.054
0.04	0.720	1.792	2.094	4.166

Table - 4
 (Frequencies vs. mass load for $x_n=2$, $r_1/r_2 = 0.5$)

$m_1/\sigma_0 r_2$	$\omega_n (m)$			
	1	2	3	4
0.0	0.851	1.765	2.757	3.754
0.01	0.834	1.783	2.536	3.867
0.02	0.826	1.818	2.371	3.942
0.03	0.817	1.836	2.217	4.054
0.04	0.757	1.853	2.095	4.167

It is found that the fundamental and the third overtone (odd overtones) gradually decrease with the increase of loading whereas the second and fourth overtones (even overtones) increase with the increase of loading. The overtones of a kettledrum due to such loading also follow the same rules. Thus an annular drum may behave like a kettledrum in the study of frequencies due to such special loading. The effect of air cavity parameter and the harmonic relationships of an annular drum have been analyzed in detail [1]. The characteristics for construction of an annular drum-head like kettledrum may be suggested which supports Gottlieb's ('79, '82) investigations (refs. 1,v).

10. APPROXIMATE EXPRESSION FOR SMALL FREQUENCY OF A LOADED ANNULUS

For small values of β_1 , we obtain from equation (50)

$$\beta_1^2(m) = \sigma_0 \left[\frac{1}{m_1 r_1 \ln \frac{r_2}{r_1}} - \frac{\pi}{2m_1 r_1 \ln \frac{r_2}{r_1}} \right] \quad (53)$$

and
$$\beta_1^2(0) = \frac{\pi}{2 r_1^2 \ln \frac{r_2}{r_1} \ln \frac{r_2}{r_1}}$$

Thus, we get

$$\omega^2(m)/\omega^2(0) = \frac{\sigma_0 r_1}{\pi m_1} \left(1 - \frac{\pi \ln \frac{r_2}{r_1}}{2 \ln \frac{r_2}{r_1}} \right). \quad (54)$$

This simply shows that the added mass (g/cm) is an important factor in the study of the altered frequencies of a freely vibrating membrane. The frequencies also depend on the relative values of r_0 , r_1 and r_2 .

11. CONCLUDING REMARKS

The membrane is first decomposed into a sequence of finite parts (e.g., like finite elements) to allow the separate pieces have different material constants (or different thicknesses and the development of the natural frequencies has been analyzed. It is found that as the mass load increases, the frequency of a loaded annular membrane decreases. The same is true in the case of a circular membrane [4]. The pitch can be altered not only by tension but also by added mass. The effect of air cavity on the natural frequencies and mode shapes of a loaded annular drum gives some information to the drum designer. The frequencies of modes (of the drum under consideration) are in order that would be of interest to the acoustic community concerned with the design of musical instruments.

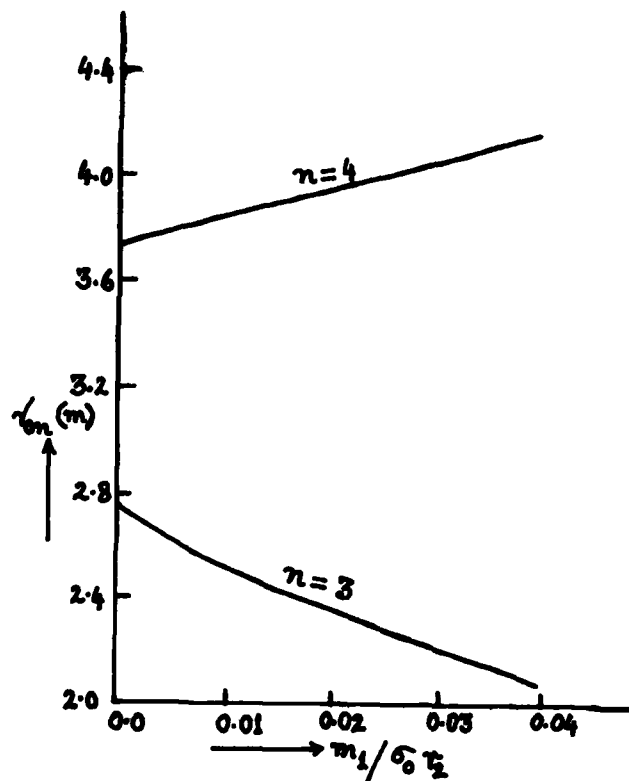


Fig. 2. Plot of $\nu_n (m)$ vs. $m_1 / \sigma_0 \tau_2$ for $\alpha_n = 2$ (circular drum)

ACKNOWLEDGMENT

The author wishes to thank Sri Chanchal De and Sri Sajal De for their help in the preparation of the manuscript.

REFERENCES

- a. P.M.Morse, Vibration and Sound, 2nd ed., McGraw-Hill, 1948.
- b. L.E.Kinsler and A.R.Frey, Fundamentals of Acoustics, 2nd ed., Wiley, New York, 1962.
- c. J.W.S.Rayleigh, The Theory of Sound, Vol. I, Dover, New York, 1945.
- d. A.H.Benade, Fundamentals of Musical Acoustics, Oxford U.P., New York, 1976.
- e. C.V.Raman and S.Kumar, "Musical Drums with Harmonic Overtones," *Nature*, **104**, 500, 1970.
- f. C.V.Raman, "The Indian Musical Drums", *Proc. Ind. Acad. Sci.*, **A1**, 179, 1935.
- g. F.Bennett, "The Mridangam of South India", *The Percussionist*, **19**(1), 24, 1981.
- h. B.S.Ramakrishna and M.M.Sondhi, "Vibrations of Indian Musical drums Regarded as Composite Membranes", *J. Acoust. Soc. Am.*, **26**, 523, 1954.
- i. T.D.Rossing and W.A.Sykes, "Acoustics of Indian Drums", *The Percussionist*, Nov. 1981. (T.D.Rossing, "The Physics of Kettledrums," *Sci.Am.*, **247**(5).

- 147, 1982).
- j. S.De, "Vibration of a Kettledrum," J. Acoust. Soc. Am., 51(5), Pt. 2, 1968-70, 1972.
- k. S.De, "On the Vibration of a Circular Membrane Backed by an Airtight Vessel," Acta Geophy. Pol., 21(3), 242-5, 1973.
- l. H.P.W.Gottlieb, "Effect of Air Cavity on the Annular Drum," J. Acoust. Soc. Am., 71(4), 1025-1027, 1982.
- m. J. Obata and T.Tesima, J.Acoust. Soc. Am., 6, 267-274, 1935.
- n. S.De, "Vibrations of a Loaded Kettledrum," J.Sound Vib. 20(1), 79-92, 1972.
- o. S.De, "Experimental Study of the Vibration Characteristics of a Loaded Kettledrum," Acustica, 40, 206, 1978.
- p. S.De, "Note on the Forced Vibration Analysis of a Loaded Kettledrum," Rev. Roum. Des Sci. Tech. Mec. Appli. (to be published), 1983.
- r. S.De, "Approximate Methods for Determining the Vibration Modes of Membranes," The Shock & Vib.Digest, 7 (9), 81-92, 1975.
- s. S.De, "Approximate Methods for Determining the Vibration Modes of Membranes," (submitted) 1982.
- t. J.Backus, The Acoustical Foundations of Music, Norton, New York, 1969.
- q. S.De, "Vibrations of Loaded Composite Membranes," Proc. Ind. Soc. Theort. & Appl. Mech.Congr., 140-152, 1977.
- u. S.De, "Solution of the Equations of Vibrating Loaded Composite Membranes of Various Boundaries," Rev. Roum. Des Sci. Tech. Mech. Appli. (to be published).
- v. H.P.W.Gottlieb, "Harmonic Properties of the Annular Membrane," J.Acoust. Soc. Am. 66(2), 647-650, 1979.
- w. S.De, "Vibrations of a Composite Annular Membrane," J. Sound Vib. 17(1), 13-23, 1971.
- x. S.De, "Vibrations of a Composite Circular Membrane," Ind. J. Pure & Appl. Math., 3(6), 1150-1168, 1972.
- y. I.N.Sneddon, Fourier Transforms, McGraw-Hill (New York, Toronto, London), 1951.
- z. Vačlaw Vodička, "Free Vibrations of a Composite Circular Membrane," J. Phys. Soc. Japan, 17(4), 14, 1962.